UNIVERSIDADE TÉCNICA DE LISBOA
INSTITUTO SUPERIOR TÉCNICO

Modelling MIMO Systems in Body Area Networks in Outdoors

Michał Łukasz Maćkowiak

Supervisor: Doctor Luís Manuel de Jesus Sousa Correia

Thesis approved in public session to obtain the
Ph.D. Degree in Electrical and Computer Engineering

Jury final classification: Pass with Merit

Jury

Chairperson: Chairman of the IST Scientific Board
Members of the Committee:
Doctor Alain Sibille
Doctor Jorge Manuel Lopes Leal Rodrigues da Costa
Doctor Luís Manuel de Jesus Sousa Correia
Doctor Custódio José de Oliveira Peixeiro
Doctor António José Castelo Branco Rodrigues

2013

UNIVERSIDADE TÉCNICA DE LISBOA
INSTITUTO SUPERIOR TÉCNICO

Modelling MIMO Systems in Body Area Networks in Outdoors

Michał Łukasz Maćkowiak

Supervisor: Doctor Luís Manuel de Jesus Sousa Correia

Thesis approved in public session to obtain the
Ph.D. Degree in Electrical and Computer Engineering

Jury final classification: Pass with Merit

Jury

Chairperson: Chairman of the IST Scientific Board
Members of the Committee:
Doctor Alain Sibille, Full Professor, Télécom Paris Tech, França
Doctor Jorge Manuel Lopes Leal Rodrigues da Costa, Professor Associado
    (com Agregação), do Instituto Superior de Ciências do Trabalho e da
    Empresa do Instituto Universitário de Lisboa
Doctor Luís Manuel de Jesus Sousa Correia, Professor Associado (com Agregação)
    do Instituto Superior Técnico, da Universidade Técnica de Lisboa
Doctor Custódio José de Oliveira Peixeiro, Professor Auxiliar do Instituto Superior
    Técnico, da Universidade Técnica de Lisboa
Doctor António José Castelo Branco Rodrigues, Professor Auxiliar do Instituto
    Superior Técnico, da Universidade Técnica de Lisboa

2013

to my beloved

Hania, Zosia and Leon

Acknowledgements

In the first place, I would like to express my deep gratitude to Professor Luis M. Correia, for patient guidance, enthusiastic encouragement, corrections and great help during my work and stay in Portugal. His broad experience, unconditional support and many useful critiques of this research work allowed to keep my progress on schedule.

My grateful thanks are also extended to Carla Oliveira for her friendship, productive ideas, a very effective cooperation and fruitful discussions throughout this work.

I would like to express my gratitude to all members of GROW and my colleagues from IST-TUL, for their support and sharing of ideas.

My gratitude to IST, for the logistics provided that made this thesis possible.

I also thank FCT for the scholarship and for all the financial support.

I would like to thank the European Commission for financing the projects in which I was involved during the period of this thesis, which are: COST 2100, COST IC1004, NEWCOM++, NEWCOM, LEXNET.

I am also grateful to all my friends, for their kind support.

I send my special acknowledgements to my parents, for their lifetime support and encouragement in what I did.

My grateful thanks are also extended to my brother, and rest of my family in Poland, because I can always count on them.

Above all, I wish to express my deep gratitude to my beloved wife Hania and my wonderful children Zosia and Leon.

Abstract

The aim of this work is to develop a radio channel model for MIMO systems applied to Body Area Networks for off-body radio links in a multipath environment. Firstly, the influence of the body on antenna performance has been evaluated. Then, the body dynamics were taken into account and model based on Motion Capture data has been developed. Finally, the propagation environment has been modelled using Geometrically Based Statistic Channel model. A patch antenna operating at 2.45 GHz is simulated in Computer Simulation Technology, near to a voxel model. Multi-Path Components are obtained for a street scenario, for a running or walking body, and for various on-body antenna placements. The propagation conditions are determined and statistics of basic channel parameters are calculated. Moreover, the analysis of MIMO capacity are performed and the optimum location of antennas are selected. The influence of the body is the highest when the antenna is attached to the body. Gain patterns are significantly modified by the body movement, as well as channel parameters. For the running body, when the antenna is located on the arm, 9 dB deep fades in the average received power are captured. The MIMO capacity strongly depends on the power imbalance between antennas.

Keywords

Channel Models. MIMO. Body Area Networks. Body Dynamics. Wearable Antennas. Statistical Modelling. Delay Spread. Angular Spread. Capacity. Performance.

Streszczenie

Celem rozprawy doktorskiej jest opracowanie modelu kanału radiowego, dla systemu MIMO zastosowanego w sieciach nasobnych (Body Area Networks) pracujących w wielodrogowym środowisku propagacyjnym. W pierwszej kolejności został uwzględniony wpływ tkanek człowieka na parametry anteny umieszczonej na ciele. Następnie, bazując na opisie ruchu (Motion Capture) została uwzględniona dynamika ciała. Środowisko propagacyjne zostało zamodelowane za pomocą geometrycznego modelu stochastycznego (Geometrically Based Statistic Channel). Antena nasobna, pracująca w paśmie 2.45 GHz została zasymulowana w programie CST (Computer Simulation Technology) przy użyciu wokselowego modelu człowieka. W pracy przedstawiono statystyczną analizę parametrów kanału radiowego (scenariusz ulicy), dla wielu anten umieszczonych na poruszającym się człowieku (chód i bieg). Ponadto, obliczona została pojemność systemu MIMO oraz wybrano optymalne położenie anten nasobnych w analizowanym scenariuszu. Wpływ tkanek człowieka jest najbardziej widoczny gdy antena jest umieszczona bezpośrednio na ciele. Dominujący wpływ na zmianę charakterystyki promieniowania anteny oraz parametry kanału radiowego ma ruch człowieka. W przypadku biegu oraz gdy antena umieszczona jest na nadgarstku, zarejestrowano wahania w poziomie odbieranego sygnału o 9 dB. Pojemność systemu MIMO zależy w głównej mierze od balansu poziomu mocy odbieranego sygnału przez anteny.

Słowa Kluczowe

Modelowanie Kanalow Radiowych. MIMO. Sieci Nasobne. Dynamika Ciała Człowieka. Modelowanie Statystyczne. Rozproszenie Opóźnienia. Rozproszenie Kątowe. Zysk Pojemność. Analiza Wydajności.

Resumo

O objectivo deste trabalho é o desenvolvimento de um modelo de canal aplicado às redes de sensores corporais, usando MIMO, para ligações com o exterior em ambiente multi-percurso. Começou por se estudar a influência do utilizador no desempenho da antena corporal. Considerou-se a mobilidade deste, criando-se um modelo baseado na captura do movimento. O ambiente de propagação foi incluído através de um modelo geométrico e estatístico do canal. Usou-se o simulador CST para estudar o desempenho de um *patch* a 2.45 GHz, junto a um modelo *voxel*. Obtiveram-se as componentes multi-percurso para o cenário de um utilizador com várias antenas, a caminhar ou a correr numa estrada. Analisaram-se as condições de propagação e as estatísticas dos parâmetros básicos do canal rádio. Com base nos valores obtidos para a capacidade MIMO, identificaram-se as melhores localizações para as antenas. Verificou-se que a influência do utilizador é maior quando a antena está em contacto com este. A mobilidade altera significativamente os diagramas de radiação e os parâmetros do canal rádio. Por exemplo, podem ocorrer desvanecimentos de 9 dB, durante uma corrida em que o utilizador usa uma antena no pulso. Verificou-se que a capacidade MIMO depende fortemente do balanço de potência entre as antenas.

Palavras-chave

Table of Contents

List of Figures

List of Tables

List of Acronyms

3D	Three Dimensional
3GPP	The 3rd Generation Partnership Project
AB_L	Left side of the Arm
AB_R	Right side of the Arm
B	Back
BAN	Body Area Network
BER	Bit Error Rate
BL	Back and Left
BLR	Back, Left and Right
BR	Back and Right
BS	Base Station
CD	Co-Directed
CIR	Channel Impulse Response
COST	European Co-operation in the Field of Scientific and Technical Research
CST	Computer Simulation Technology
CT	Computer Tomography
DC	Direct Current
DME	Discretised Material Equations
DoA	Direction of Arrival
DoD	Direction of Departure
ECG	Electrocardiogram
ETSI	European Telecommunications Standards Institute
F	Front
FB	Front and Back
FBL	Front, Back and Left
FBLR	Front, Back, Left and Right
FBR	Front, Back and Right
FDTD	Finite-Difference Time-Domain
FEM	Finite Element Method
FIT	Finite Integration Technique
FL	Front and Left
FLR	Front, Left and Right

FR	Front and Right
GBSC	Geometrically Based Stochastic Channel
GHz	Gigahertz
HE_B	Back side of the Head
HE_F	Front side of the Head
HE_L	Left side of the Head
HE_R	Right side of the Head
Hz	Hertz
IEEE	Institute of Electrical and Electronics Engineers
ISM	Industrial, Scientific and Medical
IST	Instituto Superior Técnico
L	Left
LEXNET	Low EMF Exposure Future Networks
LR	Left and Right
LT_L	Left side of the Leg
LT_R	Right side of the Leg
LW	Lines per Wavelength
LoS	Line of Sight
MAC	Medium Access Control
MGE	Maxwell's Grid Equations
MHz	Megahertz
MIMO	Multiple-Input Multiple-Output
MPC	Multi Path Component
MRI	Magnetic Resonance Imaging
MT	Mobile Terminal
MoM	Method of Moments
NEWCOM	Network of Excellence in Wireless Communications
OD	Opposite-Directed
PAD	Pattern Average Difference
PDAP	Power-Delay-Angle Profile
PDF	Probability Density Function
PDP	Power-Delay Profile
PWD	Pattern Weighted Difference
R	Right
RAM	Random Access Memory

RCP	Radio Channel Parameter
RF	Radio Frequency
RL	Ratio Limit
RMS	Root Mean Square
RT	Ray-Tracing
Rx	Receiver
SAR	Specific Absorption Rate
SIG	Special Interest Group
SISO	Single-Input Single-Output
SNR	Signal to Noise Ratio
TDD	Time Division Duplexing
THz	Terahertz
TLM	Top Loaded Monopole
TO_B	Back side of the Torso
TO_F	Front side of the Torso
TUL	Technical University of Lisbon
ToA	Time of Arrival
Tx	Transmitter
US	Uncorrelated Scattering
UTD	Uniform geometrical Theory of Diffraction
VNA	Vector Network Analyser
WA_F	Front side of the Waist
WLAN	Wireless Local Area Network
WSS	Wide-Sense Stationary
WSSUS	Wide-Sense Stationary Uncorrelated Scattering
XD	Cross-Directed

List of Symbols

α_b'	Wave attenuation constant for body tissue
α_B	Shape parameter of the Beta distribution
α_K	Shape parameter of the Kumaraswamy distribution
α_m	Material parameter for a dispersion region m
α_{3dB}	Half power beam-width
β_b'	Wave phase constant for body tissue
β_B	Shape parameter of the Beta distribution
β_K	Shape parameter of the Kumaraswamy distribution
Γ	Reflection coefficient
$\Gamma_\parallel$	Reflection coefficient for parallel polarisation
$\Gamma_\perp$	Reflection coefficient for perpendicular polarisation
Γ_b	Scatterer reflection coefficient at b^{th} bounce
Γ_i	Imaginary part of reflection coefficient
$|\Gamma_k|$	Magnitude of the reflection loss of the kth MPC
Γ_r	Real part of reflection coefficient
δ	Shift of the antenna's normal to the surface
δ_{max}	Maximum shift of the normal to the surface
δ_{min}	Minimum shift of the normal to the surface
δ_p	Penetration depth
$\delta(\cdot)$	Dirac delta distribution
$\delta\varphi_k$	Shift of the direction of maximum radiation in the azimuth plane for the kth frame
$\overline{\delta\varphi}$	Average shift of the direction of maximum radiation in the azimuth plane.
$\delta\psi_k$	Shift of the direction of maximum radiation in the elevation plane for the kth frame
$\overline{\delta\psi}$	Average shift of the direction of maximum radiation in the elevation plane.
Δd	Difference between path lengths of direct and reflected components
ΔD_0	Antenna directivity in the direction of maximum radiation difference to the reference scenario
$\Delta\epsilon_m$	Material drop in permittivity for a dispersion region m
Δf_r	Resonance frequency difference to the reference scenario
$\Delta\eta_a$	Antenna total efficiency difference to the reference scenario

ΔG_0	Antenna gain in the direction of maximum radiation difference to the reference scenario
$\overline{\Delta_G}$	Pattern Average Difference
$\Delta_{G_{nm}}$	Partial radiation pattern difference
$\overline{\Delta_{G_w}}$	Pattern Weighted Difference
Δ_K	Deviation between simulated data compared to the results coming from the Kumaraswamy distribution
ΔS_{11}	Input return loss difference to the reference scenario
Δt_s	Time resolution of Rx
ϵ	Permittivity
ϵ_0	Electric constant
ϵ_{r1}	Relative permittivity of the dielectric medium 1
ϵ_{r2}	Relative permittivity of the dielectric medium 2
ϵ_{ra}	Relative permittivity of the air
ϵ_{rb}	Relative permittivity of the body tissue
ϵ_{rm}	Relative permittivity of the material
ϵ_∞	Material permittivity at THz frequency
η_a	Antenna total radiation efficiency
θ	Co-elevation angle
$\bar{\theta}_{DoA}$	Mean DoA of MPCs in co-elevation plane
θ_{DoA_k}	DoA of the kth MPC in co-elevation plane
$\bar{\theta}_{DoD}$	Mean DoD of MPCs in co-elevation plane
θ_{DoD_k}	DoD of the kth MPC in co-elevation plane
θ_i	Angle of incidence
θ_{k_0}	Co-elevation coordinates of the vector calculated from P_b to P_a
θ_n	n^{th} azimuth angle sample
θ_r	Angle of refraction
λ	Wavelength
λ_0	Wavelength in vacuum
λ_m	Wavelength in the material
μ_{ra}	Relative permeability of the air
μ_{rb}	Relative permeability of the body tissue
π	Ratio of circle's circumference to its diameter
ρ	Correlation
$\rho_{CIR}^{k,l}$	Correlation between the CIRs obtained for the kth and l^{th} on-body antennas

$\overline{\rho^{k,l}}$	Average cross-correlation between s_k and s_l
$\rho^{k,l}$	Cross-correlation between s_k and s_l
ρ_n	Signal to Noise Ratio
$\bar{\rho}_n$	Mean SNR per Rx branch
$\rho_{P_R}^{k,l}$	Correlation between received signal envelopes obtained for the kth and l^{th} on-body antennas
ρ_s	Surface charge density
σ_a	Conductivity of the air
σ_b	Conductivity of the body tissue
$\overline{\sigma_{C_{MIMO_P}}}$	Average standard deviation of the performance of a MIMO system
$\sigma_{\overline{C_{MIMO_P}}}$	Standard deviation of the average performance of a MIMO system
$\overline{\sigma_{DoA}}$	Average spread of DoA
$\sigma_{\delta\varphi}$	Standard deviation of shift of the direction of maximum radiation in the azimuth plane.
$\sigma_{\delta\psi}$	Standard deviation of shift of the direction of maximum radiation in the elevation plane.
σ_{DoA}	Spread of DoA of MPCs
σ_{DoD}	Spread of DoD of MPCs
$\sigma_{|E|}$	Standard deviation of radiation pattern of electric field magnitude
$\sigma_{|E_R|}$	Standard deviation of the radiation pattern of electric field magnitude, for the Rayleigh distribution
$\sigma_{|E_U|}$	Standard deviation of the radiation pattern of electric field magnitude, for the Uniform distribution
σ_G	Standard deviation of gain pattern
$\sigma_{\varphi_{DoA}}$	Spread of DoA of MPCs in azimuth plane
$\sigma_{\varphi_{DoD}}$	Spread of DoD of MPCs in azimuth plane
σ_{h_k}	Standard deviation of the CIR for the kth antenna
σ_{h_l}	Standard deviation of the CIR for the lth antenna
σ_i	Ionic conductivity
$\overline{\sigma_{P_R}}$	Average standard deviation of the received power
$\sigma_{P_R^k}$	Standard deviation of the received signal envelope from the kth antenna
$\sigma_{P_R^l}$	Standard deviation of the received signal envelope from the lth antenna
$\sigma_{\overline{P_R}}$	Standard deviation of the average received power
$\sigma_{\rho^{k,l}}$	Standard deviation of cross-correlation between s_k and s_l
$\overline{\sigma_{\sigma_{DoA}}}$	Average standard deviation of the spread of DoA

$\sigma_{\overline{\sigma_{DoA}}}$	Standard deviation of the average spread of DoA
$\overline{\sigma_{\sigma_\tau}}$	Average standard deviation of the RMS delay spread
$\sigma_{\overline{\sigma_\tau}}$	Standard deviation of the average RMS delay spread
$\overline{\sigma_\tau}$	Average RMS delay spread
σ_τ	RMS delay spread
$\sigma_{\theta_{DoA}}$	Spread of DoA of MPCs in co-elevation plane
$\sigma_{\theta_{DoD}}$	Spread of DoD of MPCs in co-elevation plane
$\bar{\tau}$	Mean delay
τ	Excess delay
τ_{kl}	Delay of s_k relative to s_l
τ_k	Delay of the kth MPC
τ_{LoS}	Delay of LoS component
τ_m	Material relaxation time for a dispersion region m
τ_{max}	Maximum delay of MPC
τ_{min}	Minimum delay of MPC
$\tau_{s_{max}}$	System maximum delay
φ	Azimuth angle
$\bar{\varphi}_{DoA}$	Mean DoA of MPCs in azimuth plane
φ_{DoA_k}	DoA of the kth MPC in azimuth plane
$\bar{\varphi}_{DoD}$	Mean DoD of MPCs in azimuth plane
φ_{DoD_k}	DoD of the kth MPC in azimuth plane
φ_{k_0}	Azimuth coordinates of the vector calculated from P_b to P_a
φ_m	Azimuth of the mth incoming wave
ψ	Elevation angle
ω	Angular frequency
a_m	Minor axis of the ellipse corresponding to body part
a_M	Major axis of the ellipse corresponding to body part
$\mathbf{b}$	Vector containing magnetic faces fluxes allocated on the primary grid G_{FIT}
b_i	Magnetic faces fluxes
$B(\cdot)$	Normalisation constant to ensure that the PDF of Beta distribution integrates to unity
c	Speed of Light
$\mathrm{cov}(\cdot)$	Covariance function
$\mathbf{C_F}$	Discreet equivalent of the analytical curl operator for grid G_{FIT}
$\mathbf{\tilde{C}_F}$	Discreet equivalent of the analytical curl operator for grid $\tilde{G_{FIT}}$

C_{MIMO}	Capacity of a MIMO system
$C_{MIMO_{max}}$	Maximum capacity gain of a MIMO system
$C^p_{MIMO_{best}}$	Percentage of time when the MIMO capacity for the pth pair of on-body antennas is the best
$C_{MIMO_{min}}$	Minimum capacity gain of a MIMO system
$C^p_{MIMO_P}$	Overall performance of a MIMO system for the pth pair of on-body antennas
C_{MIMO_P}	Overall performance of a MIMO system
$\overline{C_{MIMO_P}}$	Average performance of a MIMO system for the pth pair of on-body antennas
$C^p_{MIMO_{worst}}$	Percentage of time when the MIMO capacity for the pth pair of on-body antennas is the worst
C_{SISO}	Capacity of a SISO system
$\mathbf{d}$	Vector containing electric facet fluxes allocated on dual orthogonal grid $\tilde{G_{FIT}}$
d	Distance between Tx and Rx
d_b	Partial distance of the path of the MPC
d_d	Path length of the direct component
d_i	Electric faces fluxes
d_k	Total length of the kth MPC
d_r	Path length of the reflected component
D_0	Antenna Directivity (in the direction of maximum radiation)
$\mathbf{D}$	Electric flux density
$\mathbf{e}$	Vector containing electric grid voltages allocated on the primary grid G_{FIT}
e_i	Electric grid voltages
E_0	Electric field on the surface of the human body
$|E|$	Magnitude of the electric field
$\overline{|E|}$	Average radiation pattern of electric field magnitude
$\mathbf{E}$	Electric field
$|E_d|$	Electric field magnitude of direct component
$|E_{max}|$	Maxima of the radiation pattern of the electric field magnitude
$|E_{min}|$	Minima of the radiation pattern of the electric field magnitude
E_n	Normal component of electric field
$|E_r|$	Electric field magnitude of the component towards body tissue
$\overline{|E_R|}$	Average radiation pattern of the electric field magnitude, for the Rayleigh distribution
E_t	Tangent component of electric field

$\overline{\|E_U\|}$	Average radiation pattern of the electric field magnitude, for the Uniform distribution
f_r	Resonance frequency
g	Average gains of the channel transfer matrix elements
$G(\varphi, \vartheta)$	Gain of the antenna
G_0	Antenna gain (in the direction of maximum radiation)
G_a	Gain of patch antenna
G_{FIT}	Primary grid in FIT
$G_{\tilde{FIT}}$	Dual orthogonal grid in FIT
G_h	Gain of the horn antenna
G_k	Gain pattern for k^{th} time frame
G_μ	Average gain pattern
G_{max}	Maximum of antenna gain pattern
G_{min}	Minimum of antenna gain pattern
G_{MIMO_c}	Relative MIMO channel capacity gain
G_{MIMO_s}	Relative MIMO system capacity gain
G_R	Gain of the Rx antenna
G_{R_k}	Rx antenna gain for the kth MPC
G_T	Gain of the Tx antenna
G_{T_k}	Tx antenna gain for the kth MPC
$\mathbf{h}$	Vector containing magnetic grid voltages allocated on dual orthogonal grid $G_{\tilde{FIT}}$
h	Distance from the antenna to the body
h_{dk}	Distance to the body from k^{th} antenna
h_{dl}	Distance to the body from l^{th} antenna
h_i	Magnetic grid voltages
h_k	CIRs obtained for the kth on-body antenna and the external Rx antenna
h_l	CIRs obtained for the lth on-body antenna and the external Rx antenna
h_q	q^{th} distance sample from the antenna to the body
$h(\cdot)$	Channel Impulse Response
$\mathbf{H}$	Matrix containing Channel Impulse Responses
$\mathbf{I}$	Identity matrix
j	$\sqrt{(-1)}$
$\mathbf{j_s}$	Vector containing free current density in grid cells
$\mathbf{j_t}$	Vector containing total current density in grid cells

$K(\cdot)$	Normalisation constant to ensure that the PDF of Kumaraswamy distribution integrates to unity
l_m	Length of the material
L_p	Path loss
$\mathbf{M_\epsilon}$	Material matrix containing grid cells permittivity
M_{LW}	Meshing Lines per Wavelength
$\mathbf{M_\mu}$	Material matrix containing grid cells permeability
M_{RL}	Meshing Ratio Limit
$\mathbf{M_\sigma}$	Material matrix containing grid cells conductivity
M_t	Total memory
$\mathbf{n}$	Vector containing power of noise received by each antenna
$\mathbf{\hat{n}_i}$	Surface S_i normal
N_b	Number of bounces
N_c	Number of mesh cells
N_{CIR}	Number of CIRs simulated for one antenna placement
N_f	Number of frames per walking or running period
N_h	Total number of distance samples
N_θ	Number of discrete elevation angle samples
N_k	Number of distance samples from the body for the kth antenna
N_l	Number of distance samples from the body for the lth antenna
N_m	Number of mesh lines in the material
N_{min}	Minimum number of antennas on Tx or Rx side
N_{MPC}	Number of MPCs
N_p	Number of walking or running periods
N_R	Number of Rx antennas
N_s	Number of simulations for different distribution of scatterers
N_T	Number of time frames
N_φ	Number of discrete azimuth angle samples
$p_B(\cdot)$	PDF of the Beta distribution
$p_K(\cdot)$	PDF of the Kumaraswamy distribution
P_a	Position of the antenna
P_b	Position of the body node
P_h	Rx power from the horn antenna
$P_{r_{min}}$	Sensitivity of the Rx
P_R	Received power

$\overline{P_R}$	Average received power
P_R^k	Received signal envelope from the kth on-body antenna
P_R^l	Received signal envelope from the lth on-body antenna
P_T	Transmitted power
P_x	Rx power from the test antenna
$\mathbf{q_t}$	Vector containing total charge in grid cells
r_0	Length of the vector calculated from P_b to P_a
s_k	Signal received from k^{th} antenna
s_l	Signal received from l^{th} antenna
S_{11}	Input return loss
$\mathbf{S_F}$	Discreet equivalent of the analytical divergence operator for grid G_{FIT}
$\tilde{\mathbf{S_F}}$	Discreet equivalent of the analytical divergence operator for grid $\tilde{G_{FIT}}$
S_i	Surface interface between two dielectrics
t	Absolute time
t_M	Last time frame
t_m	First time frame
t_n	Time frame
t_s	Simulation time
$\mathbf{T}$	Matrix containing normalised channel transfer gains for each pair of antennas
$\mathbf{x}$	Vector containing the transmitted symbols for a particular Tx antenna
x_a	X-coordinate of the antenna's position
x_b	X-coordinate of the body node's position
$\mathbf{y}$	Vector containing the received symbols for a particular Rx antenna
y_a	Y-coordinate of the antenna's position
y_b	Y-coordinate of the body node's position
z_a	Z-coordinate of the antenna's position
z_b	Z-coordinate of the body node's position

List of Software

CorelDraw	Corel Corporation
CST Studio	Computer Simulation Technology
Dev C++	Bloodshed Software, GNU General Public License
LaTeX	A Document Preparation System
Matlab	MathWorks
Poser	Smith Micro Software
Virtual Family	Body Voxel Models

Chapter 1

Introduction

This chapter gives a brief overview of the thesis, its main objectives and challenges, points out the novelty, and presents the contributions in the development of the models for BANs. The detailed structure of the thesis is presented as well.

1.1. Motivations

Mobile and wireless communications has been evolving very fast, enabling a better quality of life for users. The current research in the area of telecommunications considers the human body as a part of smart environment, where users can carry their own communications network, *i.e.*, Body Area Networks (BANs), [HaHa06]. In recent years, wireless communications are about to replace all wired connections in the range of BANs, which are a possible evolution of the current concept of Wireless Local Area Networks (WLANs), consisting of a network of sensors deployed along the body or inserted in clothes, allowing, among other functions, to monitor the vital signals of an individual, supply key indicators for a sports person, or other leisure activities. This trend goes in the direction of an increased concerned with the comfort and the well-being of people, increasing their own autonomy. The robust connection of wearable devices with surrounding base stations can be a very important step to include smart people with upcoming smart cities infrastructures. The small size of sensors, and their location near the body, imply the need for a sound study of the various propagation aspects, namely a proper channel characterisation. This thesis is precisely motivated by this vision of future wireless communication system, where body sensors will be widely deployed and their wireless connectivity can improve everyday life and security of people, as it gives them the ability to be on-line anytime and anywhere.

BANs have a plentiful range of potential applications, like healthcare and patient monitoring, sports monitoring, security, military and space applications, business and multimedia entertainment, among others. The range of BAN applications emphasises its interdisciplinary feature, Figure 1.1.

In healthcare, a wide range of future applications is expected, since BANs can be used in many scenarios. BANs can be applied in intensive care units for typical monitoring of vital parameters purposes, providing real time readings that need to be monitored and analysed (*i.e.*, electrocardiogram (ECG), heart sound, heart rate, electroencephalography, respiratory rate, and temperature of body). This not only makes monitoring more comfortable for the patient, but also saves medical personnel's time. Quality of life can be significantly improved, in particular for patients suffering from chronic diseases that require permanent monitoring of vital signs. BANs may allow the detection of the early signs of a disease, and monitoring transient or infrequent events. When more than one patient can be monitored in time, there is a need for synchronisation and authentication. The security, reliability and schedule of the communication for medical application are always of top importance, thus, most of medical applications are critical ones. Patient and elderly people monitoring in home environments is another attractive area of BANs applications, assisting people in maintaining independent mobility and day life activities, and preventing injuries. This application demands for low bandwidth networks, reliable links and intolerance to delays.

In sports, BANs may be used to monitor fitness-related activities, including several sensors for measuring different physiological parameters, like heart rate, energy consumption, fat percentage
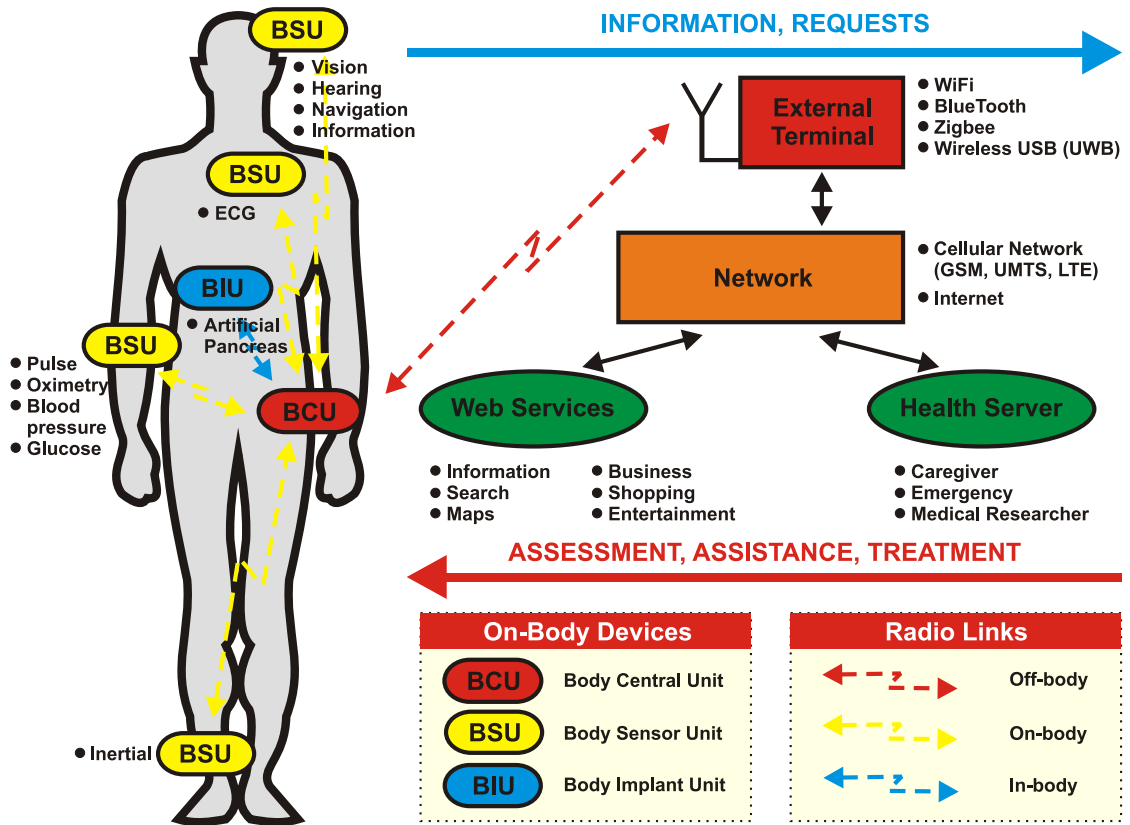
Figure 1.1. Body Centric Wireless Communications.

(bio-resistance meter), body water content or galvanic skin response. These sensors can measure and display on-time information and/or follow-up reports to a control entity (*e.g.*, professional well-being and caring personnel). Sport applications demand for high capacity systems to deliver real time information.

Security and military applications comprise smart suits for fire fighters, soldiers and support personnel in battlefields. Smart clothes use special sensors to detect bullet wounds or to monitor the body's vital signals during combat conditions, [PaJa03]. For these cases, the communication link should be reliable, as vital information is involved. Space applications include bio-sensors for monitoring the physiological parameters of astronauts during space flights (*e.g.*, ECG, temperature bio-telemeters, and sensor pills), in order to understand the impact of space flight on living systems, [Hine96].

In business, BAN devices can be used in numerous ways, such as touch-based authentication services using the body as a transmission channel (*e.g.*, data deliver on handshake). Several applications are possible, like electronic payment service, e-business card service, auto-lock or login systems. User identification/authentication, associated to biometrics, play a key role in here. Business applications have to ensure secure communications, and, in this case, the most important thing is high level security, which eliminates the risk of a third person attack.

In entertainment, wireless applications are multimedia oriented, and many times require the high speed transfer of voice, video and data together in real time. But, contrary to applications from

the previous groups, these ones tolerate some errors and, what is more important, they do not put high demands on communication security. Personal video is an example, where the central device is a video camera, which can stream video content and connect to a personal storage device, a playback device with large display, or a home media server. Another example of an entertainment application is wearable audio, where the central device is a headset (stereo audio, microphone), connecting to various devices as a smart phone, an audio player, or a hands-free car device.

For all BAN applications, the radio channel (including the strong influence of the body) takes the core position for the overall system performance. Radio propagation for wireless networks has been extensively investigated for over 20 years, mainly towards networks planning for 2G, 3G and 4G mobile communications. Simple and sophisticated models have been developed, and some of them incorporated into standards, following the activities of European Co-operation in the Field of Scientific and Technical Research (COST) 207 [COST89], 231 [COST99], 259 [COST01], 273 [COST07], 2100 [COST10], IC 1004 [COST13] in Europe and bodies such as The 3rd Generation Partnership Project (3GPP) [3GPP13], European Telecommunications Standards Institute (ETSI) [ETSI13] and Institute of Electrical and Electronics Engineers (IEEE) 802 [IEEE13a] among others, internationally. There is a strong body of knowledge for outdoor, rural and urban channels, covering "classical" use cases of communication between *e.g.*, a mobile terminal and a base station. However, emerging cases such as BANs are much less known from the radio channel viewpoint.

The goal of this thesis is to address issues related with BAN radio channel modelling, focusing in particular on off-body links. Moreover, the model should enable the analysis of Multiple-Input Multiple-Output (MIMO) systems, which can enhance performance of BANs. The gain of a MIMO system is related to some parameters, as numbers of input and output antennas and their location on the body. The location of antennas with different orientation on the body (*e.g.*, Front, Back, Left or Right) gives a greater decorrelation among links, because the influence of each obstruction in the environment is more significant. Therefore, based on the results obtained in this work, some recommendations on the desired placement of the antennas on the body should be given. Summarising, the key goal of this work is to develop channel models for the use of MIMO systems in conjunction with BANs, allowing for a more efficient communication between sensors and mobile terminals, and outside networks (cellular or wireless), in outdoor environments.

1.2. Novelty

The novelty of this thesis is to present a Radio Channel model for BANs, which takes various phenomena of propagation near the body into account. The propagation models currently in use for WLANs are not adequate for BANs, and in this work one considers the complex shape of the body, constituted by different tissues with different dielectric properties, which influence

communication from sensors placed in different parts of the body. The inclusion of the body in the radio channel introduces complex antenna-body interactions, and in this thesis the influence of body coupling (caused by the presence of tissues), as well as the arbitrary orientation of the antenna (caused by the body movement) is analysed. Moreover, this thesis explores the concept of the statistical analysis of antennas in BANs, Figure 1.2.
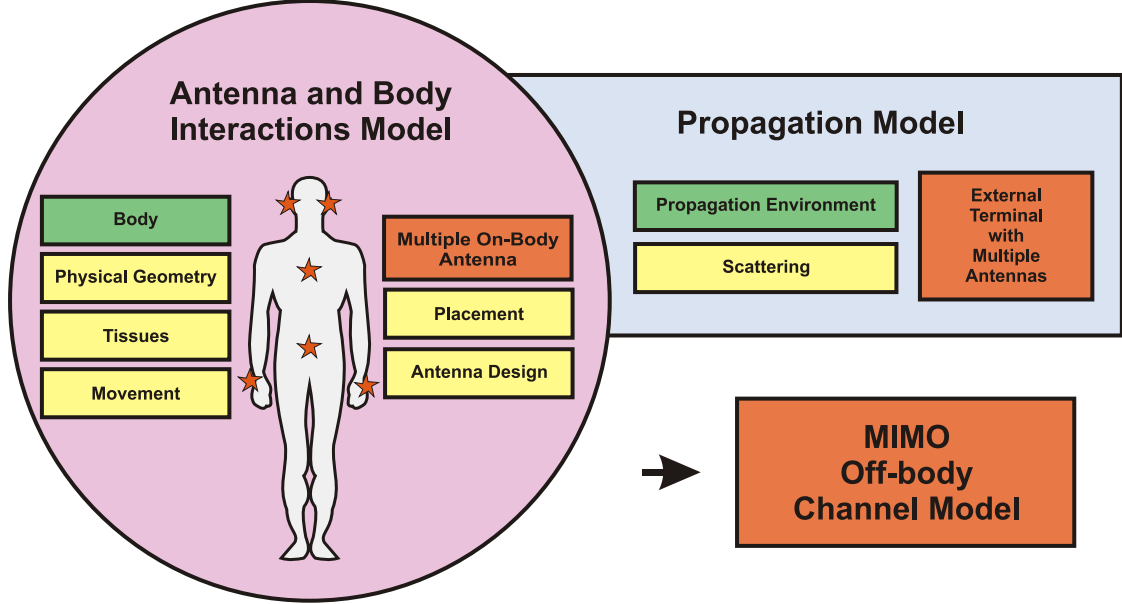
Figure 1.2. Thesis framework.

In general, the radio channel for BANs is studied mainly via measurements in an anechoic chamber or lab environments, for antennas mounted on the body. In this case, the antenna performance is hidden inside the channel model, and cannot be extracted (*e.g.*, the information about antenna orientation is neglected). Also, in existing models little work has been done in order to include various propagation environments. Therefore, a novel aspect of this thesis is to join the statistical description of an antenna with the Radio Channel model.

In the case of BANs, models are extracted from specific measurements sessions, and the results can not be extrapolated. Therefore, another novel feature of this work is that developed models and algorithms are system independent, so that they can be used for other scenarios (*i.e.*, antenna design, antenna placements, body dynamics and propagation environments). In general, the measurements provide only basic Radio Channel parameters of off-body links like path loss, but in this thesis one provides also the temporal (*i.e.*, delay spread) and angular (*i.e.*, angular spread) ones. Also, in this thesis the MIMO capacity is calculated for various antenna locations, looking for the optimum configurations regarding overall system performance.

1.3. Research Strategy and Impact

The work developed in this thesis was done within different research European frameworks and projects, such as the Seventh Framework Programme and also in COST, namely COST2100

[COST10], IC1004 [COST13], NEWCOM++ [NEWC11], NEWCOM# [NEWC13] and LE-XNET [LEXN13].

Some concepts and ideas explored by this thesis have impact on different aspects of BANs. Development of realistic and accurate BANs channel models allow to:

- analyse performance of wearable antennas in various propagation environments,
- increase transmission data rate by use of multiple antennas and optimising their location on the body,
- reduce the transmission power and extend the lifetime of devices,
- reduce exposure to electromagnetic fields of people (*i.e.*, reduction of Specific Absorption Rate (SAR)),
- assess new radio transmission techniques for BANs,
- study various Medium Access Control (MAC) protocols for BANs,
- develop network simulators for BANs.

The work presented in this thesis was already disseminated in a book chapter and several papers that were published or submitted to various conferences and journals:

- Book Chapters
  - [OlMC12a]: Oliveira,C., Mackowiak,M. and Correia,L.M., *Statistical Characterisation of Antennas in BANs*, in Guillaume de la Roche, Andres Alayon-Glazunov and Ben Allen (eds.), *LTE Advanced and Beyond Wireless Networks: Channel Modelling and Propagation*, John Wiley, Chichester, UK, 2012.
- International Journals
  - [MaCo13a]: Mackowiak,M. and Correia,L.M., "A Statistical Model for the Influence of Body Dynamics on the Radiation Pattern of Wearable Antennas in Off-Body Radio Channels", *Wireless Personal Communications*, 10.1007/s11277-013-1193-x, May 2013.
  - [MaOC12a]: Mackowiak,M., Oliveira,C. and Correia,L.M., "Radiation Pattern of Wearable Antennas: A Statistical Analysis of the Influence of the Human Body", *International Journal of Wireless Information Networks*, Vol. 19, No. 3, Sep. 2012, pp. 209-218.
- International Conferences
  - [MaCo13c]: Mackowiak,M. and Correia,L.M., "MIMO Capacity Performance of Off-Body Radio Channels in a Street Environment", accepted to *PIMRC'2013 - 24th IEEE Symposium on Personal, Indoor, Mobile and Radio Communications*, London, UK, Sep. 2013.
  - [OlMC13]: Oliveira,C., Mackowiak,M. and Correia,L.M., "Modelling On- and Off-Body Channels in Body Area Networks", invited to *IMOC'2013 - International Microwave and Optoelectronics Conference*, Rio de Janeiro, Brazil, Aug. 2013.
  - [MaCo13b]: Mackowiak,M. and Correia,L.M., "MIMO Capacity Analysis of Off-Body Radio Channels in a Street Environment", in *Proc. of VTC'2013 Spring - IEEE 77th Vehicular Technology Conference*, Dresden, Germany, June 2013.

- [MREC13]: Mackowiak,M., Rosini,R., D'Errico,R. and Correia,L.M., "Comparing Off-Body Dynamic Channel Model with Real-Time Measurements", in *Proc. of ISMICT'2013 - 7th International Symposium on Medical Information and Communication Technology*, Tokyo, Japan, Mar. 2013.

- [MaCo12b]: Mackowiak,M. and Correia,L.M., "Correlation Analysis in Off-Body Radio Channels in a Street Environment", in *Proc. of PIMRC'2012 - 23rd IEEE Symposium on Personal, Indoor, Mobile and Radio Communications*, Sydney, Australia, Sep. 2012.

- [OlMC12b]: Oliveira,C., Mackowiak,M. and Correia,L.M., "A Comparison of Phantom Models for On-Body Communications", in *Proc. of PIMRC'2012 - 23rd IEEE Symposium on Personal, Indoor, Mobile and Radio Communications*, Sydney, Australia, Sep. 2012.

- [MaCo12c]: Mackowiak,M. and Correia,L.M., "Towards a Radio Channel Model for Off-Body Communications in a Multipath Environment", in *Proc. of EW'2012 - 18th European Wireless Conference*, Poznan, Poland, Apr. 2012.

- [MaOC12b]: Mackowiak,M., Oliveira,C. and Correia,L.M., "Signal Correlation Between Wearable Antennas in Body Area Networks in Multipath Environment", in *Proc. of EuCAP'2012 - 6th European Conference on Antennas and Propagation*, Prague, Czech Republic, Mar. 2012.

- [OlMC12c]: Oliveira,C., Mackowiak,M. and Correia,L.M., "Correlation Analysis in On-Body Communications", in *Proc. of EuCAP'2012 - 6th European Conference on Antennas and Propagation*, Prague, Czech Republic, Mar. 2012.

- [OMLC11]: Oliveira,C., Mackowiak,M., Lopes,C.G. and Correia,L.M., "Characterisation of On-Body Communications at 2.45 GHz", in *Proc. of BodyNets'2011 - International Conference on Body Area Networks*, Beijing, China, Nov. 2011.

- [MOLC11]: Mackowiak,M., Oliveira,C., Lopes,C.G. and Correia,L.M., "A Statistical Analysis of the Influence of the Human Body on the Radiation Pattern of Wearable Antennas", in *Proc. of PIMRC'2011 - 22nd IEEE International Symposium on Personal, Indoor and Mobile Radio Communications*, Toronto, Canada, Sep. 2011.

- [OlMC11]: Oliveira,C., Mackowiak,M. and Correia,L.M., "Challenges for Body Area Networks Concerning Radio Aspects", in *Proc. of EW'2011 - European Wireless 2011*, Vienna, Austria, Apr. 2011.

- [MaCo11]: Mackowiak,M. and Correia,L.M., "Modelling the Influence of Body Dynamics on the Radiation Pattern of Wearable Antennas in Off-Body Radio Channels", in *Proc. of 12th URSI Commission F Triennial Open Symposium on Radio Wave Propagation and Remote Sensing*, Garmisch-Partenkirchen, Germany, Mar. 2011.

- [MaCo10]: Mackowiak,M. and Correia,L.M., "A Statistical Approach to Model Antenna Radiation Patterns in Off-Body Radio Channels", in *Proc. of PIMRC'2010 - 21st IEEE International Symposium on Personal, Indoor and Mobile Radio Communications*, Istanbul, Turkey, Sep. 2010.

Part of the work developed in this thesis was done in close collaboration with the colleagues Carla Oliveira and Carlos Lopes, who developed Ph.D. and M.Sc. thesis, respectively, in complimentary topics on BANs. This straight collaboration resulted in the publication of some joint papers, as detailed above.

1.4. Structure of the Dissertation

This work consists of eight chapters, including this one, followed by a set of annexes.

In Chapter 2, aspects related with channel modelling are described, including radio channels parameters and examples of various channel models. This work is related to MIMO systems, therefore some basic information about this technique is presented.

Chapter 3 presents the state of the art on modelling related to BANs, and discusses off-body channel in details. The electromagnetic properties of the body tissues and variability of the body geometry are described. The concept of wearable antennas and their requirements is introduced. Moreover, the existing numerical techniques including full wave methods are presented.

Chapter 4 proposes new statistical model to analyse wearable antennas in BANs, using simple theoretical approach or numerical analysis. In this chapter, a model to study the correlation between signals captured by wearable antennas is presented as well. Moreover, the method to include the realistic body movement is introduced.

In Chapter 5, the results obtained from the developed models, accounting for the body coupling (using theoretical, numerical and practical approaches) are presented and analysed. Moreover, the statistics of the antenna gain patterns on the moving body are obtained.

In Chapter 6, the developed channel model for BANs and scenarios being analysed are presented. The implementation of the simulator is presented as well, together with the assessment.

In Chapter 7, the results from simulations of the off-body channel are presented, and a deep statistical analysis of obtained Radio Channel Parameters (RCPs) (*i.e.*, propagation condition, received power, delay and angular spreads, and correlation between signal envelopes and Channel Impulse Responses (CIRs)) are performed. The MIMO capacity is calculated and selection of the best on-body placements of antennas is done.

Finally, in Chapter 8, significant conclusions are summarised and future research work is proposed.

Further detailed information can be found in Annexes. Annex A contains the user's manual and describes the required format of the config file containing input parameters for simulations. In Annex B, the electric properties of body tissues are gathered. Annex C includes the gain patterns of a patch antenna simulated on different placements on the body. In Annex D, the statistics of the gain patterns are provided, for walking and running bodies. In Annex E, extra

results of Radio Channel parameters obtained for street scenario are gathered. In Annex F, the MIMO capacity is shown for various pairs of antennas in a 2×2 MIMO system, for walking or running bodies. Annex G presents the overall performance of various pairs of antennas in a 2×2 MIMO system.

Chapter 2

MIMO Channel Models

In this chapter, aspects related with channel modelling are described, including radio channels parameters and examples of various channel models. This work is related to MIMO systems, therefore, some basic information about this technique is presented.

2.1. Channel Description

The Wireless Communications Channel, [Moli05], can be decomposed as the Transceiver, the Radio, and the Propagation ones, Figure 2.1. The Propagation Channel is the medium linking two sides of the wireless system taking ideal isotropic antennas, whereas the Radio Channel considers also the properties of Transmitter (Tx) and Receiver (Rx) antennas. On top of it, the Transceiver Channel describes the whole wireless system, including modulation and coding at Tx, and signal processing and decoding at Rx. In this work, the description of the Transceiver Channel is limited only to signal filtering at Rx, whereas coding, decoding, modulation and demodulation issues are not considered.
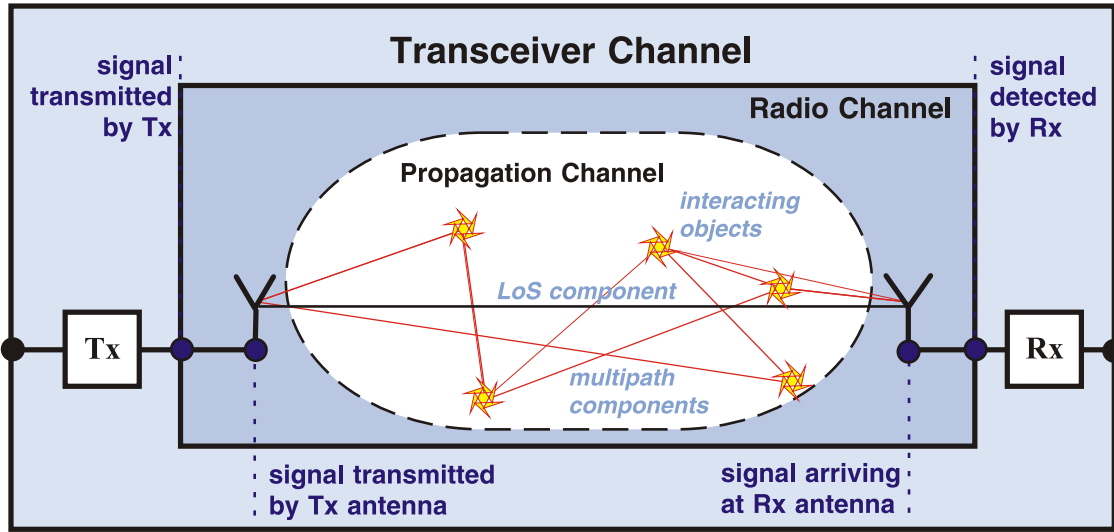
Figure 2.1. Decomposition of the channel in a wireless system.

In a wireless communications system, a signal transmitted through the Propagation Channel interacts with the environment in a very complex way. The multipath propagation phenomena is the most important feature of a channel, implying that the Rx signal is the composition of many Multi Path Components (MPCs). Three main types of propagation mechanisms can be distinguished [SJKM03]:

- specular reflection: it appears when the scattering source is smooth and large compared to the wavelength (*e.g.*, back-wall reflection),
- diffraction: it is caused by an object with sharp edges (*e.g.*, the edge of a building),
- diffuse scattering: it takes place if the dimension of the obstruction is smaller than the wavelength (*e.g.*, furniture or leaves).

The polarisation of the wave that is radiated from the antenna can be always separated into two independent components *i.e.*, vertical and horizontal. Signal transmission and interactions with the environment result in energy leaking from the vertical component into the horizontal one, and vice versa [Moli05].

Path loss is a major component in the analysis and design of the link budget of a telecommunication system. When there is only one clear Line of Sight (LoS) path between Tx and Rx, the received signal power can be calculated from [Moli05]:

$$P_R(d) = P_T G_T G_R \cdot \left(\frac{\lambda}{4\pi}\right)^2 \cdot \frac{1}{d^2} \tag{2.1}$$

where:
- P_T: transmitted power,
- G_T: gain of the Tx antenna,
- G_R: gain of the Rx antenna,
- λ: wavelength,
- d: distance between Tx and Rx.

In order to have a better estimation of signal level in urban environments at the Rx, the COST 231 Walfish-Ikegami or the COST 231 Okumura-Hata models [COST99] can be used, which has been assessed by measurements in European cities.

In multipath Radio Channels, all MPCs sum up at the Rx, in a constructive or destructive way, *i.e.*, small-scale fading or fast fading, [Skla97], which can be modelled statistically as Rayleigh or Rician distributions. Rayleigh fading is applicable when there is no dominant propagation along a LoS between the Tx and Rx. If there is a dominant LoS, the Rician distribution is applicable. In the propagation environment, the LoS component and MPCs can also be shadowed by obstacles (*e.g.*, hills, trees, buildings, walls and furniture), which leads to large-scale or slow fading. The amplitude change caused by shadowing is often modelled by a log-normal distribution. Both above mentioned fading effects overlap, and can result in huge variations of the received signal amplitude. Moreover, the fading may vary with time, position and frequency.

The Doppler shift takes place when the Tx antenna is moving relative to the Rx one, or when the signal is bounced on moving objects in the environment. Different MPCs have different Doppler shifts, which can lead to signal amplitude periodic variations (*i.e.*, frequency beating effect), [Moli05].

The coherence bandwidth is a range of frequencies over which the Radio Channel is flat, which means that the channel does not introduce distortion to signal spectral components. The coherence bandwidth is usually defined as a range of frequencies over which the frequency correlation is above 0.5, [Kosi04]. Similarly, the coherence time is the duration over which the channel is essentially invariant. The conditions of propagation in a Radio Channel change in time; however, one can assume that the channel is quasi-stationary for a period of time shorter than the time coherence.

Depending on the radio propagation scenario, the Radio Channel model should include path loss and fading effects, as it is presented in Figure 2.2.
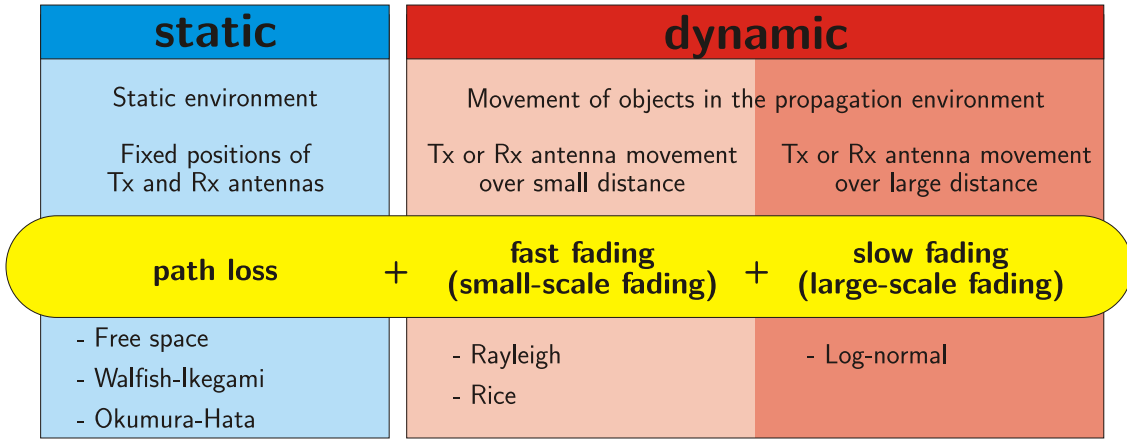
Figure 2.2. Signal path loss and fading.

The transmitted signal can be described by certain physical values (*i.e.*, amplitude, frequency, bandwidth) which are modified during propagation by all interacting objects in the environment. In order to be able to calculate signal parameters at the Rx, first the influence on MPCs of all previously mentioned propagation phenomena has to be analysed. The Rx can be described by its sensitivity $P_{r_{min}}$, time resolution Δt_s, and system maximum delay $\tau_{s_{max}}$. The signal is filtered and processed as shown in Figure 2.3; based on the time resolution, rays are grouped and cumulated, and the rays which delay exceed the receiver maximum one are dropped.
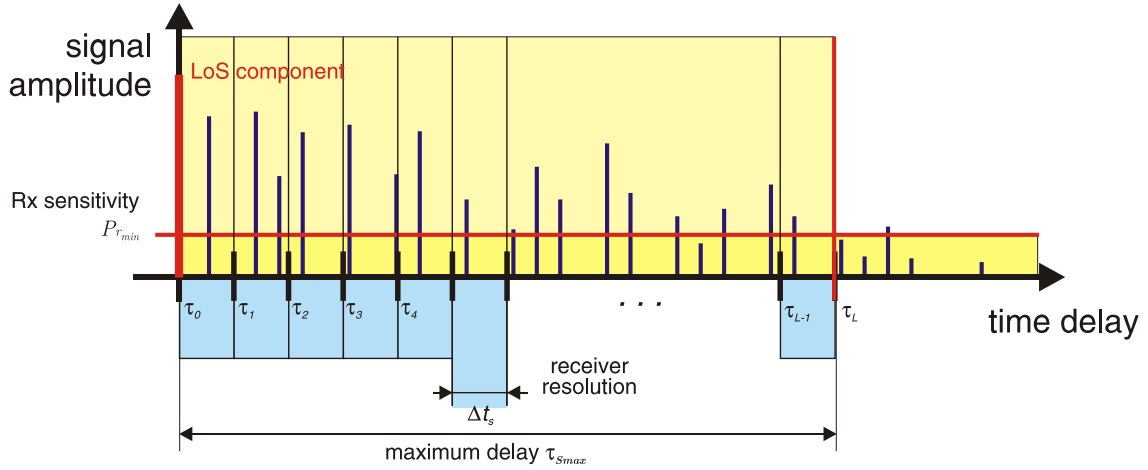
Figure 2.3. Multibounce signal processed by Rx.

2.2. Wideband Channel Models

In general, Radio Channel models can be divided into three categories: deterministic, empirical (statistical), and mixed. In deterministic models, two main approaches are known: ray tracing, and techniques solving full electromagnetic equations; the former needs a huge computational power, while the latter is highly complicated; moreover, the obtained results strongly depend on an accurate description of a specific propagation environment [SBMS04]. On the contrary, stochastic models characterise channels in a statistical way, and do not rely on site-specific descriptions [SBMS04]; these models are described by numerous parameters, which are obtained

from the analysis of many measurements, and despite the fact that this group of channel models is flexible, their accuracy is not very high. The combination of the two previously mentioned approaches results in a mixed category. Radio Channel models in this category are able to meet the conditions of the accuracy-complexity compromise.

The evolution of models that provide space-time information is presented below:

- Discrete Uniform Model [Asze96]: This model assumes that scatterers are uniformly distributed in space, within a narrow beamwidth. The correlation matrix for this model was derived. This model, does not include rules to obtain parameters like delay and Doppler spreads, which are required in simulations [LiRa99].

- Gaussian Wide Sense Stationary Uncorrelated Scattering Model [LiRa99]: This model is an example of a statistical model, assuming that scatterers are grouped into clusters. By including multiple clusters, the frequency-selective fading channel can be simulated, but this model does not give any indication on the amount and localisation of scatterers.

- Uniform Sectored Distribution Model [LiRa99]: This model assumes a uniform distribution of scatterers within a region. Magnitude and phase reflection coefficients of scatterers are generated randomly, with a uniform distribution in $[0, 1]$ and $[0, 2\pi]$, respectively. The model may be used in the simulation of angle spread on spatial diversity techniques.

- COST 259 Directional Channel Model [Corr01]: This is a physical model suitable for different radio environments, which includes macro-, micro-, and pico-cellular scenarios (*e.g.*, typical urban, bad urban, open square, indoor office, and indoor corridor). To describe this model, external parameters (*e.g.*, Base Station (BS) position, radio frequency, average BS and Mobile Terminal (MT) height), and global parameters (sets of probability density functions characterising a specific environment) are needed.

- Geometrically Based Stochastic Channel (GBSC) Model [MaCo04]: This model is a combination of deterministic and statistical features. Output parameters, like Direction of Arrival (DoA), Direction of Departure (DoD) and Time of Arrival (ToA) are calculated geometrically, depending on the positions of the Tx and Rx antennas and deployment of scatterers [LiRa99]. The layout and specification of scatterers are random. Moreover, in [Mack07], multibounce reflections are accounted for.

- Random Cluster Model [Czin07]: This is a GBSC Model for frequency selective and smoothly time variant radio channels. The most significant feature of this model is that it is parametrised directly from channel measurements by an automatic procedure. This model gives a very good agreement with measurements, however, it is useless in the cases that no measurements have been previously performed.

The GBSC model is based on the idea that the multipath characteristic of a Radio Channel is the result of signal bounce over numerous scatterers. Each scatterer is described by a random, complex reflection coefficient. The output parameters (amplitude, phase, DoA, DoD and ToA) for each MPC are calculated according to the positions of Tx and Rx antennas, and the distribution of scatterers. It is worthwhile noticing that this method is not a ray-tracing technique.

A specific phenomenon was observed by Saleh and Valenzuela [SaVa87], *i.e.*, that scatterers can be grouped into clusters, which means that in an area of a cluster there is a dense deployment of reflectors. Deployment and shape of clusters depends on the considered scenario. In conclusion, the GBSC model can be considered as a combination of deterministic (parameters like DoA, DoD and ToA are computed based on environment geometry) and statistical features (coordinates of scatterers are generated randomly, and each scatterer is described by a random reflection coefficient).

Propagation can be characterised using the Channel Impulse Response (CIR) approach, which makes an assumption that the channel is a linear filter with impulse response $h(t, \tau)$, [SJKM03]:

$$h(t, \tau) = \sum_{k=1}^{N_{\mathrm{MPC}}} h_k(t)\, \delta(\tau - \tau_k(t)) \tag{2.2}$$

where:

- t: absolute time,
- τ: excess delay,
- h_k: amplitude of the kth MPC,
- τ_k: delay of the kth MPC,
- N_{MPC}: number of MPCs.

If the statistics of the channel do not change with time, the channel is usually captured via the notion of Wide-Sense Stationary (WSS) [Moli05]. Moreover, when the contributions with different delays are uncorrelated (*i.e.*, the Uncorrelated Scatterers (US) hypothesis), it leads to the Wide-Sense Stationarity Uncorrelated Scattering (WSSUS) assumption, in which case the CIR can be written as:

$$h(\tau) = \sum_{k=1}^{N_{\mathrm{MPC}}} h_k\, \delta(\tau - \tau_k) \tag{2.3}$$

The amplitude of the kth MPC is calculated from:

$$|h_k| = \frac{|\Gamma_k|}{d_k} \frac{\lambda}{4\pi} \sqrt{G_{T_k} G_{R_k} P_T} \tag{2.4}$$

where:

- G_{T_k} and G_{R_k}: Tx and Rx antenna gains for the kth MPC, respectively,
- $|\Gamma_k|$: reflection loss of the kth MPC:

$$|\Gamma_k| = \prod_{b=1}^{N_b} |\Gamma_b| \tag{2.5}$$

- d_k: total length of the kth MPC:

$$d_k = \sum_{b=1}^{N_b+1} d_b \tag{2.6}$$

where:

- N_b: number of bounces,
- Γ_b: scatterer reflection coefficient at b^{th} bounce,
- d_b: partial distance of the path.

The Power-Delay Profile (PDP) provides an indication of the distribution of power over various paths in the multipath Propagation Channel. The Power-Delay-Angle Profile (PDAP) includes also the information about the direction of arrival of the MPCs. The MPC is described by the following angular parameters (*i.e.*, DoD and DoA in both azimuth and co-elevation planes):

- φ_{DoD_k}: azimuth angle of departure of the kth MPC,
- θ_{DoD_k}: co-elevation angle of departure of the kth MPC,
- φ_{DoA_k}: azimuth angle of arrival of the kth MPC,
- θ_{DoA_k}: co-elevation angle of arrival of the kth MPC.

2.3. Channel Parameters

Generally, parameters describing the Radio Frequency (RF) part of a wireless system can be divided into two groups, *i.e.*, Propagation Channel and system parameters. It is worthwhile noticing that parameters describing the Propagation Channel are system independent, and concern only MPCs features. In channel modelling, spatial (*i.e.*, excess delay, minimum and maximum delay, and delay spread) and temporal (*i.e.*, Tx and Rx angular spreads) MPCs parameters have to be considered, [Moli05].

First of all, the Rx power can be calculated from:

$$P_R = \sum_{k=1}^{N_{\mathrm{MPC}}} |h_k|^2 \tag{2.7}$$

The path loss is defined as:

$$L_{p[\mathrm{dB}]} = 10 \log \left[\frac{P_T}{P_R} \right] \tag{2.8}$$

A signal propagation delay is the minimum (LoS) time lag between its departure from the Tx and its arrival at the Rx:

$$\tau_{LoS} = \frac{d}{c} \tag{2.9}$$

where:

- c: speed of light.

The temporal MPCs parameters are calculated always relative to the delay of the LoS component.

- Minimum Delay τ_{min}: equal to the delay of the MPC, which arrives at the Rx antenna with minimum latency relative to the LoS component, τ_{LoS}.

- Maximum Delay τ_{max}: equal to the delay of the MPC, which arrives at the Rx antenna with maximum latency relative to τ_{LoS}.

- Mean Delay:

$$\bar{\tau} = \frac{\sum\limits_{k=1}^{N_{\mathrm{MPC}}} |h_k|^2 \, \tau_k}{\sum\limits_{k=1}^{N_{\mathrm{MPC}}} |h_k|^2} \tag{2.10}$$

- Root Mean Square (RMS) Delay Spread:

$$\sigma_\tau = \sqrt{\frac{\sum\limits_{k=1}^{N_{\mathrm{MPC}}} |h_k|^2 \, \tau_k^2}{\sum\limits_{k=1}^{N_{\mathrm{MPC}}} |h_k|^2} - \bar{\tau}^2} \tag{2.11}$$

The spatial MPCs parameters can be calculated for both sides of the radio link, [Moli05].

- Mean DoD Azimuth ($\bar{\varphi}_{DoD}$), Mean DoD Co-Elevation ($\bar{\theta}_{DoD}$), Mean DoA Azimuth ($\bar{\varphi}_{DoA}$), Mean DoA Co-Elevation ($\bar{\theta}_{DoA}$):

$$[\bar{\varphi}_{DoD,DoA}, \bar{\theta}_{DoD,DoA}] = \frac{\sum\limits_{k=1}^{N_{\mathrm{MPC}}} |h_k|^2 \, [\varphi_{DoD_k,DoA_k}, \theta_{DoD_k,DoA_k}]}{\sum\limits_{k=1}^{N_{\mathrm{MPC}}} |h_k|^2} \tag{2.12}$$

- DoD Azimuth Spread ($\sigma_{\varphi_{DoD}}$), DoD Co-Elevation Spread ($\sigma_{\theta_{DoD}}$), DoA Azimuth Spread ($\sigma_{\varphi_{DoA}}$), DoA Co-Elevation Spread ($\sigma_{\theta_{DoA}}$):

$$[\sigma_{\varphi_{DoD,DoA}}, \sigma_{\theta_{DoD,DoA}}] = \sqrt{\frac{\sum\limits_{k=1}^{N_{\mathrm{MPC}}} |h_k|^2 \, [\varphi_{DoD_k,DoA_k}, \theta_{DoD_k,DoA_k}]^2}{\sum\limits_{k=1}^{N_{\mathrm{MPC}}} |h_k|^2} - [\bar{\varphi}_{DoD,DoA}, \bar{\theta}_{DoD,DoA}]^2} \tag{2.13}$$

- DoD Spread

$$\sigma_{DoD} = \sqrt{\sigma_{\varphi_{DoD}}^2 + \sigma_{\theta_{DoD}}^2} \tag{2.14}$$

- DoA Spread

$$\sigma_{DoA} = \sqrt{\sigma_{\varphi_{DoA}}^2 + \sigma_{\theta_{DoA}}^2} \tag{2.15}$$

2.4. MIMO Channel

A MIMO system consists of N_T Tx antennas and N_R Rx ones, Figure 2.4. The relationship between input and output is:

$$\mathbf{y}(\tau) = \mathbf{H}(\tau)\mathbf{x} + \mathbf{n} \tag{2.16}$$

where:

- $\mathbf{x} = [x_1, x_2, ..., x_{N_T}]$: vector of symbols transmitted from the input antennas,
- $\mathbf{y}(\tau) = [y_1(\tau), y_2(\tau), ..., y_{N_R}(\tau)]$: vector containing symbols on the receiving site,
- $\mathbf{n}$: noise vector,
- Matrix $\mathbf{H}$ describes the total CIR of a MIMO Radio Channel with $h_{mn}(\tau)$ being CIRs (discussed in Section 2.2) between signals from the mth Tx antenna to the nth Rx one:

$$\mathbf{H}(\tau) = \begin{bmatrix} h_{11}(\tau) & h_{12}(\tau) & \cdots & h_{1N_T}(\tau) \\ h_{21}(\tau) & h_{22}(\tau) & \cdots & h_{2N_T}(\tau) \\ \vdots & \vdots & \ddots & \vdots \\ h_{N_R1}(\tau) & h_{N_R2}(\tau) & \cdots & h_{N_RN_T}(\tau) \end{bmatrix} \tag{2.17}$$
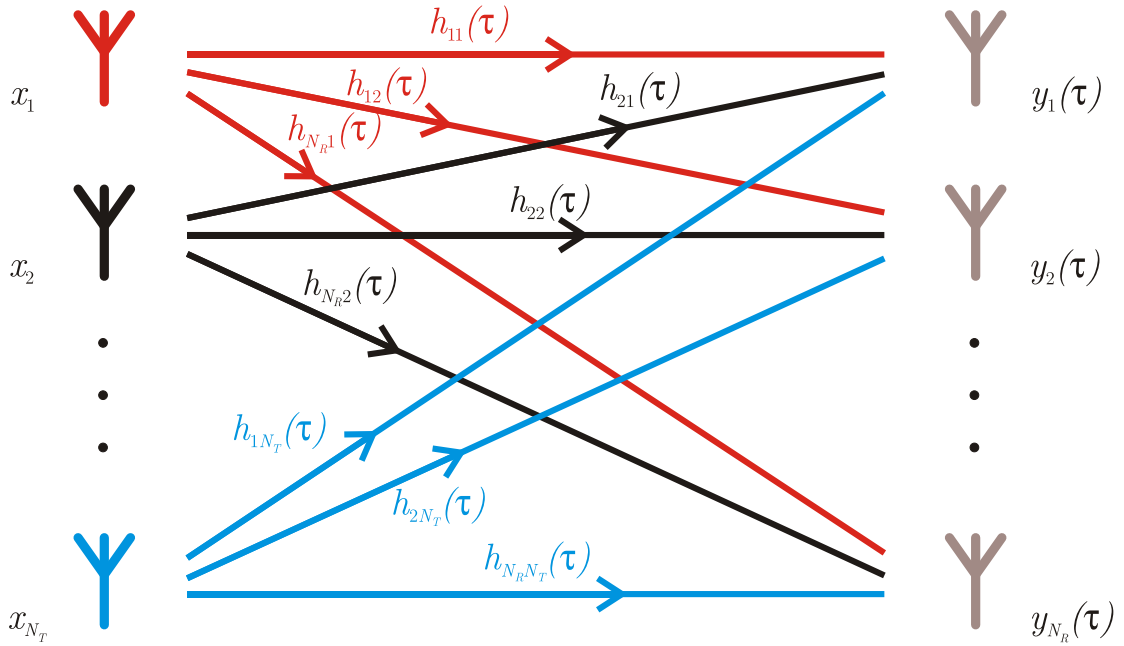
Figure 2.4. MIMO system.

The transformed MIMO system equation can be interpreted as parallel independent subchannels between Tx and Rx, [Dziu04]. The rank of matrix $\mathbf{H}$ leads to the number of parallel subchannels. In an environment rich in scatterers generating many MPCs, the number of uncorrelated subchannels is possibly high, in which case a maximum system performance is observed.

According to the general principles of information theory, the capacity of the Single-Input Single-Output (SISO) Radio Channel, C, is bounded by Shannon's rule [Proa01]:

$$C_{SISO[\text{bps/Hz}]} = log_2(1 + \rho_n) \tag{2.18}$$

where:

- ρ_n: Signal to Noise Ratio (SNR).

The theoretical capacity of a MIMO system has been presented in [Tela95] and [FoGa98]:

$$C_{MIMO\text{[bps/Hz]}} = \log_2 \left\{ \det \left[\mathbf{I}_{N_R} + \frac{\bar{\rho}_n}{N_T} \mathbf{T}\mathbf{T}^H \right] \right\} \tag{2.19}$$

where:

- $\mathbf{I}_{N_R}$: N_R-dimensional identity matrix,
- $\bar{\rho}_n$: is the mean SNR per Rx branch,
- $\mathbf{T}$: the normalised channel transfer matrix related to $\mathbf{H}$ as:

$$\mathbf{T} = \frac{1}{g}\mathbf{H} \tag{2.20}$$

- g: defined as:

$$g^2 = E\left[||\mathbf{H}||\right]^2 = \frac{1}{N_T N_R} \sum_{m=1}^{N_R} \sum_{n=1}^{N_T} |\mathbf{H}_{mn}|^2 \tag{2.21}$$

From (2.19), as a consequence of the correlation of a channel, being between zero and one, it is possible to derive the upper and lower bounds for capacity. If there is no correlation ($\rho = 0$) between parallel paths, the matrix $\mathbf{T}$ will then be the identity one, and the maximum capacity is achieved:

$$C_{MIMO_{max}\text{[bps/Hz]}} = N_{min} log_2 \left(1 + \bar{\rho}_n\right) \tag{2.22}$$

where:

$$N_{min} = min(N_T, N_R) \tag{2.23}$$

On the contrary, the minimum capacity of a MIMO channel occurs when all subchannels are totally dependent ($\rho = 1$):

$$C_{MIMO_{min}\text{[bps/Hz]}} = log_2 \left(1 + N_{min}\bar{\rho}_n\right) \tag{2.24}$$

The relative MIMO system capacity gain, G_{MIMO_s}, can be defined as the relation between the capacity of a MIMO system relative to the SISO one:

$$G_{MIMO_s} = \frac{C_{MIMO}}{C_{SISO}} \tag{2.25}$$

The relative MIMO channel capacity gain, G_{MIMO_c}, can be defined as the relation between the capacity of a MIMO system working in a given scenario relative to the minimum possible gain for a particular MIMO system:

$$G_{MIMO_c} = \frac{C_{MIMO}}{C_{MIMO_{min}}} \tag{2.26}$$

2.5. Boundary Conditions

Let the interface separating two half-space dielectrics with relative permittivities ϵ_{r1} and ϵ_{r2} be denoted by S_i with surface normal $\hat{\mathbf{n}}_{\mathbf{i}}$ directed from medium 2 into medium 1, [Bala89]. At any point on the surface, the electric field $\mathbf{E}_1$ and $\mathbf{E}_2$ on either side of the interface may be decomposed into tangential $E_{t\{1,2\}}$ and normal $E_{n\{1,2\}}$ components relative to the surface, Figure 2.5.
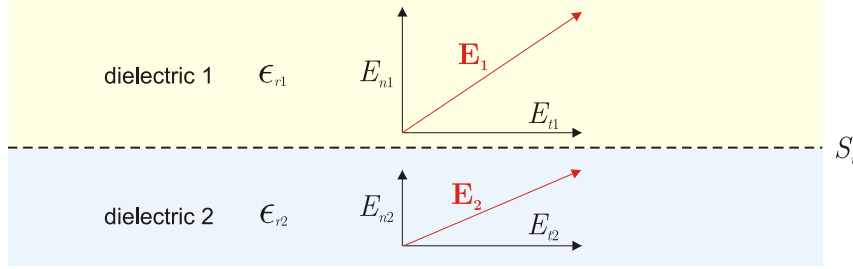
Figure 2.5. Dielectric boundary conditions.

The tangential component of $\mathbf{E}$ is continuous across the interface, [Bala89]:

$$E_{t1} = E_{t2} \tag{2.27}$$

whereas the normal component of electric flux density changes discontinuously across the interface S_i by an amount given by the surface charge density ρ_s at that point:

$$\epsilon_{r1} E_{n1} - \epsilon_{r2} E_{n2} = \rho_s \tag{2.28}$$

The calculation of the reflection coefficients of a plane wave from the half space of given electromagnetic properties is well described in literature, [Bala05]. The reflection coefficient for perpendicular and parallel polarisations, for given relative permittivity, conductivity and relative permeability (*i.e.*, for the air $\epsilon_{ra} = 1$, $\sigma_a = 0$, $\mu_{ra} = 1$, and for the half space ϵ_{rb}, σ_b, $\mu_{rb} = 1$) are as follows:

$$\Gamma_\parallel = \frac{\cos(\theta_r) - \sqrt{\frac{\sigma_b}{j\,\omega\,\epsilon_0} + \epsilon_{rb}}\,\cos(\theta_i)}{\cos(\theta_r) + \sqrt{\frac{\sigma_b}{j\,\omega\,\epsilon_0} + \epsilon_{rb}}\,cos(\theta_i)} \tag{2.29}$$

$$\Gamma_\perp = \frac{\cos(\theta_i) - \sqrt{\frac{\sigma_b}{j\,\omega\,\epsilon_0} + \epsilon_{rb}}\,\cos(\theta_r)}{\cos(\theta_i) + \sqrt{\frac{\sigma_b}{j\,\omega\,\epsilon_0} + \epsilon_{rb}}\,cos(\theta_r)} \tag{2.30}$$

where:

- ϵ_0: vacuum electric constant,
- ω: angular frequency of the incidence wave,
- θ_i: angle of incidence,

- θ_r: angle of refraction.

The angles of incidence θ_i and refraction θ_r are related to each other through Snell's law, which for the considered case reduces to [Bala89]:

$$\frac{\sin(\theta_r)}{\sin(\theta_i)} = \frac{j}{\sqrt{\epsilon_{rb}} \left(\alpha'_b + j\beta'_b \right)} \tag{2.31}$$

where:

$$\alpha'_b = \sqrt{\frac{1}{2} \left(\sqrt{1 + \left(\frac{\sigma_b}{\omega \, \epsilon_{rb}\epsilon_0} \right)^2} - 1 \right)} \tag{2.32}$$

$$\beta'_b = \sqrt{\frac{1}{2} \left(\sqrt{1 + \left(\frac{\sigma_b}{\omega \, \epsilon_{rb}\epsilon_0} \right)^2} + 1 \right)} \tag{2.33}$$

When the dielectric is a lossy medium, the angle θ_r can be a complex number. However, this value has only a theoretical meaning, being used to calculate reflection coefficients.

The electric field of an electromagnetic wave inside a material falls off exponentially from the surface as:

$$E(d) = E_0 e^{-\frac{d}{\delta_p}} \tag{2.34}$$

where δ_p is a penetration depth and measures how deep electromagnetic radiation can penetrate into a material. The concept of penetration depth is one of the many ways to describe the absorption of electromagnetic waves. For a given material, penetration depth and the wave attenuation vary with frequency.

Chapter 3

Body Area Networks

This chapter presents the state of the art on modelling related to BANs, and discusses off-body channel in details. The electromagnetic properties of the body tissues and variability of the body geometry are described. The concept of wearable antennas and their requirements is introduced. Moreover, the existing numerical techniques including full wave methods are presented.

3.1. Body Area Network Channel

BANs refer to Body Centric Wireless Communications [HaHa06], where one or more of the communicating devices are attached to the body. BAN technologies are developing rapidly, and an accurate radio channel model, which accounts for the influence of the body, is a key issue. Depending on the Propagation Channel, BANs can be split into three categories:

- In-body: Communications take place between or with implanted devices. Most of the Propagation Channel is inside the body.
- On-body: The system in which body-worn devices create a self-contained communication system. The Propagation Channel is strongly influenced by the presence of the body, and also both antennas are located very near to the body.
- Off-body: The system in which body-worn devices communicate with a remote location. The Propagation Channel is in the surroundings of the body, and the body influences the antenna on one side of the radio link.

It is worthwhile to notice that a body-to-body channel (when communications take place between wearable devices on two independently moving bodies) is a more complex example of the off-body one. In this case, both antennas on both sides of the radio link are influenced by the presence of the body.

Recently, the IEEE 802.15.6 Working Group for Wireless Personal Area Networks (WPANs), has developed guidelines to design a network system in the vicinity of a human body using short range wireless technologies for various services, [IEEE13b]. According to their recommendations, the following scenarios and frequency bands should be considered in the development of Radio Channel models for BANs, Table 3.1.

Table 3.1. IEEE 802.15.6 channel modelling scenarios recommendations.

Scenario	Description	Frequency Band [GHz]
S1	Implant to Implant	
S2	Implant to Body Surface	[0.402, 0.405]
S3	Implant to External	
S4	Body Surface to Body Surface (LoS)	
S5	Body Surface to Body Surface (NLoS)	0.013, 0.050, 0.400, 0.600, 0.900
S6	Body Surface to External (LoS)	2.400, [3.100, 10.600]
S7	Body Surface to External (NLoS)	

It is worthwhile to notice that this thesis is focused on off-body communications channel modelling. The main difference between a regular Radio Channel and an off-body one is the presence of the body on one side of the radio link, Figure 3.1. In such a channel, the body almost does not interfere with the propagation environment, but its presence leads to changes in the antenna radiation pattern, shift of the resonance frequency, changes in input impedance, and also reduction of antenna efficiency.
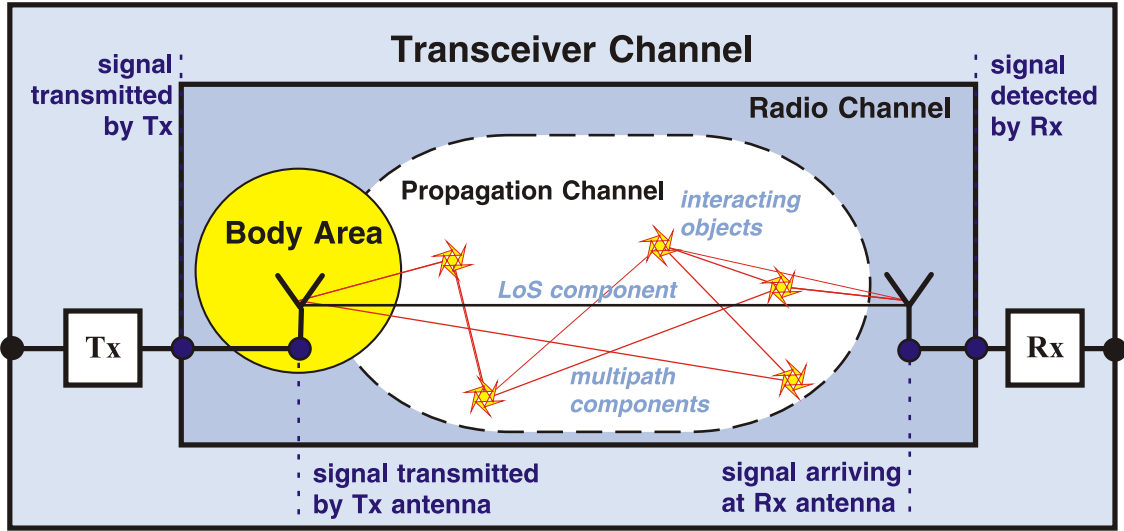
Figure 3.1. Parts of transmission channel of SISO off-body system.

In particular, off-body communications are an emerging research topic that remains little investigated, and just few contributions can be found in literature. The Radio Channel for BANs is studied mainly via measurements in an anechoic chamber or lab environments, for antennas mounted on the body. This approach overcomes the problem of intensive computation demands required by full wave simulations, but it has some other drawbacks, as reliability and repeatability, [KHGN08]. Realistic measurements are expensive, in terms of equipment usage, and very time consuming, and in many cases they can only provide basic output parameters, like path loss.

Some theoretical investigations can be found in [LRDO09], where body scattering, taken only from the arms and the trunk, was considered with a simplified geometrical description of the body (i.e., homogeneous cylinders) and simple point source antenna. Due to the simplified body geometry, the results show big differences between modelled and measured radiation patterns in the forward direction, which is very important for off-body Radio Channels. This work has been extended, and the simplified walk scenario (i.e., periodic arms displacement) has been analysed in [LKCD11].

Because of body movements, a wearable antenna is constantly changing its main radiation direction, which leads to significant changes in the radio link performance. The movement of the body is essential for performance analysis of the antennas in BANs. Body movement has been studied via measurements, [ASAH09]. An animation software (i.e., POSER, [POSE12]) together with an electromagnetic simulator was used to compare measurements with simulations, [GaHB07], [GHBN11]. Results indicate a huge influence of body movement on the performance of the whole Radio Channel, but information about antenna orientation influence is not extracted and analysed.

In [ErOu10], a dynamic channel model based on a time-variant measurement campaign has been presented. The mean channel gain and the fading component for a given on-body link

were analysed for three different body movements, in both an anechoic chamber and an indoor scenario. A similar study was developed for off-body links, and two differently polarised antennas were analysed, [RoEr12]. Moreover, in [CMAS12] and [NaHH10], the path loss and the body impact on the channel gain is characterised. The shadowing by the body is described, but the information about antenna orientation is neglected.

In [SHZM09], measurements and a statistical characterisation of the received signal amplitude transmitted from the body to a receiver, for standing and walking scenarios, were presented. This group also proposed the "everyday"channel model for BANs, [SmHL11], where data come from measurements of several human daily activities scenarios. Also in this case, the antenna performance is hidden inside the channel model, and cannot be extracted.

Various body movements were considered in [AIKT11], [AKTH11], and numerical simulations and experiments were done at 403.5 MHz.

There is also work developed on a dynamic channel characterisation for BANs, using an arm-waving phantom, [YSKO11]. This can provide simplified information about the angles of right and left arms in time (as measured in reference to the torso), but does not include a full description of antenna rotation. In [OgHo12], using a arm-waving phantom, it is shown that the combined outcome of shadowing, caused by the movement of the arms, and multipath effects has a serious impact on the BAN radio link channel.

In general, previous works analyse the whole BAN channel, but there is still a lack of a statistical modelling approach for antenna performance when located on a moving body. Moreover, there is no study presenting temporal (*i.e.*, delay spread) and angular (*i.e.*, angular spread) parameters of the Radio Channel for off-body communications. Finally, to the authors' knowledge, little work has been done in order to include various propagation environments. The statistical model of an antenna joined with the statistical modelling of the propagation environment can be one of the solutions to achieve a full Radio Channel model for BANs.

In order to be able to provide robust connections in BANs, the link budget calculation has to be redefined. The main objective is to maintain a reasonable fading margin at the lowest power consumption (*i.e.*, body centric devices are battery powered or battery less). The following parameters have to be considered:

- Tx Power: limited by energy requirements, but also by safety margins, since the antenna is located near the body,
- Tx and Rx antenna gain: antennas cannot be too directional, due to the movement of the body,
- Tissue absorption: depended on antenna near field coupling, frequency, distance from the antenna to the body, and location on the body,
- Path loss: depended on the propagation environment,
- SNR and Bit Error Rate (BER): determined by application requirements,

- Fading margins: determined by the nature of the Propagation Channel, but also by the location of the antenna on the body, and body movement.

Many of BANs applications have extremely high safety and reliability requirements [OlMC11], which determine the usage of multiple body-worn antennas. Virtual MIMO (*i.e.*, distributed MIMO) consists of clusters of antennas, on Tx and Rx sides, to behave like a multi-antennas system, Figure 3.2. The independence of the links between Tx and Rx is related to propagation conditions in the Radio Channel, and can be measured by an correlation coefficient. A condition to get MIMO channel capacity gains is the decorrelation between the various MIMO links (*i.e.*, pairs of Tx and Rx antennas). A careful choice of the position of the antennas on the body can provide partially decorrelated signal versions at the Rx, which makes the system more reliable and can improve its overall performance, [KhHa10]. In general, the difference in the SNR between signals should be similar (*i.e.*, below 10 dB) and the correlation should be low (*i.e.*, below 0.7) to provide the desired capacity gains [VaAn87].
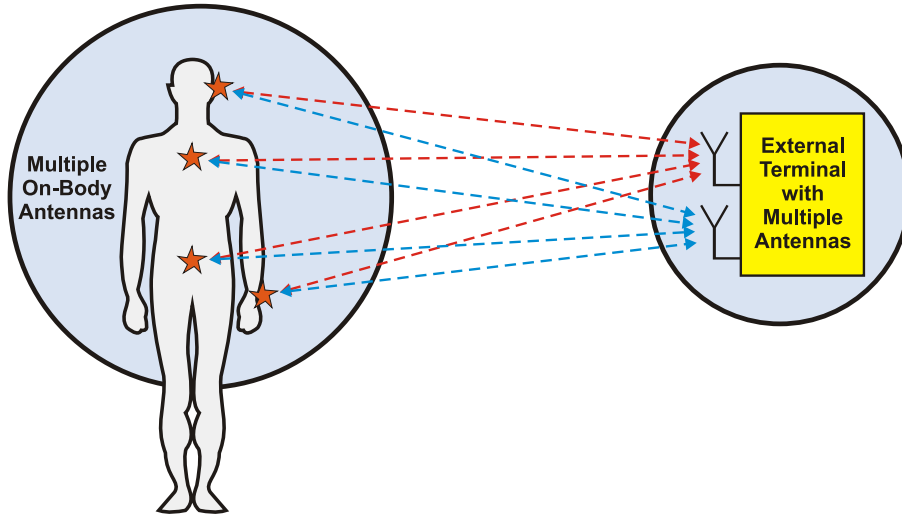
Figure 3.2. Virtual MIMO for off-body communications.

The spatial diversity for off-body communications is studied via measurements in various frequency bands in [CoSc09], [AlCS09]. The cross-correlation is calculated from fading signal envelopes, joining all the effects of the channel, *i.e.*, mobility of the body, changes in the propagation environment, and antenna-body interactions. However, this approach does not extract information about the body decorrelation effect on the arriving MPCs.

Moreover, application of MIMO can overcome the effects of deep fading by combining multiple independent fading paths. In off-body and body-to-body communications, MIMO can be applied in order to reject interference from nearby BANs. The diversity gains and outage capacities of BAN channels with transmit diversity is studied in [AAKC12]. The off-body channel performance is measured in an anechoic chamber, including various human movements and placements of the wearable antennas. It has been demonstrated that diversity exploiting two uncorrelated channels relieves the harmful effect of human movement on the channel conditions and achieves high diversity gains.

3.2. Body Modelling

The nature of the body influence can be split into two categories: antenna and body coupling, and body fading. Since the body tissues can have high values of electric permittivity and conductivity, which depend on the frequency and type of the tissue, the body disturbs the properties of the antennas located in its vicinity. The antenna and body coupling changes the radiation pattern, causes shift of the resonant frequency, and reduces the radiation efficiency. Fading is caused by the shadowing of some directions of radiations by body parts. Depending on the body posture (*i.e.*, standing, sitting or crawling), and body frame dimensions (*i.e.*, weight and height), different directions of radiation are obstructed. Also gender (*i.e.*, female or male) and age (*i.e.*, baby, child or adult) have impact on the wave absorption and pattern of shadowing. The body movements and actions imply that the pattern of shadowing is going to change. Depending on the action (*i.e.*, sit-ups, walking, running or jumping) various directions change in a different way, which can be described statistically.

The biological system of humans is an irregularly shaped dielectric medium with frequency dependent permittivity and conductivity. The amount of scattered energy depends on the body's physiological parameters and geometry, as well as the frequency and polarisation of the incident wave.

The various tissue electric parameters are presented in Figure 3.3, according to the 4-Cole-Cole Model described in [Gabr96]. Electric properties of body tissues for 0.915, 2.45 and 5.8 GHz are gathered in Annex B. The complexity of the structure and composition of biological material is such that each dispersion region is broadened by multiple contributions to it, and can be described by:

$$\epsilon(\omega) = \epsilon_\infty + \sum_{m=1}^{4} \frac{\Delta\epsilon_m}{1 + (j\,\omega\tau_m)^{(1-\alpha_m)}} + \frac{\sigma_i}{j\,\omega\,\epsilon_0} \tag{3.1}$$

where:

- ϵ_∞: permittivity in the THz frequency range,
- σ_i: ionic conductivity,
- τ_m: relaxation time for dispersion region m,
- $\Delta\epsilon$: drop in permittivity in the frequency range for dispersion region m.

With a choice of parameters appropriate to each tissue, this equation can be used to predict its dielectric behaviour over the desired frequency range. The parameters of the model were adjusted to correspond to a close fit between the model and the most comprehensive data set available for the particular tissue.

In order to be able to simulate the influence of the body with the required accuracy, various types of numerical models can be used. A simplified approach is to represent the body as a
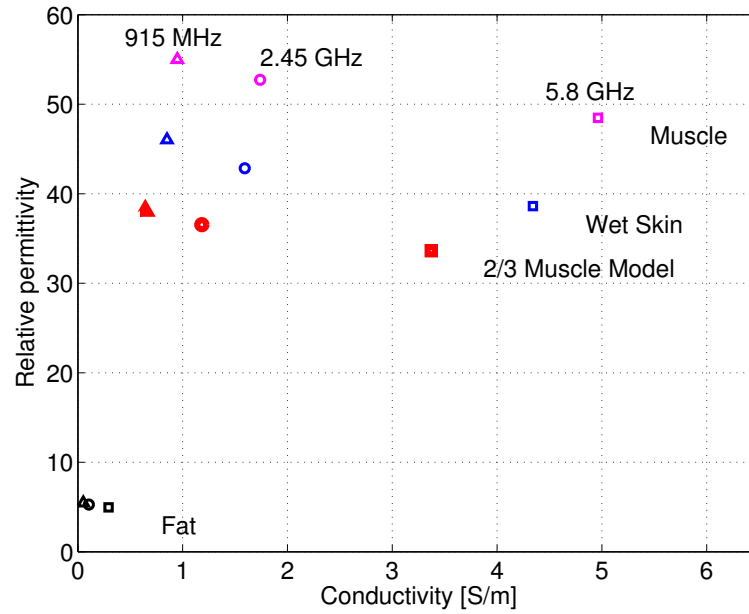
Figure 3.3. Body tissues permittivity and conductivity for 915 MHz, 2.45 GHz and 5.8 GHz.

combination of dielectric spheres and cylinders, single or multiple layer tissues, which can be used in simulations. A more advanced approach is to use mesh homogeneous phantoms where the gender, different body size, and posture can be reproduced.

A number of realistic heterogeneous body models are currently used for electromagnetic field simulations, consisting of large datasets obtained from Magnetic Resonance Imaging (MRI), Computer Tomography (CT), and anatomical images. Data is represented by voxel images of thin slices of the body, and each voxel corresponds to a particular type of the body tissue. In general, heterogeneous body models provide the highest accuracy, and are required to model in-body Propagation Channels. An example of heterogeneous body models are those from a Virtual Family [Chri10], where 2 adults (male and female) and 2 children models can be found, Figure 3.4.

Recently, an updated version of the Virtual Family (*i.e.*, Virtual Population) has been developed, which includes new models with improved quality (*i.e.*, higher resolution allowing a higher degree of precision, a more consistent tissue assignment, and further anatomical refinements), [VPop12]. The models of the Virtual Population are fully compatible with Poser, [POSE12], and SEMCAD X, [SCAD12], simulation platform. The implemented tool is based on techniques developed for animation pictures features, where the skeleton is considered rigid and the rest of the tissues are deformed based on the movements of articulated joints.

A physical phantom reproduces the shape of the body and simulates the characteristics of the biological tissues in a defined range of frequencies. A real shaped body phantom is indispensable for achieving an accurate evaluation of the antenna characteristics from measurements, and several types of phantoms can be used: liquid, gel, rubber, semi-hard, and solid. The phantoms can also be used for SAR evaluation.
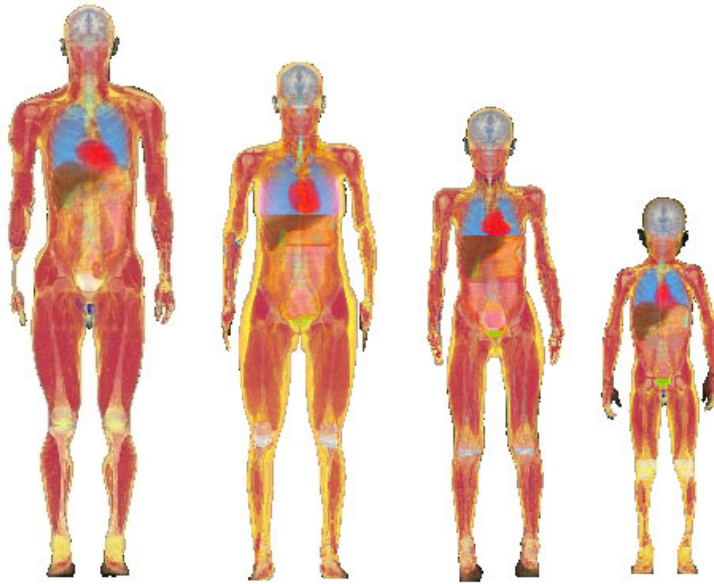
Figure 3.4. Virtual Family models (based on data taken from [Chri10]).

3.3. Wearable Antennas

The body-worn antennas concept is to include a path antenna in the clothe, which can be called as a "smart clothe". Since textile materials (*e.g.*, fleece, vellux, synthetic felt, or cordura) have good electric properties as substrates, they can be easily integrated into clothes. Such materials can be used to produce not only outfits for soldiers, emergency workers (an example is shown in Figure 3.5), uniforms for medical personnel and patients, but also for day to day clothing.

Figure 3.5. Wearable antennas integrated into a firefighter jacket (extracted from [VTHR10]).

The body-worn antennas requirements are:

- low detuning when located in a different location on the body,
- low radiation field into the tissue (*i.e.*, high efficiency, low SAR),

- good coupling to surface (*i.e.*, creeping waves in on-body communications, and free space waves in off-body ones),
- small and compact geometrical size,
- low fabrication cost and integration with front-end components and transceivers.

Modelling the influence of body tissues on antenna gain pattern seems to be one of the major problems for the estimation of off-body Radio Channels. A concept paper [Sibi08] introduced the importance of a statistical model for antennas near interfering objects. The antenna statistical model might describe changes in radiation pattern and input impedance.

In [Hall07], the importance of the development of new antennas for Body Centric Communications and tools for their analysis is presented. The measurements performed in an anechoic chamber shows that an antenna located on the body surface can suffer a 50% reduction in radiation efficiency. Also, the resonant frequency is changed, but the influence can be reduced when an extended ground plane is used. The influence of the body strongly depends on the position of the antenna and body movement.

In [ChCS09], a compact 2.45 GHz active mode-switching wearable antenna for both on- and off-body communications is presented. This antenna is very useful when a single node needs to be able to optimise communications for either on-body sensor links or off-body ones to the wider network. However, it was found that, due to the effect of antenna body coupling, the beam switching from on-body mode to off-body one was possible for antenna body separation more than 7.5 mm. Another design of the switchable wearable anntena (*i.e.*, textile microstrip patch) is presented in [LaFL12].

In [TaKi06], two antennas (*i.e.*, an inverted F patch and a dipole) have been modelled in a Method of Moments software for two cases: free space and near the lossy phantom. The results show a strong influence of the lossy material that is present in the near-field region of the antenna.

The influence of the user on the gain pattern of a mobile phone has been studied in [KTIV06], where measurements have been performed on 13 different people and head phantom. The main conclusion is that the most important factor on the performance of the antenna is the way that people hold the mobile device (*i.e.*, the grip, location and distance from the phone to the head).

In general, the modelling of the antenna near to the body can account for changes in:
- gain pattern,
- input impedance,
- radiation efficiency.

3.4. Numerical Modelling Techniques

There are numerous techniques for modelling the interaction of electromagnetic fields with physical objects and the environment, such as:

- Ray-Tracing (RT) [Glas89],
- Uniform geometrical Theory of Diffraction (UTD) [Path82],
- various full wave methods [Sadi00].

In RT, the approximation consists of using ray optics to estimate the field on a surface, and then integrating that field over the surface to calculate the transmitted or scattered fields. UTD approximates near field electromagnetic fields as quasi optical ones and uses ray diffraction to determine diffraction coefficients for each diffracting object-source combination. Full-wave methods model the domain generally by discretising space in terms of grids, and then solve Maxwell's equations at each point in the grid, for the radiated fields in the presence of all applicable border conditions. The full-wave model provides the most accurate results of antenna's parameters while computing them, such as input impedance, radiation pattern in the near and far field, gain, coupling between elements.

The full-wave method solution can be:

- time-stepping through Maxwell's equations over the whole domain for each time instant with a Finite-Difference Time-Domain (FDTD) algorithm,
- through banded matrix inversion, to calculate the weights of basis functions in Finite Element Method (FEM),
- calculating integrals using Method of Moments (MoM).

One of the techniques that uses a full-wave model is the Finite Integration Technique (FIT), which is applied in Computer Simulation Technology (CST) Microwave Studio, [CST12]. The FIT is a time-domain method very similar to the FDTD one. The FIT formulation is a very general method, and therefore can be applied to all frequency ranges, from Direct Current (DC) to high frequencies. In order to solve the discretised integral version of Maxwell equations numerically, one must define a finite calculation domain, and the CST tool generates a suitable mesh system and splits up this domain into small cuboids, so-called grid cells. The FIT method requires two orthogonal mesh systems: electric grid voltages e_i and magnetic faces fluxes b_i are allocated on the primary grid G_{FIT}, and electric facet fluxes d_i and magnetic grid voltages h_i are allocated on the dual orthogonal grid $\tilde{G_{FIT}}$, Figure 3.6.

As described in CST manual, [CST12], the spatial discretisation of Maxwell's equation is performed on these two systems. It introduces new degrees of freedom and integral values. For each grid facet one can formulate Maxwell's equations. This procedure results in discretised equations, so-called Maxwell's Grid Equations (MGE):
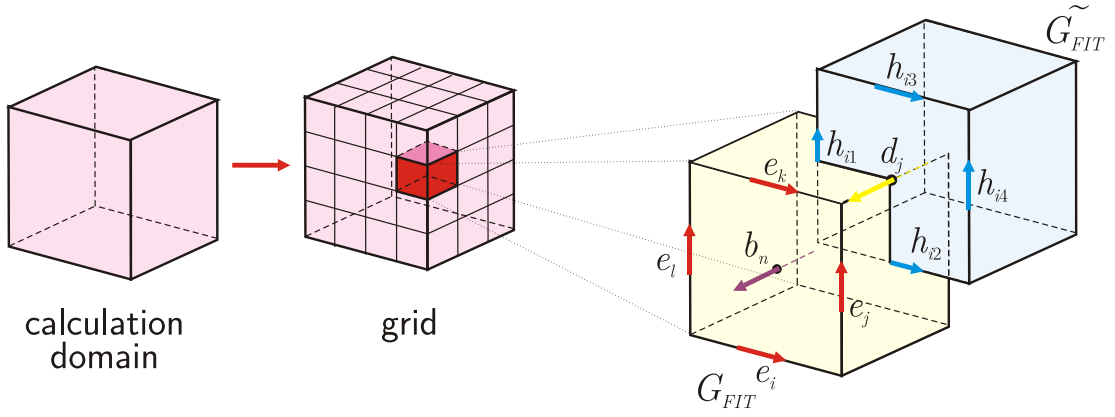
Figure 3.6. Division of calculation domain into grids in FIT (extracted from [CST12]).

$$\mathbf{C_F e} = -\frac{d}{dt}\mathbf{b} \tag{3.2}$$

$$\tilde{\mathbf{C}}_\mathbf{F}\mathbf{h} = \frac{d}{dt}\mathbf{d} + \mathbf{j_t} \tag{3.3}$$

$$\mathbf{S_F b} = 0 \tag{3.4}$$

$$\tilde{\mathbf{S}}_\mathbf{F}\mathbf{d} = \mathbf{q_t} \tag{3.5}$$

where:

- **e**: vector containing electric grid voltages allocated on the primary grid G_{FIT},
- **b**: vector containing magnetic faces fluxes allocated on the primary grid G_{FIT},
- **d**: vector containing electric facet fluxes allocated on dual orthogonal grid $\tilde{G_{FIT}}$,
- **h**: vector containing magnetic grid voltages allocated on dual orthogonal grid $\tilde{G_{FIT}}$,
- **q$_t$**: vector containing total charge in grid cells,
- **j$_t$**: vector containing total current density in grid cells,
- $\mathbf{C_F}$ and $\tilde{\mathbf{C}}_\mathbf{F}$ represent topological information as the discrete equivalents of the analytical curl operator for grid G_{FIT} and $\tilde{G_{FIT}}$, respectively,
- $\mathbf{S_F}$ and $\tilde{\mathbf{S}}_\mathbf{F}$ represent topological information as the discrete equivalents of the analytical divergence operator for grid G_{FIT} and $\tilde{G_{FIT}}$, respectively.

Discretised Material Equations (DME) are put in matrices:

$$\mathbf{d} = \mathbf{M}_\epsilon \mathbf{e} \tag{3.6}$$

$$\mathbf{b} = \mathbf{M}_\mu \mathbf{h} \tag{3.7}$$

$$\mathbf{j_t} = \mathbf{M_\sigma}\mathbf{e} + \mathbf{j_s} \tag{3.8}$$

where:

- $\mathbf{M_\epsilon}$: material matrix containing grid cells permittivity,
- $\mathbf{M_\mu}$: material matrix containing grid cells permeability,
- $\mathbf{M_\sigma}$: material matrix containing grid cells conductivity,
- $\mathbf{j_s}$: vector containing free current density in grid cells.

MGE together with DME are providing the full description to solve the electromagnetic field problem on the discrete grid space. For the loss-free case, one can formulate the so-called leap-frog scheme to compute them:

$$\mathbf{h}^{i+1} = \mathbf{h}^i - \Delta t \frac{\mathbf{C_F}\mathbf{e}^{i+1/2}}{\mathbf{M_\mu}} \tag{3.9}$$

$$\mathbf{e}^{i+3/2} = \mathbf{e}^{i+1/2} + \Delta t \frac{\tilde{\mathbf{C}}_\mathbf{F}\mathbf{h}^{i+1} - \mathbf{j_t}^{i+1}}{\mathbf{M_\epsilon}} \tag{3.10}$$

Every method that tries to describe a real world problem using a numerical model introduces errors. It is the result of using models that are not identical to the real world and the nature of the numerical simulation methods. A good understanding of sources and influence of these errors is essential to know how to minimise them, and how to interpret the obtained results. The errors from disagreements between the simulation model and reality depends on the types of models used in the simulation domain (*i.e.*, the geometrical details and electric parameters). The errors from simulation depends on mesh discretisation error, simulation accuracy (*i.e.*, truncation error), boundary conditions, and other interpolation and numerical errors.

CST offers different kinds of solver modules, [CST12]:

- Transient Solver: This is a very flexible time domain simulation module that is capable of solving any kind of S-parameter or antenna problem. It simulates the structure at a previously defined port using a broadband signal. Broadband simulation enables to obtain the S-parameters for the entire desired frequency range and, optionally, the electromagnetic field patterns at various desired frequencies from only one calculation run.
- Frequency Domain Solver: Like the transient solver, the main task for the frequency domain solver module is to calculate S-parameters. Due to the fact that each frequency sample requires a new simulation run, the relationship between calculation time and frequency steps is linear. Therefore, the frequency domain solver usually is faster when only a small number of frequency samples needs to be calculated.
- Eigenmode Solver: In cases of strongly resonant loss-free structures, where the resonant fields are to be calculated, the eigenmode solver is very efficient. The eigenmode solver can not be used with open boundaries or discrete ports.

- Integral Equation Solver: The areas of application for the integral equation solver are S-Parameter and Far-field calculations. The integral equation solver is of special interest for electrically large models. The discretisation of the calculation area is reduced to object boundaries, and thus leads to a linear equation system with less unknowns than volume methods. The integral equation solver is available for plane wave excitation and discrete face ports. Electric and open boundaries are supported. Far field monitors and surface current monitors can be set in the Frequency Domain Solver with a surface mesh.

The calculation domain has to be subdivided into small cells on which MGE must be solved. CST can use the FIT formulation on orthogonal Cartesian grids or on tetrahedral ones. The mesh influences the accuracy and speed of simulation.

In general, there are three ways to define a hexahedral mesh, [CST12]:

- Manual Meshing: A manual mesh can be defined at any time, even before the geometrical model is generated. This is an old-fashioned way, and it is not recommended.
- Automatic Mesh Generation with an Expert System: It is the most effective way of working with CST. The mesh generator determines the important features of the structure and automatically creates a mesh, which represents the structure and the fields equally well. This means that the frequency range and dielectrics, metallic edges, *etc.*, are considered by the expert system, but certain mesh properties for individual shapes can also be set manually. At the first level, this mesh generator is governed by only a few settings.
- Adaptive Mesh Refinement (Energy Based or Expert System Based): Adaptive meshing replaces expertise by repeatedly running the simulation and evaluating the solutions. Usually regions with high field concentration or field gradients are recognised where the mesh needs to be locally refined. If the deviation in the results falls below a given accuracy level, the adaptation terminates. This approach always improves the start solution at the expense of simulation time. Since the CST expert mesher always guarantees a reasonable initial mesh, and thus a good starting solution for the mesh adaptation process, the number of steps is normally small.

There are a few settings to modify in order to obtain highly efficient meshes, [CST12]:

- M_{LW} Lines per Wavelength (LW): minimum number of mesh lines in each coordinate direction based on the highest frequency of evaluation.
- M_{RL} Ratio Limit (RL): ratio between the biggest and smallest distance between mesh lines. There is an increase on mesh quality when high aspect ratios exist, *e.g.*, edge coupled microstrip. An alternative to the ratio limit, the Smallest mesh step can be entered directly as absolute value rather than defining it relatively via the biggest mesh step and ratio limit. The Smallest mesh step determines the simulation speed.
- Lower mesh Limit: maximum mesh step to be used for the mesh creation, regardless of the setting in lines per wavelength. The maximum step width of the mesh is determined by

dividing the smallest face diagonal of the bounding box of the calculation domain by this number.

The meshing procedure is performed in 3D, which defines a hexahedral mesh for the given voxel model setup. The automatic mesh generation procedure performed in one direction is presented in Figure 3.7.

M_{RL} puts boundaries on the size of the mesh cells, and limits them, so that:

$$M_{RL} \geq \frac{l_{mc_{max}}}{l_{mc_{min}}} \tag{3.11}$$

where:

- $l_{mc_{max}}$: maximum mesh cell length,
- $l_{mc_{min}}$: minimum mesh cell length.
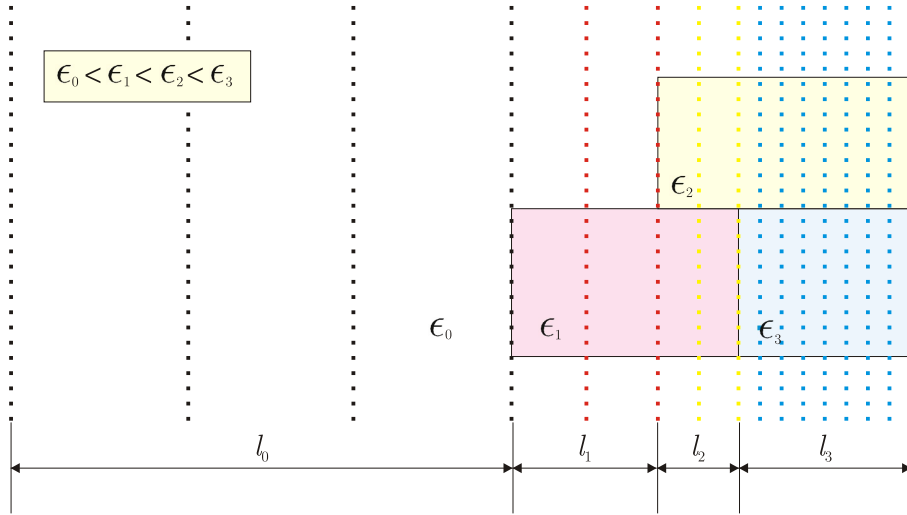
Figure 3.7. Automatic mesh generation procedure in one direction.

The number of mesh lines can be calculated from:

$$N_m = \frac{l_m}{\lambda_m} \cdot M_{LW} \tag{3.12}$$

where:

- l_m: length of the material,
- λ_m wavelength in the material:

$$\lambda_m = \frac{\lambda_0}{\sqrt{\epsilon_{rm}}} \tag{3.13}$$

where:

- λ_0: wavelength in the vacuum,
- ϵ_{rm}: relative permittivity of the material.

This expression is only valid if M_{RL} allows to define a detailed meshing as required for the tissue:

$$M_{RL} \geq \sqrt{\epsilon_{rm}} \tag{3.14}$$

Otherwise, the meshing for a given tissue is performed with a lower resolution, and the global parameter M_{LW} is not fulfilled.

Chapter 4

Statistical Modelling of Antennas on a Body

This chapter proposes a new statistical model to analyse wearable antennas in BANs, using a simple theoretical approach or numerical analysis. In this chapter, a model to study the correlation between signals captured by wearable antennas is presented as well. Moreover, the method to include realistic body movement is introduced.

4.1. Concept and Scenarios

The importance of the statistical study of wearable antennas performance in the vicinity of the body has been reported in [Sibi08]. Following that idea, this thesis considers the antenna as a stochastic component of the radio channel, and studies the influence that the presence of the body has on antennas performance. This presence leads to changes in the antenna gain pattern, which depend on the distance to its surface.

Modelling of the antenna gain pattern in BANs has been decomposed as presented in Figure 4.1.
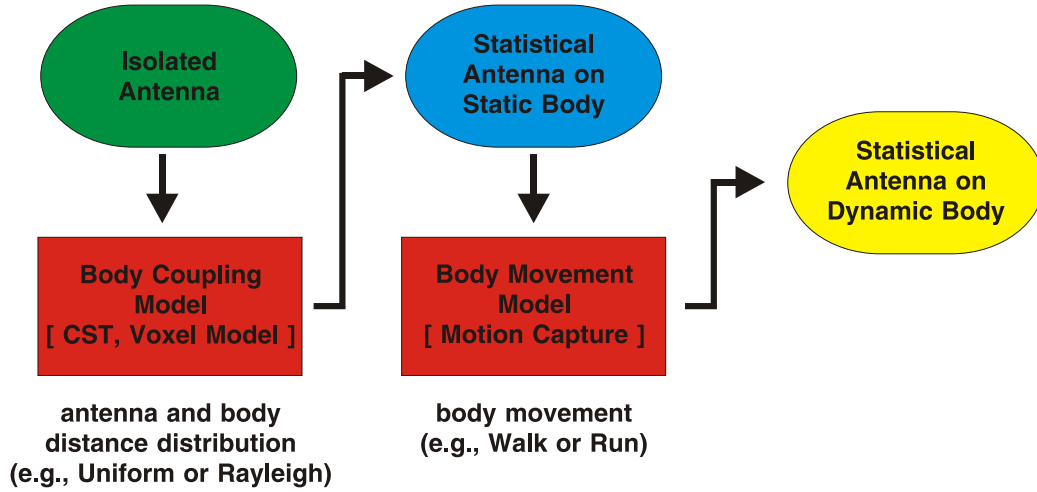
Figure 4.1. Statistical modelling of antennas on a body.

At the first stage, the influence of the presence of the static body (*i.e.*, body coupling) is analysed. In this case, due to the variance of tissues properties and various geometrical dimensions, a key role is played by the location of the antenna on the body. This approach can be analysed via theoretical, numerical or experimental approaches.

At the second stage, body dynamics are taken into account. The novel aspect of this thesis is to present a very realistic model of body dynamics, and the corresponding influence on antenna gain pattern from a statistical viewpoint. Firstly, statistics of the variations of the normal to the surface of an antenna located on a moving body are calculated. Then, taking the statistical gain pattern obtained for the static body, and previously calculated variations of the antenna orientation, the statistical gain pattern of a wearable antenna on a moving body is derived. By using this method, it is possible to describe and include body behaviour scenarios in Radio Channel simulators. This is of great importance, as antenna rotation has a huge impact on the performance of the whole transmission channel. Due to the movement of the antenna located at the BAN side of the radio link, the antenna located at the other side of the link captures significant signal variations in the angular power profile.

A practical segmentation of the human body is introduce, together with orientation, as shown in Figure 4.2. In order to identify the location of the antenna on the body, the label related to a particular body segment and orientation is used.
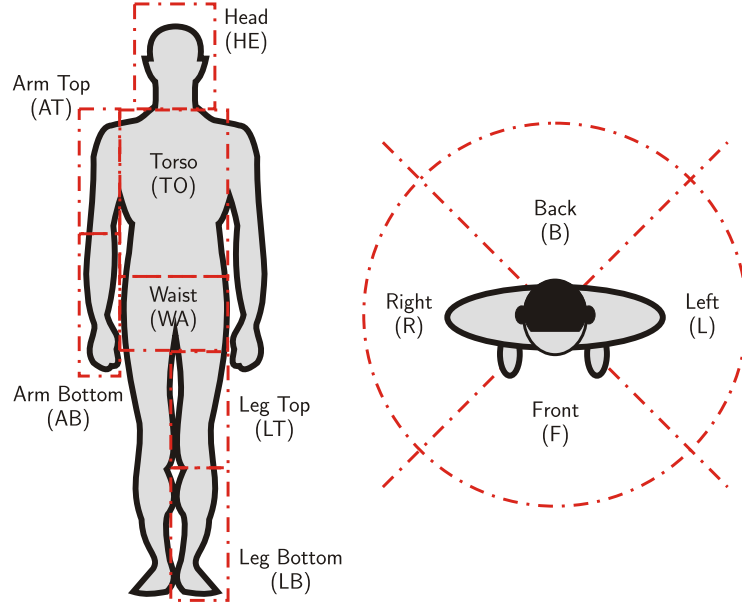
Figure 4.2. Body segmentation and orientation.

The performance of the antenna can be analysed for selected Industrial, Scientific and Medical (ISM) frequency bands (*i.e.*, 0.915, 2.45 and 5.8 GHz). Moreover, as body parts have different physical dimensions and are composed of various tissues (*e.g.*, Skin, Fat or Muscle), the model should account for the placement of the antenna on the body (*e.g.*, Head, Chest, Arm or Leg). Finally, the influence of the body movement on the orientation of the antenna strongly depends on the placement, which is related to the movement of the specific body segment.

Body dynamics can be imported from the POSER database, and snap-shot frames are presented in Figure 4.3. Due to the periodic nature of body dynamics (*i.e.*, running and walking), the Motion Capture description contains only 30 looped time frames, with a duration of 1/30 s each. These frames correspond to the duration of one walking or running periods, starting with the right foot and the left hand forward.

In this work, a patch antenna, [MCCF07], for the 2.45 GHz band is considered, Figure 4.4. Because of the antenna's small dimensions and flat configuration, it can be easily integrated into clothes or equipment. Also, because of the low radiation into the body, its presence does not lead to a significant distortion of antenna performance parameters (*i.e.*, resonance frequency, gain and radiation efficiency). The detailed description of this antenna can be found in [MCCF07].

In this work, selected locations of antennas on the body are analysed:

- TO_F: on the front side of the Torso,
- WA_F: on the front side of the Waist,
- HE_F: on the front side of the Head,
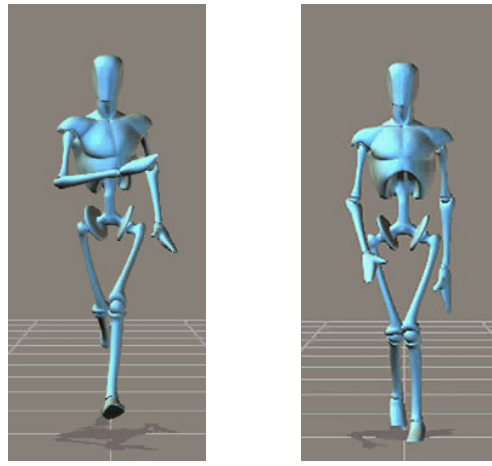
(a) running body (b) walking body

Figure 4.3. Motion Capture snap-shot frames of the body movement (extracted from [POSE12]).
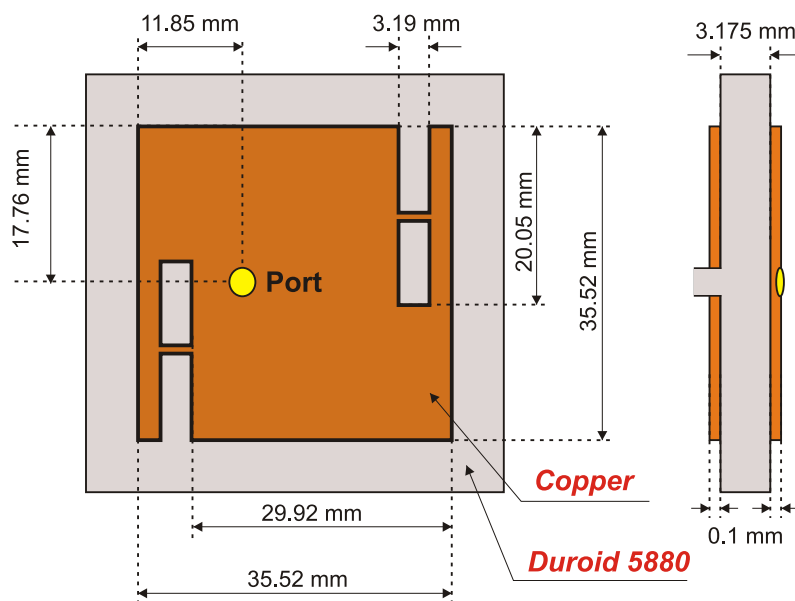
Figure 4.4. Patch antenna with switchable slots in a closed configuration [MCCF07].

- HE_B: on the back side of the Head,
- HE_L: on the left side of the Head,
- HE_R: on the right side of the Head,
- AB_L: on the left side of the Arm,
- AB_R: on the right side of the Arm,
- TO_B: on the back side of the Torso,
- LT_L: on the left side of the Leg,
- LT_R: on the right side of the Leg.

In case of a MIMO system with 2 wearable antennas, the correlation depends on the mutual location of the antennas (*i.e.*, Front, Back, Left and Right), the statistical analysis being performed for the following classes:

- Co-Directed (CD): both antennas are located on the same side.

- Cross-Directed (XD): one antenna is located on the Back or on the Front, whereas the other one is placed on the Left or Right.
- Opposite-Directed (OD): one antenna is located on the Back and the other on the Front, or one antenna is located on the Left and the other on the Right.

In case of a MIMO system with more than 2 antennas, classes considering the total number of sides covered (*i.e.*, from 1 to 4), and a subclass label, including combinations of those sides, are proposed in Table 4.1.

Table 4.1. Possible classes of wearable antennas in MIMO system.

number of the sides	subclass labels
1	F, B, L, R
2	FB, FL, FR, BL, BR, LR
3	FBL, FBR, FLR, BLR
4	FBLR

4.2. Theoretical Model

Since the radiated far field of an antenna in the vicinity of the body is a combination of direct and reflected fields, the influence of the body on the radiation pattern of the electric field strongly depends on the distance of the antenna to the body. A very simple model is taken as a first approach to the more realistic, but also more complex, problem.

In order to compute the statistical behaviour of an antenna near the body, a very simple model based on image theory is introduced. Since the model is based on geometry, calculations are very fast compared to full wave methods. But this modelling approach does not reproduce all the phenomena that are caused by the presence of the body (*i.e.*, reduction of antenna efficiency, and mutual coupling between antenna and the body). Also, in reality, the size of the body cannot be considered much larger than the wavelength for 0.915, 2.45 and even 5.8 GHz, so the model can be considered just as a first approximation. This simple approach has been chosen because of its low computational complexity, and in order to have a glimpse of the possible range of changes in the radiation pattern of the electric field of the antenna placed in the vicinity of the body.

Firstly, the wave reflection by an infinite plane half space is being analysed, Figure 4.5, for an antenna at a height h from the plane.

The reflection coefficient for reflected component for perpendicular and parallel polarisations are calculated according to (2.29) and (2.30), respectively.

In order to model various antenna positions on several locations on the body, a simple geometrical approach has been considered. The infinite plane half space is replaced by an elliptical shaped medium, which dimensions (*i.e.*, a_m minor and a_M major axes) depend on the corresponding part of the body, Figure 4.6.
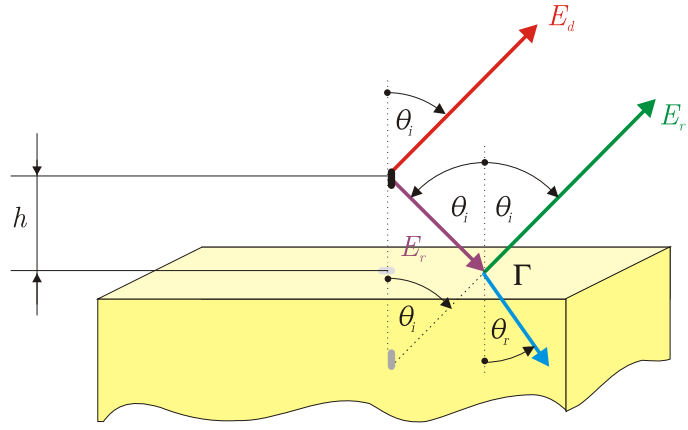
Figure 4.5. Model for the estimation of the radiation pattern of the electric field of an antenna located over infinite lossy dielectric half space.
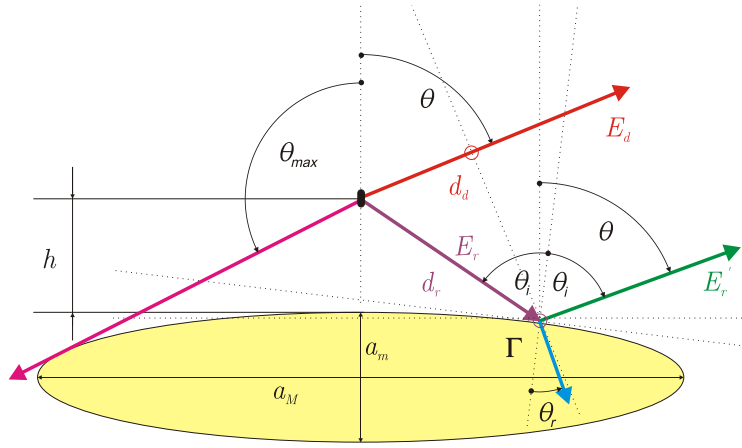
Figure 4.6. Simple model for the estimation of the radiation pattern of the electric field of an antenna located in the vicinity of a body.

In this case, the angle of incidence θ_i is no longer equal to the radiation angle θ, depending also on the distance between the antenna and the ellipse. The angle θ_i for a given θ, h, a_m and a_M, can be found from geometrical considerations. In case θ is larger than the shadowing angle θ_{max}, the antenna does not radiate directly in this direction, and its electric field is $E(\theta, \varphi) = 0$. Otherwise, the total field in the far-field is the result of the sum between the direct component E_d, and the reflected one, E_r. The total field above the body tissue can be written as:

$$E(\theta, \varphi, h) = E_d(\theta, \varphi) + E_r(\theta, \varphi, h)\Gamma(\theta, \varphi, h)\, e^{j\frac{2\pi}{\lambda}\Delta d} \tag{4.1}$$

where:

- $\Delta d = d_r - d_d$
- d_r and d_d are the path lengths of the reflected and direct components, respectively.

The magnitude of the electric field is given by:

$$|E(\theta, \varphi, h)| = \sqrt{|E_d|^2 + |E_r|^2 \, |\Gamma|^2 + 2 \, |E_d| \, |E_r| \, (\Gamma_r \cos\left(\frac{2\pi}{\lambda}\Delta d\right) - \Gamma_i \sin\left(\frac{2\pi}{\lambda}\Delta d\right))} \qquad (4.2)$$

where:

- $\Gamma_r = \mathrm{Re}\left\{\Gamma\right\}$
- $\Gamma_i = \mathrm{Im}\left\{\Gamma\right\}$

In the practical scenario of a BAN, the distance of the antenna to the body can vary in time, which can be described statistically by a Probability Density Function (PDF), $p(h)$. In this case, the average value $\overline{|E(\theta)|}$ for the radiation pattern of the electric field magnitude and its standard deviation $\sigma_{|E|}(\theta)$ can be obtained from:

$$\overline{|E(\theta, \varphi)|} = \int_0^\infty |E(\theta, \varphi, h)| \, p(h) dh \qquad (4.3)$$

$$\sigma_{|E|}(\theta, \varphi) = \int_0^\infty \sqrt{\left(|E(\theta, \varphi, h)| - \overline{|E(\theta, \varphi)|} \right)^2} \, p(h) dh \qquad (4.4)$$

4.3. Numerical Model

In this section, by using numerical model, the statistical behaviour of the radiation pattern of an antenna located over various parts of the body is investigated, Figure 4.7. Contrary to theoretical approach, full wave simulations can reproduce, with high accuracy, the phenomena that are caused by the presence of the body (*i.e.*, mutual coupling between antenna and the body, body shadowing, and reduction of antenna efficiency).
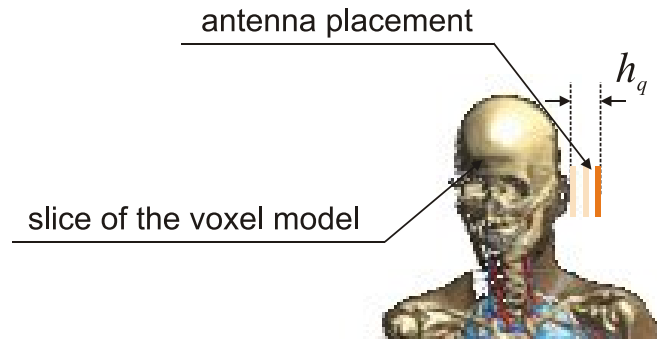
Figure 4.7. Numerical model for an antenna placed near the head (voxel head extracted from [Chri10]).

When an antenna is located on the body, its performance parameters are modified by the presence of the tissues, and the amount of change depends on the distance to the surface. In the practical scenario for a BAN, the distance of the antenna to the body can vary in time, which can be described statistically. Various possible distance distributions can be analysed, *e.g.*, Uniform or "locally" Rayleigh. The Uniform Distribution models the possible range of changes of radiation

pattern within the distance interval, limited by the maximum realistic distance of antenna to the body (*e.g.*, wearable antenna placed on a coat). The Rayleigh Distribution describes a realistic scenario in BANs, where the distribution parameters are defined by the features of the antenna location on the clothe: goes from 0 to a large value, and it is concentrated on a central distance.

In general, the average and standard deviation of the gain pattern, for an antenna placed on the body, can be calculated depending on:

- distribution of the distance between antenna and body surface (*e.g.*, Uniform or Rayleigh),
- antenna types (*e.g.*, patch),
- antenna placements (*e.g.*, Head, Chest, Arm or Leg),
- body types (*i.e.*, gender, age, frame dimensions weight and height).

One of the possible tools is CST [CST12], which is a full wave simulation software, described in detail in Section 3.4. In order to model body influence, the voxel model provided by Virtual Family [Chri10] is used, which is presented in Section 3.2. Furthermore, in order to reduce the calculation domain (*i.e.*, speed up the simulations), the voxel model can be sliced into several parts. For example, the analysis of the performance of an antenna placed on the head does not require to model the whole body, as other fragments of the body (*i.e.*, chest, arms, and legs) have little influence on the gain pattern. It is recommended to use at least 4 body segments, for the respective antenna placement, as presented in Table 4.2.

Table 4.2. Considered voxel model segments for respective antenna placements.

voxel model segment	antenna placement
Head	HE_F, HE_B, HE_L, HE_R
Chest	TO_F, TO_B, WA_F
Arm	AB_L, AB_R
Leg	LT_L, LT_R

The electric parameters of the tissues (*i.e.*, conductivity and relative permittivity) are obtained from the 4-Cole-Cole Model [Gabr96], described in Section 3.2. It is worthwhile to notice that this study can be performed using another full wave simulator and voxel model.

By performing simulations of the antenna located with different distances from the body h_q (a discretisation of the distance is considered, in terms of index q), one obtains a set of gain patterns $G(\theta_n, \varphi_m, h_q)$ (θ_n and φ_m being discrete values of the usual spherical coordinates). The distance sample h_q depends on the distribution of the distance to body, and on the total number of distance samples N_h (*i.e.*, the accuracy of the study). From the set of simulated gain patterns, it is possible to calculate the average one:

$$G_\mu(\theta_n, \varphi_m) = \frac{1}{N_h} \sum_{q=1}^{N_h} G(\theta_n, \varphi_m, h_q) \tag{4.5}$$

where:

- h_q: is the qth distance sample,
- N_h: is the total number of distance samples,
- θ_n: is the azimuth angle sample,
- φ_m: is the elevation angle sample.

The standard deviation of the gain pattern can be calculated from:

$$\sigma_G(\theta_n, \varphi_m) = \sqrt{\frac{1}{N_h} \sum_{q=1}^{N_h} (G(\theta_n, \varphi_m, h_q) - G_\mu(\theta_n, \varphi_m))^2} \qquad (4.6)$$

The average and the standard deviation of the gain pattern should be used in Radio Channel simulators to calculate multipath components, therefore, being used as linear quantities. However, usually, results for an antenna's gain pattern are shown in a logarithmic scale, hence, the above mentioned entities are presented in dB. In this work, the following convention is used:

$$G_{\mu \pm \sigma}(\theta_n, \varphi_m)_{[\text{dBi}]} = 10 \log(G_\mu(\theta_n, \varphi_m) \pm \sigma_G(\theta_n, \varphi_m)) \qquad (4.7)$$

$$\sigma_G(\theta_n, \varphi_m)_{[\text{dB}]} = 10 \log(\sigma_G(\theta_n, \varphi_m)) \qquad (4.8)$$

The minimum, G_{min}, and maximum, G_{max}, of the gain pattern are calculated from the set of distance samples:

$$G_{min}(\theta_n, \varphi_m)_{[\text{dBi}]} = 10 \log(\min_{h_q} \{G(\theta_n, \varphi_m, h_q)\}) \qquad (4.9)$$

$$G_{max}(\theta_n, \varphi_m)_{[\text{dBi}]} = 10 \log(\max_{h_q} \{G(\theta_n, \varphi_m, h_q)\}) \qquad (4.10)$$

The antenna gain in the direction of maximum radiation is defined as:

$$G_0 = \max \{G(\theta, \varphi)\} \qquad (4.11)$$

The radiation efficiency is related to the antenna gain by:

$$\eta_a = \frac{G_0}{D_0} \qquad (4.12)$$

where:

- D_0: is antenna directivity in the direction of maximum radiation.

In order to evaluate the difference between a general gain pattern G and a reference one G_{ref} (*e.g.*, the gain pattern of the isolated antenna), first the partial pattern difference, calculated for a particular direction of radiation, can be calculated:

$$\Delta_{G_{nm}} = \frac{|G(\theta_n, \varphi_m) - G_{ref}(\theta_n, \varphi_m)|}{G_{ref}(\theta_n, \varphi_m)} \qquad (4.13)$$

In general, two parameters are defined, *i.e.*, the Pattern Average Difference (PAD):

$$\overline{\Delta_G} = \frac{1}{N_\varphi N_\theta} \sum_{n=1}^{N_\varphi} \sum_{m=1}^{N_\theta} \Delta_{G_{nm}} \tag{4.14}$$

and the Pattern Weighted Difference (PWD):

$$\overline{\Delta_{G_w}} = \frac{\sum\limits_{n=1}^{N_\varphi} \sum\limits_{m=1}^{N_\theta} \Delta_{G_{nm}} G_{ref}(\theta_n, \varphi_m)}{\sum\limits_{n=1}^{N_\varphi} \sum\limits_{m=1}^{N_\theta} G_{ref}(\theta_n, \varphi_m)} \tag{4.15}$$

where:

- N_θ: is number of discrete elevation angle samples,
- N_φ: is number of discrete azimuth angle samples.

The difference between these two parameters is that $\overline{\Delta_G}$ treats changes of the gain pattern in all directions equally, whereas $\overline{\Delta_{G_w}}$ weights these changes by the gain pattern.

As these simulations introduce discretisation errors (*e.g.*, calculation domain meshing resolution), the influence of the simulation parameters should be evaluated, in order to achieve the required accuracy and reasonable speed of calculations. The patch antenna has been modelled in free space and near the voxel body model. Performing a single simulation does not provide information about the accuracy of the solution. The FIT method guarantees that the discretisation error decreases with an increasing number of mesh cells. This property can be used to check the accuracy by refining the mesh, re-running the simulation and comparing results. It is, however, important to find a good compromise between mesh density (affecting the simulation time) and accuracy. Simulations were performed in a personal computer with Intel Core 2 Duo @ 2.40 GHz processor and 3 GB of Random Access Memory (RAM). The Transient Solver was used with an excitation signal in the band [0.3, 2.6] GHz. Table 4.3 presents the simulation time t_s and total memory M_t required for each run, which are proportional to the number of mesh cells N_c.

Table 4.3. Complexity of selected meshing parameters scenarios.

M_{RL}	10			7	
M_{LW}	14	12	10	16	10
N_c [10^6]	8.8	5.7	3.5	2.4	0.7
M_t [GB]	2.8	2.0	1.3	0.9	0.4
t_s [min]	33.9	22.4	10.9	10.2	2.3

When modelling an isolated patch antenna in CST, the following parameters have been calculated:

- Gain: $G_a = 6.6$ dBi,

- Total radiation efficiency: η_a=80 %,
- Resonance frequency: $f_r = 2.44$ GHz,
- Input return loss: $S_{11} = -12.4$ dB.

When comparing output parameters of the antenna in free space and near the voxel model head for a $\{M_{LW}{=}14,\ M_{RL}{=}10\}$ meshing setup, the difference in resonance frequency is 0.02 GHz. The S_{11}, calculated for the resonance frequency is higher (*i.e.*, worst) by 2.0 dB when the antenna is located near the voxel head model. The gain is reduced by -1.2 dB, and also the total efficiency is lower by -1.0 dB (which is equal to -20%).

The input impedance (*i.e.*, resonance frequency f_r) and antenna's radiation parameters (*i.e.*, antenna gain G_0, radiation efficiency η_a, gain pattern difference $\overline{\Delta_G}$ and $\overline{\Delta_{G_w}}$) were analysed in order to decide on the optimal meshing setup for simulation of the antenna in presence of the voxel body model in CST. In Table 4.4, the results for all assessment scenarios are presented, and the difference is calculated in reference to the $\{M_{LW}{=}14,\ M_{RL}{=}10\}$ scenario.

Table 4.4. Patch antenna parameters simulated with different meshing parameters.

M_{RL}	10			7	
M_{LW}	14	12	10	16	10
S_{11} [dB]	-10.30	-10.43	-10.56	-11.49	-10.36
ΔS_{11} [dB]	-	-0.13	-0.26	-1.19	-0.06
f_r	2.460	2.462	2.455	2.455	2.492
$\frac{\Delta f_r}{f_r}$ [%]	-	0.09	-0.19	-0.19	1.31
η_a [dB]	-1.93	-1.97	-1.86	-1.86	-1.85
$\Delta\eta_a$ [dB]	-	-0.04	0.07	0.07	0.08
G_0 [dBi]	5.39	5.37	5.47	5.34	6.00
ΔG_0 [dB]	-	-0.02	0.08	-0.05	0.61
$\overline{\Delta_G}$ [%]	-	2.38	5.43	3.67	12.79
$\overline{\Delta_{G_w}}$ [%]	-	0.99	1.77	1.98	10.67

The meshing obtained for $\{M_{LW}{=}14,\ M_{RL}{=}10\}$ is considered as the most accurate one, due to the largest number of mesh cells used. The total efficiency and the gain are calculated using the far field monitor at 2.45 GHz.

The S_{11} curves for all analysed meshing setups are presented in Figure 4.8. Results obtained for all meshing setup except $\{M_{LW} = 10,\ M_{RL} = 7\}$ have similar resonant frequencies, around 2.46 GHz. The magnitude of the S_{11} parameter is lower by 1 dB also for $\{M_{LW} = 16,\ M_{RL} = 7\}$ meshing, but this parameter is not essential for the antenna gain pattern analysis, therefore acceptable.

The changes δ_r of the parameters relative to the case of the maximum number of mesh cells N_{cmax} (*i.e.*, setup with $\{M_{LW}{=}14,\ M_{RL}{=}10\}$) are presented in Figure 4.9, being defined as:

$$\delta_r(N_c) = \frac{|f(N_c) - f(N_{cmax})|}{f(N_{cmax})} \qquad (4.16)$$
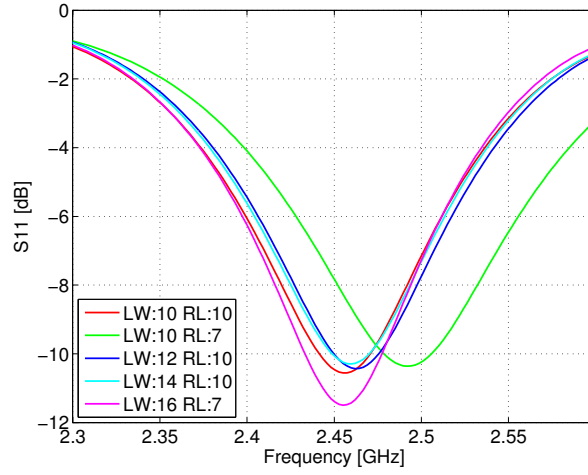
Figure 4.8. Comparison of S_{11} curves for patch antenna calculated for various meshing parameters.
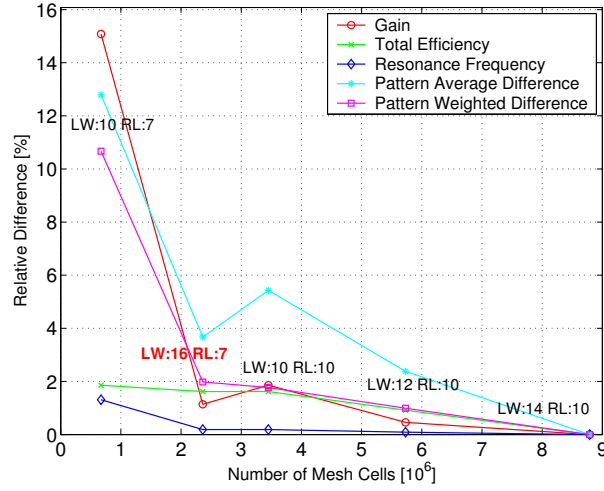
Figure 4.9. Relative error of patch antenna parameters for various meshing scenarios.

For all meshing setups, except $\{M_{LW}=10, M_{RL}=7\}$, the relative error to the reference scenario is below 5%. The meshing with $\{M_{LW}=16, M_{RL}=7\}$ is characterised by a moderate number of mesh cells, and the results obtained from simulations are similar to meshing scenarios $\{M_{LW}=12, M_{RL}=10\}$ and $\{M_{LW}=10, M_{RL}=10\}$. Therefore, the $\{M_{LW}=16, M_{RL}=7\}$ setup can be considered as the optimal one in terms of complexity and accuracy.

4.4. Modelling of Signal Correlation

Many of BANs applications have extremely high safety and reliability requirements, which determine the usage of multiple body-worn antennas. In BANs, multiple antennas can be placed on various locations on the body (*e.g.*, Head, Chest, Waist, Arm or Leg) and with various orientations (*i.e.*, Front, Back, Left and Right). For off-body communications, the signal is transmitted by an external antenna, propagates in the environment, and is captured by wearable antennas. A condition to get MIMO channel capacity gains is decorrelation between the various MIMO links (*i.e.*, pairs of Tx and Rx antennas). At various antennas, the received signals are

different, as they are modified by body coupling, shifted in time, and attenuated. Body coupling depends on the placement and distance from the antenna to the body, whereas body shadowing is determined by the direction of the incoming wave. In this model, the statistical study is performed for various separations of antennas from the body, and azimuth of incoming waves, Figure 4.10.
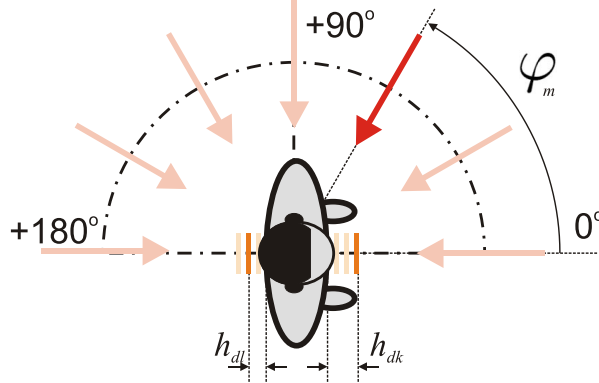
Figure 4.10. Correlation Model.

In this thesis, the problem is studied by full wave numerical simulations with plane wave excitation, which represents a single multipath component. In order to evaluate the difference, the signals s_k and s_l received at different antennas can be cross-correlated, [Orfa96]:

$$(s_k * s_l)(h_{dk}, h_{dl}, \varphi_m, \tau_{kl}) = \int_{-\infty}^{\infty} s_k(h_{dk}, \varphi_m, t) s_l(h_{dl}, \varphi_m, t + \tau_{kl}) \, dt \tag{4.17}$$

where:

- h_{dk} and h_{dl}: distances to the body from k^{th} and l^{th} antennas, respectively,
- φ_m: azimuth of the mth incoming wave,
- t: absolute time,
- τ_{kl}: delay of s_k relative to s_l.

As the received signals can be shifted in time, the maximum value of the cross-correlation can be used to align signals in time, hence, taking the worst case scenario (*i.e.*, the highest cross-correlation between signals):

$$\rho^{k,l}(h_{dk}, h_{dl}, \varphi_m) = \max_{\tau_{kl}} \left\{ (s_k * s_l)(h_{dk}, h_{dl}, \varphi_m, \tau_{kl}) \right\} \tag{4.18}$$

The average cross-correlation and the standard deviation between the kth and l^{th} pair of antennas, which are located with N_k and N_l distance samples from the body, for a specific azimuth φ_m, is:

$$\overline{\rho^{k,l}(\varphi_m)} = \frac{1}{N_k N_l} \sum_{k=1}^{N_k} \sum_{l=1}^{N_l} \rho^{k,l}(h_{dk}, h_{dl}, \varphi_m) \tag{4.19}$$

$$\sigma_\rho^{k,l}(\varphi_m) = \sqrt{\frac{1}{N_k N_l} \sum_{k=1}^{N_k} \sum_{l=1}^{N_l} \left[\rho^{k,l}(h_{dk}, h_{dl}, \varphi_m) - \overline{\rho^{k,l}(\varphi_m)} \right]^2} \qquad (4.20)$$

The average cross-correlation and the standard deviation can also be calculated as a function of the distance of the kth antenna to the body surface, for the N_m azimuth samples:

$$\overline{\rho^{k,l}(h_{dk})} = \frac{1}{N_l N_m} \sum_{l=1}^{N_l} \sum_{m=1}^{N_m} \rho^{k,l}(h_{dk}, h_{dl}, \varphi_m) \qquad (4.21)$$

$$\sigma_\rho^{k,l}(h_{dk}) = \sqrt{\frac{1}{N_l N_m} \sum_{l=1}^{N_l} \sum_{m=1}^{N_m} \left[\rho^{k,l}(h_{dk}, h_{dl}, \varphi_m) - \overline{\rho^{k,l}(h_{dk})} \right]^2} \qquad (4.22)$$

Finally, the global average cross-correlation and the standard deviation is given by:

$$\overline{\rho^{k,l}} = \frac{1}{N_m} \sum_{m=1}^{N_m} \overline{\rho^{k,l}(\varphi_m)} \qquad (4.23)$$

$$\sigma_\rho^{k,l} = \sqrt{\frac{1}{N_m} \sum_{m=1}^{N_m} \overline{\rho^{k,l}(\varphi_m)}^2} \qquad (4.24)$$

As the cross-correlation depends on the mutual location of the antennas (*i.e.*, Front, Back, Left and Right), the statistical analysis is performed for the CD, XD and OD classes. The average and the average standard deviation can be calculated for the specific class in the usual way. It is expected that for CD and OD antennas the average cross-correlation will be the highest and the lowest, respectively. In the case of XD antennas, the average cross-correlation should be moderated, however, the highest values for the standard deviation are expected.

4.5. Modelling of Body Dynamics

Capturing the movement of the body is essential for the analysis of the antenna performance. The model for body movement is based on data taken from Motion Capture analysis. Such data consist of a static component (*i.e.*, skeleton hierarchy information, which is composed of several nodes, linked to each other by a translation vector) and a dynamic one (*i.e.*, motion data), which is a list of rotations of the nodes for each time frame of the body movement. The node position is calculated from the position of a previous node in the model hierarchy by solving a forward kinematics problem [Cube06], well known from robotics. This modelling approach can be applied to any object (*e.g.*, human body or animal), and can describe any movement (*e.g.*, walking, running, jumping, crawling or dancing) in a frame-by-frame manner. One of the

data formats is Biovision Hierarchy (BVH) [DCSZ10], which is not used directly for modelling of antenna orientation, but provides the required body movement characteristics.

In order to measure shifts of the antenna orientation, a reference coordination system has to be selected. In this model, the reference direction is the front of the body, azimuth φ and elevation ψ angles being calculated as presented in Fig. 4.11, taking the usual coordinates system.
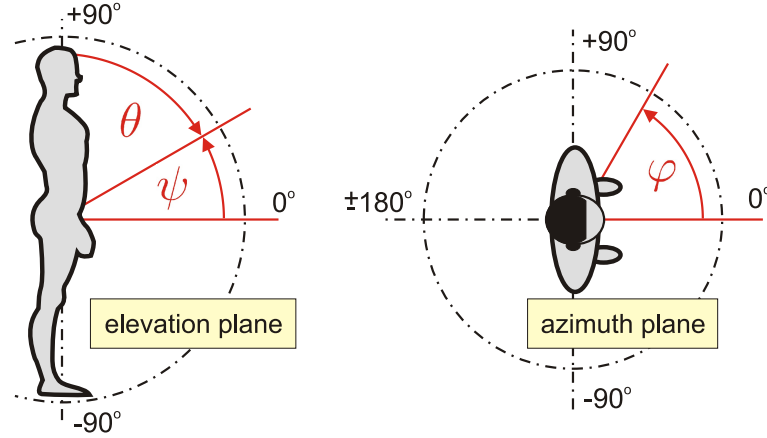
Figure 4.11. Body directions, in the usual spherical coordinates system.

The model considers the antenna as an additional node, which is derived from the desired body node (*e.g.*, head, chest, hand or knee). This approach allows one not only to calculate the position of the antenna $P_a(x_a, y_a, z_a)$, but also to determine its normal to the body surface. Many types of BAN antennas for off-body communications (*e.g.*, a patch antenna [MCCF07]) have the direction of maximum radiation normal to the surface. The shifts in azimuth $\delta\varphi_k$ and elevation $\delta\psi_k$ planes are calculated for each time frame k of the body movement. In this case, the normal to the surface is obtained from the vector, calculated from the body node, $P_b(x_b, y_b, z_b)$, to the antenna one, P_a. The spherical coordinates co-elevation θ_{k_0} and azimuth φ_{k_0} of this vector have to be calculated:

$$\theta_{k_0} = \arccos\left(\frac{\Delta z}{r_0}\right) \tag{4.25}$$

$$\varphi_{k_0} = \arcsin\left(\frac{\Delta y}{r_0 \sin(\theta_{k_0})}\right) \tag{4.26}$$

where:
- $r_0 = \sqrt{(\Delta x)^2 + (\Delta y)^2 + (\Delta z)^2}$
- $\Delta x = x_a - x_b$, $\Delta y = y_a - y_b$, $\Delta z = z_a - z_b$

The shift $\delta\psi_k$ in the elevation plane is given by:

$$\delta\psi_k = 90° - \theta_{k_0} \tag{4.27}$$

whereas the shift $\delta\varphi_k$ in the azimuth plane is:

$$
\delta\varphi_k = \begin{cases}
-180° - \varphi_{k_0}, & \Delta x < 0 \text{ and } \varphi_{k_0} < 0 \\
180° - \varphi_{k_0}, & \Delta x < 0 \text{ and } \varphi_{k_0} \geq 0 \quad (4.28) \\
\varphi_{k_0}, & \text{other cases}
\end{cases}
$$

In what follows, all output parameters are defined for the azimuth plane, however, for the elevation one the definition is similar. Average $\overline{\delta\varphi}$ and standard deviation $\sigma_{\delta\varphi}$, are calculated for all time frames:

$$
\overline{\delta\varphi} = \frac{1}{N_T} \sum_{k=1}^{N_T} \delta\varphi_k \tag{4.29}
$$

$$
\sigma_{\delta\varphi} = \sqrt{\frac{1}{N_T} \sum_{k=1}^{N_T} \left(\delta\varphi_k - \overline{\delta\varphi}\right)^2} \tag{4.30}
$$

where:

- N_T: total number of time frames.

Regarding the statistics of the normal to the surface, it was found that Kumaraswamy and Beta Distributions are the ones that best fit the selected data. These distributions can be used for variables that are lower and upper bounded, which is the case for angles in this problem, as the rotation of the normal to the body surface is constrained (*i.e.*, depending on the body movement, and antenna location). The PDF of the Beta Distribution, [MaMy78], with shape parameters α_B and β_B, for the random variable δ, is:

$$
p_B(\delta; \alpha_B, \beta_B) = \frac{\gamma_B^{\alpha_B - 1}(1 - \gamma)^{\beta_B - 1}}{B(\alpha_B, \beta_B)} \tag{4.31}
$$

where:

$$
\gamma_B = \frac{\delta - \delta_{min}}{\delta_{max} - \delta_{min}} \tag{4.32}
$$

- δ_{min} and δ_{max}: minimum and maximum shifts of the normal to the surface, respectively,
- $B(\alpha_B, \beta_B)$: normalisation constant to ensure that the probability integrates to unity.

The PDF of the Kumaraswamy Distribution, [Kuma80], with shape parameters α_K and β_K, is:

$$
p_K(\delta; \alpha_K, \beta_K) = \frac{\alpha_K \beta_K \gamma^{\alpha_K - 1}(1 - \gamma^{\alpha_K})^{\beta_K - 1}}{K(\alpha_K, \beta_K)} \tag{4.33}
$$

where:

- $K(\alpha_K, \beta_K)$: normalisation constant to ensure that the probability integrates to unity.

The mean calculated from simulated data $\overline{\delta\varphi}$ can be compared to the one coming from the Kumaraswamy Distribution $\text{E}_\text{K}(\overline{\delta\varphi})$, for which there is a deviation defined as:

$$\Delta_K \overline{\delta\varphi} = E_K(\overline{\delta\varphi}) - \overline{\delta\varphi} \tag{4.34}$$

A similar parameter can be defined for the standard deviation:

$$\Delta_K \sigma_{\delta\varphi} = E_K(\sigma_{\delta\varphi}) - \sigma_{\delta\varphi} \tag{4.35}$$

where:

- $\sigma_{\delta\varphi}$: standard deviation calculated from simulated data,
- $E_K(\sigma_{\delta\varphi})$: standard deviation coming from the Kumaraswamy Distribution.

To calculate the gain pattern on a dynamic body, first, one has to obtain $G(\psi, \varphi)$, which is an average gain pattern for the desired placement on the static body. This average gain pattern is calculated for an antenna which distance to the body surface is changing with a given distribution (*e.g.*, Rayleigh with a maximum probable distance of 2 cm); it was taken for several samples of the distance. Instead of taking the average gain pattern, a percentile (*e.g.*, 90th percentile) approach can be taken for system design. Then, the gain pattern, including the shift of the direction of maximum radiation of the antenna, is given by:

$$G_k(\psi, \varphi) = G(\psi + \delta\psi_k, \varphi + \delta\varphi_k) \tag{4.36}$$

This modelling approach still does not reproduce all the phenomena that are caused by the presence of the moving body. The whole body moves, and when the movement of the antenna is analysed (*e.g.*, located on the chest), some radiation directions can be additionally obstructed by the presence of other body segments (*e.g.*, hands). Since the model is geometry based, calculations are very fast compared to full wave methods. Moreover, it is very complex to obtain realistic and dynamic body models (*e.g.*, voxel models), which are required by full wave modelling approaches.

From the set of previously calculated gain patterns for all time frames of body movement, it is possible to calculate the average gain pattern:

$$G_\mu(\psi, \varphi) = \frac{1}{N_T} \sum_{k=1}^{N_T} G_k(\psi, \varphi) \tag{4.37}$$

and the standard deviation:

$$\sigma_G(\psi, \varphi) = \sqrt{\frac{1}{N_T} \sum_{k=1}^{N_T} [G_k(\psi, \varphi) - G_\mu(\psi, \varphi)]^2} \tag{4.38}$$

Chapter 5

Results of Statistical Behaviour of Antennas on a Body

In this chapter, the results obtained from the developed models, accounting for the body coupling (using theoretical, numerical and practical approaches) are presented and analysed. Moreover, the statistics of the antenna gain patterns on the moving body are obtained.

5.1. Body Coupling

5.1.1. Theoretical Approach

Simulations were performed for the scenarios described in Table 5.1, and always only one group of parameters were changed while the other two were set as the Reference Scenario. The radiation pattern of the electric field of the antenna near the body for both parallel and perpendicular polarisations were calculated for 3 frequency bands (*i.e.*, 915 MHz, 2.45 GHz and 5.8 GHz), 4 different body tissues (*i.e.*, Fat, Muscle, Wet Skin and 2/3 Muscle and 1/3 Fat equivalent model) and 3 different positions (*i.e.*, Torso, Head and Arm). The Uniform Distribution in the range [0, 10] cm and Rayleigh Distribution with mode 2 cm antenna to body distance were used to calculate statistics of the radiation pattern of the electric field for all scenarios. The dimensions of the ellipse (*i.e.*, a_m and a_M) corresponding to particular body parts were set as shown in Table 5.1, [HeUl09].

Table 5.1. Scenarios for the theoretical approach.

Scenarios	Frequency [GHz]	Tissue	Position (a_M, a_m) [cm]
Reference	2.45	2/3 Muscle	Torso (40, 10)
Other	0.915	Fat	Head (15, 15)
	5.8	Muscle	Arm (5, 5)
		Wet Skin	

Figure 5.1 shows the radiation pattern of the electric field for the antenna located over an infinite plane half space, for $\{0, 2.5, 5, 7.5, 10\}$ cm. A large variation in the radiation pattern, reaching 15 dB, can be observed when the distance of the antenna to the plane is changed only by 10 cm. As expected, an increasing distance results in a higher number of minima and maxima in the radiation pattern of the electric field.
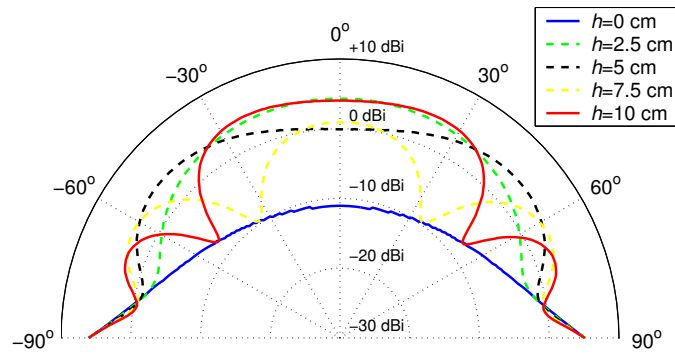
Figure 5.1. The radiation pattern of the normalized electric field of an antenna located over an infinite half space, for electric properties set to the values of the 2/3 Muscle Model, 2.45 GHz, and parallel polarisation.

Examples of average radiation pattern of the electric field and its standard deviation for parallel polarisation, for 915 MHz, for Uniform and Rayleigh Distributions are presented in Figure 5.2.

As Rayleigh Distribution has its mode for $h = 2$ cm, and decays fast with the increase of the distance, the maximum and minimum values of the radiation pattern were calculated for $h \in [0, 10]$ cm. For θ smaller than $75°$, the average radiation pattern for the Uniform Distribution $\overline{|E_U|}$ is greater than the one for the Rayleigh distribution $\overline{|E_R|}$, and for higher θ they are the same, rising up to 2 for $90°$. Also for angles smaller than $75°$, the maximum average radiation pattern for $\overline{|E_U|}$ is equal to 1.2 and only 0.8 for $\overline{|E_R|}$. For angles up to $80°$, $\overline{|E_R|}$ is below 1, which means a dominant destructive interference between direct and reflected components. In the case of the antenna located over half space, the shape of the radiation pattern strongly depends on the distance between antenna and body.
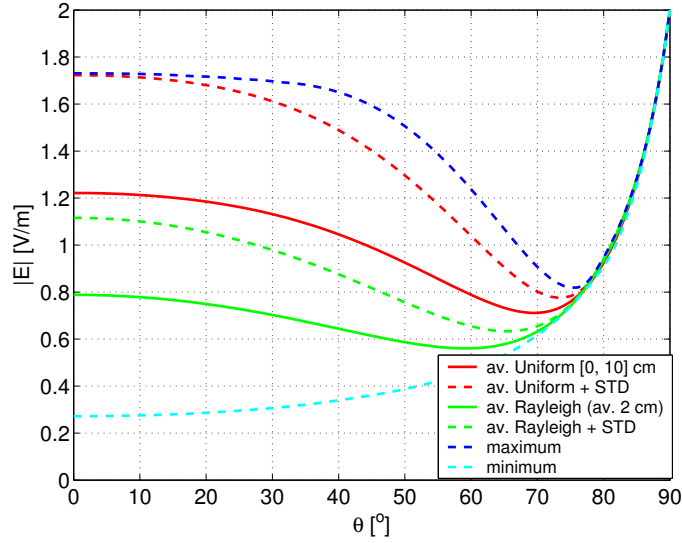
Figure 5.2. The average radiation pattern of electric field of antenna located over infinite half space, for electric properties set to the values of the 2/3 Muscle Model, for 915 MHz, for parallel polarisation.

The full set of statistical values of radiation pattern of the electric field (*i.e.*, the average $\overline{|E_U|}$ and the standard deviation $\sigma_{|E_U|}$ for the Uniform Distribution, the average $\overline{|E_R|}$ and the standard deviation $\sigma_{|E_R|}$ for the Rayleigh Distribution, $|E_{max}|$ maximum, and $|E_{min}|$ minimum) for both parallel and perpendicular polarisations, for selected angles of radiation $\{0°, 15°, 30°, 45°, 60°, 75°, 90°\}$, for the Reference Scenario, are gathered in Table 5.2.

For $\theta = 0°$, all results for both parallel and perpendicular polarisations are the same (*i.e.*, $\Gamma_{\parallel} = \Gamma_{\perp}$). The range of changes in the radiation pattern of the electric field is very high (*i.e.*, from 0 to 1.9) and depends on the angle of incidence. The average radiation pattern and standard deviation depend on the antenna behaviour as well as polarisation. $\sigma_{|E_R|}$ is always less than $\sigma_{|E_U|}$ due to the fact that, in the Uniform Distribution, the antenna is changing position with the same probability whereas in Rayleigh Distribution distance changes less. For parallel and perpendicular polarisations, the maximum $\sigma_{|E_U|}$ is 0.45 and 0.6, whereas the maximum $\sigma_{|E_R|}$ is 0.35 and 0.5, respectively. In both cases, the standard deviation is large compared to the average.

Table 5.2. Statistical parameters for isotropic antenna over an ellipse for the Reference Scenario.

$|E|, \sigma_{|E|}$ [V/m]		θ						
		0°	15°	30°	45°	60°	75°	90°
pol.	$\overline{|E_U|}$	1.24	1.21	1.12	1.03	1.10	1.12	0.99
$\parallel$	$\sigma_{|E_U|}$	0.44	0.45	0.44	0.44	0.39	0.33	0.19
	$\overline{|E_R|}$	1.44	1.40	1.32	1.19	0.99	0.80	0.87
	$\sigma_{|E_R|}$	0.30	0.31	0.33	0.36	0.33	0.17	0.13
	$|E_{min}|$	0.28	0.40	0.30	0.36	0.42	0.65	0.77
	$|E_{max}|$	1.72	1.71	1.68	1.65	1.57	1.51	1.57
pol.	$\overline{|E_U|}$	1.24	1.21	1.15	1.08	1.19	1.25	0.92
$\perp$	$\sigma_{|E_U|}$	0.44	0.46	0.47	0.51	0.52	0.58	0.57
	$\overline{|E_R|}$	1.44	1.41	1.36	1.27	1.09	0.76	0.68
	$\sigma_{|E_R|}$	0.30	0.31	0.35	0.41	0.44	0.39	0.47
	$|E_{min}|$	0.28	0.39	0.26	0.25	0.19	0.10	0.01
	$|E_{max}|$	1.72	1.73	1.72	1.78	1.80	1.85	1.87

The maximum standard deviation is almost 0.5 for the Uniform Distribution at 0.915 and 5.8 GHz, and Rayleigh at 5.8 GHz, and equal to 0.3 for Rayleigh at 0.915 GHz, Figure 5.3. For angles up to 60°, the difference in $\sigma_{|E_U|}$ for both frequencies is less than 0.05, whereas $\sigma_{|E_R|}$ for 5.8 GHz is 0.25 higher than for 0.915 GHz for angles up to 75°. It is worthwhile to notice that for 5.8 GHz, for angles up to 60°, σ_{E_R} is very close to $\sigma_{|E_U|}$, which can be explained by the fact that the wavelength is comparable to the antenna movement also for the Rayleigh Distribution.
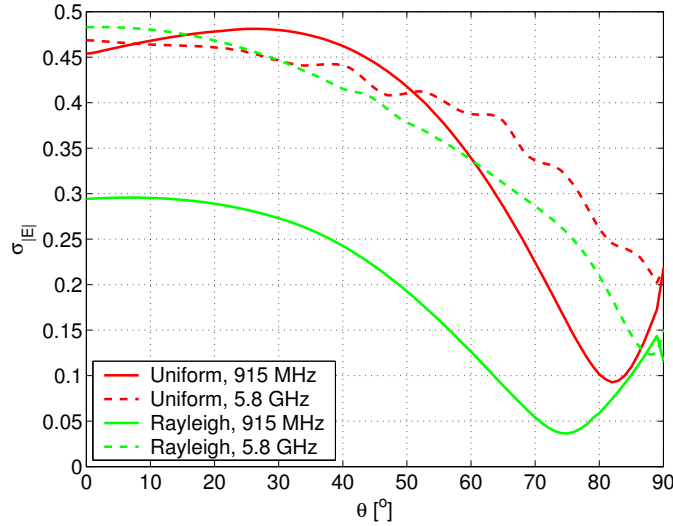
Figure 5.3. Comparison of standard deviations for parallel polarisation, 915 MHz and 5.8 GHz, 2/3 Muscle tissue, and Torso position.

For the Uniform Distribution, the maximum standard deviation is almost 0.5 for Muscle and 0.25 for Fat, Figure 5.4. For θ less than Brewster's angle for parallel polarisation, $\sigma_{|E_U|}$ and $\sigma_{|E_R|}$ for Fat are two times less than for Muscle. This is because Fat has significantly lower values of a permittivity and conductivity (*i.e.*, it does not contain water), therefore, this type

of tissue has a weaker influence on the radiation pattern of antenna than others. The minimum standard deviation for parallel polarisation is obtained always for radiation angles equal to Brewster's angle, which depends on the electrical properties of body tissues. For Fat and Rayleigh Distribution, the minimum value of standard deviation is equal to 0.03 for $\theta = 75°$. In this direction, the changes of the radiation pattern are minimal.
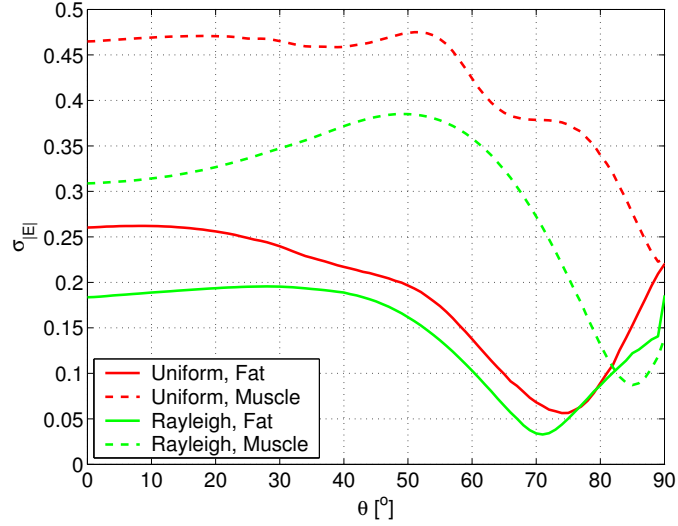
Figure 5.4. Comparison of standard deviation for parallel polarisation, Fat and Muscle tissues, 2.45 GHz, and Torso position.

The maximum radiation angle strongly depends on the dimensions of the body part, and also on the maximum distance from the antenna to the body, Figure 5.5.
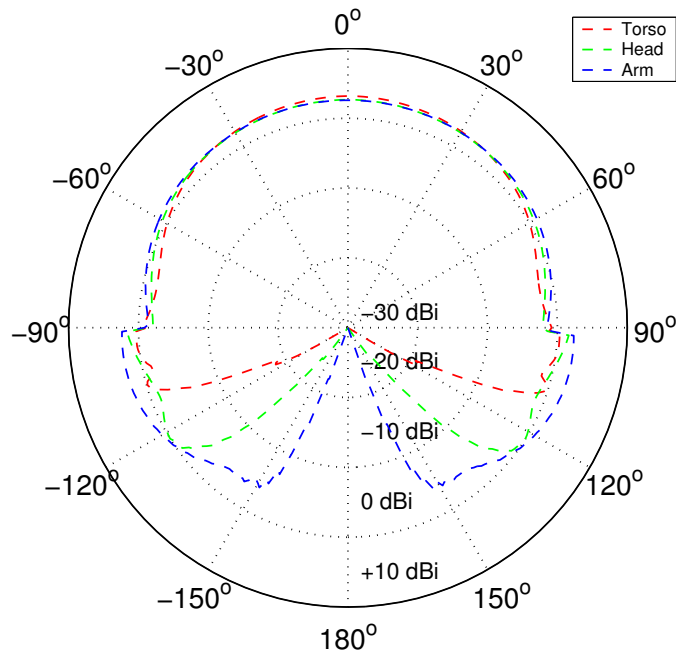
Figure 5.5. Comparison of average radiation pattern for the Rayleigh Distribution, for various positions on the body.

Concerning the location of the antenna over Torso, Head and Arm, the antenna is radiating up to 110°, 130° and 155°, respectively. As it is expected, the largest maximum radiation angle

has been obtained for the smallest body part (*i.e.*, Arm). For all positions on the body, the average radiation pattern, for angles up to the maximum radiation angle, is changing from -3 dB to +3 dB, with maximum radiation for 0°, minimum for 90°, and sharp transition to 0 for the maximum radiation angle.

Preliminary calculations with basic theoretical models show that the body causes important changes in the antenna radiation pattern. Depending on the distance of the antenna to the body, the reflected component can have a constructive or destructive effect on the total radiated field. Also, the placement of the antenna is important, and among analysed tissues, the Muscle has highest influence (*i.e.*, the highest permittivity and conductivity) whereas Fat has the lowest. This confirms the validity of the proposed concept of an antenna statistical model describing the changes in its overall performance (*e.g.*, radiation pattern, efficiency, and input impedance), which can then be included in standards and Radio Channel models. In general, the standard deviation is large, and one expects significant changes of the gain pattern of antenna, which is radiating towards body tissues (*e.g.*, a dipole antenna placed parallel to the body surface).

5.1.2. Numerical Approach

This section presents a statistical analysis of the several gain pattern of the patch antenna, calculated at different distances between antenna and body. In order to speed up simulations, the model of the 26-years female provided by Virtual Family has been sliced into 4 parts. The following locations and antenna orientations being analysed: Head, Chest, Arm and Leg. This model is one of the two adult voxels provided by Virtual Family, and it was selected because it is the one that generates fewer mesh cells. It was decided to use only one voxel, because very specific body parts are being studied and no great changes are expected between genders. To perform a more detailed study, one should consider not only both genders, but also different morphologies (*i.e.*, fat, thin, tall *etc.*). Two distance distributions are analysed: Uniform in range $[0, 2\lambda]$ at 2.45 GHz, and Rayleigh with a mode of 2 cm. Simulations were performed for 20 samples of the distance, which were calculated according to the distribution. The gain patterns of the patch located near the Head for $\{0, \frac{1}{2}\lambda, \lambda, \frac{3}{2}\lambda, 2\lambda\}$, as well as the gain pattern for an isolated patch are presented in Figure 5.6.

The highest variations are observed in the direction of the body and at the side lobes. For the antenna attached to the Head (*i.e.*, $h = 0$), the gain in the forward direction is the lowest, and also for all other distances is less than the gain for the isolated antenna. To investigate better the change in the gain pattern when the antenna is moving closer to the body, $\overline{\Delta_{G_w}}$ was calculated relative to the isolated antenna for all analysed scenarios for the Uniform Distribution, Figure 5.7.

For all body parts, the change of the gain pattern is the strongest when the antenna is located at a distance $h = 0$. This is because the coupling between the body and antenna is the highest, resulting in a significant reduction of antenna radiation efficiency, which affects the overall shape
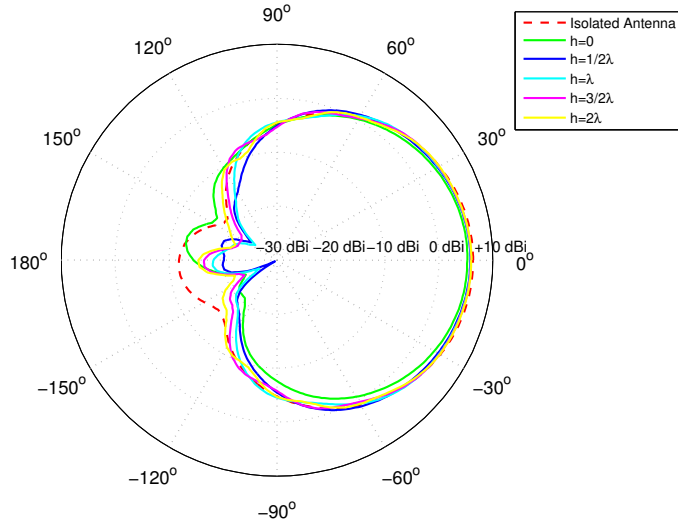
Figure 5.6. Gain patterns of a patch antenna for various distances to the Head.
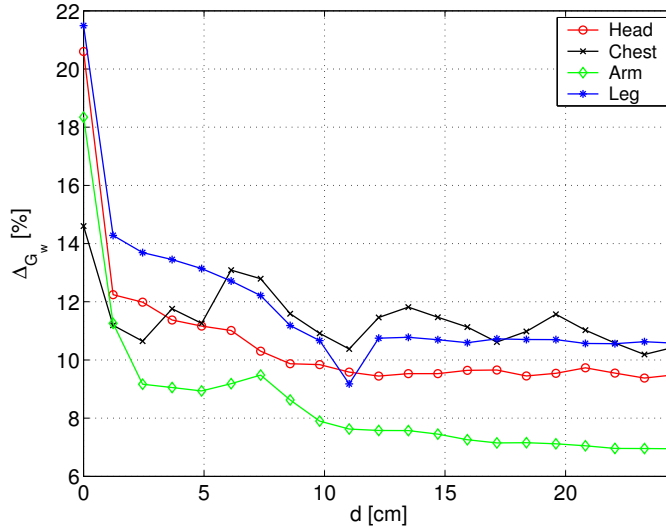
Figure 5.7. PWD for all analysed body regions for a distance range of $[0, 2\lambda]$ at 2.45 GHz.

of the gain pattern. In general, moving the antenna away from the body results in a smaller value of $\overline{\Delta_{G_w}}$; however, this is not a monotonous trend, especially in the case of the location on the Chest.

The statistics of the gain pattern (*i.e.*, G_μ, $G_{\mu+\sigma}$, G_{min} and G_{max}) of the antenna located near the Head relative to the isolated antenna are shown in Figure 5.8.

The average gain pattern strongly depends on the distribution of the distances between antenna and body. The range of changes of the gain pattern is the highest in the backward direction (*i.e.*, $\varphi = 180°$), being almost 8 dB. However, the changes in this direction are not important for off-body communications.

The average gain pattern G_μ together with the standard deviation σ_G, for selected azimuth angles of radiation $\varphi = \{0°, 90°, 180°\}$, for all body parts is shown in Table 5.3.
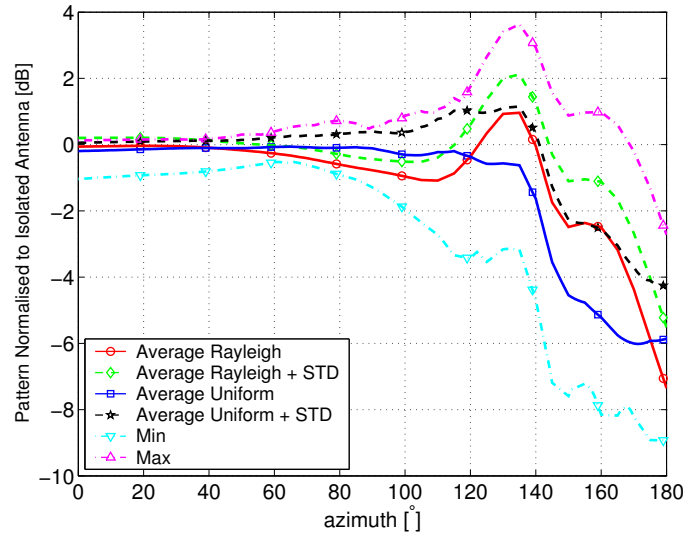
Figure 5.8. Statistics of the gain pattern of the antenna located near the Head for Uniform and Rayleigh Distributions relative to the gain pattern of the isolated antenna.

Table 5.3. G_μ and σ_G for selected φ and for $\theta = 90°$.

		φ	Head	Chest	Arm	Leg
G_μ[dBi]	Uniform	0°	6.2	6.5	6.2	6.1
		90°	-4.9	-5.5	-4.8	-5.0
		180°	-17.7	-22.8	-17.7	-21.4
	Rayleigh	0°	6.3	6.6	6.4	6.2
		90°	-5.6	-6.6	-6.1	-5.7
		180°	-19.2	-21.8	-16.6	-21.3
σ_G[dB]	Uniform	0°	-6.1	-6.7	-4.6	-4.9
		90°	-13.9	-13.6	-12.5	-13.1
		180°	-21.1	-26.1	-15.7	-24.3
	Rayleigh	0°	-5.7	-7.7	-5.1	-4.2
		90°	-16.5	-18.4	-13.4	-15.1
		180°	-22.0	-27.4	-15.3	-23.8

The average gain pattern in the forward direction (*i.e.*, $\varphi = 0°$) varies slightly among body regions, between 6.1 dB and 6.6 dB. Therefore, the antenna is well isolated from the body, and changes in the antenna gain are moderated. In the backward direction (*i.e.*, $\varphi=180°$), the lowest gain is obtained for Chest and Leg, due to the large attenuation of the body tissues. For all body regions, the highest σ_G is observed for the forward direction, and for both distance distributions for Arm and Leg, it is higher by 2 dB compared to other body regions. However, the absolute values of the standard deviation are low, and small variations of the gain with the distance are expected. In the backward direction, independent on the distance distribution and of the body region, σ_G is very low. The reason is that in the backward direction the average gain pattern is very low.

The comparison between average gain patterns, for the Rayleigh Distribution, for all body regions, as well as the gain pattern of the isolated antenna are presented in Figure 5.9. Average

$\overline{\Delta_G}$ and $\overline{\Delta_{G_w}}$ calculated relative to the isolated antenna, for all analysed locations and both distributions, are gathered in Table 5.4.
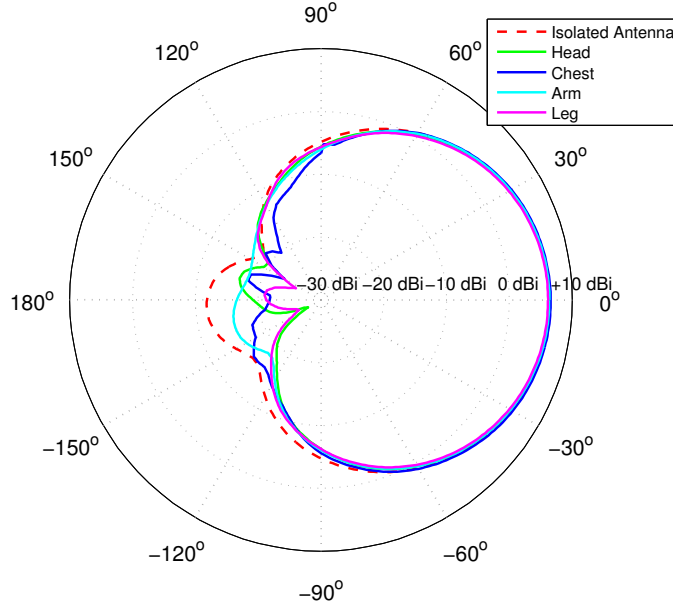
Figure 5.9. Comparison of the average gain patterns, for the Rayleigh Distribution, and various body regions.

Table 5.4. PAD and PWD as compared to the isolated antenna.

		Head	Chest	Arm	Leg
$\overline{\Delta_G}_{[\%]}$	Uniform	12.1	22.2	9.7	16.0
	Rayleigh	18.1	24.3	18.7	22.9
$\overline{\Delta_{G_w}}_{[\%]}$	Uniform	4.8	9.8	4.1	6.3
	Rayleigh	6.9	11.0	7.4	9.3

The relative change of the average radiation pattern for an antenna located on the Chest can reach 24%, relative to the isolated antenna. For both distance distributions and all body regions, $\overline{\Delta_G}$ is higher than $\overline{\Delta_{G_w}}$. In the case of the Uniform Distribution, when the antenna is located with the maximum distance equal to $h = 2\lambda$ (i.e., around 24.5 cm), $\overline{\Delta_{G_w}}$ and $\overline{\Delta_G}$ are lower compared to the Rayleigh Distribution. This is because the influence of the body is weaker when the antenna is moved away from the body.

The main outcome of this study are the average patterns and corresponding standard deviations. The study is performed only for a patch antenna (i.e., which is used throughout this thesis), but it can be easily extended to others. These results show that the patch is well isolated from the body (i.e., similar gain for different placements and low standard deviation), which will ensure the stability of the system.

Other results, of the statistical gain patterns obtained from this study, are gathered in Annex C.

5.1.3. Experiment

The absolute gain of the antenna, G, can be measured through gain transfer techniques, using standard gain antennas (*e.g.*, horn antenna) [Bala05]:

$$G_{[\text{dBi}]} = G_{h[\text{dBi}]} + 10log(\frac{P_x}{P_h}) \tag{5.1}$$

where:

- G_h is the absolute gain of the horn antenna,
- P_x and P_h are the received powers of the test and horn antennas, respectively.

Measurements were carried out in an anechoic chamber located at IST premises. The transmitted power was set to 0 dBm, and the frequency to 2.45 GHz.

A calibrated horn antenna, with G_h=11.25 dBi and half power beam-width α_{3dB}=48° located at about 4 m away, was used as receiver. The patch, isolated or on the body, was the transmitter. The system enables to sequentially retrieve the received power, the phase and the rotation angle, generating the gain pattern. The total azimuth gain pattern is obtained from measurement of the co- and x-polarised patterns, achieved by positioning the horn antenna in the planes $\theta = 0°$ and $\theta = 90°$.

The measurement setup is indicated in Figure 5.10. Volunteers were placed on a rotating positioner, keeping a constant velocity of 2°/s in clockwise rotation.
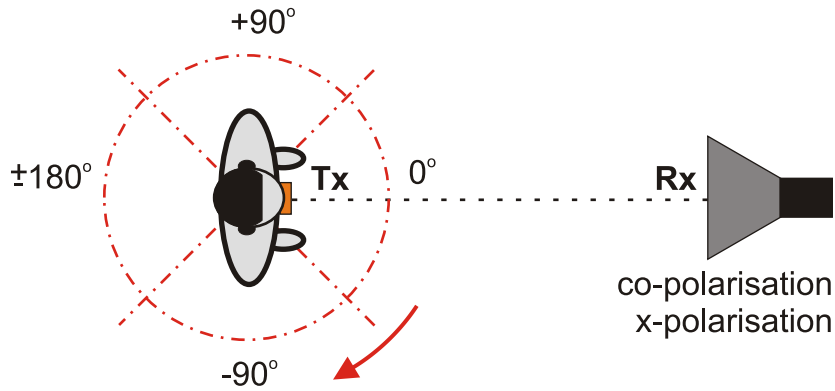
Figure 5.10. Measurement setup.

Two sets of measurements were conducted: one for the isolated patch, and another for the patch on the body. In the latter, the patch was placed at $\{0, 2, 4\}$ cm (*i.e.*, $\{0, 1/6\lambda, 1/3\lambda\}$), from the Chest of the testers, Figure 5.11.

When measuring the isolated patch antenna, the following parameters have been obtained: G_a=6.42 dBi; f_r=2.43 GHz; S_{11}=−14.95 dB. These values agree with the ones from literature, [MCCF07].

Figure 5.11. Measurement environment.

The average gain patterns for the antenna located near the Chest for distances $\{0, 2, 4\}$ cm from the body, as well as the measured gain pattern for the isolated antenna, are presented on Figure 5.12.
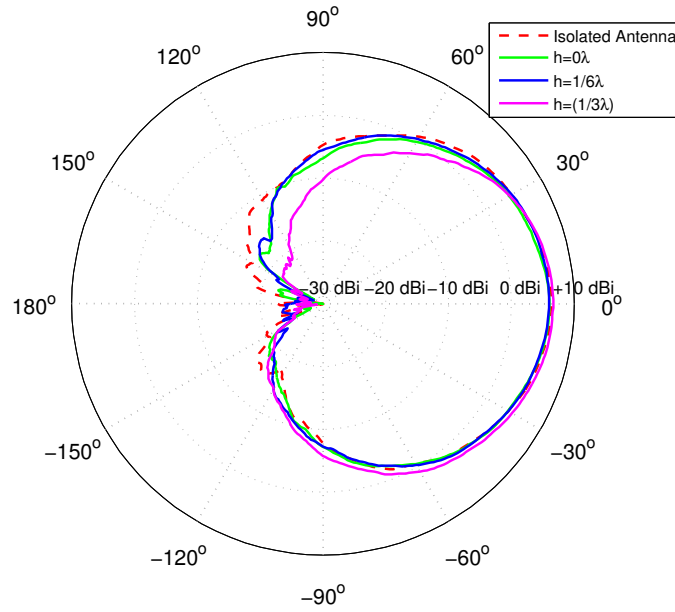
Figure 5.12. Average radiation patterns for various distances.

A general comment to the measured gain patterns is that the backward lobe is suppressed by the support structure of the positioner. Similarly to simulations, when the antenna is on the body, the highest variations to the gain pattern are observed in the direction of the body and on the side lobes. For the antenna at the highest distance to the Chest (*i.e.*, $h = 4$ cm), the gain in the forward direction is the highest. For the other distances, the gain in the body case is less than the isolated one.

The statistics of the gain pattern (*i.e.*, G_{μ}, G_{min} and G_{max}) of the antenna located near the Chest relative to the isolated one are shown in Figure 5.13. Changes in the gain pattern are higher near the Chest, reaching almost 15 dB, which is in line with CST results. Again, the

plot is not symmetric, due to the natural asymmetry of the body. The average gain pattern is similar to the one of the isolated antenna in the range $[-30°, 30°]$. In the range $[-170°, -30°]$, the average gain pattern of the patch on the body is always below the isolated antenna one, with a great decay on gain values for angles below $-110°$. Only in backwards, it is above the isolated patch gain pattern, with a maximum of 3 dB at $-170°$, these results being influenced by the support structure. An opposite effect is found in the symmetric range $[30°, 180°]$.
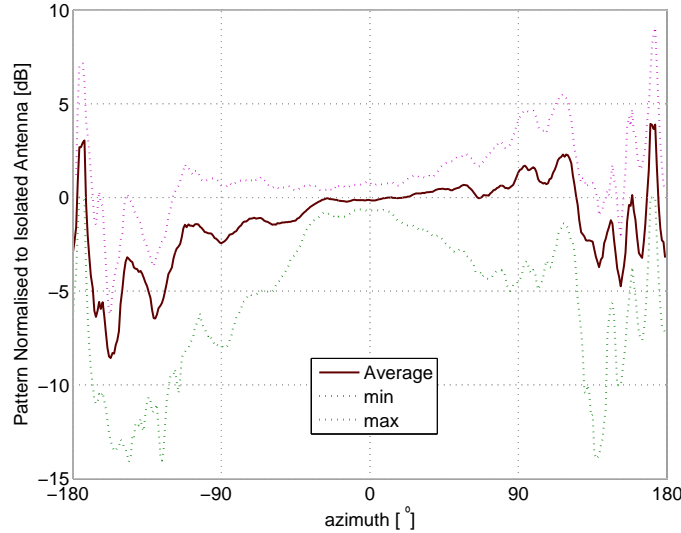
Figure 5.13. Statistics of the measured gain pattern of the antenna located near the Chest, relative to the isolated one.

Table 5.5 summarises the statistics of the measured gain pattern, averaged over the 3 sample distances. Because of the few number of points, the interval of variations is indicated, instead of giving the standard deviation.

Table 5.5. G_μ for selected measured φ and for $\theta = 90°$.

	φ	Isolated	Body	
			Average	Range
	0°	6.4	6.3	[5.7, 7.3]
G_μ[dBi]	90°	-4.7	-7.1	[-12.7, -4.0]
	180°	-22.8	-26.0	[-30.0, -22.4]

When the patch is in front of the Chest, the gain in the forward direction (*i.e.*, $\varphi = 0°$) is 0.1 dB less than for the isolated case, with a range of changes of less than 1 dB. But, for the side lobes, *e.g.*, for $\varphi = 90°$, differences less than 2.4 dB are found, with a higher possible range of changes. It is worthwhile to notice that the measured bodies are different from the voxel model used in the case of simulations.

Generally, these results are in line with the simulation ones, although in backwards there is an obvious influence of the measurement system. Figure 5.14 confirms this, by presenting the average gain patterns obtained through CST and measurements, for the isolated antenna and for the antenna on the body. In the azimuth range $[-90°, 90°]$, the area of interest for

off-body communications, no large changes are observed between CST and measurements: for the isolated antenna, an average difference of 0.6 dB is found; for the antenna on the body, an average difference of 0.9 dB is found.
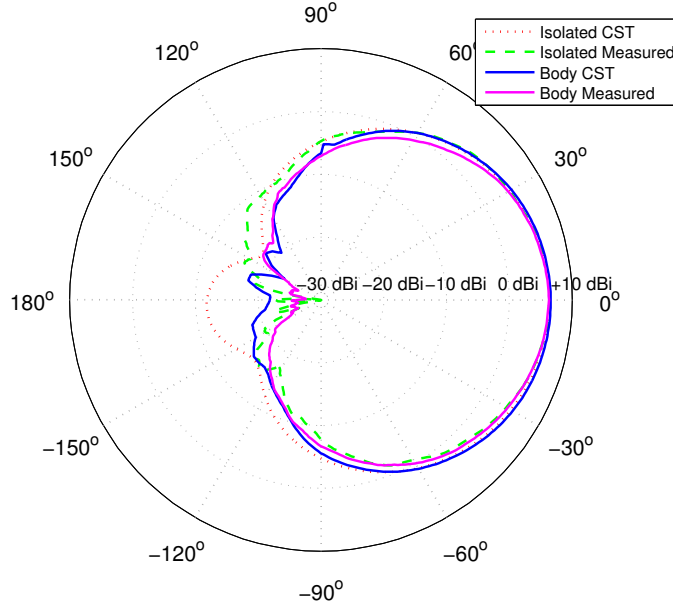
Figure 5.14. Comparison between CST and measurements.

Although measurements deal with the whole BAN channel, they are too resource- and time-consuming, compared to CST simulations. Moreover, when using CST it is possible to obtain full gain patterns of antenna (*i.e.*, in both azimuth and elevation planes). The good agreement between measurements and simulations suggest that CST is a creditable tool to characterise wearable antennas.

5.2. Signal Correlation

To calculate correlation, the following placements of the patch antenna, [MCCF07], are analysed: TO_F, WA_F, HE_F, HE_B, HE_L, HE_R, AB_L, AB_R and TO_B.

Simulations were run for 11 samples of the distance, which were calculated according to the Uniform Distribution in the range $[0, 2\lambda]$ (*i.e.*, $[0, 24.5]$ cm). Also, a plane wave excitation has been swept over the range $[0°, 180°]$ with a resolution of $5°$ (*i.e.*, 36 samples). This gives a total number of 396 full wave simulations, each simulation taking about 15 minutes, using an Intel Xeon X5600 $4 \times$ Quad-Core workstation.

Before performing the calculations of the cross-correlation, in Matlab, all signals were resampled, in order to have the same time resolution (32 ps) and the same number of samples (250), which corresponds to the duration of 8 ns. For all 9 considered placements of antennas, the total number of possible pairs is equal to $\binom{9}{2} = 36$. Therefore, for each pair of antennas, there are

$11 \times 11 \times 36 = 4\,356$ possible configurations of distances and excitations. As there are 36 pairs of antennas, a total number of $156\,816$ correlations were calculated.

Firstly, the average and the standard deviation of cross-correlation has been calculated for all possible combinations of pairs of antennas. In Table 5.6, the statistics of the cross-correlation and the allocation to the class are presented. The proposed classification of the mutual orientation of antennas is in agreement with the obtained values of the average cross-correlation, where for any pair of OD antennas the average cross-correlation is less than for the XD one. Also, for the pairs of XD antennas the average cross-correlation is less than for the CD one. Due to the similar conditions of the links, CD antennas are characterised by high values of cross-correlation, as a result of coupling and interactions between the antenna and the body.

Table 5.6. The matrix with the definition of the classes, and simulated values of the average and standard deviation of cross-correlation.

		average correlation								
		TO_F	WA_F	HE_F	HE_B	HE_L	HE_R	AB_L	AB_R	TO_B
standard deviation	TO_F		0.97	0.95	**0.65**	0.77	0.81	0.78	0.79	**0.66**
	WA_F	0.03		0.95	**0.65**	0.77	0.81	0.79	0.79	**0.65**
	HE_F	0.07	0.06		**0.69**	0.77	0.81	0.78	0.79	**0.69**
	HE_B	**0.09**	**0.10**	**0.06**		0.76	0.78	0.77	0.80	0.94
	HE_L	0.15	0.15	0.15	0.14		**0.70**	0.96	**0.69**	0.77
	HE_R	0.12	0.12	0.12	0.13	**0.08**		**0.69**	0.95	0.77
	AB_L	0.14	0.14	0.14	0.14	0.06	**0.08**		**0.69**	0.77
	AB_R	0.12	0.12	0.12	0.12	**0.10**	0.08	**0.09**		0.77
	TO_B	**0.10**	**0.11**	**0.08**	0.16	0.14	0.13	0.14	0.13	

CD	co-directed	XD	cross-directed	OD	oposit-directed

In Figure 5.15, the results for average cross-correlation and standard deviation are presented. As the antennas are oriented in the same direction, the highest average cross-correlation is obtained for the CD class, being 0.95; in this case, the standard deviation is the lowest, equal to 0.07. This means that the signals received by the CD pair of antennas are very similar, and correlation between them changes slightly with the azimuth of the incoming wave and the distance from the antenna to the body. The lowest average cross-correlation is obtained for the OD class, being 0.67, which has also a low standard deviation, equal to 0.09. In this case, body shadowing results in significant deformation of the received signals. In the case of the XD class, the average cross-correlation is 0.79 and the standard deviation is the largest, being 0.13, because, this class is the transition between CD and OD, which results in a high standard deviation and a moderate average correlation. Therefore, in this case, the arriving signals can be either low or highly correlated.
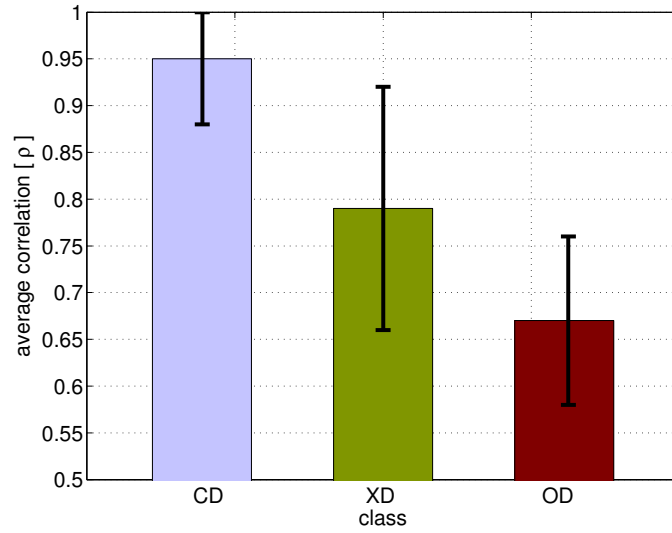
Figure 5.15. Average and standard deviation of cross-correlation for the various classes.

The statistics of cross-correlation for a selected pair of antennas (*i.e.*, TO_F & WA_F, HE_L & TO_B and WA_F & HE_B), which are representative from the classes, depending on the azimuth of the incoming wave, are presented in Figure 5.16.
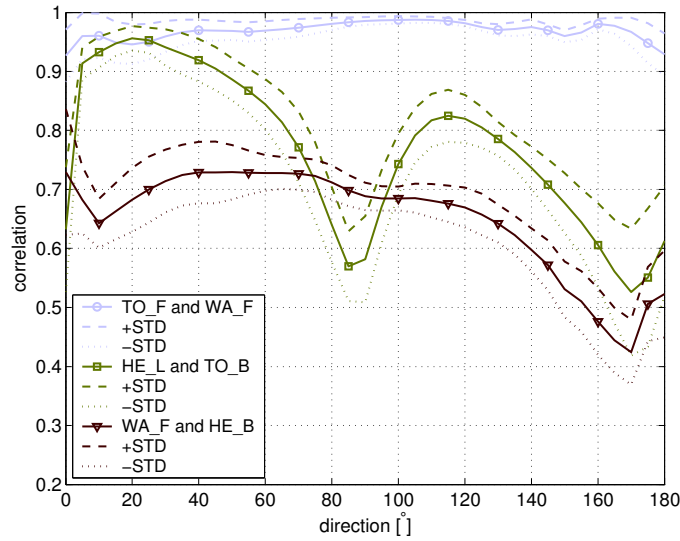
Figure 5.16. Average and standard deviation of cross-correlation for selected pairs of antennas.

The average cross-correlation in the pair TO_F & WA_F is very high, above 0.93, with very small standard deviation, especially in the side direction (*i.e.*, 90°). In general, for the pairs of antennas located on the same side of the body, the average cross-correlation does not depend on the direction of the incoming wave. In case of the HE_L & TO_B pair, cross-correlation depends on the direction, and varies a lot. The lowest values of cross-correlation are obtained in the side and back directions, when one antenna is in LoS conditions and the other is shadowed. For the pair WA_F & HE_B, the lowest average cross-correlation is obtained, for 170°, and there is also a local minimum at 10°. In the case of 170°, the HE_B antenna is in LoS, whereas the WA_F one is shadowed by the torso. The attenuation and distortion caused by the head

is weaker than the one from the torso, which is the reason why the cross-correlation for $10°$ is higher than for $170°$.

The standard deviation for the various classes, for various directions, is presented in Figure 5.17. There are peaks of standard deviation at $\{0°, 90°, 180°\}$, which can be explained by the fact that those are the borders of antenna orientations (*i.e.*, front, side and back). At those directions, the antennas that are more spaced from the body can be already in LoS with the incoming wave, whereas others can be still shadowed by the presence of the body (especially in the case of CD antennas).
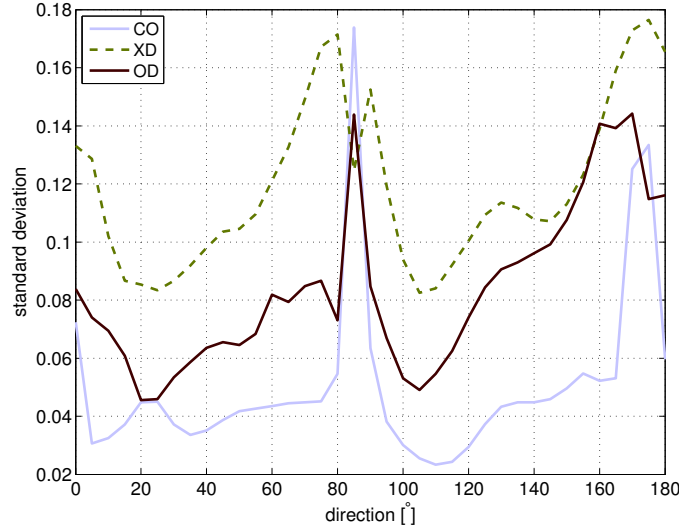
Figure 5.17. Standard deviation of correlation for the several classes, for various directions of the incoming wave.

The statistics of cross-correlation for a given class, depending on the distance between antenna and body surface, are presented in Figure 5.18. As the coupling between the body and the antenna gets weaker with distance, the average cross-correlation increases. There is an exception for the OD class in the distance range $[0, 2]$ cm (*i.e.*, when the antenna is attached to the skin or it is very close to it). For all classes, the standard deviation is decreasing up to 5 cm, and then it becomes constant, which means that the coupling of the body can be neglected.

To conclude, the difference between signals captured by antennas located on various placements on the body is evaluated by the cross-correlation coefficient. This has been done for different directions of the incoming waves, and various antenna and body separations. The results of the study are in line with the mutual orientation of the antennas, and the pairs of antennas can be split into 3 classes: CD, XD and OD. As expected, the correlation is the lowest for the OD class, and the highest for the CD one.
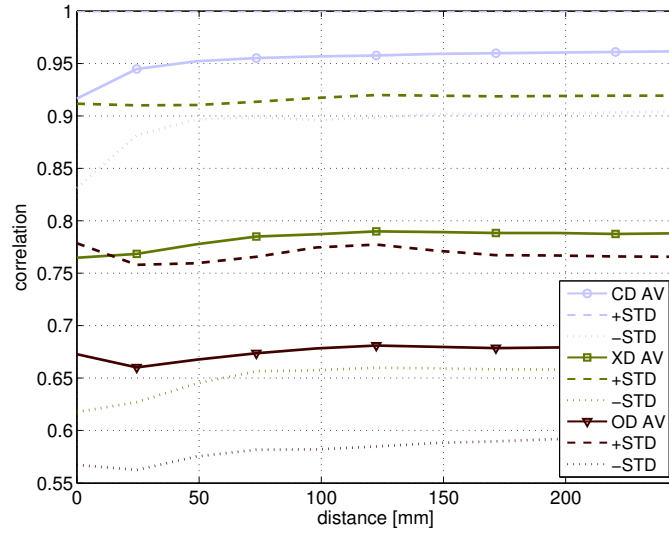
Figure 5.18. The average and standard deviation of cross-correlation for the various classes, for several distances from the body.

5.3. Body Dynamics

The following locations of antennas on the dynamic body are being analysed: Head, Chest, Arm and Leg. Two scenarios are analysed: the walking or running bodies, which are the most typical human day-to-day activities, and examples of the fast and slow movement scenarios, respectively. The statistics of changes in the direction of maximum radiation are calculated over a single period only.

When the antenna is located on the Arm, shifts of the normal to the body surface for the running or walking bodies are presented in Figure 5.19. When the antenna is located on the Arm, it is expected that the change of the antenna orientation in both azimuth and elevation planes is significant. In the azimuth plane and the running body, the direction of maximum radiation is changing 100°. When walking, the change of the antenna orientation is much smaller than in the case of running.

In order to evaluate the influence of body movement on the change of the normal to the surface, a statistical analysis was performed. The average and range of change in the antenna orientation for all analysed antenna placements, for the walking or running bodies, are presented in Figure 5.20.

As expected, the range of changes for the running body is always larger than for the walking one. The largest variation in antenna orientation is obtained for the Arm placement and the running body. Considering the average direction of maximum radiation, for both movement scenarios and respective antenna placements, results are similar and depend directly on the side of the body (*i.e.*, front or left). The exception is the elevation plane for the antenna located on the Chest, which is tilted down by 10° for the running scenario compared to the walking one. In this case, the body is always bent to the front.
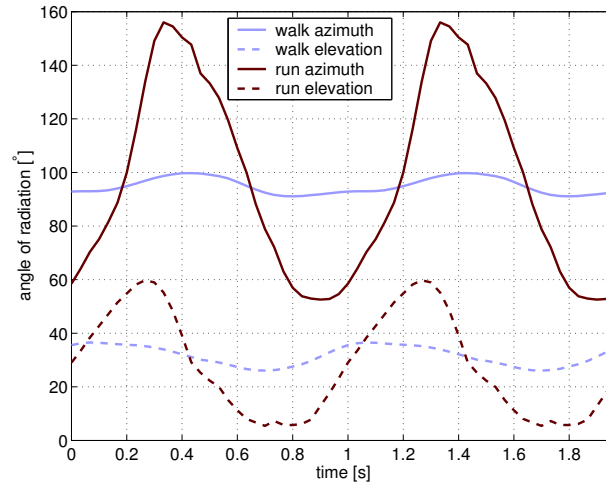
Figure 5.19. The normal to the body surface of a wearable antenna placed on the Arm, for the walking or running bodies.

(a) azimuth plane $(\overline{\delta\varphi})$

(b) elevation plane $(\overline{\delta\psi})$
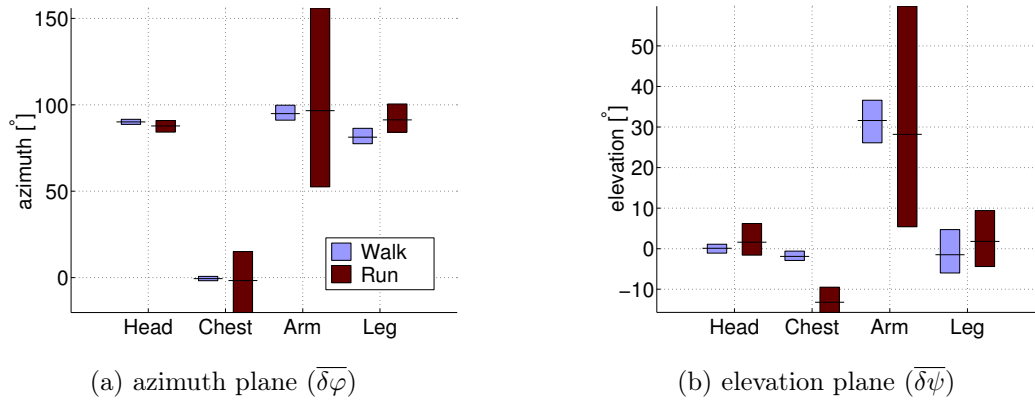
Figure 5.20. Average and range of change in the normal to the body surface of a wearable antenna for the walking or running bodies.

The standard deviation of the change in the normal direction to the body surface is presented in Figure 5.21. The placement of the antenna on the Arm when running results in the highest standard deviation, which is $37°$ and $19°$ for azimuth and elevation angles, respectively. For all antenna placements and walking, the standard deviation is below $4°$, which is very small compared with the typical 3 dB beam width of antennas used in BANs. Also for the walking body, the standard deviation for the Arm placement and azimuth plane is 11 times lower than for the running one. Therefore, it is expected that the walking body will have not significant impact on the gain pattern changes of wearable antennas. The Chest antenna location and running body results in a significant standard deviation in the azimuth plane of almost $13°$, and some changes in the gain pattern are expected. For both movement scenarios, the most stable placement for the antenna is the Head, where the standard deviation in both planes is below $2°$.

The antenna orientation data obtained from motion capture analysis have been interpolated (by an interpolation factor of 5), which is a good approximation, as the body moves in a smooth way. By analysing all histograms, it has been found that they are J-shaped in most cases, however, in some cases they are concentrated around the mean value. The Beta and Kumaraswamy

(a) azimuth plane ($\sigma_{\delta\varphi}$) (b) elevation plane ($\sigma_{\delta\psi}$)
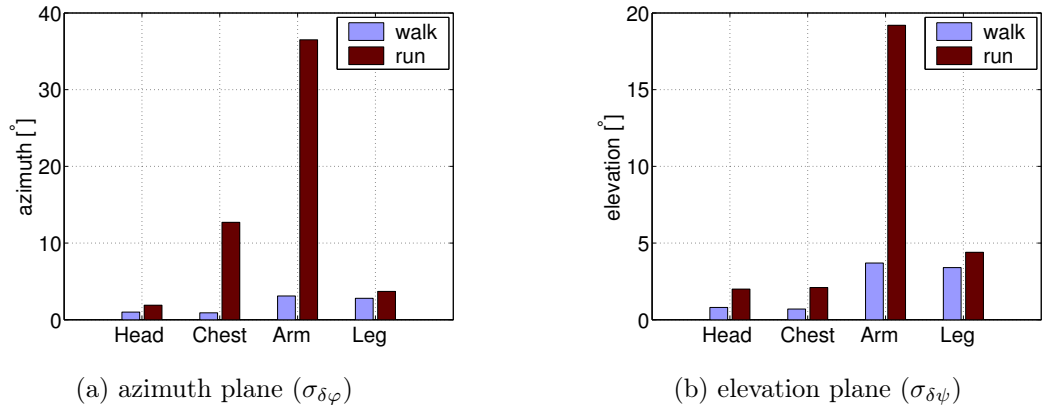
Figure 5.21. Standard deviation of change in normal to the body surface for walking and running bodies.

distributions have been used to fit the data. The example of the distribution of the normal to the body surface, for the running body and Arm placement is presented in Figure 5.22.

(a) Arm location (b) Head location
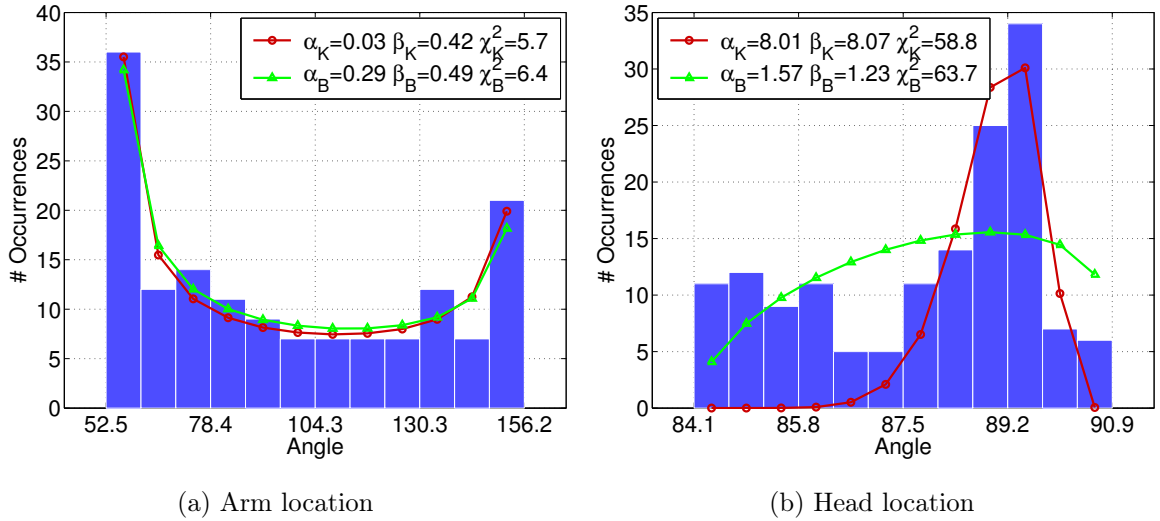
Figure 5.22. Histograms and distribution fitting of the normal direction to the body surface for the running body in the azimuth plane.

Goodness of fit has been analysed by the chi-square (χ_B^2 and χ_K^2) test, [GrNi96], and evaluation of the correlation between the simulation data and their estimates (ρ_B and ρ_K), Table 5.7.

On average, the Kumaraswamy Distribution fits better than the Beta one (lower χ^2 error and higher correlation). In the majority of the cases, both functions give the χ^2 value lower than the threshold $\chi_{95\%}^2 = 18.31$ for a 95% confidence interval, which means that the fitting is successful. In this case, the shape parameters have values as follows, $\alpha_k \in [0.01, 0.53]$ and $\beta_k \in [0.24, 0.81]$. For the other cases, the deviation in mean (i.e., $\Delta_K \overline{\delta\psi}$ and $\Delta_K \overline{\delta\varphi}$) and standard deviation (i.e., $\Delta_K \sigma_{\delta\psi}$ and $\Delta_K \sigma_{\delta\varphi}$) is not more than 1.2° and 1.8°, respectively, Table 5.8. These values are small compared with the typical 3 dB beam width of antennas used in BANs, thus, being acceptable. In general, the fitting with the Kumaraswamy Distribution is considered successful and sufficient.

Table 5.7. Measures of goodness of fit for Beta and Kumaraswamy distributions ($\chi^2_{95\%}=18.31$) and estimated shape parameters for Kumaraswamy distribution.

			χ^2_B	χ^2_K	ρ_B	ρ_K	α_K	β_K
Run	Hand	φ	6.4	5.7	0.96	0.96	0.03	0.42
		θ	6.7	6.9	0.96	0.96	0.01	0.45
	Chest	φ	4.5	4.8	0.97	0.97	0.07	0.24
		θ	87.8	89.3	0.64	0.64	0.54	0.86
	Head	φ	63.7	58.8	0.31	0.88	8.01	8.07
		θ	31.4	32.7	0.79	0.78	1.67	3.43
	Leg	φ	124.5	39.9	0.62	0.93	4.47	34.67
		θ	56.1	56.6	0.37	0.37	0.67	0.81
Walk	Hand	φ	16.0	16.8	0.78	0.77	0.27	0.49
		θ	2.4	2.4	0.98	0.98	0.17	0.30
	Chest	φ	2.1	2.1	0.99	0.99	0.01	0.37
		θ	13.3	13.3	0.81	0.81	0.53	0.81
	Head	φ	0.5	0.4	1.00	1.00	0.16	0.36
		θ	0.7	0.9	1.00	0.99	0.14	0.24
	Leg	φ	22.1	22.3	0.70	0.70	0.51	0.74
		θ	31.1	31.0	0.70	0.70	0.37	0.77

Table 5.8. Deviation in mean and standard deviation between the data and the Kumaraswamy Distribution (for unsuccessful fitting cases).

			$\Delta_K\overline{\delta\psi}, \Delta_K\overline{\delta\varphi}$ [°]	$\Delta_K\sigma_{\delta\psi}, \Delta_K\sigma_{\delta\varphi}$ [°]
Run	Chest	θ	0.1	0.1
	Head	φ	-1.2	1.2
		θ	0.3	0.3
	Leg	φ	0.9	1.8
		θ	-0.2	-0.0
Walk	Leg	φ	0.1	-0.2
		θ	0.7	-0.1

As a study case, a patch antenna, [MCCF07], operating at the 2.45 GHz band, has been used, placed parallel to the body. The average gain pattern of the antenna located on various positions on a static body, which is required to calculate statistical gain patterns for the dynamic case, is taken from the Section 5.1.2. Figure 5.23 presents the antenna gain, G_s, when located on the static body.

Based on the statistical description of the direction of maximum radiation of the antenna, and the gain pattern when it is located on the Arm on the static body (*i.e.*, taken from the numerical simulations in CST, the statistics of the gain pattern (*i.e.*, average G_μ, standard deviation bars, the minimum G_{min}, and maximum G_{max}) are presented in Figure 5.24.

Due to the huge variation of the antenna orientation for the running body and Arm placement, the standard deviation of the gain pattern is also very high in all directions. As expected,
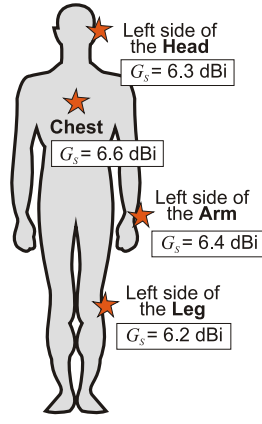
Figure 5.23. Placements and gains of the antenna on the static body.
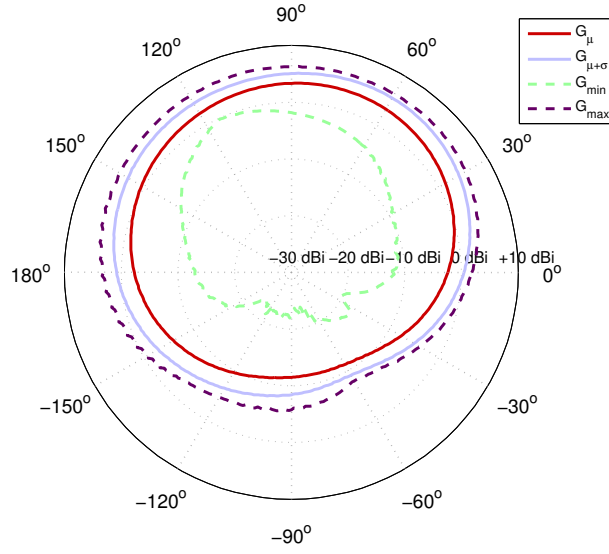
Figure 5.24. Statistics of the gain pattern of the patch antenna placed on the Arm for the running body.

on average, the gain is the highest in the direction corresponding to the average shift in the normal direction to the body surface for the particular antenna placement. Table 5.9 presents the statistics in the direction of maximum radiation (*i.e.*, $\overline{\delta\psi}$ and $\overline{\delta\varphi}$).

Table 5.9. G_μ and σ_G for the direction of maximum radiation $(\overline{\delta\theta}, \overline{\delta\varphi})$.

		Head	Chest	Arm	Leg
G_μ[dBi]	Static	6.3	6.6	6.4	6.2
	Walk	6.3	6.6	6.3	6.1
	Run	6.3	6.3	4.0	6.1
σ_G[dB]	Walk	-18.2	-21.3	-14.7	-15.8
	Run	-16.4	-7.7	-0.4	-13.3
σ_{Gnorm}[dB]	Walk	-24.5	-27.9	-21.0	-21.9
	Run	-22.7	-14.0	-4.4	-19.4

For the walking body, the gain in the direction of maximum radiation is similar to the static one, ranging in $[6.1, 6.6]$ dBi. In general, the standard deviation in this direction is below -15 dB,

which is more than 20 dB below the average gain. As expected, the walking body has little impact on the gain pattern of wearable antenna. For the running body, the maximum gain for the Arm placement is 4 dBi, which is more than 2 dB below other cases. The standard deviation for the Arm placement is very high, being 16 dB higher than in the case of Head, which is the most stable location for the antenna. In this case, changes introduced by running body on the gain pattern are significant and have to considered in the whole Radio Channel.

Table 5.10 presents the statistics for selected directions of radiation, *i.e.*, $\psi=0°$ and $\varphi=\{0°, 90°, 180°\}$. On average, in the body forward direction (*i.e.*, $\psi=0°$ and $\varphi=0°$), the highest gain is obtained when the antenna is placed on the Chest. In the side direction (*i.e.*, $\psi=0°$ and $\varphi=90°$) the highest gain is for Head and Leg. For the Arm placement, the average radiation is the highest in the backward direction (*i.e.*, $\psi=0°$ and $\varphi=180°$).

Table 5.10. G_μ and σ_G for selected φ and for $\psi = 0°$.

		φ	Head	Chest	Arm	Leg
G_μ[dBi]	Walk	0°	-6.3	6.5	-5.2	-4.2
		90°	6.3	-6.7	4.4	6.0
		180°	-5.5	-20.6	-4.6	-7.3
	Run	0°	-5.5	6.0	-2.4	-6.3
		90°	6.3	-6.3	3.3	6.1
		180°	-6.1	-20.9	-2.3	-5.3
σ_G[dB]	Walk	0°	-18.5	-16.6	-13.7	-11.1
		90°	-18.6	-14.0	-5.0	-9.8
		180°	-17.8	-28.9	-13.7	-16.6
	Run	0°	-14.1	-5.8	-2.8	-12.9
		90°	-15.5	-7.9	0.2	-10.6
		180°	-15.9	-25.5	-2.1	-13.0
σ_{Gnorm}[dB]	Walk	0°	-12.2	-23.1	-8.5	-6.9
		90°	-24.9	-7.3	-9.4	-15.8
		180°	-12.3	-8.3	-9.1	-9.3
	Run	0°	-8.6	-11.8	-0.4	-6.6
		90°	-21.8	-1.6	-3.1	-16.7
		180°	-9.8	-4.6	0.2	-7.7

When the antenna is placed on the Head, the movement scenario almost does not change the gain pattern. This placement of the antenna results in the lowest standard deviation in the front and side directions. The standard deviation for both movement scenarios for the Head and Leg is very low, below -14 dB and -10 dB, respectively. Therefore, it will have no impact on the performance of the off-body link.

The average gain patterns for the running body and all antenna placements, for $\theta=0$ plane, are presented in Figure 5.25. When the antenna is located on the Chest, the highest gain is in the front, while when it is located on the left side of the Head, Arm and Leg, the highest radiation is in the left side direction, as expected. On average, when the antenna is located on the Head

or Leg, the gain is higher than on the Arm only for $\varphi=[45°, 150°]$. This means that the huge variation of the antenna orientation, in the case of the Arm, results in a more uniform radiation pattern.
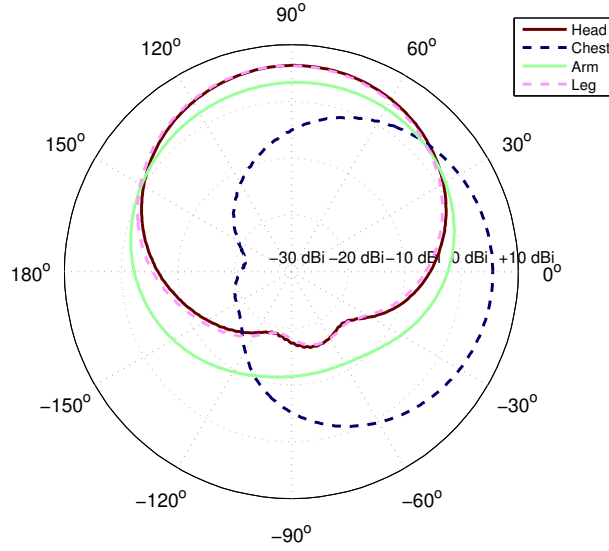
Figure 5.25. Comparison of average gain patterns for the running body.

The average and standard deviation of the radiation pattern, in both planes (in the antenna coordinates, where $\varphi=0$ and $\psi=0$ correspond to the direction of maximum radiation), for the running body and Arm placement are compared with the static one in Figure 5.26. When the body is moving, the average radiation pattern is blurred (*i.e.*, gets more uniform). It is worthwhile to notice that the standard deviation is the highest on the extremes of the radiation angles, and not in the direction of maximum radiation. The reason is that the antenna is oriented in this direction for a short time (*i.e.*, the radiation is maximum), and then moves away from it (*i.e.*, the radiation is low).

(a) static body

(b) average pattern for the running body

(c) standard deviation for the running body
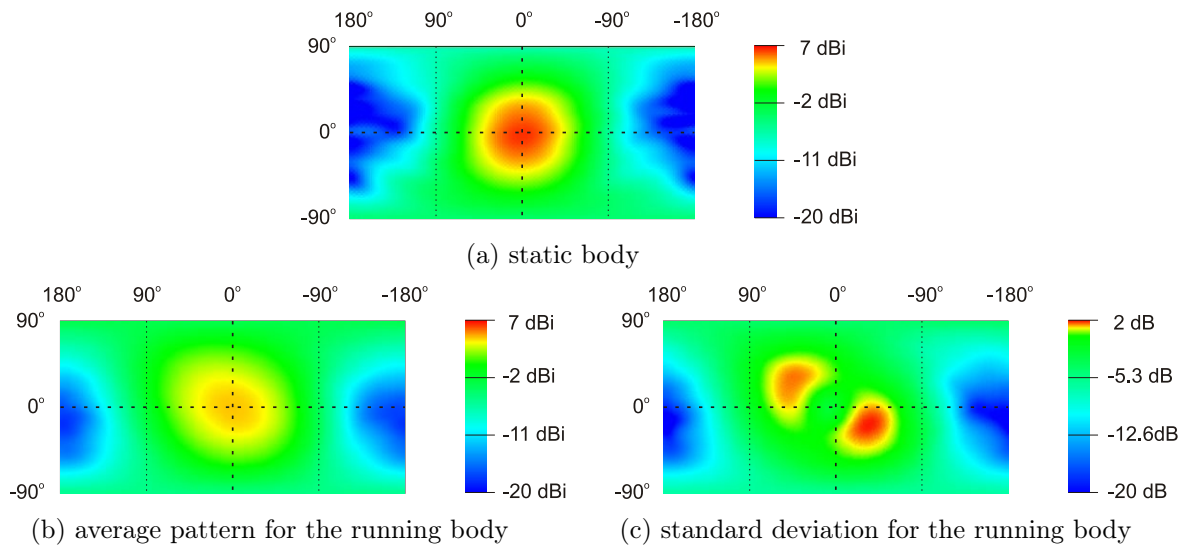
Figure 5.26. Antenna located on the Arm.

A similar scenario of moving body has been considered by importing a homogeneous surface body model from POSER into CST. Simulations have been performed for the time snap-shots of body posture for 15 walking frames (*i.e.*, taking each 2 frames). The comparison of the average gain patterns obtained from the body movement model and full wave simulations is presented in Figure 5.27.

(a) body movement model   (b) full wave simulations in CST
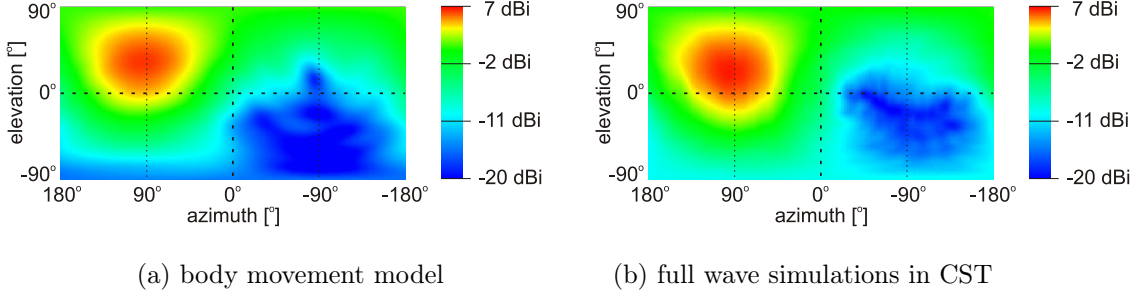
Figure 5.27. Average radiation pattern for the Arm placement and the walking body.

In general, the model reproduces very accurately the trace of the direction of maximum radiation of the antenna. The difference in the shape of the radiation pattern comes from the body model used (*i.e.*, heterogeneous voxel model and surface model), additional body shadowing (*i.e.*, which cannot be fully reproduced using the body movement model), and meshing errors from CST (*i.e.*, due to misalignment of the antenna structure with the mesh, which varies when the antenna is rotated). The PWD calculated between the patterns is 20%, whereas the average gains obtained from the body movement model and simulations in CST, are 6.3 and 6.7 dBi, respectively. It is worthwhile to notice that, for the patch antenna modelled in CST near to the voxel and the surface models, PWD can reach 10%, [OlMC12b]. Finally, one confirms that body dynamics can have a significant impact on the performance of the whole off-body link, especially for a running body and the location of the antenna on an Arm.

Other results, of the gain patterns for moving body, are gathered in Annex D.

Chapter 6

Channel Model

In this chapter, the developed channel model for BANs and scenarios being analysed are presented. The implementation of the simulator is presented as well, together with the assessment. Moreover, the placement of antennas, the propagation scenario, and system parameters are defined.

6.1. Concept and Parameters

In order to model the radio link between on-body antennas and external terminal, one has to consider the influence of the body (*i.e.*, body coupling and body movements) and account for propagation environment (*i.e.*, multipath propagation). Therefore, the modelling of the off-body Radio Channel has been separated into several steps, as presented in, Figure 6.1.
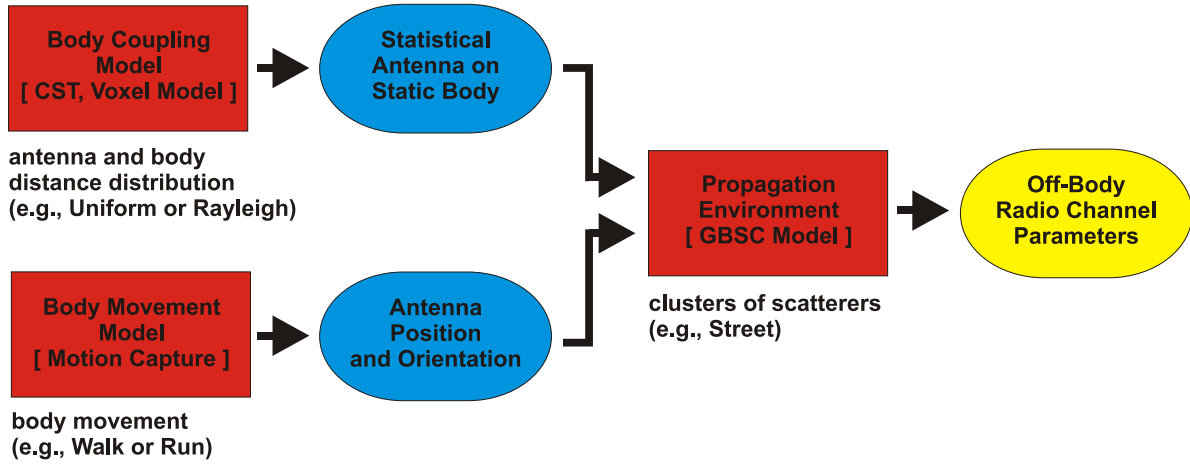
Figure 6.1. Modelling concept of off-body Radio Channel.

In a first stage, for the static body, the gain pattern of the antenna is calculated using the numerical model, as presented in Section 4.3. The result is the statistical antenna gain pattern on the static body, taking into account the body coupling effect. In this way, various types of antennas, and a wide range of bodies can be modelled. Also, the modelling can be performed for various antenna on-body placements.

In a second stage, the antenna position and orientation on the moving body are calculated, taking realistic description from Motion Capture, as presented in Section 4.5. Although the presented statistical gain patterns are antenna dependent, the changes in the antenna orientation are independent from the antenna design, and the method is generally usable. By using this model, any body movement scenario can be considered in a frame-by-frame manner.

Finally, the propagation environment is modelled using the GBSC model and the parameters of the Radio Channel are determined. In the GBSC model, the multipath characteristic of the Radio Channel is the result of signal bounce over numerous scatterers. The MPCs are calculated according to the positions and orientation of the on-body antenna (taking into account the shift of the radiation pattern), position of external antenna, and the distribution of scatterers. As the wearable antennas can be located at different heights, the GBSC model includes a 3D description of the environment, and shifts of the antenna orientation in the azimuth and elevation planes. The output parameters are calculated, as presented in Section 2.3.

Therefore, a flexible and novel method to model Radio Channels in off-body communications is proposed. Using this approach, both the temporal (*i.e.*, delay spread) and angular (*i.e.*, angular

spread) parameters can be characterised. Developed models and algorithms are not system dependent, so that they can be used for other systems, and not just for the one chosen for example.

In order to have a statistical viewpoint on the propagation conditions in the particular type of the environment, a number of simulations, N_s, are performed (*i.e.*, each time for randomly generated scatterers). For each randomised environment, the body is always moving along the same path with the desired behaviour (*i.e.*, walking or running). Therefore, for a given time frame t_n (which always occurs for the same body posture and position in the cell), the variations in output parameters comes from the differences in the propagation environment. In what follows, all statistics are defined for the delay spread, however, for the other output parameters the definition is similar. The average $\overline{\sigma_\tau(t_n)}$ and the standard deviation $\sigma_{\sigma_\tau}(t_n)$ are calculated by:

$$\overline{\sigma_\tau(t_n)} = \frac{1}{N_s} \sum_{s=1}^{N_s} \sigma_\tau(t_n, s) \tag{6.1}$$

$$\sigma_{\sigma_\tau}(t_n) = \sqrt{\frac{1}{N_s} \sum_{s=1}^{N_s} \left[\sigma_\tau(t_n, s) - \overline{\sigma_\tau(t_f)} \right]^2} \tag{6.2}$$

Moreover, the statistics can be averaged in a required range of time frames:

$$\Delta t = t_M - t_m \tag{6.3}$$

where t_m and t_M are the first and the last time frames, respectively. The average $\overline{\sigma_\tau}$, the standard deviation of the average $\sigma_{\overline{\sigma_\tau}}$ and the average standard deviation $\overline{\sigma_{\sigma_\tau}}$ are calculated by:

$$\overline{\sigma_\tau}^{\Delta t} = \frac{1}{\Delta t} \sum_{n=t_m}^{t_M} \overline{\sigma_\tau(t_n)} \tag{6.4}$$

$$\sigma_{\overline{\sigma_\tau}}^{\Delta t} = \sqrt{\frac{1}{\Delta t} \sum_{n=t_m}^{t_M} \left[\overline{\sigma_\tau(t_n)} - \overline{\sigma_\tau}^{\Delta t} \right]^2} \tag{6.5}$$

$$\overline{\sigma_{\sigma_\tau}}^{\Delta t} = \sqrt{\frac{1}{\Delta t} \sum_{n=t_m}^{t_M} \left[\sigma_{\sigma_\tau}(t_n) \right]^2} \tag{6.6}$$

It is important to note that when the body is uniformly moving along the axis, the interval of time frames $[t_m, t_M]$ corresponds directly to a distance interval $[d_m, d_M]$.

The power imbalance between received signals for the kth and l^{th} on-body antennas, and the external Rx antenna (*i.e.*, $P_R^k(t_n)$ and $P_R^l(t_n)$) is:

$$\Delta P_R{}^{k,l}(t_n)_{[\text{dB}]} = \left| 10 \log \left[\frac{P_R^k(t_n)}{P_R^l(t_n)} \right] \right| \tag{6.7}$$

Envelope correlation is a measure of how much a signal in one branch behaves like another. The correlation between received signal envelopes obtained for the kth and l^{th} on-body antennas is:

$$\rho_{P_R}^{k,l} = \frac{\text{cov}(P_R^k(t), P_R^l(t))}{\sigma_{P_R^k(t)}\sigma_{P_R^l(t)}} \tag{6.8}$$

where:

- $\text{cov}(\cdot)$: covariance function,
- $\sigma_{P_R^k(t)}$ and $\sigma_{P_R^l(t)}$: standard deviations of the received signal envelopes for the kth and l^{th} on-body antennas, respectively.

The correlation between the CIRs obtained for the kth and l^{th} on-body antennas, and the external Rx antenna, (*i.e.*, h_k and h_l) for each time frame is, [Orfa96]:

$$\rho_{CIR}^{k,l}(t_n) = \frac{\text{cov}(h_k(t_n), h_l(t_n))}{\sigma_{h_k(t_n)}\sigma_{h_l(t_n)}} \tag{6.9}$$

where:

- $\sigma_{h_k(t_n)}$ and $\sigma_{h_l(t_n)}$: standard deviations of the CIR for the kth and l^{th} on-body antennas, respectively.

For a given pair of antennas, the percentage of time when the MIMO capacity is the best is:

$$C_{MIMO_{best}}^p = \frac{\sum\limits_{n=1}^{N_T} \text{best}(C_{MIMO}^p(t_n))}{N_T} \cdot 100\% \tag{6.10}$$

where:

- $C_{MIMO}^p(t_n)$: the MIMO capacity, for the pth pair of antennas, for t_n time frame,
- $\text{best}(\cdot)$: equal to 1 when $C_{MIMO}^p(t_n)$ is the highest (*i.e.*, compared to all other antenna pairs for t_n frame), 0 otherwise.

For a given pair of antennas, the percentage of time when the MIMO capacity is the worst is:

$$C_{MIMO_{worst}}^p = \frac{\sum\limits_{n=1}^{N_T} \text{worst}(C_{MIMO}^p(t_n))}{N_T} \cdot 100\% \tag{6.11}$$

where:

- $\text{worst}(\cdot)$: equal to 1 when $C_{MIMO}^p(t_n)$ is the lowest (*i.e.*, compared to all other antenna pairs for t_n frame), 0 otherwise.

In order to deeper analyse the performance of on-body antennas, a parameter that compares obtained values of the MIMO capacity with other ones is required. Therefore, the overall performance of given pair of antennas can be evaluated for each time frame:

$$C_{MIMO_P}^p(t_n) = \frac{C_{MIMO}^p(t_n) - \min_p\left\{C_{MIMO}^p(t_n)\right\}}{\max_p\left\{C_{MIMO}^p(t_n)\right\} - \min_p\left\{C_{MIMO}^p(t_n)\right\}} \qquad (6.12)$$

where:

- $\min_p\left\{C_{MIMO}^p(t_n)\right\}$ and $\max_p\left\{C_{MIMO}^p(t_n)\right\}$: the minimum and maximum MIMO capacity (*i.e.*, obtained among all antenna pairs for t_n frame), respectively.

6.2. Model Implementation

The model is able to simulate physical radio link between multiple on-body antennas and antennas located at external position. The simulation can be performed for several time frames, for the moving body (*i.e.*, taking precise information of the location of antennas and their orientation). All needed parameters describing physical conditions in an environment and the specification of the system can be given by the user. The simulator can be run automatically many times, which allows to average results and calculate statistics for outputs. The program is able to cooperate with other applications and well know specialised programs, like Matlab and LaTeX. In general, to make implementation easy, and to enable further extensions of the functionalities, the structure of the simulator is as flexible as possible. The structure of the simulator can be decomposed into several independent blocks: Config, Environment, Body Motion, Antenna, GBSC Algorithm and MPC, which are governed by a Simulator Manager one, Figure 6.2.
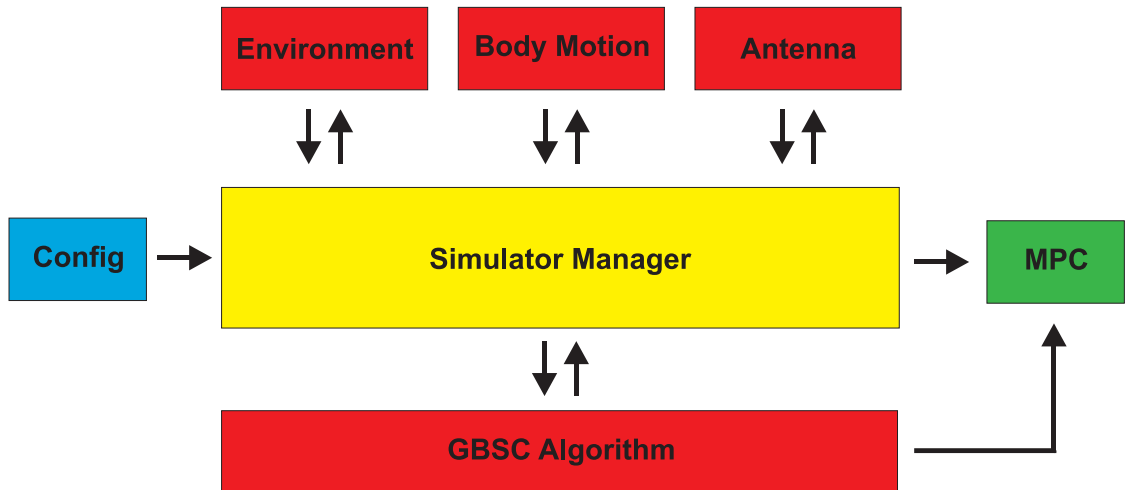
Figure 6.2. Structure of the simulator.

The Config block is associated to input parameters, which are later used by the algorithm one, and also determine the way that the GBSC Algorithm works. The Environment block consists of a set of clusters and scatterers distributed within a specific region, described by their reflection

coefficients. The Body Motion block updates the current positions of the body and calculates position of the on-body antennas and their orientations. The Antenna block is responsible for providing the antennas gain patterns, according to the current antennas orientations. The GBSC Algorithm block contains the heart of the program, where the physical Radio Channel is simulated and the output signals are calculated. This block establishes the relation between input parameters and MPCs. In the MPC block, system parameters are taken into account and all MPCs are exported as CIR. In order to have more control on the data flow in the simulator, the Simulator Manager block is used.

The simulator has been programmed in object oriented C++, which allows to keep each logical module in a different class. Configuration parameters are kept in an eXtensible Markup Language (XML) file, and the simulator itself can be run from command lines including various config files. More information needed to run the simulator can be found in Annex A. The files containing antenna gain patterns, and detailed information about antennas position and orientation (*i.e.*, prepared according to required body movement characteristics) are prepared by other developed programs. The detailed definition of the required file format, can be found in Annex A. The flow of information in the simulator during one simulation is depicted in Figure 6.3.
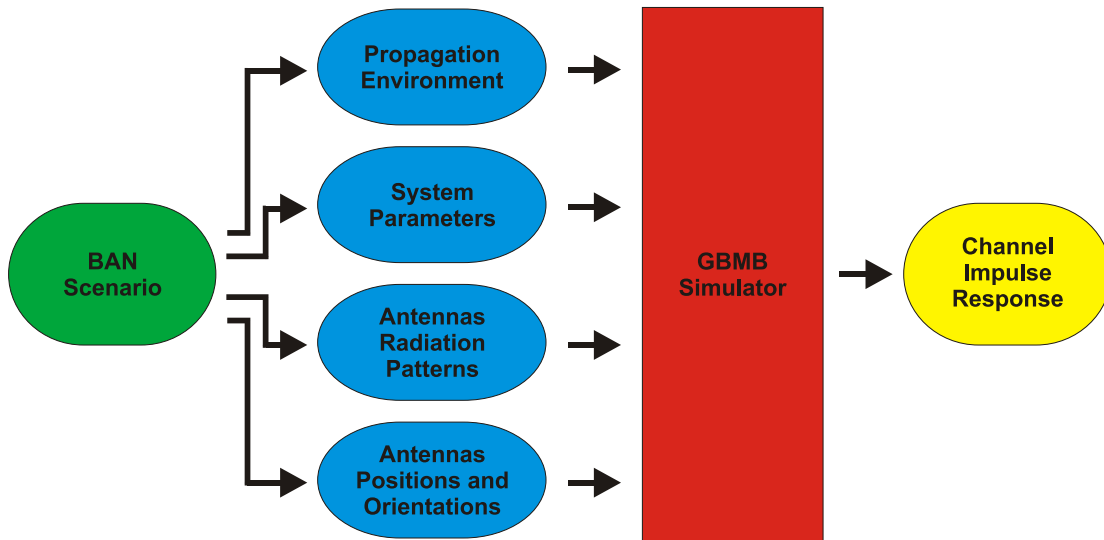
Figure 6.3. Data flow in the simulator.

When the configuration file is read, the environment for simulations is created. For each time frame, the location of the antennas are updated, according to the description of the body movement. Next, existing paths in the environment are calculated. These paths are summed up and the system parameters are taken into account, resulting in CIR between particular pairs of input and output antennas. The same calculations are performed for all combinations of input and output antennas.

6.3. Model Assessment

A wideband Top Loaded Monopole (TLM) antenna is used, [RoEr12], which presents an impedance matching band in [2.33, 11] GHz with respect to a reflection coefficient lower than -7 dB, with a total efficiency on the body of 70% in [2.36, 5] GHz. The presence of a ground plane in the antenna design makes its radiation characteristics less affected by the presence of the body. The TLM gain pattern is presented in Figure 6.4.
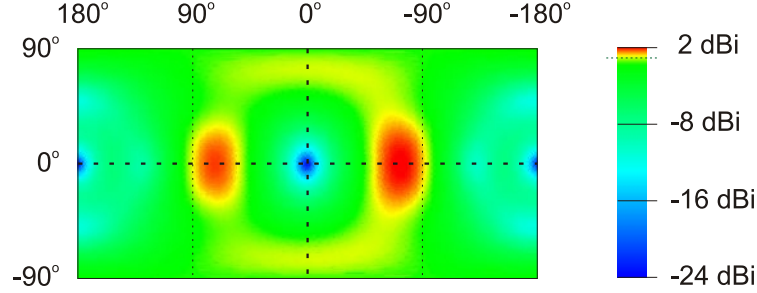
Figure 6.4. TLM gain pattern at 2.45 GHz.

A walking scenario is analysed, the Motion Capture description contains only N_f=30 looped time frames, with a duration of 1/30 s each. A room scenario has been considered, Figure 6.5. A set of 6 clusters, of 3 scatterers each, has a Uniform Distribution in the room. The power transmitted from the wearable antenna is 1 mW, and the isotropic Rx antenna is located on the wall at a 1.2 m height. The body is walking on a straight line, in the middle of the room (*i.e.*, y=2.5 m), in $x \in [1, 4]$ m.
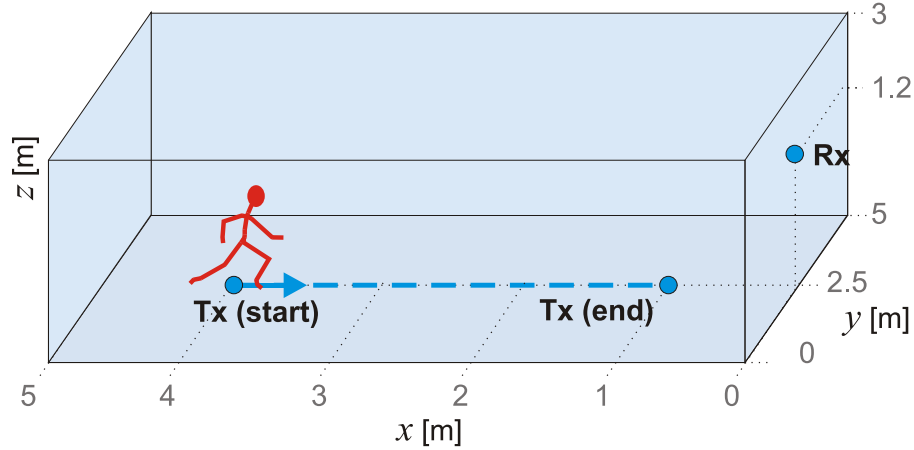
Figure 6.5. Indoor scenario.

When the MPCs contribution is not considered, the indoor scenario reduces to the respective anechoic chamber one.

The measured data used for comparison with simulated results come from a real-time measurement campaign, [RoEr12]. It was specifically realised to characterise off-body dynamic channels at 2.45 GHz. The test-bed was mainly composed of a Vector Network Analyser (VNA), whose

first port was connected to the Tx antenna, placed on a 1.2 m high mast. The second port was connected to the on-body antennas, located on the right ear, of a male subject, acting as the Rx. The antennas are TLM, and several walking cycles were repeated by the human subject, to characterise the dynamic aspects of the off-body transmission channels.

The path loss is calculated as defined in (2.8). The simulations of the path loss for the anechoic chamber scenario, for all considered antenna placements, and measured path loss for the HE_R location, are presented in Figure 6.6.
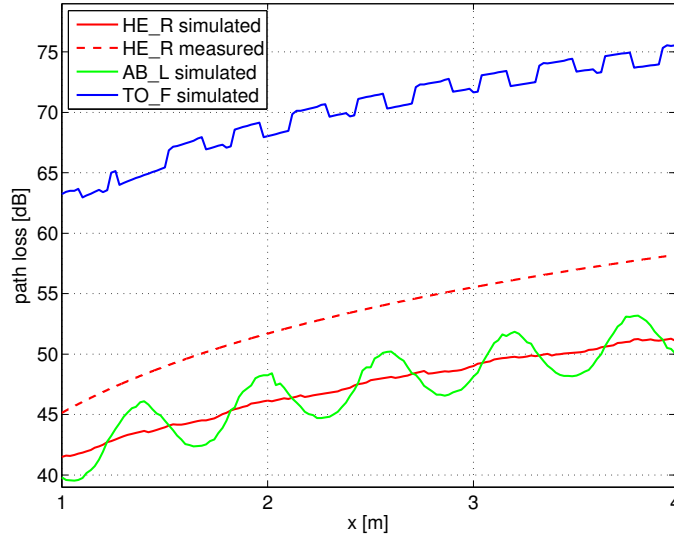
Figure 6.6. Path loss for various antenna placements in an anechoic chamber scenario.

For the HE_R position, the average difference of path loss between measured and simulated data is 7.1 dB, with a standard deviation of 1.5 dB (*i.e.*, taking all the samples into account). This gap can be due to differences between the measured and simulated scenario, to the movement performed by the subject, to the micro-variation of the exact antenna position, and to the simulated body physical characteristic (dielectric properties, shape and dimensions) that were accounted for. Moreover, the polarisation effect is not taken into account during simulations, where it is inherently considered while performing real measurements. However, even considering these factors of variability, the comparison of the path loss of the simulated and measured curves show a good agreement. On average, from simulations results it can be seen that for the TO_F placement the path loss is 25 dB more than for other placements. In this case, the antenna gain is very low (*i.e.*, null radiation up to -25 dBi). In a walking period, the largest variations in the path loss are registered for AB_L (*i.e.*, 10 dB difference).

The simulated results for the path loss for the HE_R placement, for the indoor scenario, are presented in Figure 6.7.

The average difference between measurements and simulations are 4.5 dB, with a standard deviation of 0.1 dB. Both results follow the same trend of the extracted mean path loss for simulation and measurements (*i.e.*, the standard deviation of the difference is very low), and the gap in the values can be due to differences in the simulated environment, node on-body
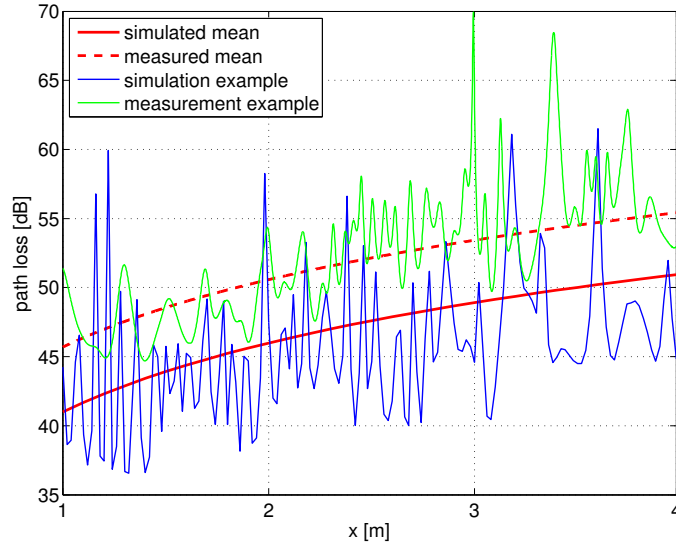
Figure 6.7. Path loss for the HE_R placement, for the indoor scenario.

position, movement performed and body characteristics, with respected to those accounted for during measurements.

6.4. Scenarios

In simulations, the following placements of the patch antenna, [MCCF07], are analysed: TO_F, WA_F, HE_F, HE_B, HE_L, HE_R, AB_L, AB_R and TO_B, Figure 6.8.
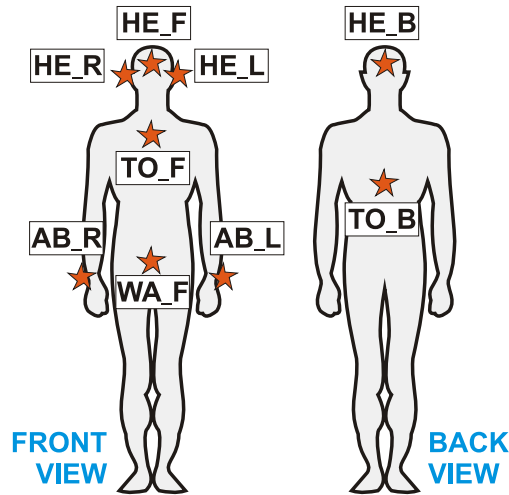
Figure 6.8. Considered antenna placements.

The statistical antenna radiation patterns, accounting for the body coupling are taken from Section 5.1.2. It is worthwhile to notice that the Head gain pattern is considered for HE_F, HE_B, HE_L and HE_R placements; Chest gain pattern is applied for TO_F, TO_B and WA_F placements; Arm gain pattern is used for AB_L and AB_R. The narrowband case has been considered, with the Rx bandwidth equal to 1 MHz, which corresponds to a time resolution equal to 1 μs.

In this thesis, a micro-cell street scenario has been considered, Figure 6.9.
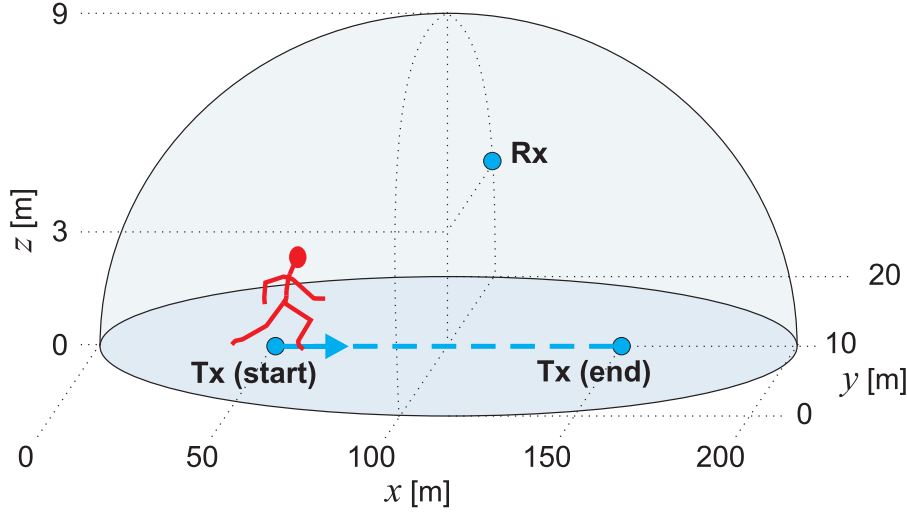
Figure 6.9. Street scenario.

A set of 10 clusters, of 3 scatterers each, has a Uniform Distribution in the half space of an ellipsoid. The power transmitted from the wearable antenna is 0 dBm, and an isotropic Rx antenna is located on the wall of a surrounding building at 3 m height. A noise level of -100 dBm is considered. The body is moving (*i.e.*, walking or running) on a straight line, in the middle of the street (*i.e.*, y=10 m), in $x \in [50, 150]$ m. The running speed was set to 14.4 km/h, and walking to 4.8 km/h, [KmPN96]. This corresponds to N_p=25 or N_p=75 periods of running and walking, respectively. Due to the periodic nature of the body dynamics, the Motion Capture description contains only N_f=30 looped time frames, with a duration of 1/30 s each. In order to obtain statistical parameters, each dynamic scenario has been repeated N_s=30 times (for a random distribution of scatterers).

The total number of obtained CIRs, for a particular antenna placement and dynamic scenario is:

$$N_{CIR} = N_p \cdot N_f \cdot N_s \tag{6.13}$$

Therefore, for each antenna placement, and the running and walking bodies, the total number of performed simulations is 22 500 and 67 500, respectively. To obtain the CIRs for the more demanding body movement (*i.e.*, walking body), 0h30 of simulations was required (and 1h00 more to obtain the parameters and their statistics) using a laptop with a Core i5 Processor and 8Gb of RAM.

Chapter 7

MIMO Capacity in BANs

In this chapter, the results from simulations of the off-body channel are presented. The selection of the best on-body placements of antennas is done, based on the values of MIMO capacity.

7.1. Radio Channel Parameters

7.1.1. Propagation Conditions

Firstly, the propagation conditions are analysed, precisely in the case when the 3 dB beam width of the Tx antenna is directed towards the Rx position, LoS being considered. The percentage of LoS links for the walking or running bodies is gathered in Table 7.1.

Table 7.1. Percentage of LoS propagation for walking or running bodies.

| | LoS propagation [%] | | | |
	HE_F	AB_L	AB_R	TO_B
Walk	39.3	19.2	0.0	40.5
Run	38.3	26.1	0.0	39.5

The percentage of LoS cases depends mostly on the antenna placement, and the results are similar for both movement scenarios, with the exception of the left arm (*i.e.*, AB_L) case. In the case of the running body, the movement of the arm is very large, and the AB_L antenna is in LoS in 7% more time than for walking. The LoS or NLoS conditions for the running body, is presented in Figure 7.1.
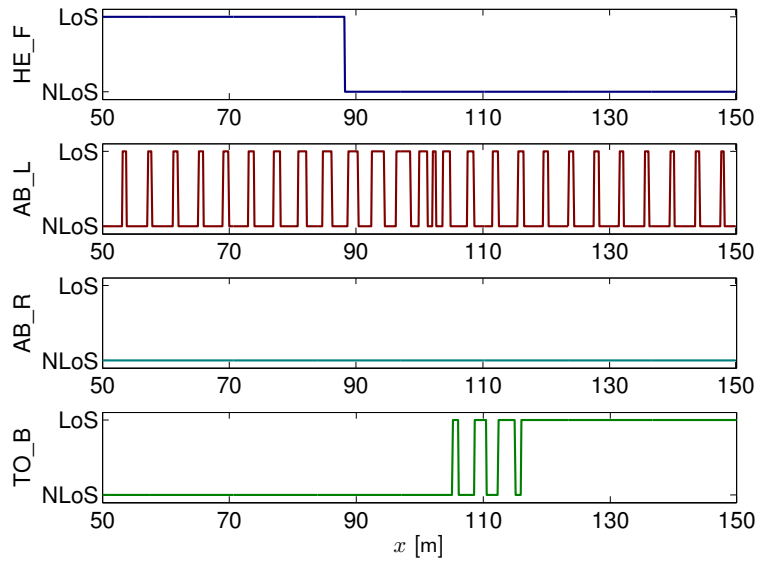
Figure 7.1. Propagation conditions for the running body.

As the Rx is located on the left side of the body, the antenna placed on the right arm (*i.e.*, AB_R) is always in NLoS. The antenna placed on the forehead (*i.e.*, HE_F) is in LoS until 87 m, then its gain towards the Rx antenna is decreasing, and it becomes NLoS. The antenna on the back (*i.e.*, TO_B) is in NLoS when the body is approaching the Rx antenna, until 105 m. As the torso during Run is waving to the left and right, in $x \in [105, 115]$ m the propagation conditions are changing, then after 115 m the TO_B antenna stays in LoS. In the case of AB_L, the propagation conditions are changing from LoS to NLoS and vice-versa, due to the large variation of the direction of maximum radiation of the antenna.

7.1.2. Received Power

The received power is calculated as defined in (2.7). The average received power $\overline{P_R(t_n)}$ for the walking or running bodies, is presented in Figure 7.2. For antennas located on the left and right side (*i.e.*, AB_R and AB_L), the obtained values are symmetric relative to the position of the Rx (*i.e.*, x=100 m). The maximum received power is obtained when the body is close to the Rx in both cases. Also, similar values of the received power are obtained for antennas on the front (*i.e.*, HE_F) and on the back (*i.e.*, TO_B), but for different cell edges. For the HE_F antenna, when the body is approaching the Rx, the received power is slightly increasing due to the decreasing distance between antennas. In general, for the same distance range there is 3 times more walking periods than running ones, which results in more dense oscillations of the received power (the same is observed for other output parameters).

(a) walking body   (b) running body
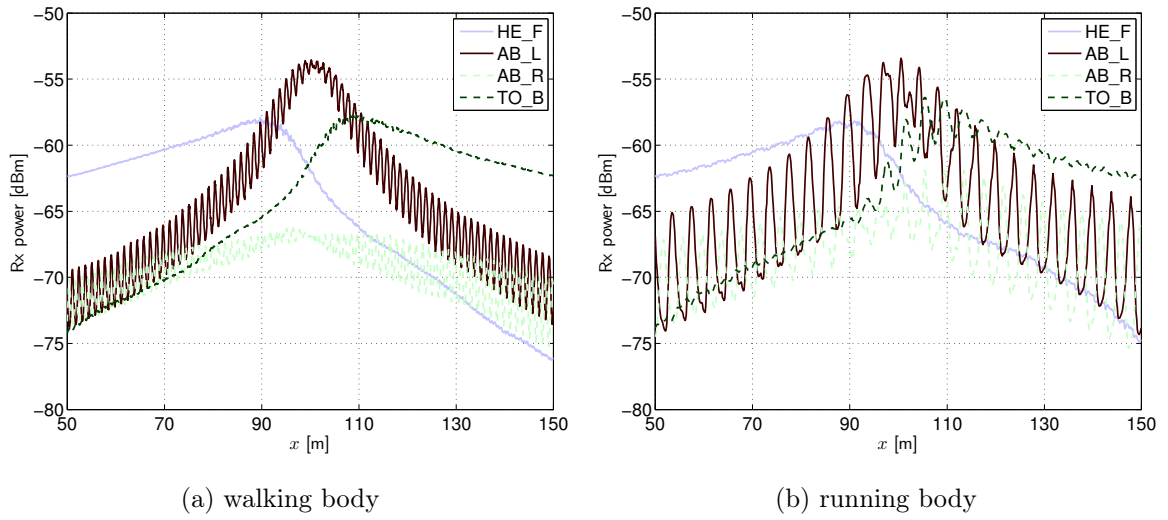
Figure 7.2. Average received power $\overline{P_R(t_n)}$.

The statistics of the received power for the running body, calculated for selected paths, are presented in Table 7.2. The received power depends strongly on the propagation conditions and on the distance between antennas. In general, when the body is approaching the Rx (*i.e.*, $x \in [50, 85]$ m) and is far away from it, the highest $\overline{P_R}$ is obtained for the HE_F antenna, equal to -61 dBm. This location also results in the lowest fast-fading depth for both movement scenarios, as the HE_F location is considered as the most stable. When the body is passing the Rx (*i.e.*, $x \in [85, 115]$ m), the highest $\overline{P_R}$ equal to -59 dBm is received from AB_L, which is expected, as the antenna is directed towards the Rx, however, it is varying a lot (*i.e.*, 9 dB deep fades) for the running body. In this case, the body movement has significant impact on the performance of the off-body link. In the case of the walking body the changes in $\overline{P_R}$ are much less, with a maximum at the cell edge equal to 4 dB. On average, the lowest $\overline{P_R}$ equal to -68 dBm is captured from AB_R, as the antenna is always in NLoS conditions. It is expected that the large power imbalance between the AB_R antenna and other ones can result in poor overall performance, when virtual MIMO is used (*i.e.*, for the antenna pairs including this one).

Table 7.2. Received power for the running body, calculated for selected paths.

	x [m]	propagation	$\overline{P_R}$	$\sigma_{\overline{P_R}}$	$\overline{\sigma_{P_R}}$
			[dBm]	[dB]	
HE_F	[50, 150]	Mix	-64.4	4.8	3.3
	[50, 85]	LoS	-60.7	1.1	1.6
	[85, 115]	NLoS	-62.1	3.2	2.5
	[115, 150]	NLoS	-70.1	2.2	4.7
AB_L	[50, 150]	Mix	-64.8	5.2	2.4
	[50, 85]	Mix	-67.4	3.7	2.7
	[85, 115]	Mix	-59.1	3.5	1.5
	[115, 150]	Mix	-67.0	3.7	2.6
AB_R	[50, 150]	NLoS	-68.3	2.9	3.3
	[50, 85]	NLoS	-69.3	2.2	3.2
	[85, 115]	NLoS	-66.1	1.7	3.6
	[115, 150]	NLoS	-69.2	3.2	3.0
TO_B	[50, 150]	Mix	-64.2	4.8	3.2
	[50, 85]	NLoS	-69.8	2.0	4.5
	[85, 115]	Mix	-61.7	3.4	2.7
	[115, 150]	LoS	-60.8	1.2	1.7

7.1.3. Delay Spread

The delay spread is calculated as defined in (2.11). The average $\overline{\sigma_\tau(t_n)}$ and the standard deviation $\sigma_{\sigma_\tau}(t_n)$ of the delay spread for the running body, are presented in Figure 7.3. The largest variations in the delay spread are registered for AB_L. It is the lowest in the centre of the cell, 30 ns, but as the body moves to the cell edge it rises up to 105 ns. In this case, the multipath richness of the Radio Channel is significant. Also, in the centre of the cell and due to large variations of the antenna orientation, the difference of the delay spread in one run period can reach 60 ns.

(a) average $\overline{\sigma_\tau(t_n)}$ (b) standard deviation $\sigma_{\sigma_\tau}(t_n)$
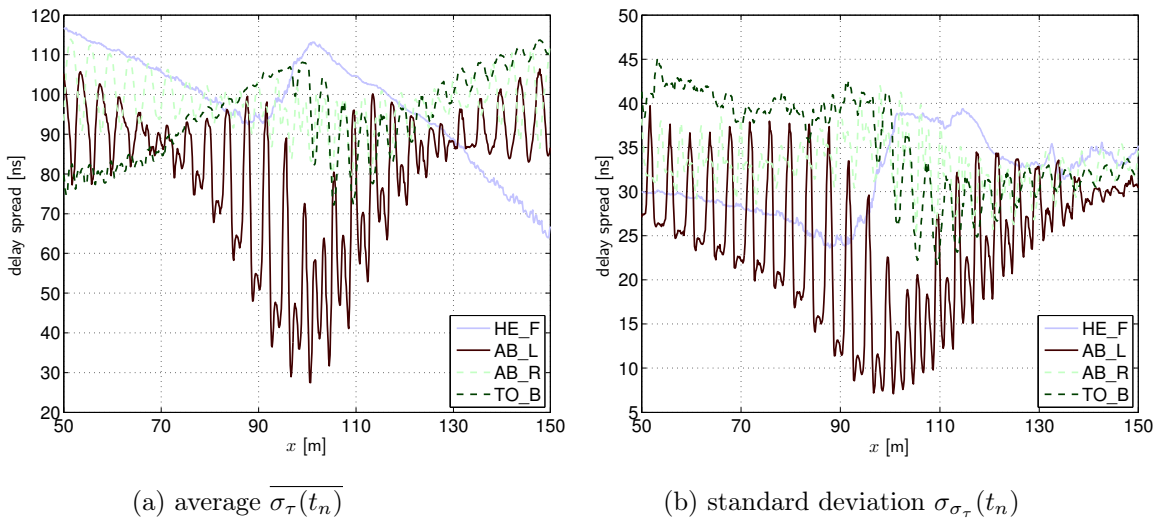
Figure 7.3. Delay spread for the running body.

The statistics of the delay spread for the running body, calculated for selected paths, are presented in Table 7.3. In general, $\overline{\sigma_\tau}$ is higher when the antenna is in NLoS or it is farther away from the Rx. In this case, the signal is reaching the Rx antenna via reflections on the randomly distributed scatterers, which results in larger delays of the MPCs. The highest value of $\overline{\sigma_{\sigma_\tau}}$, 40 ns, is obtained for the NLoS case and the TO_B antenna, when the body is in the cell edge (*i.e.*, $x \in [50, 85]$ m). The $\overline{\sigma_\tau}$ for HE_F, AB_R and TO_B ranges in [87, 107] ns, with the $\sigma_{\overline{\sigma_\tau}}$ up to 10 ns. The lowest $\overline{\sigma_\tau}$, equal to 61 ns, is obtained for AB_L, when the body is close to the Rx (*i.e.*, $x \in [85, 115]$ m), which is expected, as the LoS component is dominant (*i.e.*, low multipath richness of the Radio Channel).

Table 7.3. Delay spread for the running body, calculated for selected paths.

	x [m]	propagation	$\overline{\sigma_\tau}$	$\sigma_{\overline{\sigma_\tau}}$	$\overline{\sigma_{\sigma_\tau}}$
			[ns]		
HE_F	[50, 85]	LoS	106.7	6.2	28.3
	[85, 115]	NLoS	102.9	6.6	33.3
AB_L	[50, 85]	Mix	88.1	9.0	27.6
	[85, 115]	Mix	61.3	18.7	18.1
AB_R	[50, 85]	NLoS	100.6	6.0	33.2
	[85, 115]	NLoS	93.4	6.0	34.5
TO_B	[50, 85]	NLoS	86.7	6.7	40.3
	[85, 115]	Mix	96.3	10.3	34.6

7.1.4. Spread of the Direction of Arrival

For a fixed radio link, the spatial parameters can be calculated for both ends of the radio link, however, when the Tx antenna is located on a dynamic body, the DoD depends also on the orientation of the on-body antenna. Therefore, in this thesis only DoA spread is calculated as defined in (2.15). The average DoA spread $\overline{\sigma_{DoA}(t_n)}$ for the walking body is presented in Figure 7.4. At the centre of the cell, for the AB_L antenna the DoA spread is the lowest, 15° (*i.e.*, the power of LoS component is dominant), but it increases to 45° in the cell edge (*i.e.*, MPCs arrive from different directions). The results for HE_F and TO_B are similar for the opposite cell edges, a small difference coming from the placement of the antenna on different heights on the body.

The statistics of the DoA spread for the walking body, calculated for selected paths, are presented in Table 7.4. The DoA spread increases when the antenna is in NLoS or it is farther away from the Rx. Therefore, for all antenna placements, the $\overline{\sigma_{DoA}}$ is lower when the body is close to the Rx, and it is the lowest for AB_L, equal to 20°. This value is 2 times lower than the average for AB_R, which is constantly in NLoS. The average of the standard deviation $\overline{\sigma_{\sigma_{DoA}}}$ is varying in [9°, 13°]. Except for AB_L, the standard deviation of the average DoA $\sigma_{\overline{\sigma_{DoA}}}$ is below 6°. Similar results for the DoA spread have been obtained for both walking or running bodies (*i.e.*, bodies were moving along the same path and had the same orientations with the Rx).
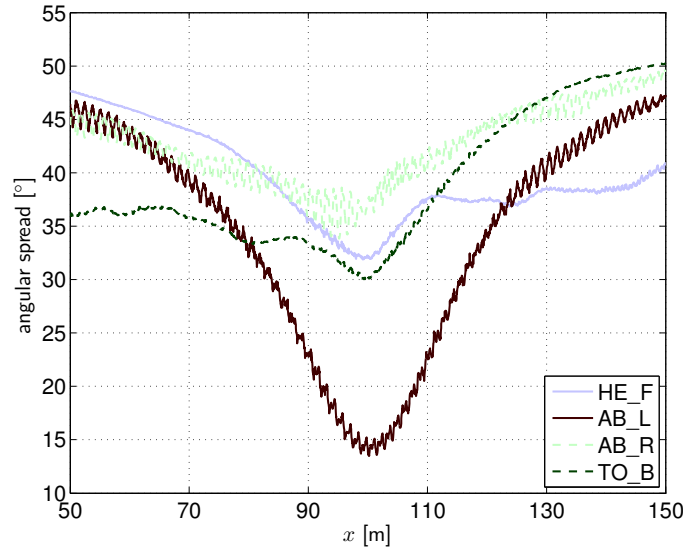
Figure 7.4. Spread of DoA for the walking body.

Table 7.4. Spread of DoA for the walking body, calculated for selected paths.

	x [m]	propagation	$\overline{\sigma_{DoA}}$	$\sigma_{\overline{\sigma_{DoA}}}$	$\overline{\sigma_{\sigma_{DoA}}}$
			[°]		
HE_F	[50, 150]	Mix	39.4	4.1	13.4
	[85, 115]	NLoS	35.2	2.1	11.4
AB_L	[50, 150]	Mix	34.1	10.3	11.1
	[85, 115]	Mix	20.2	4.7	9.0
AB_R	[50, 150]	NLoS	42.6	3.7	12.6
	[85, 115]	NLoS	38.7	2.2	12.7
TO_B	[50, 150]	Mix	38.9	6.3	13.0
	[85, 115]	Mix	33.7	2.7	11.7

The detailed information of RCPs for the street scenario is gathered in Annex E.

7.1.5. Correlation between Received Signal Envelopes

The correlation between received signal envelopes is calculated as defined in (6.8). The correlation between signal envelopes has been calculated for all possible combinations of antennas, and the statistics have been calculated for the general classes, Figure 7.5.

In general, similar results for the correlation have been obtained for both walking and running bodies. The highest correlation is obtained, when both antennas are located on the front side, being on average equal to 0.60 (a value of correlation being 0.70 or less can be used as the guideline for successful diversity operation).c In this case, the running body is characterised by slightly higher standard deviation, equal to 0.10. The largest differences between signals are found for antennas located on the front and back sides. The average correlation is equal to -0.30, which means that signals follow opposite trends. In this case, the envelopes of the two on-body antennas do not exhibit the same fading behaviour, which translates into a lower probability

(a) walking body   (b) running body
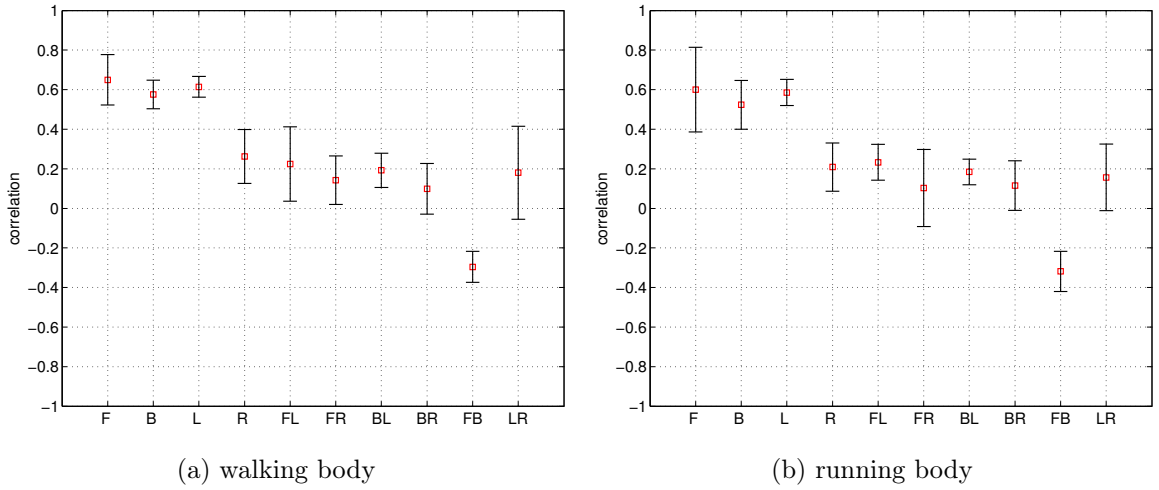
Figure 7.5. The correlation between received signal envelopes for the antenna class.

of having both antennas in a null at the same time. When at least one antenna is located on the right side and is constantly in NLoS conditions (*i.e.*, R, LR, FR or BR class), the average correlation is very low, ranging in $[0.10, 0.25]$. Also, in this case the signals do not fade, peak, increase, and decrease at the same time.

The lower the envelope correlation in a diversity system, the larger the achievable diversity gain. Therefore, the independent fading of the signals can be obtained, by the placement of the antennas in opposite sides of the body.

7.1.6. Correlation between Channel Impulse Responses

The correlation between CIRs is calculated as it is defined in (6.9). The average correlation for a selected pair of antennas (*i.e.*, TO_F & WA_F, HE_F & AB_L and HE_L & HE_R), which are representative of various classes, is presented in Figure 7.6. In this study, in order to obtain several incoming rays, the filtering of MPCs at the Rx with a time resolution equal to 50 ns has been considered.

For TO_F & WA_F, the correlation is high, $\overline{\rho_{CIR}} \in [0.7, 0.85]$, but when the body is passing the Rx (*i.e.*, $x \in [100, 115]$ m), it drops down to 0.6. This variation occurs due to a transition of propagation conditions from LoS to NLoS. In the case of antennas located on different sides of the head (*i.e.*, HE_L & HE_R), the correlation is the lowest, $\overline{\rho_{CIR}} \in [0.2, 0.45]$. In this case, the channels do not exhibit the same behaviour, which is required by the MIMO system. For the HE_F & AB_L, when one antenna is located on the arm, and the direction of maximum radiation is rapidly changing, the correlation is varying a lot, and a difference of 0.4 during a single running period is registered. In the case of the walking body, the changes in correlation are much less, with a maximum at the cell edge equal to 0.15. When the body is approaching the Rx, the correlation is increasing and reaching its maximum when the body is close to the Rx, then, it sharply goes down. In general, for the same distance range, there are 3 times more walking periods than running ones, which results in more dense oscillations of the correlation.

(a) walking body   (b) running body
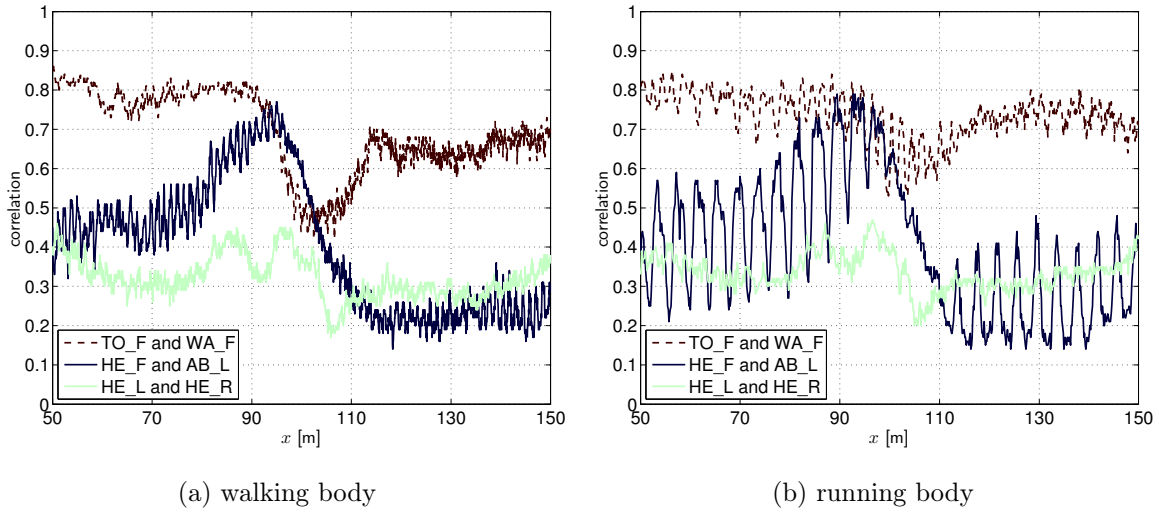
Figure 7.6. Average correlation for a selected pair of antennas.

The average correlation and the standard deviation have been calculated for all possible combinations of antenna pairs. In Table 7.5, the statistics of the correlation for the running body and the allocation to the class are presented.

Table 7.5. Average and standard deviation of correlation for the various classes for the running body.

		TO_F	WA_F	HE_F	HE_B	HE_L	HE_R	AB_L	AB_R	TO_B
					average correlation					
	TO_F		0.73	0.55	**0.20**	0.44	0.33	0.41	0.34	**0.26**
	WA_F	0.22		0.53	**0.19**	0.44	0.33	0.42	0.35	**0.24**
	HE_F	0.24	0.24		**0.27**	0.49	0.43	0.41	0.34	**0.22**
standard deviation	HE_B	**0.16**	**0.16**	**0.22**		0.49	0.44	0.42	0.34	0.55
	HE_L	0.26	0.26	0.26	0.26		**0.34**	0.61	**0.39**	0.45
	HE_R	0.19	0.19	0.22	0.22	**0.18**		**0.32**	0.40	0.34
	AB_L	0.25	0.26	0.25	0.24	0.25	**0.17**		**0.35**	0.43
	AB_R	0.21	0.21	0.20	0.20	**0.20**	0.19	**0.19**		0.36
	TO_B	**0.20**	**0.18**	**0.16**	0.22	0.25	0.19	0.24	0.21	

CD	co-directed	XD	cross-directed	OD	oposit-directed

It is worthwhile to notice that the Rx is located on the left side of the street, and when the Tx antenna is on the right side of the body, it is always in NLoS. Therefore, when one of the Tx antennas is on the right side (*i.e.*, HE_R or AB_R), the average correlation is similar for all classes, $\overline{\rho_{CIR}} \in [0.34, 0.44]$. The average correlation for CD antennas depends on the side of the body, being the lowest for the right side (*i.e.*, AB_R & HE_R), 0.4. In this case, both antennas are in NLoS and the received MPCs are quite different. The most similar signals (*i.e.*, $\overline{\rho_{CIR}}$=0.73) are captured for WA_F & TO_F antennas, as they move in a similar way, and are placed close to each other. The highest standard deviation, 0.26, is obtained for some of the antennas in the XD class; in this case, the average correlation is $\overline{\rho_{CIR}} \in [0.34, 0.49]$, being lower when the one of the antenna is located on the right side of the body. The lowest correlation

is obtained for OD antennas, in particular for HE_B & WA_F, equal to 0.19. In this case, the gain of the MIMO system can be the highest, however, one has also consider the power imbalance. However, in the case of antennas located on the opposite side, but on the Head, the average correlation is higher, equal to 0.27 and 0.34, for HE_F & HE_B and HE_L & HE_R, respectively. In this case, the antennas are placed at the same height, and with a small spacing between them.

The statistics for CD, XD and OD antennas are presented in Table 7.6.

Table 7.6. The average and standard deviation of the correlation for CD, XD and OD antennas for walking or running bodies.

		CD	XD	OD
$\overline{\rho_{CIR}}$	Walk	0.56	0.39	0.27
	Run	0.56	0.40	0.28
$\sigma_{\rho_{CIR}}$	Walk	0.22	0.22	0.17
	Run	0.23	0.23	0.18

In general, similar results have been obtained for both walking and running bodies. The proposed classification of the mutual orientation of antennas is in agreement with the obtained values of the average correlation, where for OD antennas the average correlation is less than for the XD ones. Also, for the XD antennas, the average correlation is less than for the CD ones. The standard deviation for the walking body is less than for the running one, which can be explained by walking being less dynamic than running, but the difference is very low. In the case of OD antennas, the standard deviation is 0.05 less than for the two other classes (*i.e.*, CD and XD).

7.2. MIMO Capacity

The MIMO capacity is calculated as defined in (2.19). The average capacity, the capacity boundaries and Rx power, for the running body, for a particular pair of antennas (*i.e.*, WA_F & TO_B) are presented in Figure 7.7.

As the Tx antennas are located on opposite sides of the body, the Rx power is symmetric and similar for the opposite edges of the cell. At the cell edges, the power imbalance (6.7) is high, above 10 dB, and the capacity is close to the lower bound. The minimum power imbalance between Tx antennas is obtained when the body is close to the Rx (*i.e.*, $x = 100$ m), which results in higher capacity (*i.e.*, close to the upper bound). In the centre of the cell, the difference between capacity in one running period can reach 4 bps/Hz.

The average capacity for a selected pair of antennas (*i.e.*, TO_F & WA_F, HE_F & AB_L and HE_L & HE_R), which are representative from various classes, is presented in Figure 7.8.

In the case of the TO_F & WA_F pair, the difference between cell edges is very high (*i.e.*, 20 bps/Hz on the left side and 6 bps/Hz on the right one). When the body is approaching the

(a) capacity   (b) Rx power
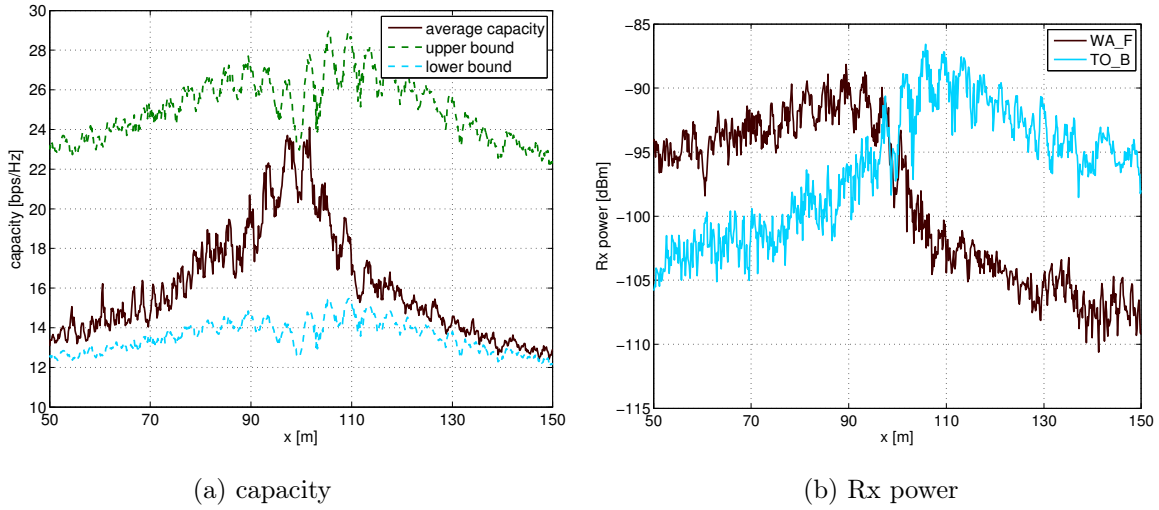
Figure 7.7. Averages for 2×2 MIMO with WA_F & TO_B antennas, for the running body.
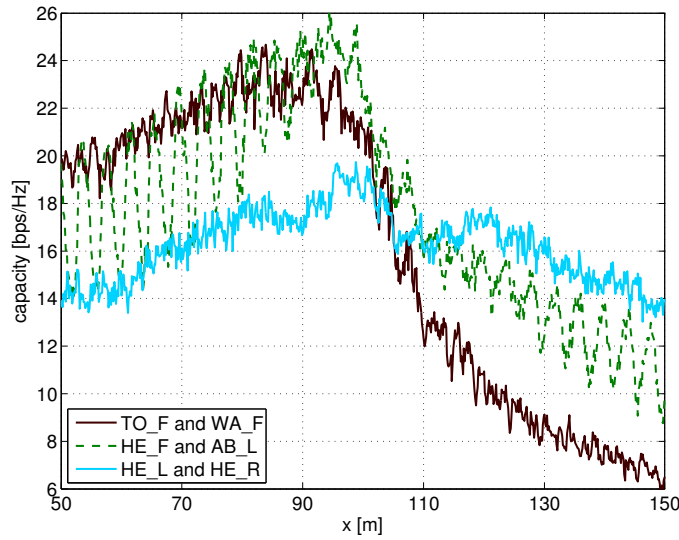
Figure 7.8. Average capacity for selected pair of antennas from the CD, XD and OD antenna classes, for the running body.

Rx, the capacity is increasing and reaching its maximum, 24 bps/Hz, when the body is close to the Rx, then, it sharply goes down. For the HE_F & AB_L, when one antenna is located on the arm, and the direction of maximum radiation is rapidly changing, the capacity is varying a lot, and a difference of 6 bps/Hz during a single running period is registered. In the case of antennas located on different sides of the head (*i.e.*, HE_L & HE_R), the capacity is equal to 14 bps/Hz on both sides of the cell edges, and the maximum is obtained when the body is close to the Rx, equal to 19.2 bps/Hz.

The statistics of the capacity and the capacity channel gain, for the same pair of antennas, for the running body, calculated for selected paths, are presented in Table 7.7. The results for other pair of antennas are gathered in Annex F.

In the case of CD antennas (*i.e.*, TO_F & WA_F), the standard deviation of the average capacity, $\sigma_{\overline{C_{MIMO}}}$, is the highest, being 6.2 bps/Hz. For all pairs of antennas, the different

Table 7.7. The capacity and the capacity channel gain, for selected pair of antennas, for the running body, calculated for selected paths.

	x [m]	$\overline{C_{MIMO}}$	$\sigma_{\overline{C_{MIMO}}}$	$\overline{\sigma_{C_{MIMO}}}$	$\overline{G_{MIMO_c}}$	$\sigma_{\overline{G_{MIMO_c}}}$	$\overline{\sigma_{G_{MIMO_c}}}$
		[bps/Hz]					
TO_F	[50, 150]	16.41	6.23	2.21	1.45	0.17	0.17
&	[50, 85]	21.60	1.37	2.25	1.59	0.05	0.16
WA_F	[85, 115]	19.40	4.02	2.34	1.53	0.09	0.17
	[115, 150]	8.78	1.77	2.06	1.26	0.08	0.18
HE_F	[50, 150]	17.91	4.36	1.90	1.38	0.18	0.15
&	[50, 85]	19.70	2.75	2.06	1.46	0.17	0.15
AB_L	[85, 115]	21.40	3.19	2.02	1.45	0.17	0.13
	[115, 150]	13.29	1.85	1.61	1.24	0.10	0.16
HE_L	[50, 150]	16.35	1.39	1.79	1.36	0.14	0.16
&	[50, 85]	16.10	1.28	1.94	1.43	0.06	0.18
HE_R	[85, 115]	17.59	0.95	1.72	1.17	0.06	0.12
	[115, 150]	15.67	1.13	1.71	1.47	0.07	0.17

location of the scatterers results in the average standard deviation of the capacity, $\overline{\sigma_{C_{MIMO}}}$, ranging in $[1.7, 2.3]$ bps/Hz. The average capacity channel gain, $\overline{G_{MIMO_c}}$, for the whole distance range (*i.e.*, $x \in [50, 150]$ m) is in $[1.36, 1.46]$, whereas, the standard deviation of the average capacity channel gain, $\sigma_{\overline{G_{MIMO_c}}}$, and the average standard deviation of the capacity channel gain, $\overline{\sigma_{G_{MIMO_c}}}$, is below 0.2.

The average capacity and the standard deviation have been calculated for all possible combinations of antenna pairs. In Figure 7.9, the statistics of the capacity for the running body and the allocation to the class are presented.

Figure 7.9. Capacity statistics for all possible antenna pairs, for the running body.

In general, the largest standard deviation is obtained for the CD antennas. For this class, the average capacity strongly depends on the side where the antennas are placed. As the Rx antenna is located on the left, the highest average capacity was obtained for both antennas located on the left side of the body (*i.e.*, HE_L & AB_L), equal to 19 bps/Hz. The largest differences between the average capacity are obtained for the antennas in the XD class, the average capacity is higher by 4 bps/Hz, when one antenna is located on the left side of the body. For the OD class, the average capacity is similar for all cases, $\overline{C_{MIMO}} \in [16.0, 17.2]$ bps/Hz, being slightly higher for HE_L & AB_R. In this case, one antenna is located on a stable location (*i.e.*, Head), whereas the other (*i.e.*, Arm) is rapidly changing the direction of maximum radiation, producing strong decorrelation in the channel, thus, a higher capacity gain.

The statistics for CD, XD and OD antennas are presented in Table 7.8. In general, the average capacity is similar for all classes, being slightly higher for the CD antennas, equal to 17.2 bps/Hz. In the case of OD antennas, the standard deviation is the lowest, being 2 times lower than in the CD class. These results confirm that when antennas are placed on the opposite sides of the body, they have better conditions to achieve a more stable performance. The high values of standard deviation in the CD antennas, comes from the similar propagation condition of both antennas at the same time. The capacity is high and low, when antennas are in LoS and NLoS, respectively.

Table 7.8. The average and standard deviation of the correlation for CD, XD and OD antennas, for the running body.

	CD	XD	OD
$\overline{C}$	17.2	16.7	16.3
σ_C	5.7	4.1	2.9

The statistics for 4×4 MIMO system, with respect to the general classes are presented in Figure 7.10. Increasing number of antennas on both sides of the radio link increases the boundaries of possible capacity gains, which results in higher values of the average capacity. In general, for all classes the average capacity varies between 29 and 34 bps/Hz, and is higher when at least one antenna is located on the left side of the body (*i.e.*, FL, BL, LR, FBL, FLR, BLR or FBLR classes). In this case, the left antenna receives strong signal, which increase the SNR and improves obtained values of the capacity. Therefore, when there are no antennas on the left side (*i.e.*, FBR class), the average capacity is the lowest, equal to 29 bps/Hz. Due to body movements and change of the position of the body in the cell, the standard deviation of the capacity is very high, the maximum being in the case of the FL class, equal to 10 bps/Hz. Moreover, for OD antennas, the standard deviation is almost 2 times higher in case of the FB class than for the LR one.

In general, the results show that the usage of virtual MIMO in BANs can benefit from the capacity gain and enhancement of the overall performance of off-body links. However, one has to carefully select the placement of the antennas, according to requirements of the application. On the one hand, in the case of strong power imbalances between antennas, the system cannot
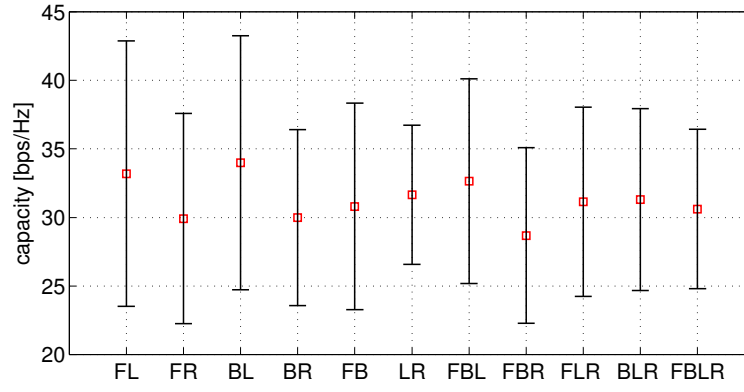
Figure 7.10. The capacity for the antenna class, for the running body.

benefit from the capacity gains. On the other, this can lead to significant diversity gain, and improve the outage of the Radio Channel.

Other results, for the study of MIMO capacity for the street scenario, is gathered in Annex F.

7.3. Optimum Antenna Placement

This study indicates which are the best locations for antennas in a given scenario, to optimise the MIMO capacity gain. First of all, the percentage indicating the best (6.10) or the worst (6.11) performances is calculated, Figure 7.11.
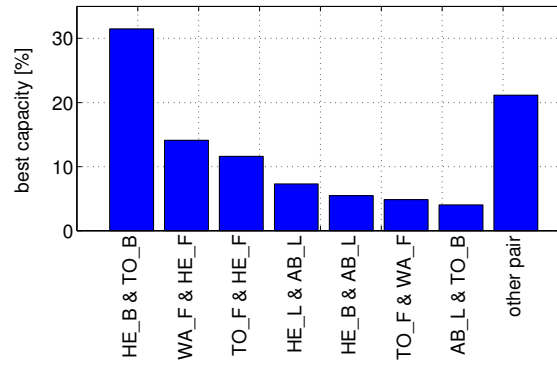
(a) the best capacity
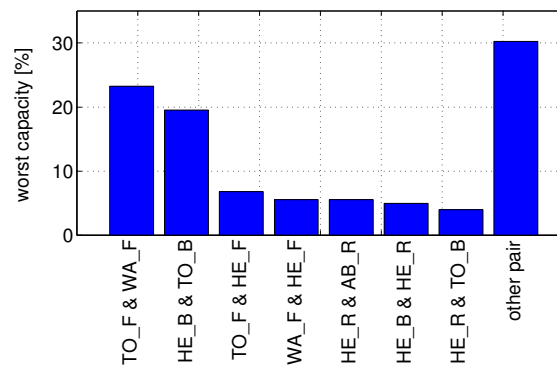
(b) the worst capacity

Figure 7.11. The best and the worst pairs of antennas for MIMO 2×2 for the running body.

At the same time, the best and the worst results of capacity are obtained for HE_B & TO_B pair, being 32% (*i.e.*, the best result) and 19% of time (*i.e.*, the second worst result), respectively. This means that when body is approaching Rx (*i.e.*, back antennas are in NLoS), this pair performs the worst, whereas when it is retreating from the Rx (*i.e.*, back antennas are in LoS), it performs the best. Similar performance is observed, when both antennas are located on the front (*i.e.*, HE_F & TO_F, HE_F & WA_F and TO_F & WA_F). In general, the worst performance is obtained for TO_F & WA_F antennas, equal to 23% of the time. In this case, as shown before, the correlation between CIR is usually high (due to the short distance between antennas). Moreover, for half of the time, both antennas are in NLoS with the Rx, which results in low SNR, thus, low capacity. It is worthwhile to notice that when one antenna is located on the right side (*i.e.*, this antenna is always in NLoS), the pair is never performing with the best capacity.

The MIMO performance is calculated as defined in (6.12). The overall performance averaged over all time frame, $\overline{C^p_{MIMO_P}}$, for the best antenna pairs is presented in Figure 7.12.
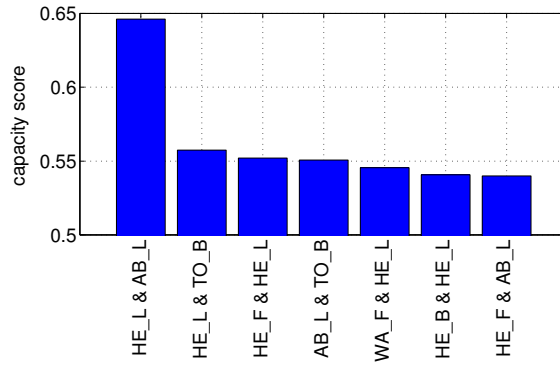
Figure 7.12. The overall performance of antenna pairs for MIMO 2×2 for the running body.

The results indicate that the HE_L & AB_L pair outperforms the others, with the average overall performance being $\overline{C^p_{MIMO_P}}$=0.64. The overall performance of this pair, for all position in the cell is presented in Figure 7.13.
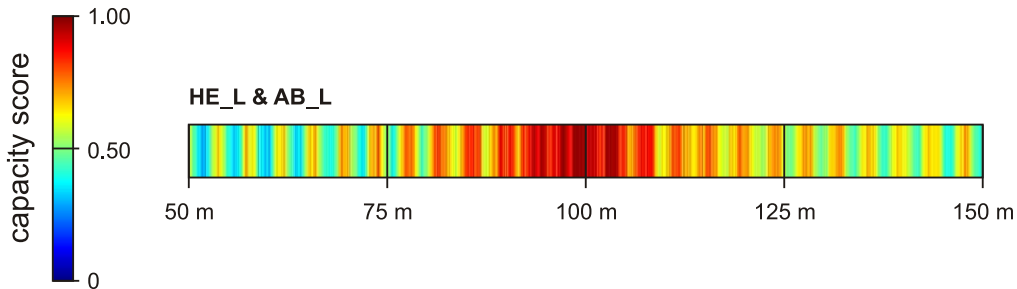
Figure 7.13. The overall performance for the HE_L & AB_L pair, for the running body.

This pair of antennas performs well in the whole range of body movement, especially when the body is passing the Rx. Due to the body movement, cyclic drops in the overall performance are registered, when the AB_L antenna is in NLoS with the Rx (especially in the cell edges). Therefore, this pair should be selected for the optimum location of antennas, Figure 7.14. The

other best pairs, obtained similar results of the average overall performance being approximately equal to $\overline{C_{MIMO_P}^{p}}$=0.55. It is worthwhile to notice that all the best pairs of antennas have at least one antenna located on the left side of the body.
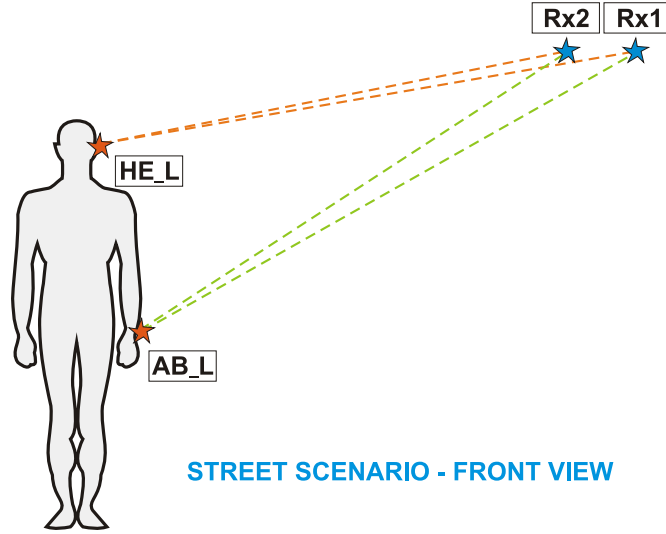
Figure 7.14. The optimum placement of the on-body antennas in the Street scenario.

Table 7.9 summarises the performance of the HE_L & AB_L pair, and presents the average capacity, and the average capacity channel and system gains, for selected paths.

Table 7.9. The average capacity, and the average capacity channel and system gains, for the HE_L & AB_L pair, for the running body, for selected paths.

x [m]	$\overline{C_{MIMO}}$ [bps/Hz]	$\overline{G_{MIMO_s}}$	$\overline{G_{MIMO_c}}$
[50, 150]	19.56	1.67	1.53
[50, 85]	18.04	1.67	1.52
[85, 115]	24.13	1.69	1.58
[115, 150]	17.33	1.66	1.51

In general, using this placement of the antennas gives high capacity system gain, $\overline{G_{MIMO_s}}$=1.67, therefore, by using off-body virtual MIMO system, 67% more data, with respect to the SISO link, can be transmitted. The average capacity for this pair reaches, $\overline{C_{MIMO}}$=24.1 bps/Hz, when the body is passing the Rx. In this case, the average capacity system and channel gains are, $\overline{G_{MIMO_s}}$=1.69, and, $\overline{G_{MIMO_c}}$=1.58, respectively. At the cell edges, the average capacity is 6 bps/Hz lower than in the centre.

The presented results of the overall performance are valid for the scenario considered in this thesis. However, this approach can be used for other ones, taking into account other antennas, and required placements on the body. Also different dynamics scenarios and propagation environments can be simulated.

Other results, for the study of the capacity performance, are gathered in Annex G.

Chapter 8

Conclusions

This chapter draws final conclusions to the work. The thesis summary, main conclusions, and recommendations for the future work are presented.

8.1. Summary

This thesis is organised in eight chapters, which are followed by a set of annexes. Chapter 1, besides the main objectives and challenges, points out the novelty, and presents the contributions of this thesis in the development of the models for BANs, and provides as well as the detailed structure of the thesis.

In Chapter 2, a brief introduction of the wireless communications channel is made, including a description of main phenomena that take place in the propagation. Also, the review of channel models is made and the GBSC model is presented in detail, providing the definition of various radio channel parameters. Finally, the MIMO system is described, and MIMO capacity is presented and discussed.

In Chapter 3, the state of the art on modelling related to BANs is made. The BAN transmission channel can be split into three categories including off-body among others (*i.e.*, in-body and on-body), and as this is the relevant one to this work, its main characteristics are presented. The electromagnetic properties of the body tissues and variability of the body geometry are discussed, and possible methods of body modelling are presented (*e.g.*, voxel models) as well. The concept of wearable antennas and their requirements is introduced, and the importance of a statistical model for antennas near the body is motivated. At the end of this chapter, the existing numerical techniques including full wave methods are presented, and the main features of CST simulation environment, which was used to obtain important results of this thesis, are described in details.

Chapter 4 proposes a new statistical model to analyse the performance of wearable antennas in BANs. Firstly, the simple model based on image theory is introduced, and the method to calculate a statistical radiation pattern of the electric field, depending on the antenna to body distance distribution, is presented. Then, a patch antenna near the body has been modelled in CST with various meshing options, in order to select the optimum one in terms of complexity and accuracy. In this chapter, the study of correlation between signals captured by wearable antennas is presented as well. Finally, the novel model to account for the realistic body movements is described.

In Chapter 5, the results obtained from the developed models, accounting for the body coupling (using theoretical, numerical and practical approaches), signal correlation and body dynamics are presented and analysed. The results presented in this chapter are also taken as an input for the developed model of a BAN radio channel.

In Chapter 6, the developed channel model for BANs is presented, and its implementation in the developed simulator is also described. The whole off-body radio channel is considered using the GBSC model, and the influence of the propagation environment is taken into account. Fundamental assessment procedures are described, and a comparison with the measurement data is provided.

In Chapter 7, the results from simulations of street scenario are presented, followed by a deep statistical analysis of obtained radio channel parameters for off-body communication. The performance analysis of MIMO system in various scenarios and configurations is presented as well. The selection of the best on-body placements of antennas is done, based on the obtained values for MIMO capacity.

Finally, in the current chapter, thesis summary, main conclusions, and recommendations for future work are presented.

8.2. Main Results

The link budget for BANs has to be redefined, therefore, new parameters have to be accounted for, *e.g.*, antenna gain pattern changes, tissue absorption, transmitted power limited by the safe margins, influence of body dynamics, and the distance between antenna and the body. Moreover, a cross-layer perspective for BANs is required, which comprises cooperation and knowledge sharing between the various system layers. This thesis stresses the core position of the Radio Channel on the overall system, prompting the strong influence of the human body, addressing the wide range of BANs scenarios and discussing strategies to improve connectivity problems (*e.g.*, smart deployment of on-body antennas). In general, a good and deep understanding of the Radio Channel models in BANs can help improving the QoS of applications.

The novel aspect of this thesis is a statistical analysis of the gain patterns of an antenna, calculated at different distances between antenna and body. This approach allows one to consider the antenna gain pattern no longer as a deterministic, but rather stochastic, component of the link budget, when developing Radio Channel models for BANs.

This can be evaluated using a very simple model based on image theory, which gives a glimpse of the possible range of changes in the radiation pattern of the electric field. A comprehensive statistical study on the variations of radiation patterns was carried out for various scenarios (*i.e.*, frequencies, body sizes, and tissues). When the antenna is located over an ellipse, for a Uniform Distribution of the distance between antenna and body, the average radiation pattern is slightly changing among scenarios. The change of the average radiation pattern is a little more visible for the Rayleigh Distribution, especially for 0.915 GHz, where the antenna to body distance is changing only a little compared to the wavelength. The standard deviation of the radiation pattern varies significantly over radiation angles, and also for various frequencies and tissues. This confirms the validity of the proposed concept of an antenna statistical model. Among analysed tissues, Muscle has the highest influence (*i.e.*, the highest permittivity and conductivity) whereas Fat has the lowest one. In general, the standard deviation of the average radiation pattern is higher for the perpendicular polarisation than for the parallel one.

However, it is advised to perform full wave simulations, in order to obtain realistic antenna gain patterns and account for the body coupling. The influence of the body is the highest when

the antenna is attached to the body, due to the strongest coupling between the body and the antenna, and reduction of the antenna radiation efficiency. As the main relative variations of the gain pattern are observed in the backward direction, where the radiation level is very low, the Pattern Weighted Difference (PWD) is always lower than the Pattern Average Difference (PAD). In the case when the antenna is located near the Chest with a Rayleigh Distribution, the PWD can reach 11%, and the the PAD can be as high as 24%, relative to the isolated antenna case. These results show that the patch is well isolated from the body (*i.e.*, similar gain for different placements and low standard deviation), which will ensure stability of the system.

The measurement campaign complemented the numerical study, providing results from the whole complex BAN channel, in an anechoic chamber. Results from measurements are in line with the CST ones, showing that, in the area of interest for off-body communications, no large changes between the two approaches are observed.

The difference between received signals captured by wearable antennas in a BAN is evaluated by the cross-correlation coefficient. The statistical study is performed for various separations of antennas from the body, which determine the coupling between the body and the antenna. In a multipath environment, multiple copies of the signal can arrive from an arbitrary direction, however, in this work the components are investigated separately (*i.e.*, one at the time). The wearable antennas are placed with different distances to the body in the range $[0, 2\lambda]$ (*i.e.*, 11 samples uniformly distributed), and the wave is coming from a direction in the range $[0°, 180°]$ (*i.e.*, 36 samples uniformly distributed). For a multiple antennas system, the cross-correlation between signals is an important measure of the spatial diversity, indicating possible gains of the MIMO system. The average and standard deviation of cross-correlation are analysed for various pairs of antennas, which can be split into 3 classes: Co-Directed (CD), Cross-Directed (XD) and Opposite-Directed (OD). As expected, the cross-correlation is the lowest for antennas located on different sides of the body (*i.e.*, OD) equal to 0.67, and is the highest for the antennas on the same side (*i.e.*, CD) equal to 0.95. Therefore, in the case of OD class, the diversity gain should be higher than for the CD one. The largest variations in average cross-correlation are observed for the XD class, which is also characterised by the highest standard deviation, equal to 0.13. In this case, depending on the azimuth, the signals received from the on-body antennas can be either low or highly correlated. A low cross-correlation is obtained when an antenna is in LoS with the incoming wave, while the other is shadowed by the body (which is determined by the placement of the antenna and its distance to the body, as well as the direction of the incoming wave). In general, the direction has a more significant impact on the cross-correlation than the distance between the antenna and the body.

Additionally, this thesis presents a very realistic model of body dynamics, and the corresponding influence on antenna gain patterns from a statistical viewpoint. By using this method, it is possible to describe and include body movement scenarios in Radio Channel simulators. This is of great importance, as antenna rotation has a huge impact on the performance of the whole transmission channel. Due to the movement of the antenna located at the BAN side of the radio

link, the antenna located at the other side of the link captures significant signal variations, and changes in the angular power profile. The gain patterns are significantly modified by the body movement, which depend on the antenna placement. As expected, when the antenna is mounted on the Arm, the standard deviation of the change in normal to the body surface is the highest among all placements, reaching 19° and 37° for the running body, for elevation and azimuth angles, respectively. The standard deviation for the walking body is much smaller compared to the running one, for all antenna placements, being always less than 4°. Therefore, the walking body does not have a significant influence on the gain pattern of the patch. The Kumaraswamy Distribution has been considered as the best fit for variations in the direction normal to the surface. In general, when the antenna is placed on a very dynamic body segment (*e.g.*, Arm and running body), the maximum gain of average gain pattern is reduced. Moreover, the shape of the gain pattern is more uniform relative to the static body, and the standard deviation is very high. This mean that body dynamics can have a very important impact on the performance of the whole off-body link, especially for highly dynamic scenarios (*e.g.*, running body).

The influence of the propagation environment can be taken into account, including previously obtained antenna gains and body dynamic characteristics, in the GBSC model. Therefore, a flexible and novel method to model Radio Channels in off-body communications is proposed. Using this approach, both the temporal (*i.e.*, delay spread) and angular (*i.e.*, angular spread) parameters can be characterised. Also, the study of the MIMO capacity for various antenna locations can be performed, and the optimum configurations can be selected. The developed models and algorithms are not system dependent, so they can be used for other systems, and not just for the one chosen for example.

A BAN with patch antennas operating at 2.45 GHz and 9 possible locations on the body has been analysed: TO_F, WA_F, HE_F, HE_B, HE_L, HE_R, AB_L, AB_R and TO_B. Simulations have been performed for one propagation environment scenario (*i.e.*, street), and two body movements (*i.e.*, walking and running bodies).

Basic Radio Channel parameters, as the propagation conditions (*i.e.*, LoS, NLoS and Mixed), the received power, the delay spread and DoA spread are obtained, and a statistical analysis of results is provided. As expected, output parameters strongly depend on the body movement, especially when the antenna is located on AB_L. For the running body, the propagation conditions change rapidly, and 9 dB deep fades in the average received power are captured, in contrast to 4 dB for the walking body in the cell edge. Therefore, the body movement can determine the connectivity of the radio link. The lowest average delay spread, 61 ns, is obtained for the AB_L antenna when the body is closed to the Rx. In this case, the multipath channel richness is low (*i.e.*, the dominant role has the LoS component). As expected, when the antenna is in NLoS, the average standard deviation of the delay spread is the highest, reaching 40 ns in the cell edge (*i.e.*, strong contribution from the MPCs). The average DoA spread depends on the location of the body in the cell, being minimum when the body is close to the Rx (*i.e.*, for AB_L it is 20°, and [33°, 39°] for other placements).

In order to measure how much a signal in an on-body antenna behaves like another, the envelope correlation is calculated. The largest differences between signals are found for antennas located on the front and back sides (the absolute average envelope correlation is equal to 0.30, which is below 0.70 that can be used as the guideline for successful diversity operation). Therefore, the independent fading of the signals (*i.e.*, high diversity gain) can be obtained, by the placement of the antennas in the opposite sides of the body.

In this thesis, the correlations between CIRs are obtained, and a statistical analysis of results is provided. As expected, the correlation is the lowest for antennas located on different sides of the body (*i.e.*, OD), equal to 0.28, and is the highest for antennas on the same side (*i.e.*, CD), equal to 0.56. The lowest correlation is obtained for HE_B & WA_F, equal to 0.19, and this placement provides the best diversity among the analysed scenarios. However, because of the strong power imbalance, this does not lead to a good performance of the MIMO system. In general, when one antenna is located on the right side of the body (*i.e.*, NLoS conditions), the correlation is lower, being similar for all classes, [0.34, 0.44]. Due to the randomness of the propagation environment, large variations of body postures, and changes of body location in the cell, the standard deviation of the correlation is always above 0.16. The largest standard deviation was obtained for the XD and OD classes and the running body, equal to 0.23. Therefore, the state of the channel strongly depends on the body dynamics and general position of the body in reference to the Rx.

Moreover, the 2×2 MIMO capacity for 36 possible combinations was obtained, and a statistical analysis of results is provided. The average capacity strongly depends on the power imbalance between antennas. Because the Rx is located on the left, the average capacity is the highest when both antennas are located on the left side of the body (*i.e.*, HE_L & AB_L), equal to 19.2 bps/Hz. When one antenna is located on the Arm (*i.e.*, AB_L), the changes of the direction of maximum radiation of antenna, results in a difference of 6 bps/Hz during a single running period. Again, this confirms the strong impact of body dynamics on the overall performance. For antennas located on the right, the average capacity is lower (*i.e.*, close to the bottom bound), however, the standard deviation is also low. As expected, the lowest standard deviation, equal to 2.9 bps/Hz, is obtained for the OD antennas. In this case, due to strong power imbalances between antennas, the system can not benefit from the capacity gains, but can improve the outage of the Radio Channel exploring diversity gain. In general, for the considered scenario, the results indicates that the HE_L & AB_L pair outperforms other ones, with average overall performance being 0.64. The main reason is good propagation conditions along body movement in the cell (*i.e.*, most of the time antennas are in LoS with the Rx), and low power imbalance.

The final conclusion of this thesis, is that the usage of virtual MIMO in BANs can benefit from the capacity gain and enhancement of the overall performance of off-body links. Moreover, this thesis stresses the importance of the statistical modelling of the antennas, which has to be taken into account, when developing a real system for off-body communications. From the results presented in this thesis, one can conclude that body dynamics play a dominant role in the BAN

link budget, especially in the case of highly dynamic scenarios like running body, which can be even more important in real scenarios of human daily life. In order to minimise the outage of the system, multiple on-body antennas can be distributed on various locations on the body (*i.e.*, with different orientation), which increase the independence of links (*i.e.*, decrease the correlation between them).

8.3. Future Work

One considers that this thesis is an important step towards the development of a general radio channel model for off-body communications. However, in future work, some improvements can be done in order to approximate the model to real conditions.

In this study, polarisation is not taken into account, but future studies can build a model for the polarisation using the same body movement concept. Moreover, it is required to implement in the simulator the antenna patterns with polarisation, and to analyse body and channel depolarisation effects.

Another interesting aspect is to develop, and include in modelling of body dynamics, a model accounting for the shadowing of the body segments (*e.g.*, hands). The model can consider the attenuation of the body, depending on the type of the tissues and the thickness of the segment. This approach can also lead to model exposure of the body (*i.e.*, calculation of SAR) coming from the on-body devices.

Many objects in the environment can change their position in time, which can be emulated by the appearance, movement, and disappearance of clusters and scatterers. This can be done, by implementing the velocity vectors for the clusters and scatterers in the simulator.

New types of scenarios can be implemented in the simulator. So far, only ellipsoid and cuboid scattering regions are included in the simulator. The option to have many overlaying and different volumes in one environment can be a solution for this problem. Furthermore, the separated scattering regions, can be associated with different objects having different statistical properties (*i.e.*, volume distributions and reflection coefficients).

Above all, it is required to perform simulations of a wide range of scenarios, taken from the measurements sessions, and compare and validate obtained results. This analysis should cover a wide range of: propagation environments, antenna designs, antenna placements, bodies, and frequencies. This can be achieved, by establishing cooperation with other researchers working on BAN channel modelling (*i.e.*, performing measurement of BANs) and participation in various research projects. The goal of this cooperation should be a common framework between research institutes, and a common database of results. Finally, the model should be implemented in real systems and applications.

Annex A. User's Manual

Before running the simulator application, properly prepared config file containing input parameters have to be created. The config file has an XML tree structure, where input parameters are divided into three main groups (*i.e.*, environment, simulator, system). The structure of the first section, which defines parameters that describe scenario and control simulator behaviour, is presented in Figure A.1.

```
<simulator>
    <projectName>street_run</projectName>          %name of the project
    <scenario>Street</scenario>                    %scenario name
    <scenarioType>Outdoor</scenarioType>           %scenario type
    <timeFrames>750</timeFrames>                   %number of the time frames
    <runNumber>1</runNumber>                        %number of simulator runs
    <runStart>0</runStart>                          %starting number
    <environmentPeriod>750</environmentPeriod>      %environment generation period
    <environmentExport>0</environmentExport>        %export environment
                                                    %0:no, 1:yes
    <patternExport>0</patternExport>               %export antenna patterns
                                                    %0:no, 1:yes
</simulator>
```

Figure A.1. Parameters describing scenario and controlling simulator's behaviour.

The structure of the environment section, which describes the shape of the scattering region, and defines numbers of clusters and scatterers, is presented in Figure A.2.

```
<environment>
    <numberClusters>10</numberClusters>            %number of clusters
    <numberScatterers>3</numberScatterers>         %number of scatterers
    <maxBounce>2</maxBounce>                        %maximum number of bounces
    <xLen>200</xLen>                                %x dimension [m]
    <yLen>20</yLen>                                 %y dimension [m]
    <zLen>10</zLen>                                 %z dimension [m]
    <rClst>1</rClst>                                %cluster radius [m]

    <shapeType>2</shapeType>                        %scattering region shape
                                                    %0:cuboid, 1:sphere, 2:ellipsoid
    <aElipse>100</aElipse>                          %dimension x axis [m]
    <bElipse>10</bElipse>                           %dimension y axis [m]
    <cElipse>9</cElipse>                            %dimension z axis [m]
    <xElipse>100</xElipse>                          %x: ellipse centre [m]
    <yElipse>10</yElipse>                           %y: ellipse centre [m]
    <zElipse>0</zElipse>                            %z: ellipse centre [m]
</environment>
```

Figure A.2. Parameters describing propagation environment.

The last group defines system parameters like carrier frequency and transmitted power, Figure A.3. Moreover, parameters within this groups define the MIMO system (*i.e.*, numbers of input and output antennas, and spacing between antennas). The radiation patterns can be loaded from XML files, and allocated to antennas. For the body side, the movement scenario

can be loaded from XML files, which contain the position of the antennas during the movement (*i.e.*, in frame-by-frame manner).

```
<system>
    <frequency>2400000000</frequency>          %carrier frequency [Hz]
    <txPower>1</txPower>                        %Tx power [W]
    <txNumber>2</txNumber>                      %number of Tx antennas
    <rxNumber>2</rxNumber>                      %number of Rx antennas

    <xTx>50</xTx><yTx>10</yTx><zTx>0</zTx>      %(x, y, z) center position of Tx
    <dxTx>0</dxTx><dyTx>0</dyTx><dzTx>0</dzTx>  %automatic location of Tx antennas
                                               %(only when modeTx=0)

    <xRx>100</xRx><yRx>20</yRx><zRx>3</zRx>     %(x, y, z) center position of Rx
    <dxRx>1</dxRx><dyRx>0</dyRx><dzRx>0</dzRx>  %automatic location of Rx antennas
                                               %(only when modeRx=0)
    <patterns>2</patterns>                     %number of gain patterns to load
    <pattern1>antenna_iso.xml</pattern1>       %1st file with gain pattern
    <pattern2>antenna_head.xml</pattern2>      %2nd file with gain pattern

    <motionTx>motion_run_25.xml</motionTx>     %movement file for Tx
    <modeTx>2</modeTx>                         %movement mode of Tx
                                               %0:taken by dxTx, dyTx dzTx
                                               %1:manual
                                               %2:taken from motionTx file

    <Tx1>                                      %parameters for 1st Tx antenna
        <patId>1</patId>                       %selection of the gain pattern
        <location>TO_F</location>              %antenna on-body placement
    </Tx1>
    <Tx2>                                      %parameters for 2nd Tx antenna
        <patId>1</patId>                       %selection of the gain pattern
        <location>HE_F</location>              %antenna on-body placement
    </Tx2>

    <modeRx>0</modeRx>                         %movement mode of Rx
                                               %0:taken by dxRx, dyRx dzRx
                                               %1:manual
                                               %2:taken from motionRx file

    <Rx1>                                      %parameters for 1st Rx antenna
        <patId>0</patId>                       %selection of the gain pattern
        <rotTheta>0</rotTheta>                 %rotation in elevation plane
        <rotPhi>0</rotPhi>                     %rotation in azimuth plane
    </Rx1>
    <Rx2>                                      %parameters for 2nd Rx antenna
        <patId>0</patId>                       %selection of the gain pattern
        <rotTheta>0</rotTheta>                 %rotation in elevation plane
        <rotPhi>0</rotPhi>                     %rotation in azimuth plane
    </Rx2>
</system>
```

Figure A.3. Parameters describing system parameters including configuration and properties of MIMO antennas, and body movement scenario.

The antenna parameters are defined using the XML file, where the gain pattern is defined in all directions, and some general information are provided, Figure A.4.

```
<antenna>
    <patternType>head_location</patternType>  %type of the pattern
    <pattern>                                  %THETA in [0 180]
                                               %PHI in [0 360]

        <t0>
            <p0>0.286061377957</p0>            %gain for THETA=0 and PHI=0
            (...)                              %definition for other PHI
            <p360>0.286061377957</p360>
        </t0>
        (...)                                  %definition for other THETA
        <t180>
            <p0>0.155544450691</p0>
            (...)
            <p360>0.155544450691</p360>
        </t180>
    </pattern>
    <patternParams>
        <gmin>-30.9220211085</gmin>            %minimum of antenna gain
        <gminTheta>105</gminTheta>             %THETA direction of minimum gain
        <gminPhi>330</gminPhi>                 %PHI direction of minimum gain
        <gmax>6.2938306166</gmax>              %maximum of antenna gain
        <gmaxTheta>90</gmaxTheta>              %THETA direction of maximum gain
        <gmaxPhi>180</gmaxPhi>                 %PHI direction of maximum gain
    </patternParams>
</antenna>
```

Figure A.4. Definition of the antenna gain pattern.

The body movement including detailed information about the antennas locations and orientations (*i.e.*, *antennaXX*), body skeleton nodes positions (*i.e.*, *nodeXX*), and body position and orientation (*i.e.*, *body*) is defined using the XML file, Figure A.5.

```
<motion>
    <motionName>run</motionName>           %name of the body motion

    <antenna1>                             %antenna location on the body
        <antennaName>AB_L</antennaName>    %antenna placement
        <frame0>                           %first time frame
            <t>29.0398230679</t>           %antenna elevation rotation [deg]
            <p>58.4842542678</p>           %antenna azimuth rotation [deg]
            <x>34.939964538</x>            %x position [cm]
            <y>18.0048595714</y>           %y position [cm]
            <z>106.422218218</z>           %z position [cm]
        </frame0>
        (...)                              %definition for other time frames
    </antenna1>
    (...)                                  %definition for other antennas

    <node0>                                %node location in reference to body
        <nodeName>hip</nodeName>           %body node name
        <frame0>                           %first time frame
            <x>-0.13740384</x>             %x position [cm]
            <y>-5.12231386</y>             %y position [cm]
            <z>102.01250362</z>            %z position [cm]
        </frame0>
        (...)                              %definition for other time frames
    </node0>

    <body>                                 %body position in the cell
        <frame0>                           %first time frame
            <t>0</t>                       %body elevation rotation [deg]
            <p>-90</p>                     %body azimuth rotation [deg]
            <x>0</x>                       %x position [cm]
            <y>0</y>                        %y position [cm]
            <z>0</z>                        %z position [cm]
        </frame0>
        (...)                              %definition for other time frames
    </body>
    <motionFrames>30</motionFrames>        %number of time frames
    <motionAntennas>5</motionAntennas>     %number of antennas
    <skeletonNodes>27</skeletonNodes>      %number of body nodes
</motion>
```

Figure A.5. Definition of the body movement scenario.

Annex B. Tissues Properties

Electric properties of selected body tissues for 0.915, 2.45 and 5.8 GHz are presented in Table B.1.

Table B.1. Electric properties of selected body tissues.

	0.915 GHz			2.45 GHz			5.8 GHz		
	ϵ_{rb}	σ_b [S/m]	δ_p [cm]	ϵ_{rb}	σ_b [S/m]	δ_p [cm]	ϵ_{rb}	σ_b [S/m]	δ_p [cm]
Aorta	44.740	0.701	5.125	42.530	1.435	2.430	38.230	4.345	0.767
Bladder	18.920	0.385	6.112	18.000	0.685	3.318	16.240	1.857	1.169
Blood	61.310	1.545	2.768	58.260	2.545	1.612	52.540	6.506	0.602
BodyFluid	68.900	1.641	2.755	68.210	2.478	1.785	64.780	6.674	0.648
BoneCancellous	20.760	0.344	7.131	18.550	0.805	2.874	15.390	2.148	0.991
BoneCortical	12.440	0.145	12.980	11.380	0.394	4.578	9.674	1.154	1.454
BoneMarrow	5.501	0.041	30.760	5.297	0.095	12.880	4.963	0.285	4.167
BrainGreyMatter	52.650	0.949	4.122	48.910	1.808	2.072	44.000	4.987	0.717
BrainWhiteMatter	38.840	0.595	5.618	36.170	1.215	2.647	32.620	3.494	0.880
Cartilage	42.600	0.789	4.460	38.770	1.756	1.908	32.150	4.891	0.631
Cerebellum	49.350	1.270	3.025	44.800	2.101	1.715	39.980	4.995	0.684
CerebroSpinalFluid	68.610	2.419	1.914	66.240	3.458	1.272	60.470	7.840	0.537
Cervix	49.750	0.964	3.952	47.610	1.726	2.141	43.360	4.803	0.738
Colon	57.870	1.087	3.776	53.880	2.038	1.930	48.460	5.570	0.674
Cornea	55.170	1.401	2.896	51.620	2.295	1.683	46.530	5.664	0.650
Duodenum	65.020	1.193	3.643	62.160	2.211	1.909	56.480	6.314	0.641
Dura	44.390	0.966	3.741	42.030	1.669	2.084	37.880	4.309	0.770
EyeSclera	55.230	1.173	3.434	52.630	2.033	1.913	47.810	5.466	0.682
Fat	5.460	0.051	24.230	5.280	0.105	11.700	4.955	0.293	4.048
Gland	59.650	1.044	3.982	57.200	1.968	2.056	52.050	5.721	0.679
Heart	59.800	1.238	3.382	54.810	2.256	1.761	48.950	5.862	0.644
Kidney	58.560	1.401	2.975	52.740	2.429	1.609	46.750	5.896	0.627
Lens	46.550	0.798	4.601	44.630	1.504	2.376	40.690	4.370	0.785
Liver	46.760	0.861	4.282	43.030	1.686	2.086	38.130	4.642	0.718
LungDeflated	51.370	0.864	4.463	48.380	1.683	2.212	43.750	4.821	0.739
LungInflated	21.970	0.459	5.527	20.480	0.804	3.018	18.510	2.077	1.116
Lymph	59.650	1.044	3.982	57.200	1.968	2.056	52.050	5.721	0.679
Muscle	55.000	0.948	4.210	52.730	1.739	2.233	48.480	4.962	0.754
Nail	12.440	0.145	12.980	11.380	0.394	4.578	9.674	1.154	1.454
Nerve	32.490	0.578	5.316	30.140	1.089	2.701	27.220	2.941	0.954
Ovary	50.360	1.298	2.988	44.700	2.264	1.594	38.690	5.284	0.638
Pancreas	59.650	1.044	3.982	57.200	1.968	2.056	52.050	5.721	0.679
Prostate	60.510	1.216	3.459	57.550	2.168	1.875	52.210	5.948	0.655
Retina	55.230	1.173	3.434	52.630	2.033	1.913	47.810	5.466	0.682
SkinDry	41.330	0.872	3.995	38.010	1.464	2.257	35.110	3.717	0.857
SkinWet	46.020	0.850	4.303	42.850	1.592	2.203	38.620	4.342	0.771
SpinalChord	32.490	0.578	5.316	30.140	1.089	2.701	27.220	2.941	0.954
Spleen	57.090	1.280	3.205	52.450	2.238	1.738	46.940	5.672	0.652
Stomach	65.020	1.193	3.643	62.160	2.211	1.909	56.480	6.314	0.641
Tendon	45.800	0.724	5.017	43.120	1.685	2.090	36.750	5.255	0.627
Thymus	59.650	1.044	3.982	57.200	1.968	2.056	52.050	5.721	0.679
Thyroid	59.650	1.044	3.982	57.200	1.968	2.056	52.050	5.721	0.679
Tongue	55.230	0.942	4.245	52.630	1.803	2.153	47.810	5.235	0.711
Tooth	12.440	0.145	12.980	11.380	0.394	4.578	9.674	1.154	1.454
Trachea	41.970	0.776	4.504	39.730	1.449	2.330	35.940	4.080	0.792
Uterus	61.060	1.276	3.315	57.810	2.247	1.815	52.350	6.047	0.645

Annex C. CST Simulations

This annex includes the gain patterns of a patch antenna [MeCa06] operating in the 2.45 GHz band, which was simulated in CST, with different distances to the voxel body model. Simulations were performed for 4 antenna placements, *i.e.*, Head, Chest, Arm and Leg, and the distance from the body surface in range $[0, 2\lambda]$, Figure C.1.

(a) Head

(b) Chest

(c) Arm

(d) Leg
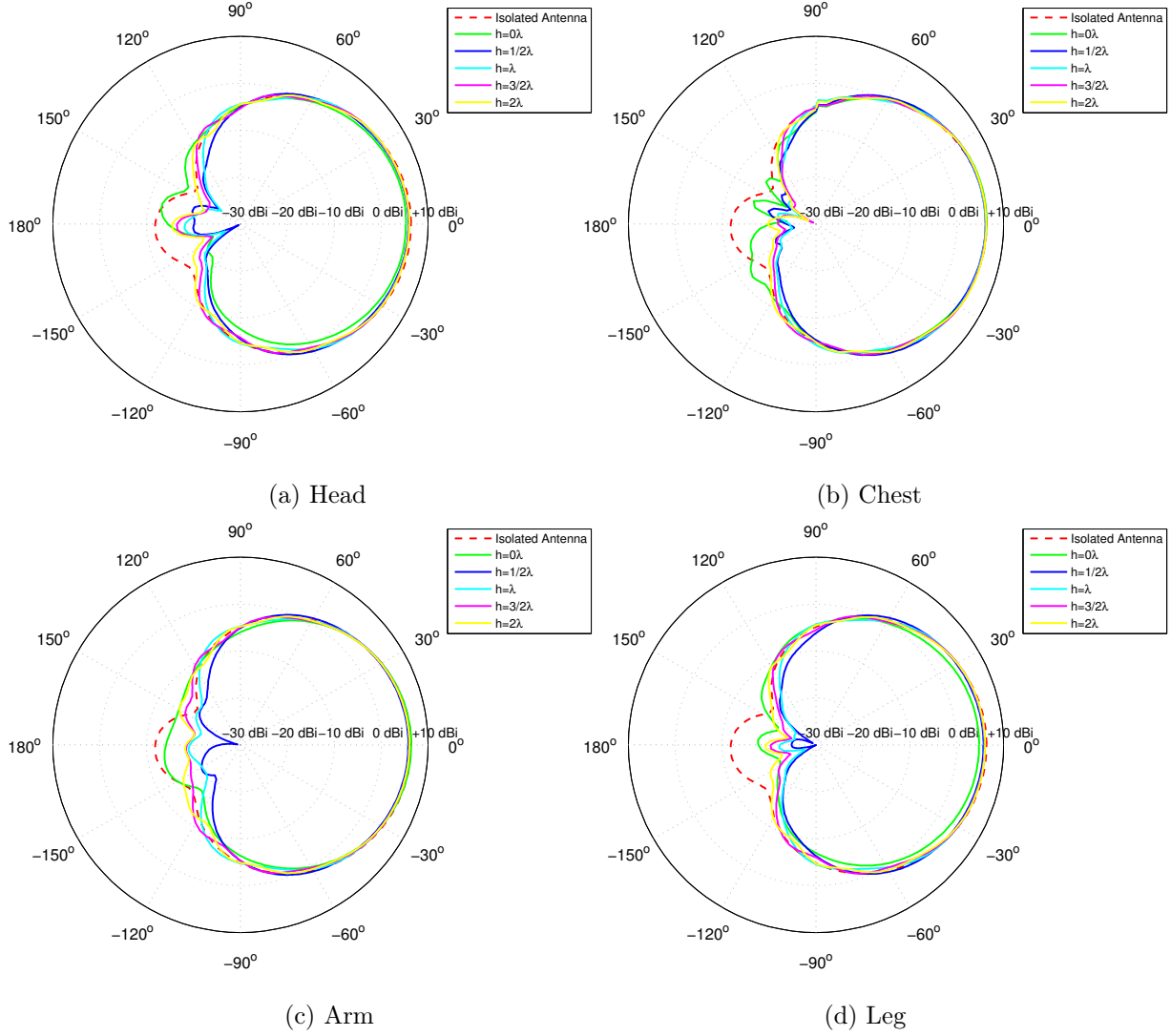
Figure C.1. The gain patterns of a patch antenna near the body with distance in $[0, 2\lambda]$.

The statistics of the gain patterns of a patch antenna, for the Uniform distance Distribution, in $[0, 2\lambda]$), are presented in Figure C.2.
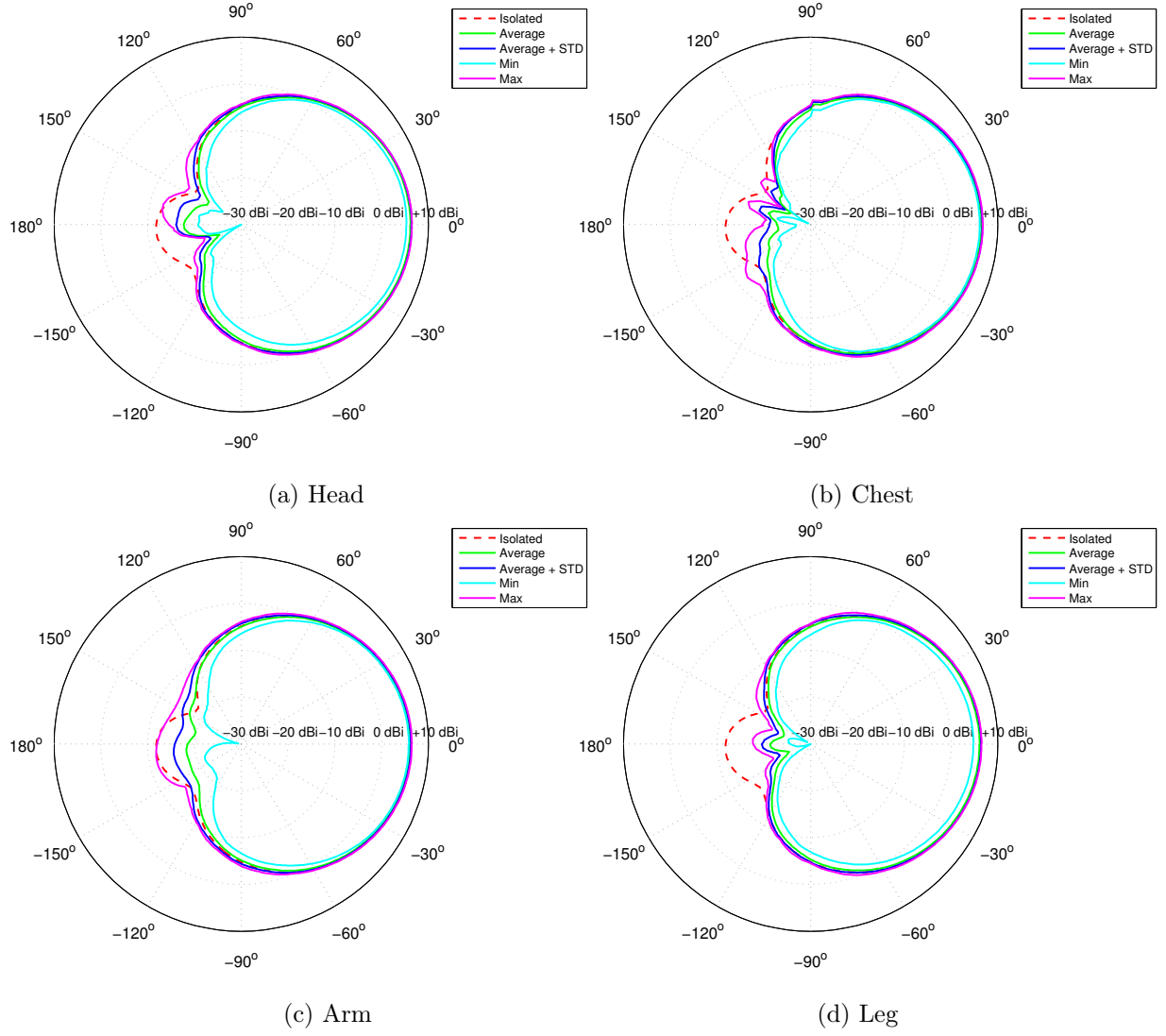

(a) Head

(b) Chest

(c) Arm

(d) Leg

Figure C.2. The statistics of the gain patterns of a patch antenna, for the Uniform distance Distribution.

The statistics of the gain patterns of a patch antenna, for the Rayleigh distance Distribution, with a mode of 2 cm, are presented in Figure C.3.
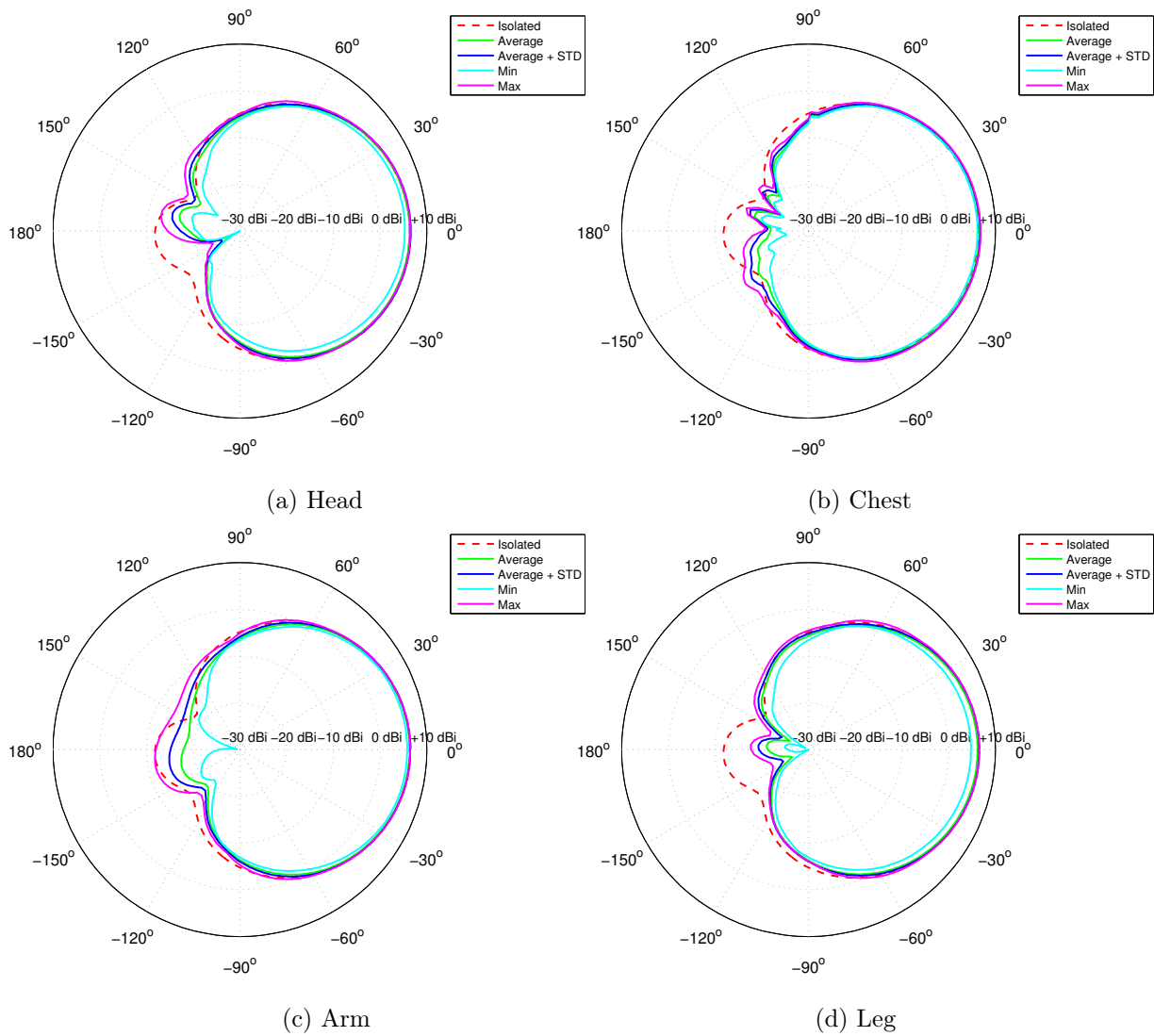

(a) Head

(b) Chest

(c) Arm

(d) Leg

Figure C.3. The statistics of the gain patterns of a patch antenna, for the Rayleigh distance Distribution.

The statistics of the gain patterns of a patch antenna, located near the body relative to the isolated case, are shown in Figure C.4.
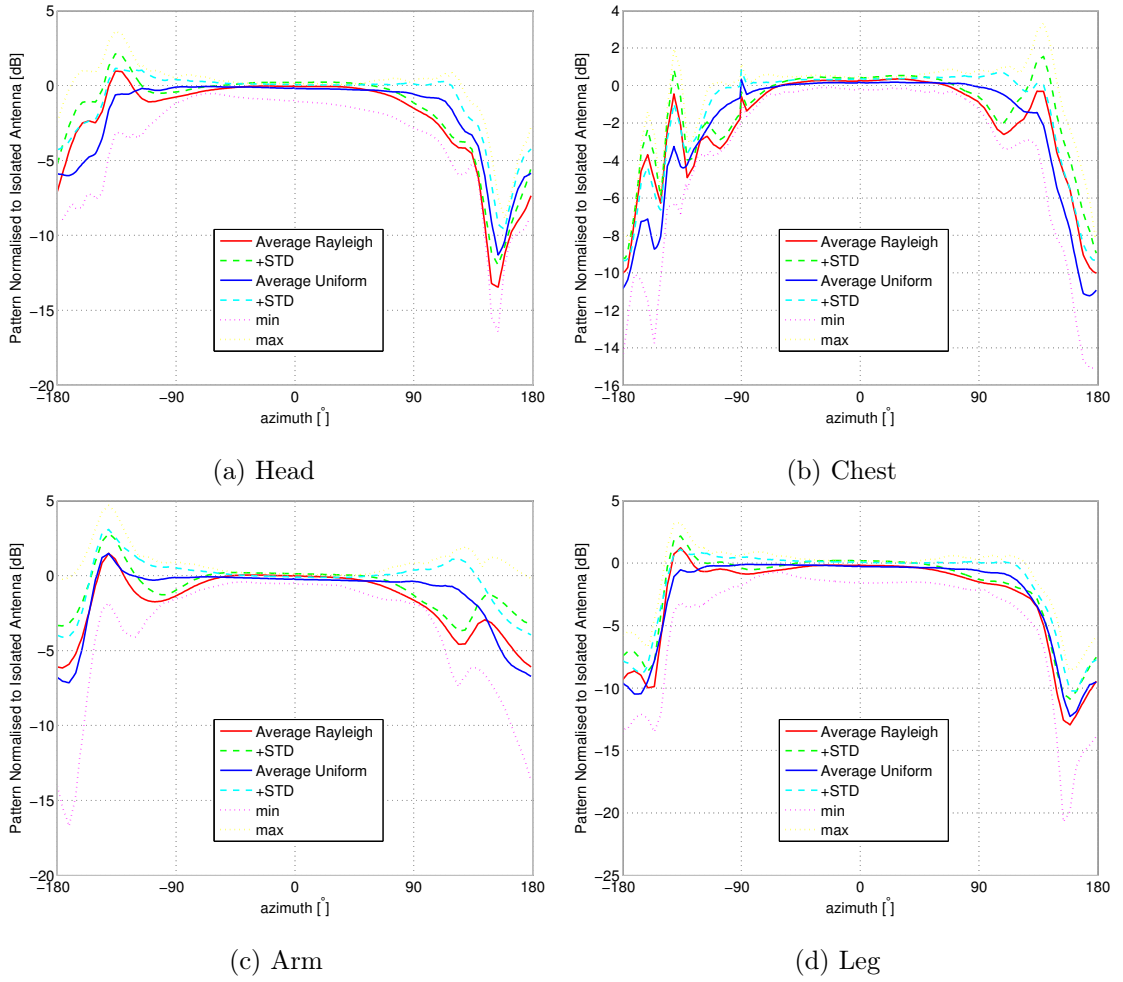

(a) Head

(b) Chest

(c) Arm

(d) Leg

Figure C.4. The statistics of the gain patterns of a patch antenna, located near the body relative to the isolated case.

Annex D. Body Dynamics

This annex includes the gain patterns of a patch antenna, [MCCF07], operating at 2.45 GHz, which is located on the walking or running body.

The statistics of the gain patterns (presented in the body coordinates), for the walking body, and for the Head, Chest, Arm and Leg placements, are presented in Figure D.1.
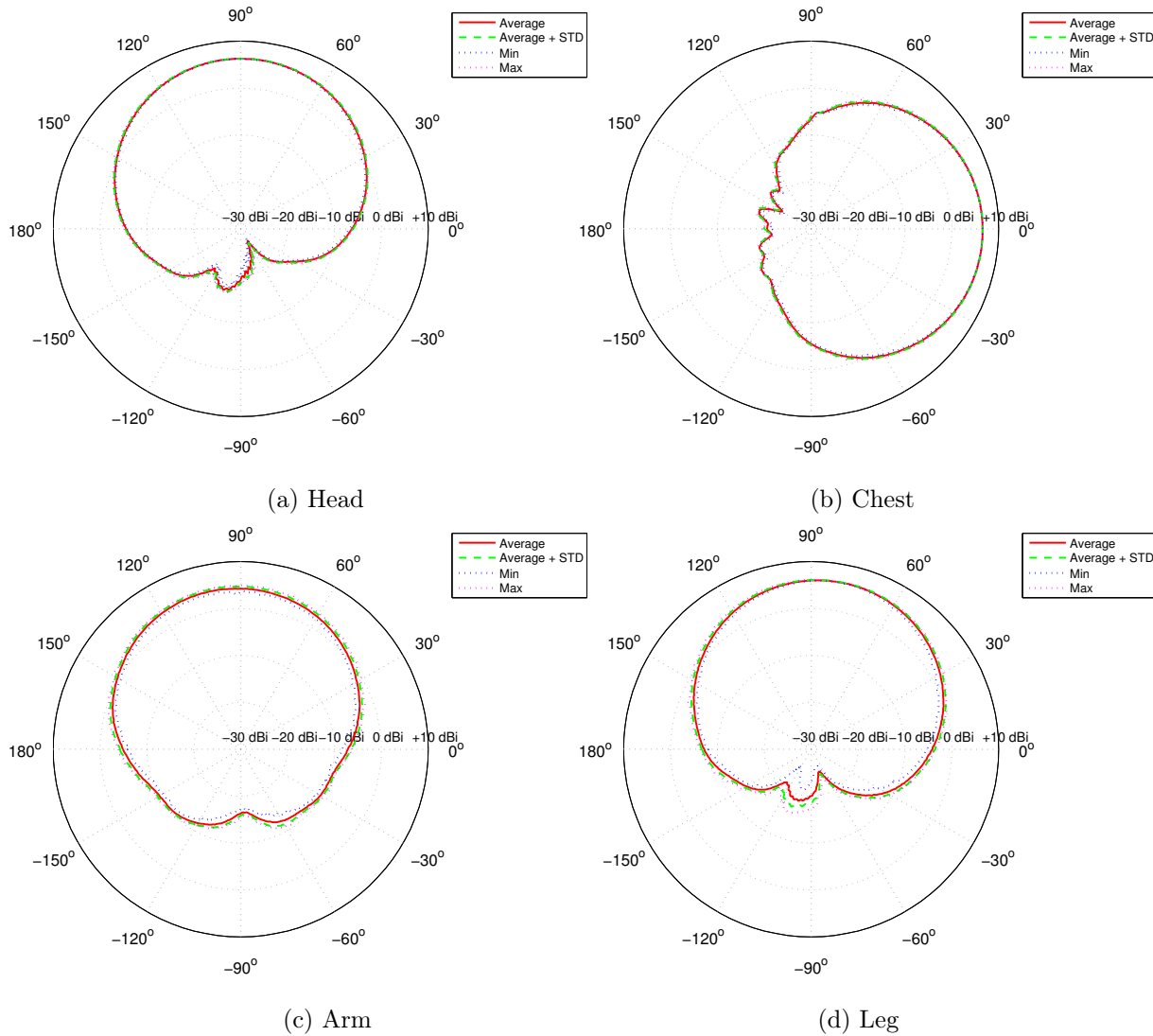

(a) Head

(b) Chest

(c) Arm

(d) Leg

Figure D.1. The statistics of the gain patterns, for the walking body.

The statistics of the gain patterns (presented in the body coordinates), for the running body, and for the Head, Chest, Arm and Leg placements, are presented in Figure D.2.
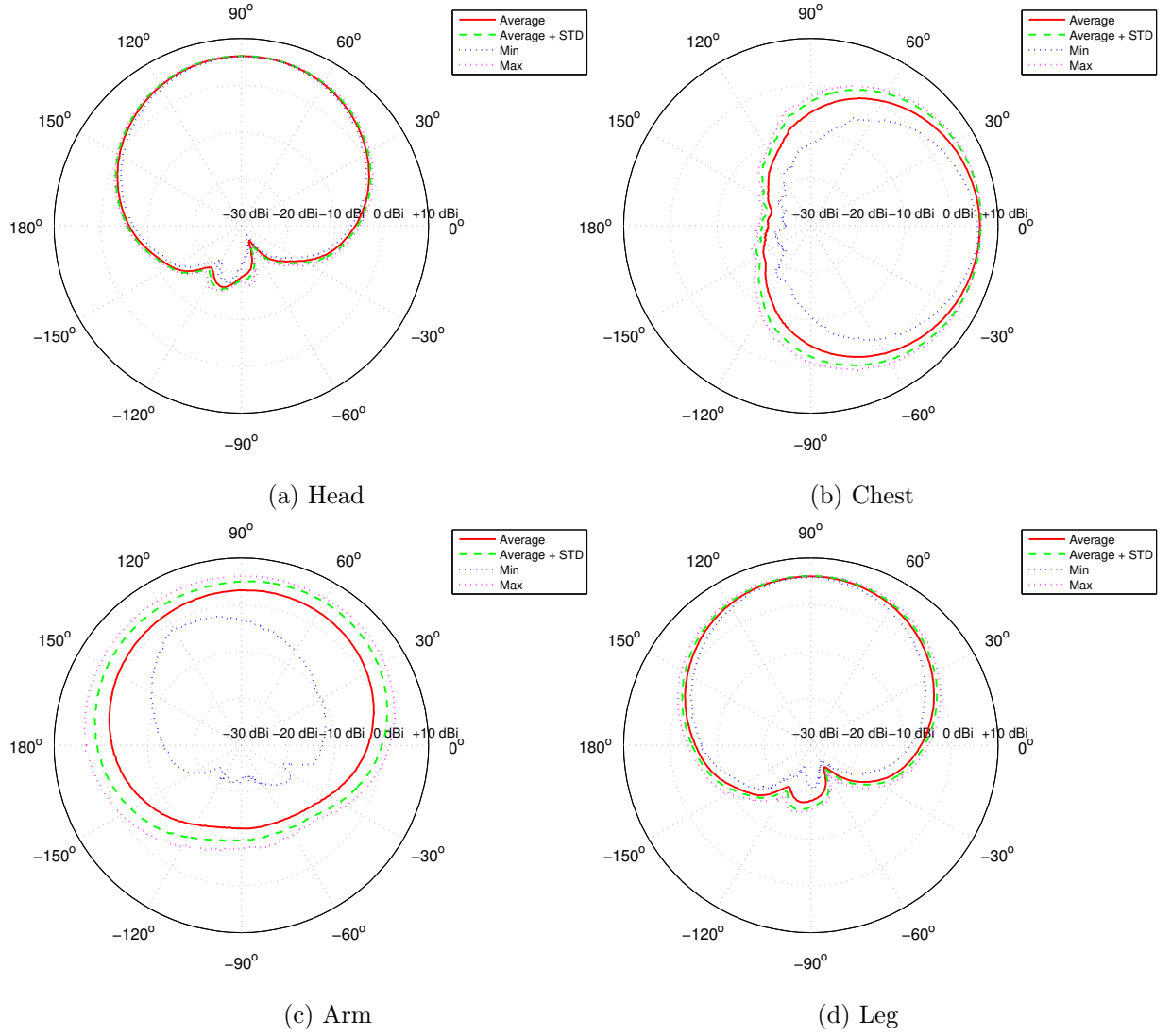

(a) Head

(b) Chest

(c) Arm

(d) Leg

Figure D.2. The statistics of the gain patterns, for the running body.

Fitting of the normal direction to the body surface (in the azimuth plane), for the walking body, is presented in Figure D.3.
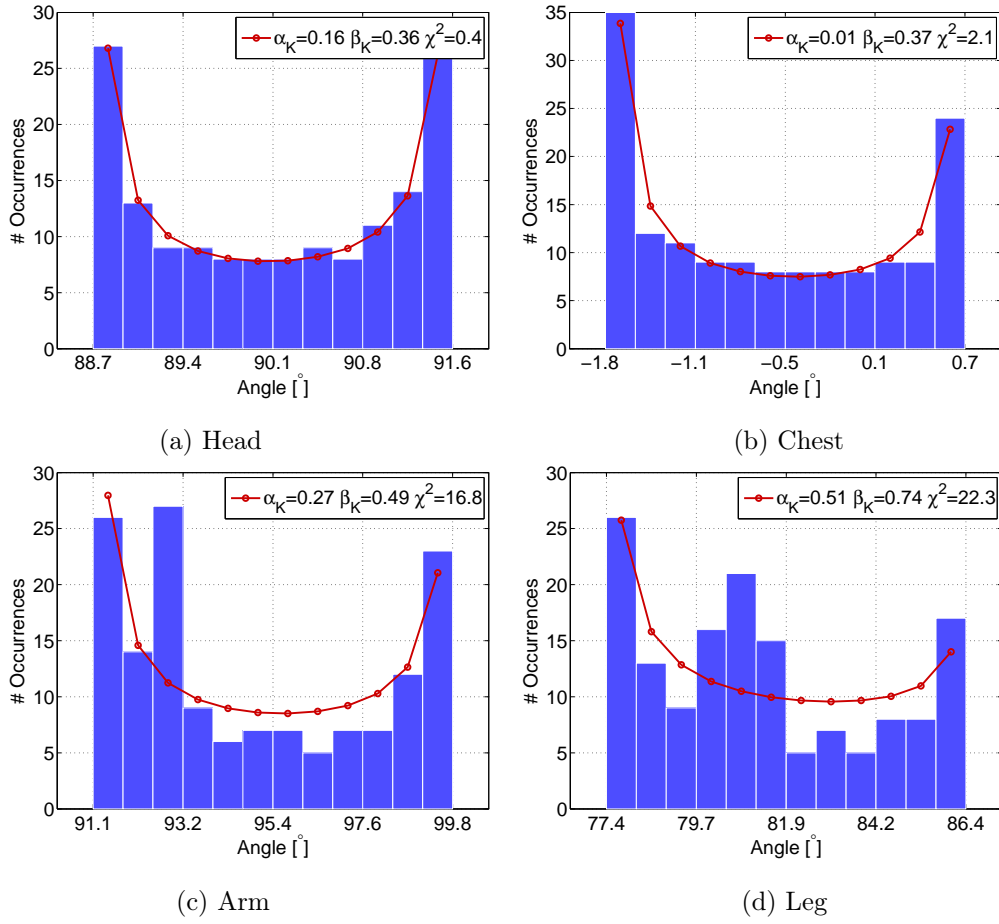

(a) Head

(b) Chest

(c) Arm

(d) Leg

Figure D.3. Fitting of the normal direction to the body surface (in the azimuth plane), for the walking body.

Fitting of the normal direction to the body surface (in the elevation plane), for the walking body, is presented in Figure D.4.

(a) Head

(b) Chest

(c) Arm

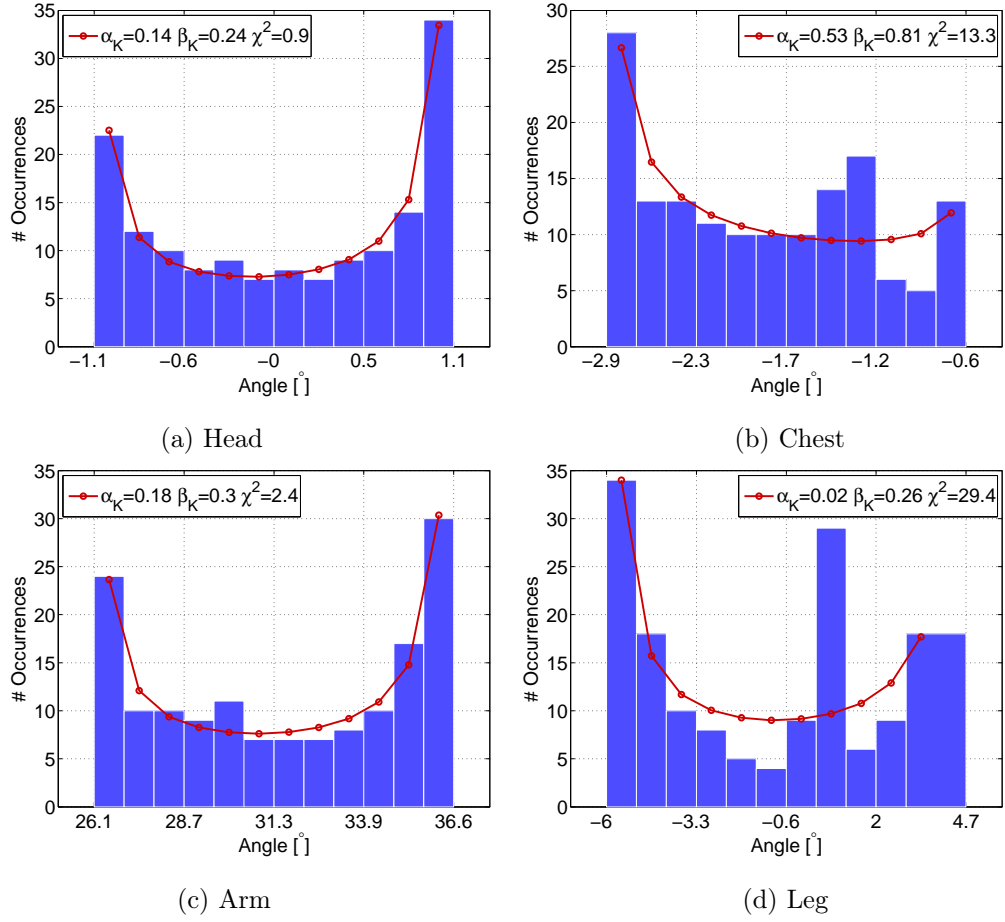(d) Leg

Figure D.4. Fitting of the normal direction to the body surface (in the elevation plane), for the walking body.

Fitting of the normal direction to the body surface (in the azimuth plane), for the running body, is presented in Figure D.5.

(a) Head

(b) Chest

(c) Arm

(d) Leg
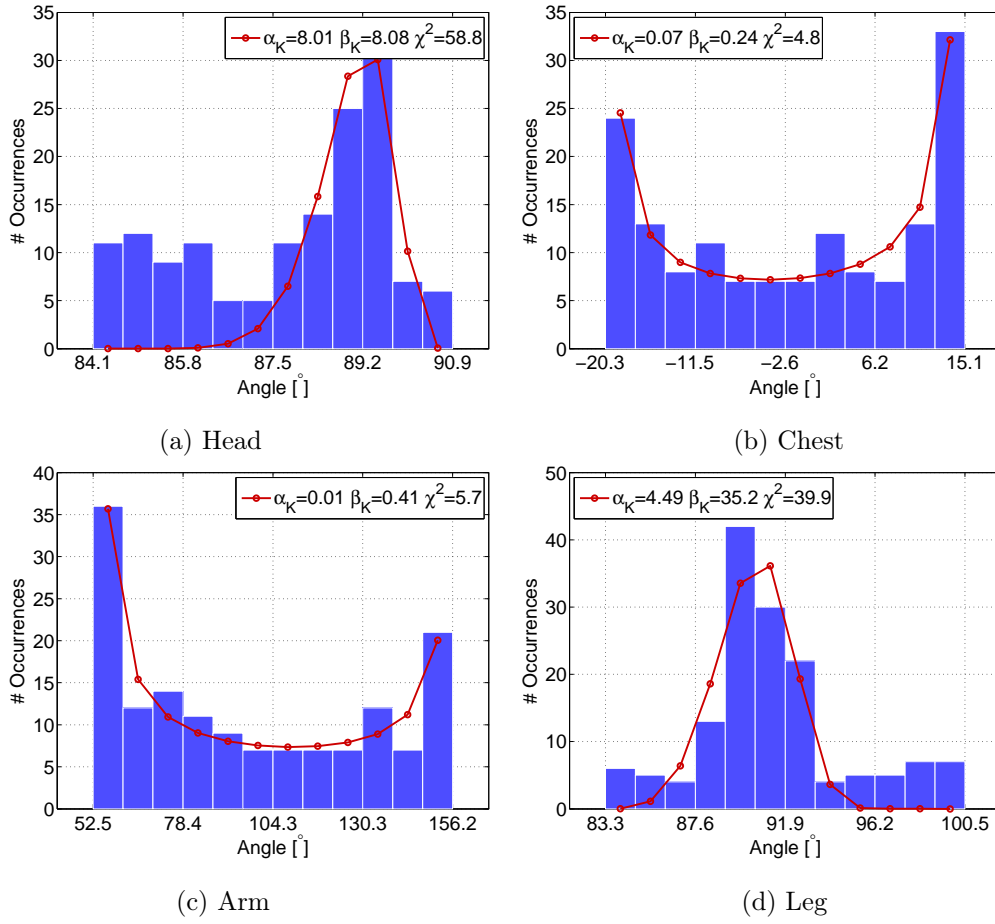
Figure D.5. Fitting of the normal direction to the body surface (in the azimuth plane), for the running body.

Fitting of the normal direction to the body surface (in the elevation plane), for the running body, is presented in Figure D.6.
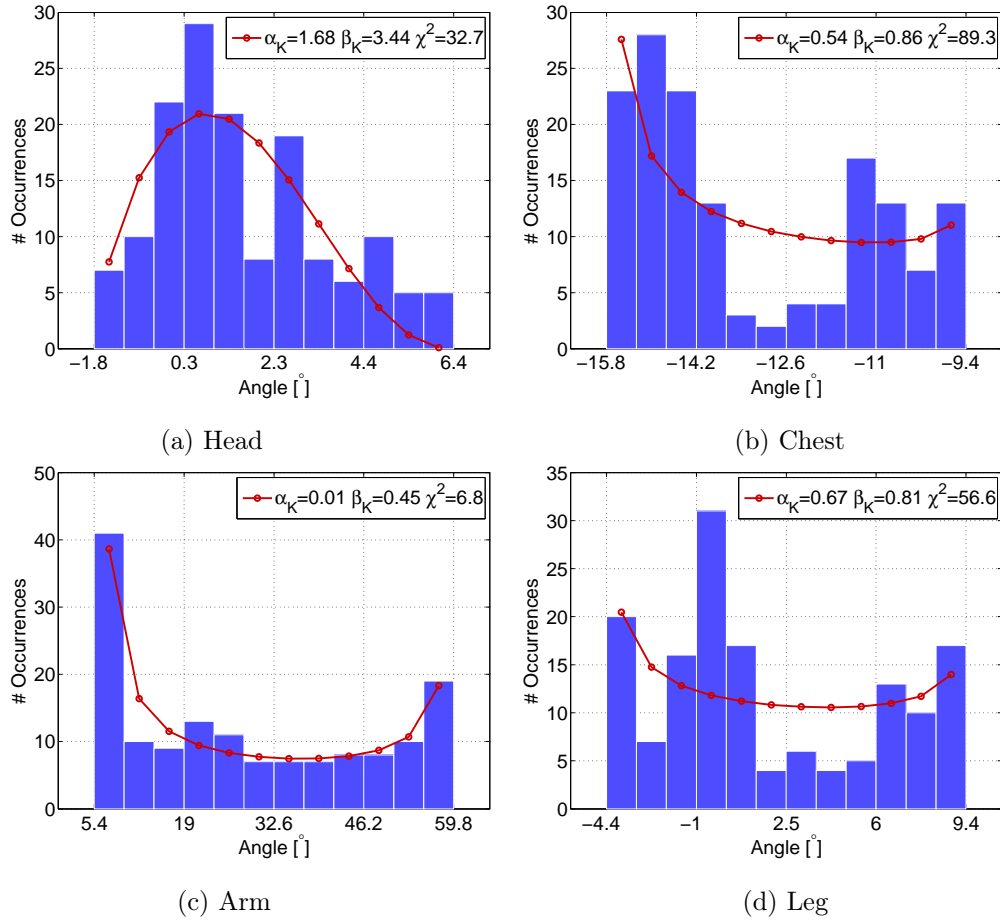

(a) Head

(b) Chest

(c) Arm

(d) Leg

Figure D.6. Fitting of the normal direction to the body surface (in the elevation plane), for the running body.

The average and standard deviation of the gain pattern, in both planes (in the antenna coordinates, where $\varphi=0$ and $\psi=0$ corresponds to the direction of maximum radiation), for the walking and running scenarios, are compared with the static one in Figure D.7, Figure D.8, Figure D.9 and Figure D.10.

(a) static body

(b) average for the walking body

(c) standard deviation for the walking body

(d) average for the running body

(e) standard deviation for the running body
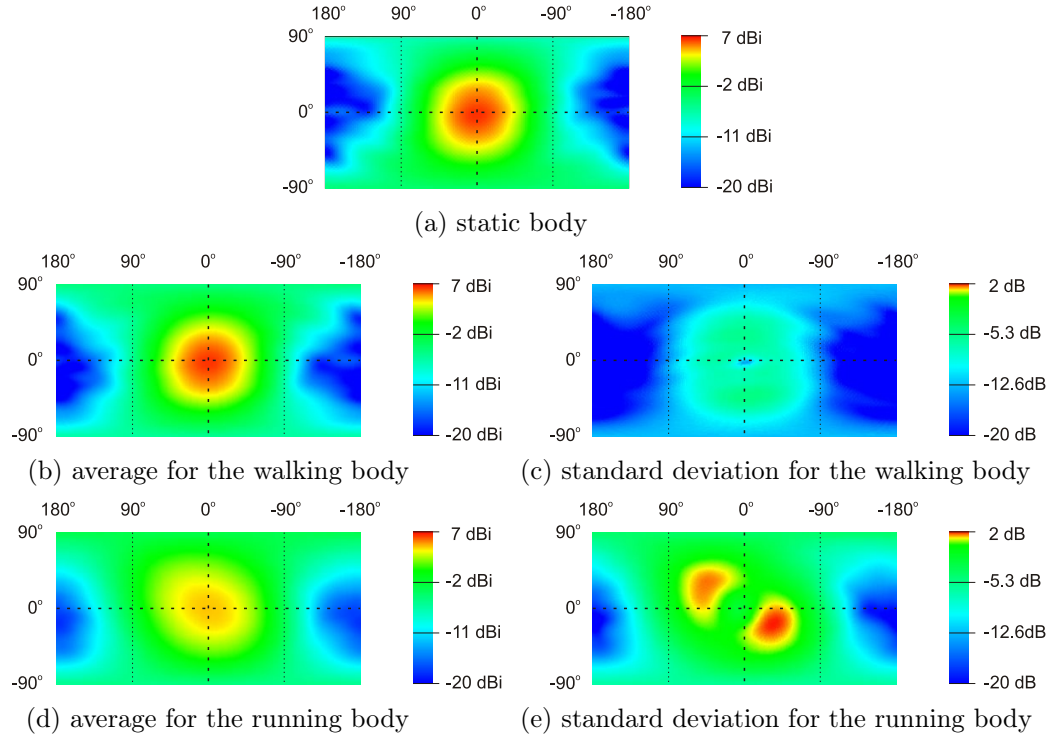
Figure D.7. The average and standard deviation of the gain pattern for the Arm placement.

(a) static body

(b) average for the walking body

(c) standard deviation for the walking body

(d) average for the running body

(e) standard deviation for the running body
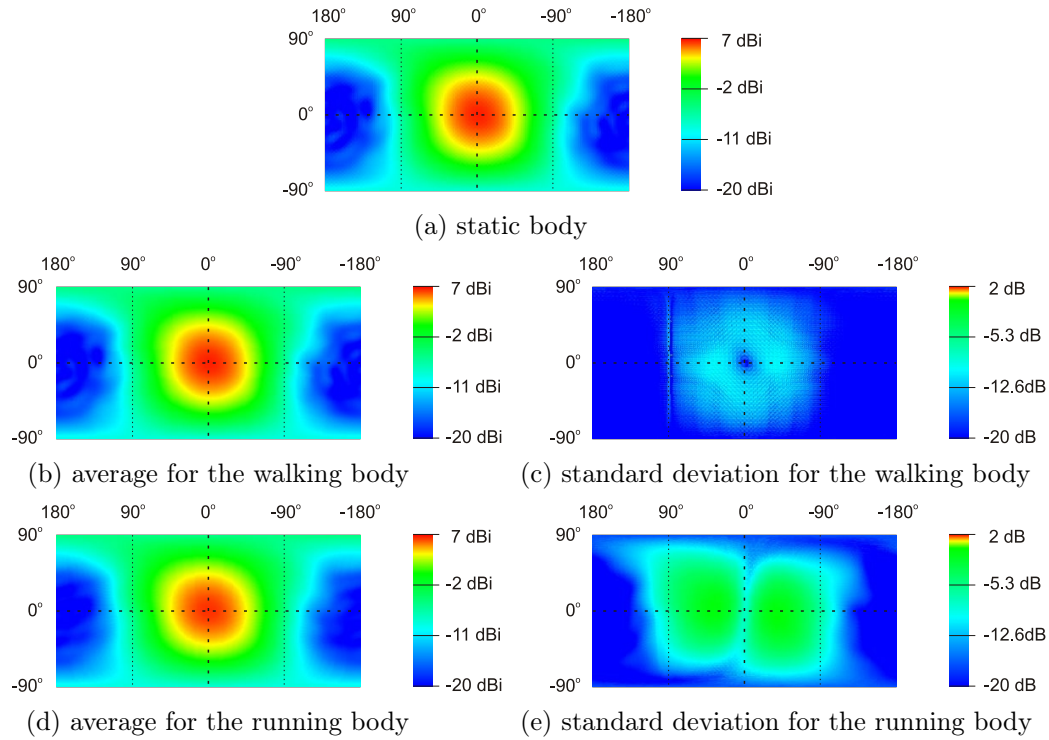
Figure D.8. The average and standard deviation of the gain pattern for the Chest placement.

(a) static body

(b) average for the walking body

(c) standard deviation for the walking body

(d) average for the running body

(e) standard deviation for the running body
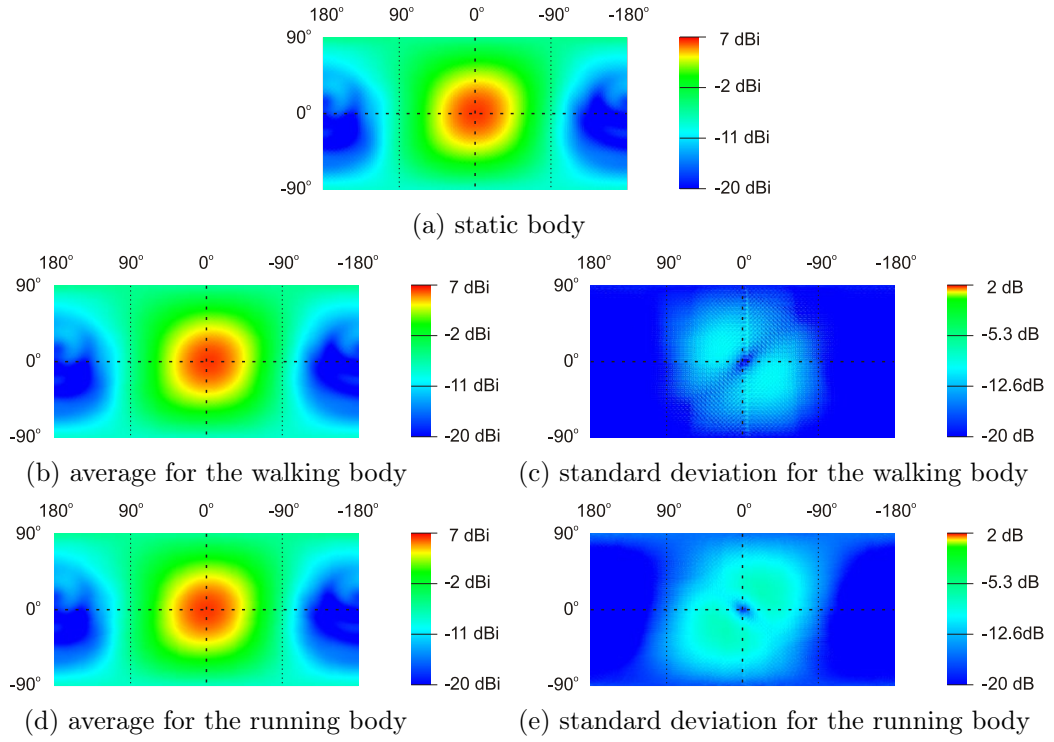
Figure D.9. The average and standard deviation of the gain pattern for the Head placement.

(a) static body

(b) average for the walking body

(c) standard deviation for the walking body

(d) average for the running body

(e) standard deviation for the running body

Figure D.10. The average and standard deviation of the gain pattern for the Leg placement.

Annex E. Radio Channel Parameters
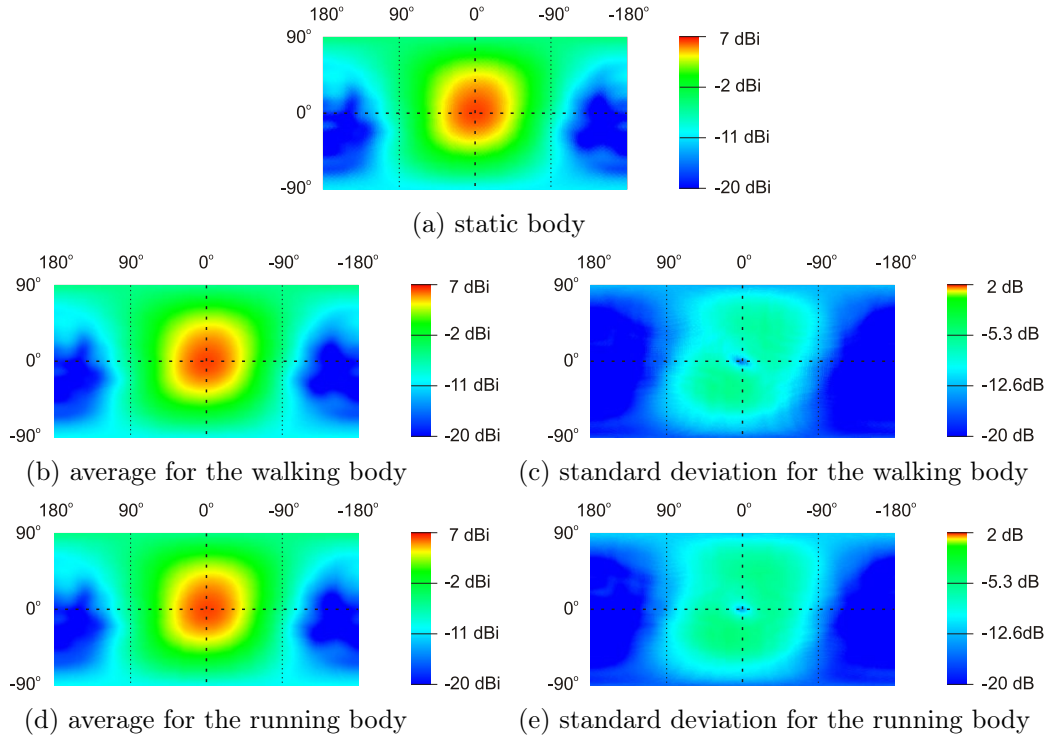
The average and the standard deviation of the received power for the running body, are presented in Figure E.1.

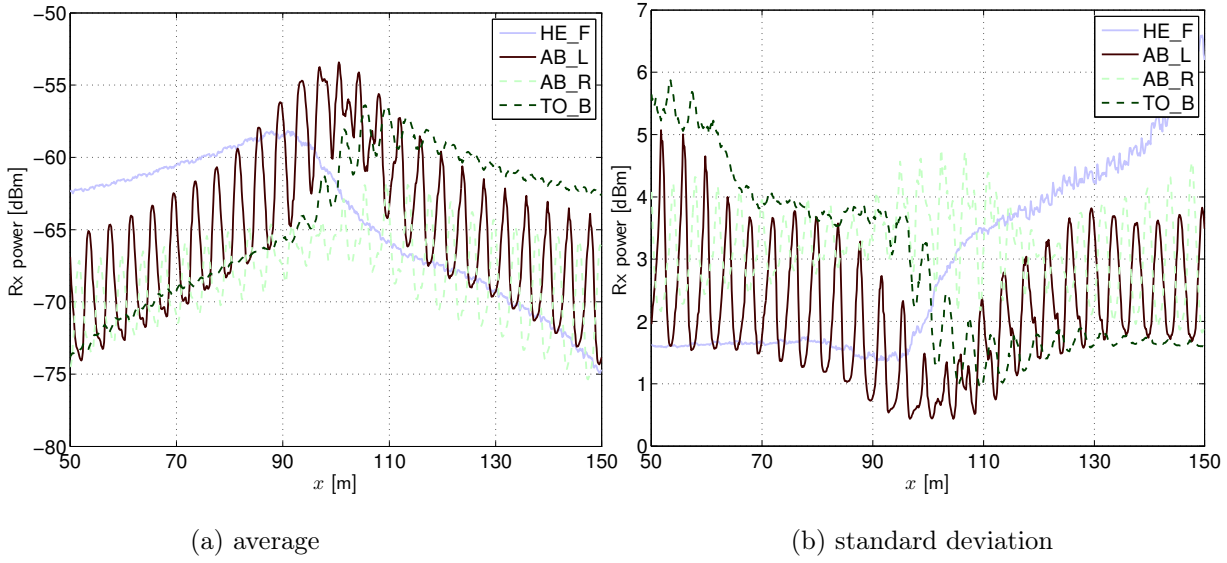(a) average   (b) standard deviation

Figure E.1. Received power for the running body.

The statistics of the received power for the running body, calculated for selected paths, are presented in Table E.1.

Table E.1. Received power for the running body, calculated for selected paths.

	x [m]	propagation	$\overline{P_R}$	$\sigma_{\overline{P_R}}$	$\overline{\sigma_{P_R}}$
			[dBm]	[dB]	
HE_F	[50, 150]	Mix	-64.4	4.8	3.3
	[50, 85]	LoS	-60.7	1.1	1.6
	[85, 115]	NLoS	-62.1	3.2	2.5
	[115, 150]	NLoS	-70.1	2.2	4.7
AB_L	[50, 150]	Mix	-64.8	5.2	2.4
	[50, 85]	Mix	-67.4	3.7	2.7
	[85, 115]	Mix	-59.1	3.5	1.5
	[115, 150]	Mix	-67.0	3.7	2.6
AB_R	[50, 150]	NLoS	-68.3	2.9	3.3
	[50, 85]	NLoS	-69.3	2.2	3.2
	[85, 115]	NLoS	-66.1	1.7	3.6
	[115, 150]	NLoS	-69.2	3.2	3.0
TO_B	[50, 150]	Mix	-64.2	4.8	3.2
	[50, 85]	NLoS	-69.8	2.0	4.5
	[85, 115]	Mix	-61.7	3.4	2.7
	[115, 150]	LoS	-60.8	1.2	1.7

The average and the standard deviation of the received power for the walking body, are presented in Figure E.2.
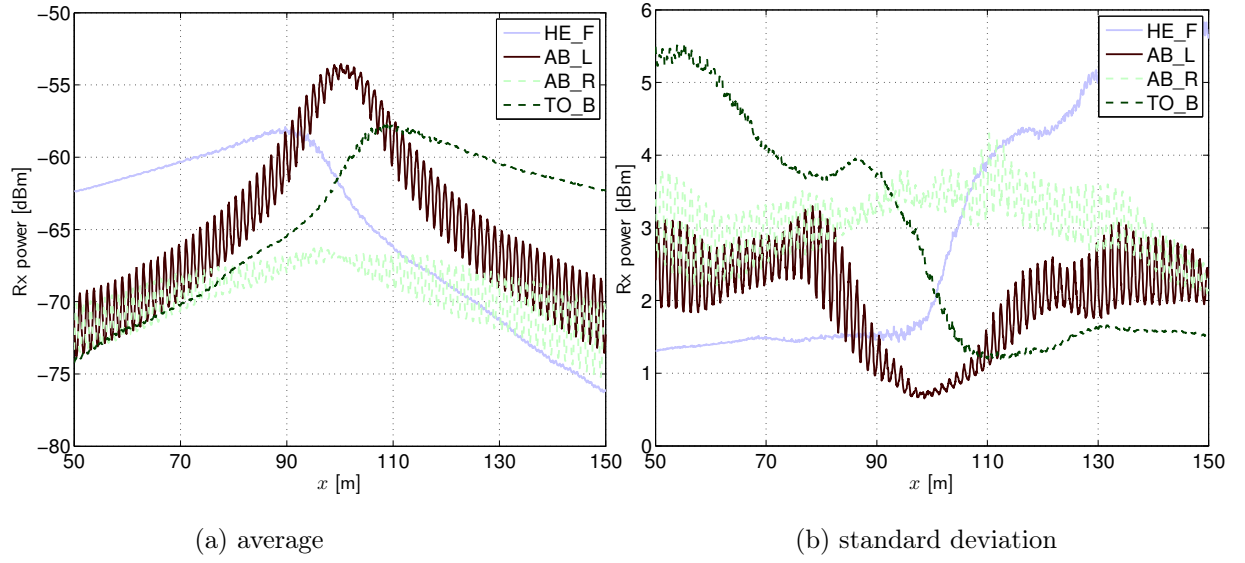

(a) average

(b) standard deviation

Figure E.2. Received power for the walking body.

The statistics of the received power for the walking body, calculated for selected paths, are presented in Table E.2.

Table E.2. Received power for the walking body, calculated for selected paths.

	x [m]	propagation	$\overline{P_R}$	$\sigma_{\overline{P_R}}$	$\overline{\sigma_{P_R}}$
			[dBm]	[dB]	
HE_F	[50, 150]	Mix	-65.0	5.7	3.4
	[50, 85]	LoS	-60.6	1.1	1.4
	[85, 115]	NLoS	-62.2	3.4	2.7
	[115, 150]	NLoS	-72.0	2.6	4.9
AB_L	[50, 150]	Mix	-64.7	5.5	2.1
	[50, 85]	NLoS	-68.3	2.9	2.5
	[85, 115]	Mix	-57.8	2.9	1.2
	[115, 150]	NLoS	-67.1	3.0	2.2
AB_R	[50, 150]	NLoS	-69.4	2.0	3.1
	[50, 85]	NLoS	-70.1	1.6	3.0
	[85, 115]	NLoS	-67.5	0.7	3.5
	[115, 150]	NLoS	-70.4	1.9	3.0
TO_B	[50, 150]	Mix	-64.3	5.0	3.2
	[50, 85]	NLoS	-70.5	2.1	4.5
	[85, 115]	Mix	-61.6	3.1	2.6
	[115, 150]	LoS	-60.6	1.1	1.5

The average and the standard deviation of the delay spread for the running body, are presented in Figure E.3.
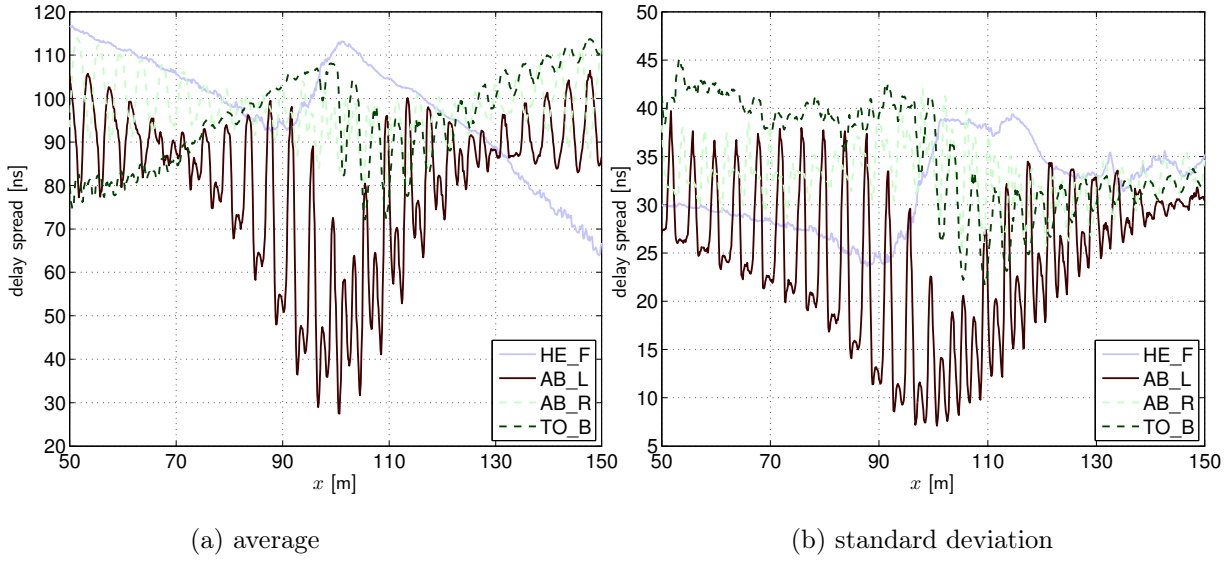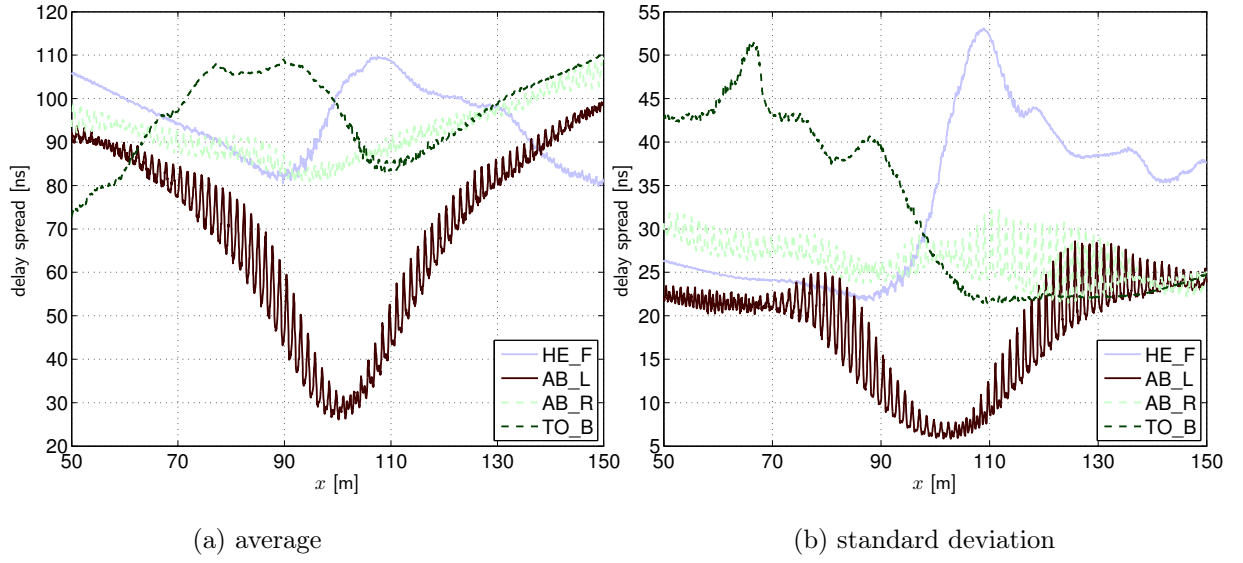
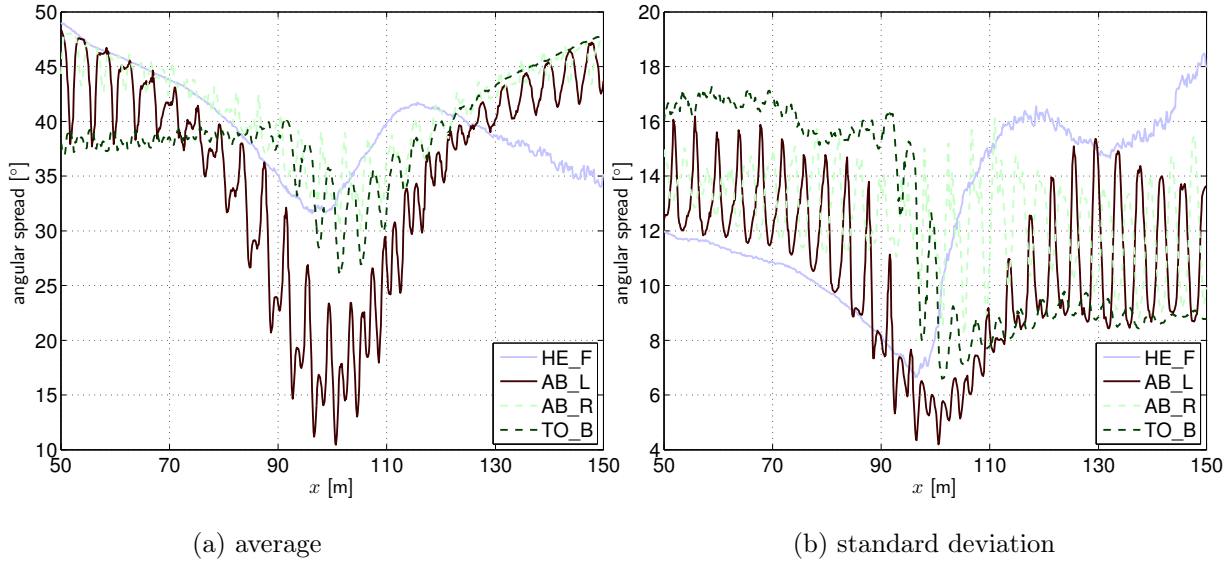

(a) average

(b) standard deviation

Figure E.3. Delay spread for the running body.

The statistics of the delay spread for the running body, calculated for selected paths, are presented in Table E.3.

Table E.3. Delay spread for the running body, calculated for selected paths.

	x [m]	propagation	$\overline{\sigma_\tau}$	$\sigma_{\overline{\sigma_\tau}}$	$\overline{\sigma_{\sigma_\tau}}$
			[ns]		
HE_F	[50, 150]	Mix	97.7	12.9	31.9
	[50, 85]	LoS	106.7	6.2	28.3
	[85, 115]	NLoS	102.9	6.6	33.3
	[115, 150]	NLoS	84.3	10.8	34.1
AB_L	[50, 150]	Mix	80.4	17.6	25.4
	[50, 85]	Mix	88.1	9.0	27.6
	[85, 115]	Mix	61.3	18.7	18.1
	[115, 150]	Mix	88.9	7.8	28.3
AB_R	[50, 150]	NLoS	97.7	6.6	33.1
	[50, 85]	NLoS	100.6	6.0	33.2
	[85, 115]	NLoS	93.4	6.0	34.5
	[115, 150]	NLoS	98.4	5.7	31.7
TO_B	[50, 150]	Mix	95.0	10.5	35.6
	[50, 85]	NLoS	86.7	6.7	40.3
	[85, 115]	Mix	96.3	10.3	34.6
	[115, 150]	LoS	102.2	7.8	31.0

The average and the standard deviation of the delay spread for the walking body, are presented in Figure E.4.

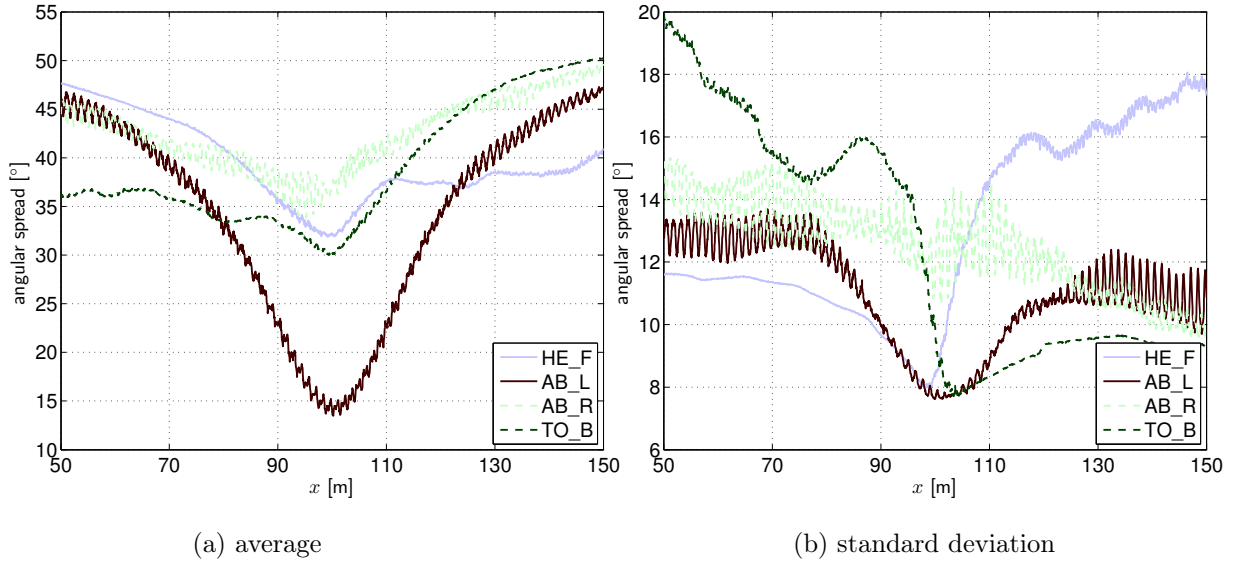

(a) average

(b) standard deviation

Figure E.4. Delay spread for the walking body.

The statistics of the delay spread for the walking body, calculated for selected paths, are presented in Table E.4.

Table E.4. Delay spread for the walking body, calculated for selected paths.

	x [m]	propagation	$\overline{\sigma_\tau}$	$\sigma_{\overline{\sigma_\tau}}$	$\overline{\sigma_{\sigma_\tau}}$
			[ns]		
HE_F	[50, 150]	Mix	95.0	8.4	34.1
	[50, 85]	LoS	95.6	6.1	24.3
	[85, 115]	NLoS	96.8	10.7	37.8
	[115, 150]	NLoS	92.7	7.6	38.9
AB_L	[50, 150]	Mix	69.7	21.0	19.1
	[50, 85]	NLoS	80.5	9.1	21.2
	[85, 115]	Mix	42.0	11.0	10.3
	[115, 150]	NLoS	82.6	11.2	22.3
AB_R	[50, 150]	NLoS	92.3	6.4	26.2
	[50, 85]	NLoS	91.1	3.2	27.9
	[85, 115]	NLoS	85.9	2.9	26.2
	[115, 150]	NLoS	98.8	4.6	24.5
TO_B	[50, 150]	Mix	96.6	9.8	33.3
	[50, 85]	NLoS	93.6	11.4	43.4
	[85, 115]	Mix	96.6	9.5	30.0
	[115, 150]	LoS	99.6	6.8	22.7

The average and the standard deviation of the DoA spread for the running body, are presented in Figure E.5.

(a) average

(b) standard deviation

Figure E.5. DoA spread for the running body.

The statistics of the DoA spread for the Run scenario, calculated for selected paths, are presented in Table E.5.

Table E.5. DoA spread for the running body, calculated for selected paths.

	x [m]	propagation	$\overline{\sigma_{DoA}}$	$\sigma_{\overline{\sigma_{DoA}}}$	$\overline{\sigma_{\sigma_{DoA}}}$
			[°]		
HE_F	[50, 150]	Mix	39.5	4.4	13.0
	[50, 85]	LoS	44.0	2.9	10.9
	[85, 115]	NLoS	35.8	3.1	11.2
	[115, 150]	NLoS	38.2	2.2	16.0
AB_L	[50, 150]	Mix	35.4	9.6	10.9
	[50, 85]	Mix	40.7	4.6	12.9
	[85, 115]	Mix	22.8	6.2	7.6
	[115, 150]	Mix	40.9	3.8	11.2
AB_R	[50, 150]	NLoS	41.2	4.3	12.6
	[50, 85]	NLoS	43.8	2.3	13.4
	[85, 115]	NLoS	35.9	2.5	12.4
	[115, 150]	NLoS	43.1	2.7	12.0
TO_B	[50, 150]	Mix	39.0	4.5	12.7
	[50, 85]	NLoS	38.4	0.5	16.3
	[85, 115]	Mix	34.7	3.7	11.6
	[115, 150]	LoS	43.4	3.1	9.0

The average and the standard deviation of the DoA spread for the walking body are presented in Figure E.6.

(a) average

(b) standard deviation

Figure E.6. DoA spread for the walking body.

The statistics of the DoA spread for the walking body, calculated for selected paths, are presented in Table E.6.

Table E.6. DoA spread for the walking body, calculated for selected paths.

	x [m]	propagation	$\overline{\sigma_{DoA}}$	$\sigma_{\overline{\sigma_{DoA}}}$	$\overline{\sigma_{\sigma_{DoA}}}$
			[°]		
HE_F	[50, 150]	Mix	39.4	4.1	13.4
	[50, 85]	LoS	44.1	2.5	11.3
	[85, 115]	NLoS	35.2	2.1	11.4
	[115, 150]	NLoS	38.2	0.9	16.5
AB_L	[50, 150]	Mix	34.1	10.3	11.1
	[50, 85]	NLoS	39.6	4.9	12.7
	[85, 115]	Mix	20.2	4.7	9.0
	[115, 150]	NLoS	40.6	4.9	10.9
AB_R	[50, 150]	NLoS	42.6	3.7	12.6
	[50, 85]	NLoS	42.0	2.0	14.0
	[85, 115]	NLoS	38.7	2.2	12.7
	[115, 150]	NLoS	46.5	1.8	11.0
TO_B	[50, 150]	Mix	38.9	6.3	13.0
	[50, 85]	NLoS	35.5	1.2	16.6
	[85, 115]	Mix	33.7	2.7	11.7
	[115, 150]	LoS	46.9	2.8	9.4

The statistics of the power imbalance, calculated between various links, for the general antenna classes are presented in Figure E.7.

(a) walking body

(b) running body
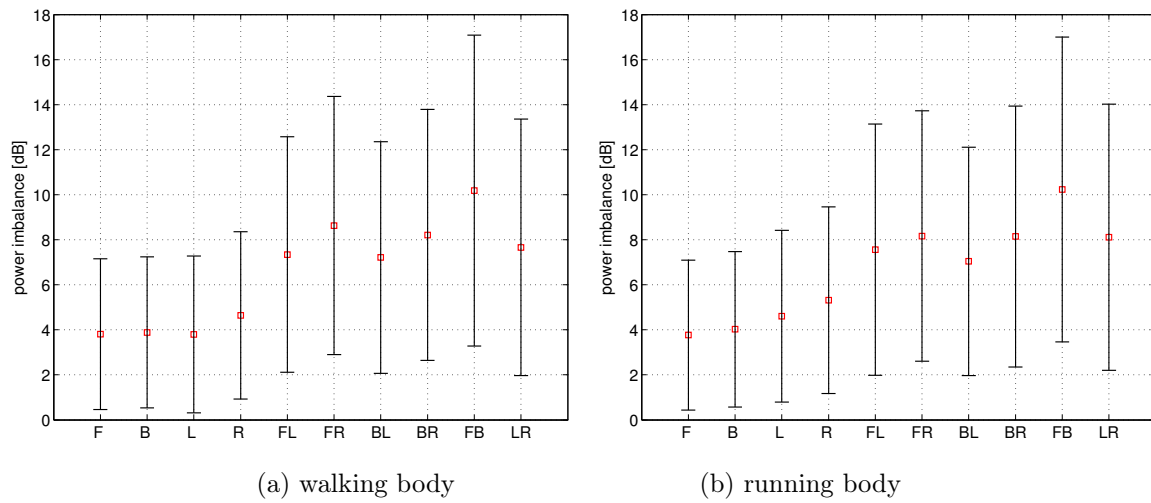
Figure E.7. The power imbalance calculated for the general antenna classes.

Annex F. MIMO Capacity

This annex, shows the average capacity, and the upper and lower bounds for capacity, for various pairs of antennas in 2×2 MIMO system, for walking or running bodies.
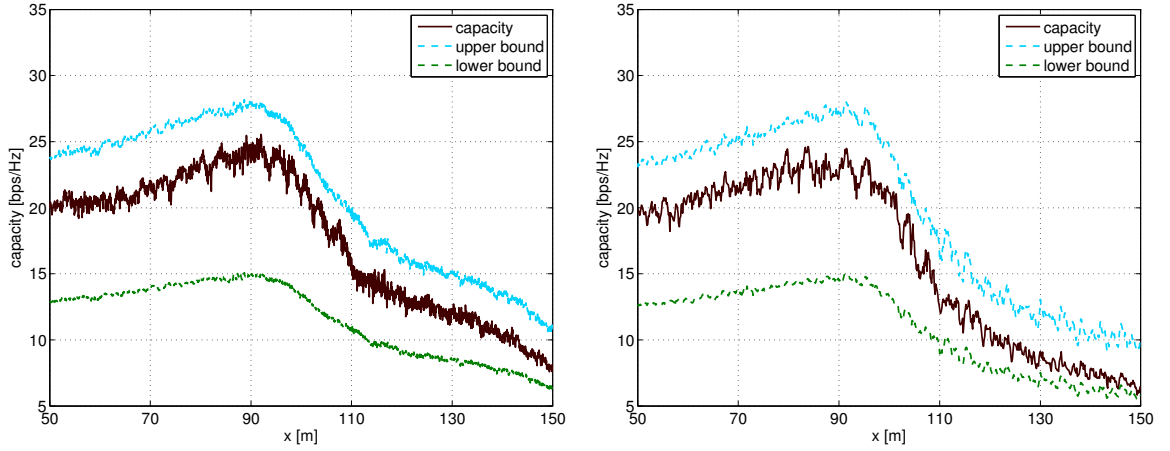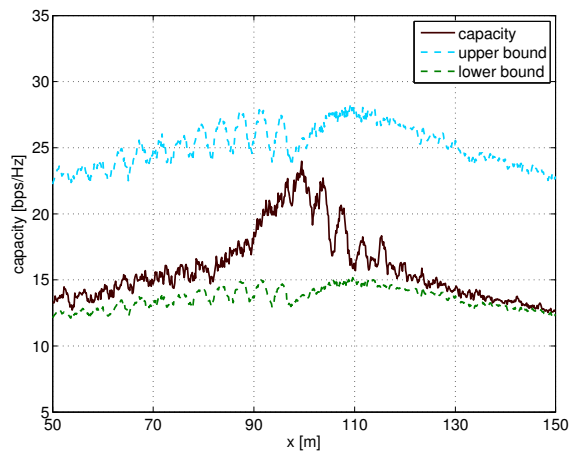

(a) walking body (b) running body

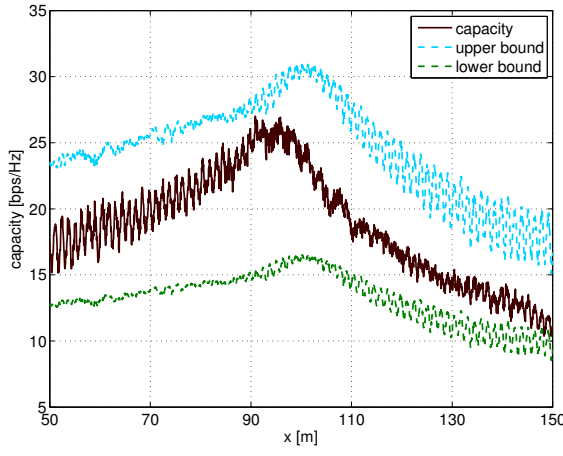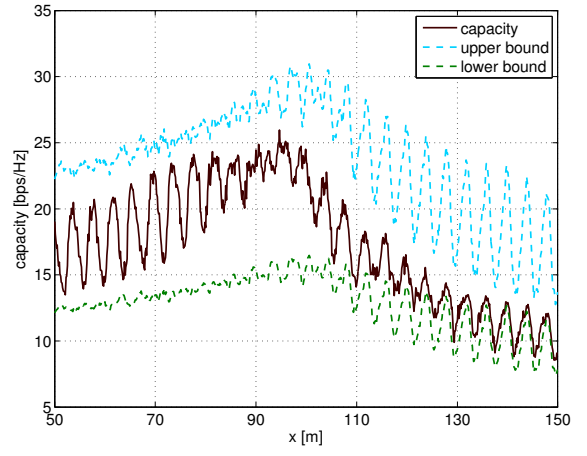Figure F.1. The MIMO capacity for the TO_F and WA_F antenna pair.
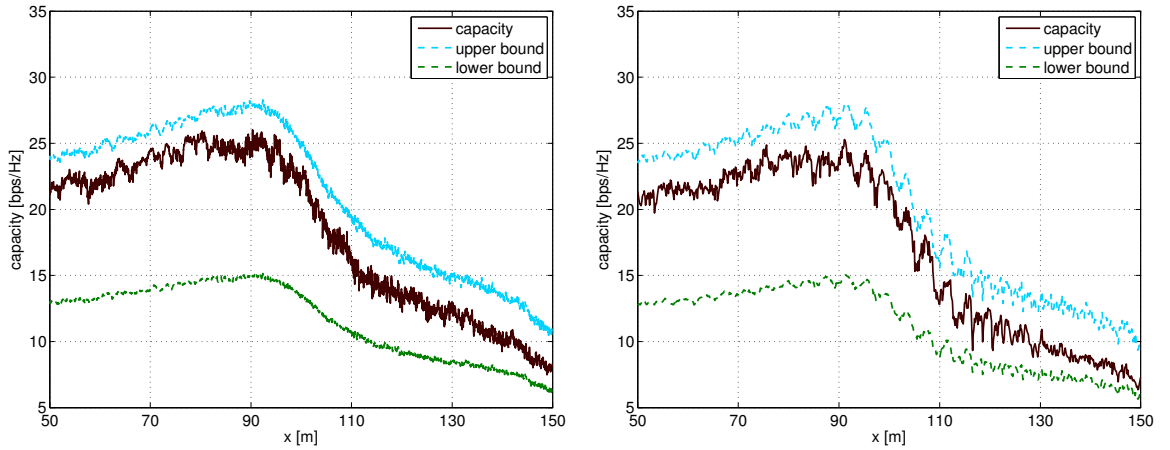
(a) walking body (b) running body

Figure F.2. The MIMO capacity for the TO_F and HE_F antenna pair.
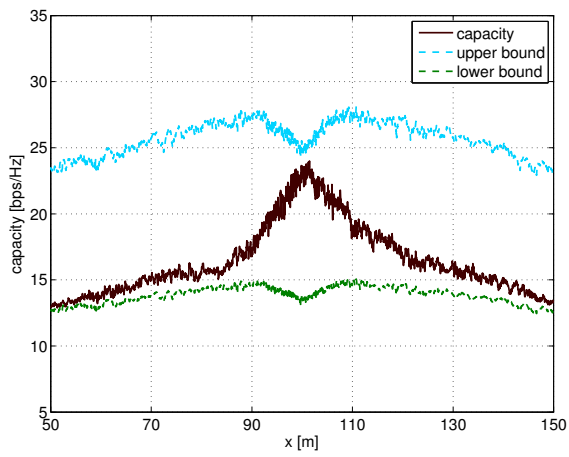
(a) walking body   (b) running body

Figure F.3. The MIMO capacity for the TO_F and HE_B antenna pair.
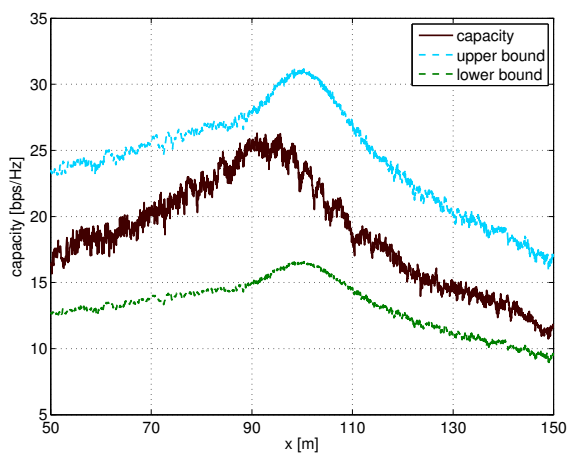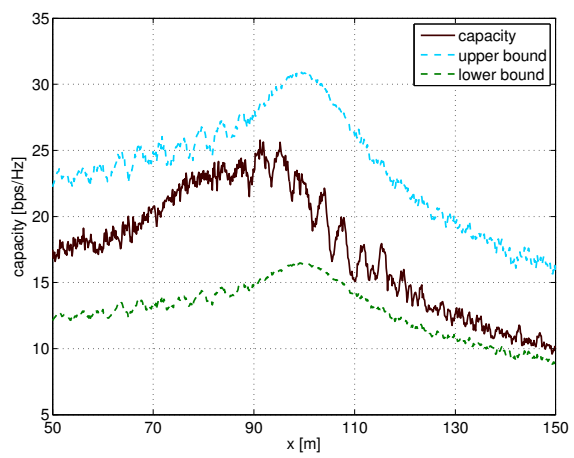
(a) walking body   (b) running body

Figure F.4. The MIMO capacity for the TO_F and HE_L antenna pair.
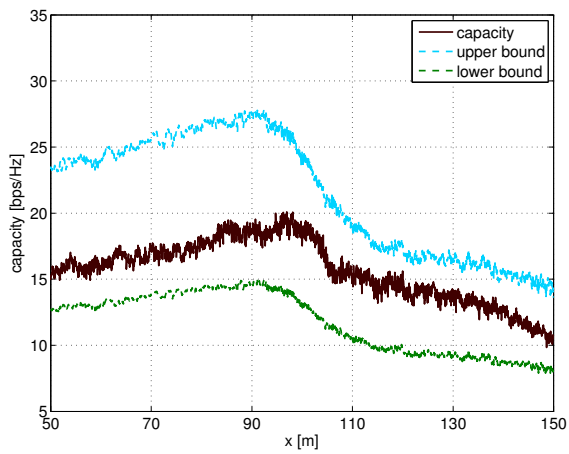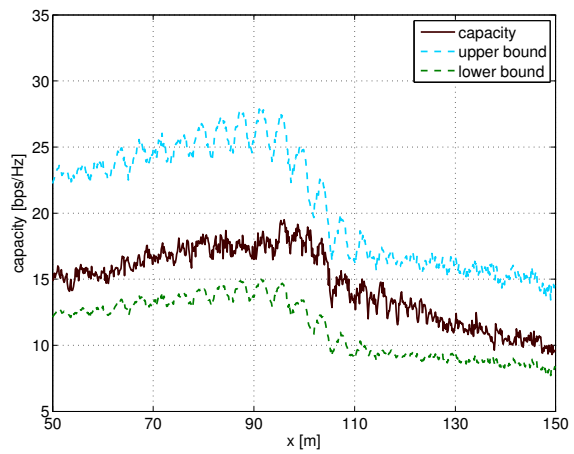
(a) walking body   (b) running body

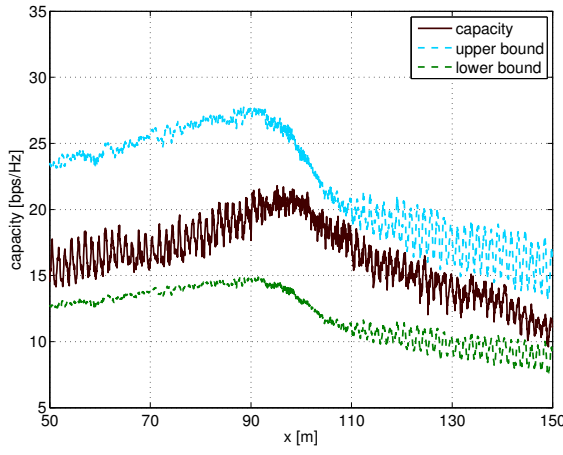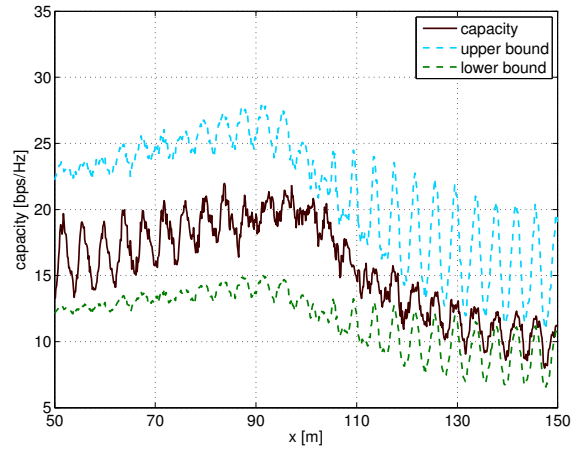Figure F.5. The MIMO capacity for the TO_F and HE_R antenna pair.

(a) walking body   (b) running body

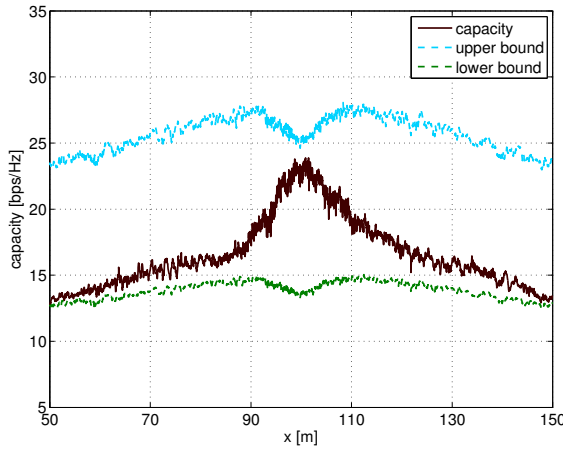Figure F.6. The MIMO capacity for the TO_F and AB_L antenna pair.

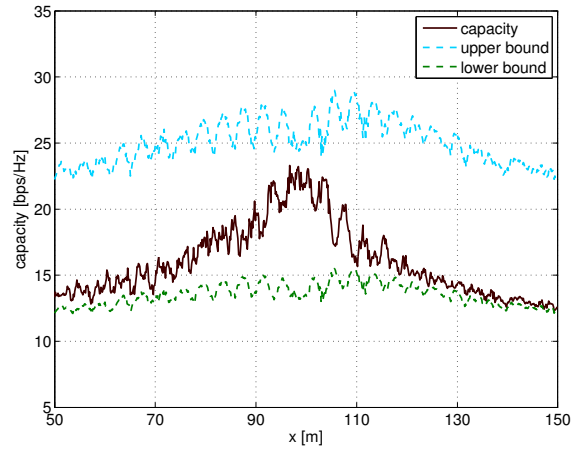(a) walking body   (b) running body

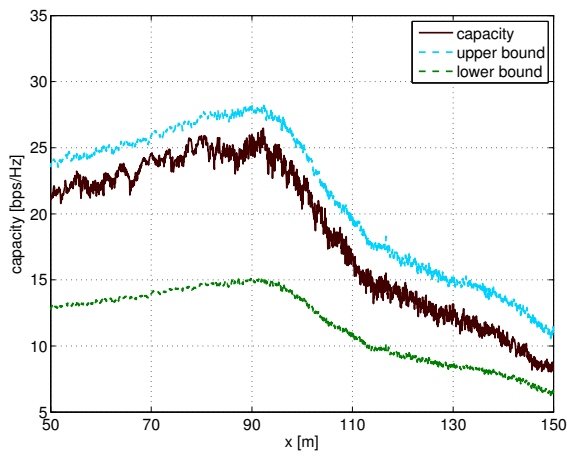Figure F.7. The MIMO capacity for the TO_F and AB_R antenna pair.

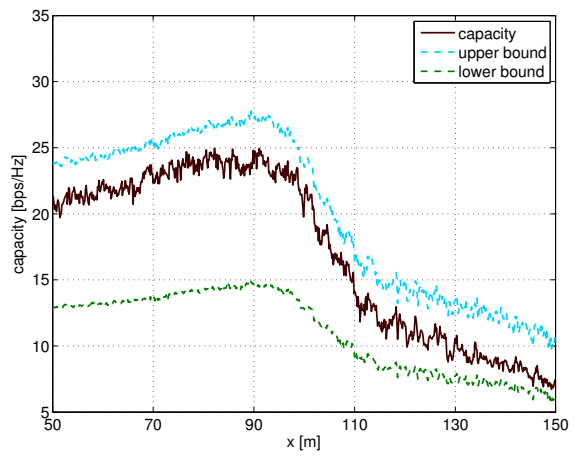(a) walking body   (b) running body

Figure F.8. The MIMO capacity for the TO_F and TO_B antenna pair.

(a) walking body   (b) running body

Figure F.9. The MIMO capacity for the WA_F and HE_F antenna pair.

(a) walking body   (b) running body

Figure F.10. The MIMO capacity for the WA_F and HE_B antenna pair.

(a) walking body   (b) running body

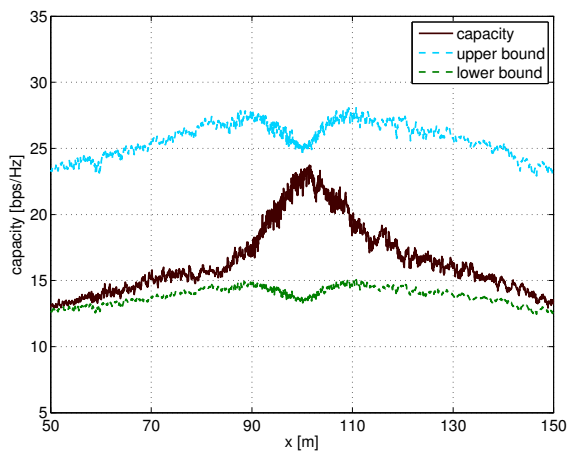Figure F.11. The MIMO capacity for the WA_F and HE_L antenna pair.

(a) walking body　　　　　　　　(b) running body
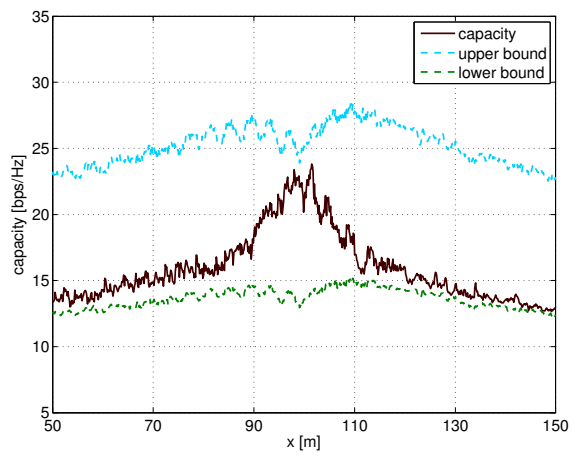
Figure F.12. The MIMO capacity for the WA_F and HE_R antenna pair.

(a) walking body　　　　　　　　(b) running body

Figure F.13. The MIMO capacity for the WA_F and AB_L antenna pair.

(a) walking body　　　　　　　　(b) running body

Figure F.14. The MIMO capacity for the WA_F and AB_R antenna pair.

(a) walking body

(b) running body

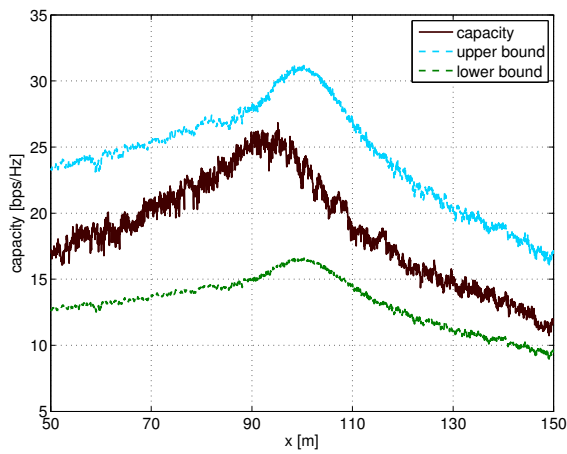Figure F.15. The MIMO capacity for the WA_F and TO_B antenna pair.

(a) walking body

(b) running body

Figure F.16. The MIMO capacity for the HE_F and HE_B antenna pair.

(a) walking body

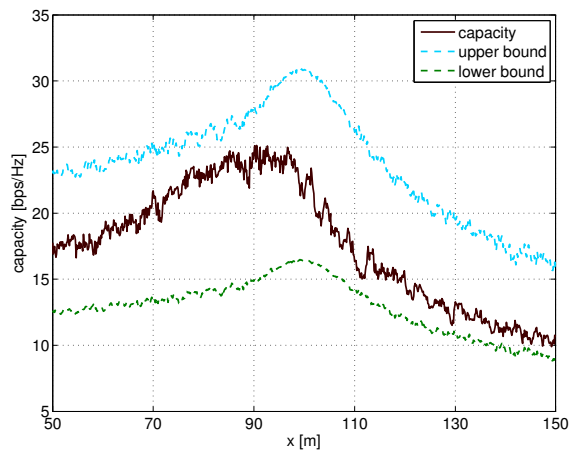(b) running body

Figure F.17. The MIMO capacity for the HE_F and HE_L antenna pair.
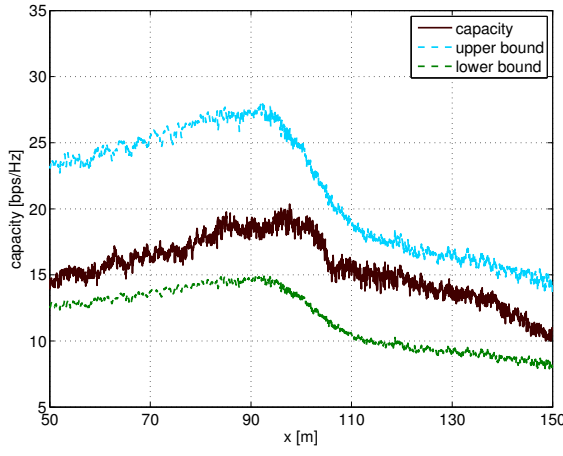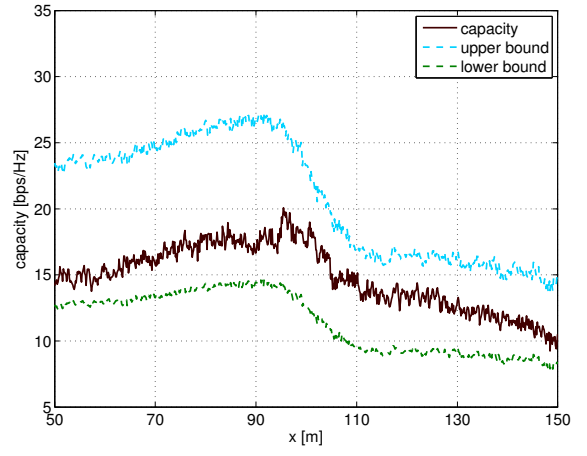
(a) walking body   (b) running body

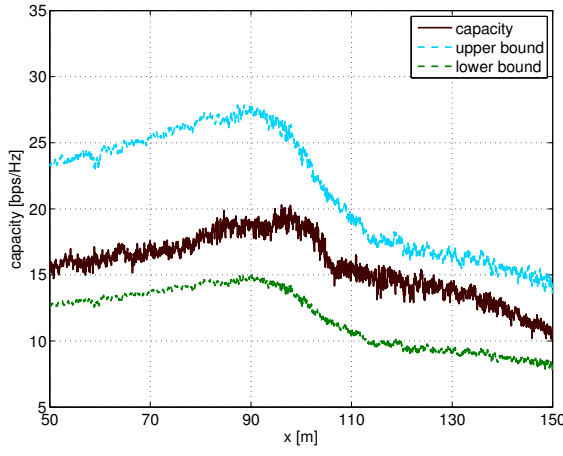Figure F.18. The MIMO capacity for the HE_F and HE_R antenna pair.
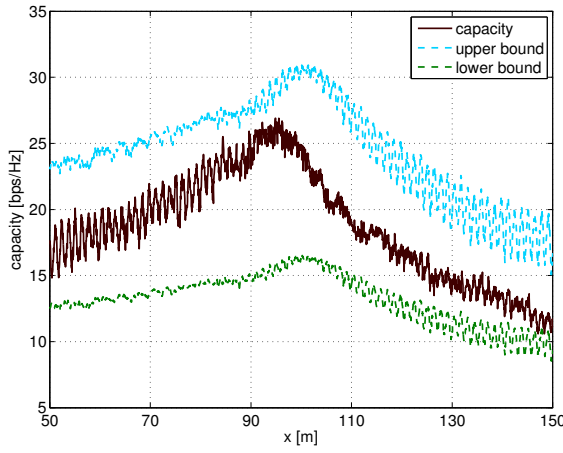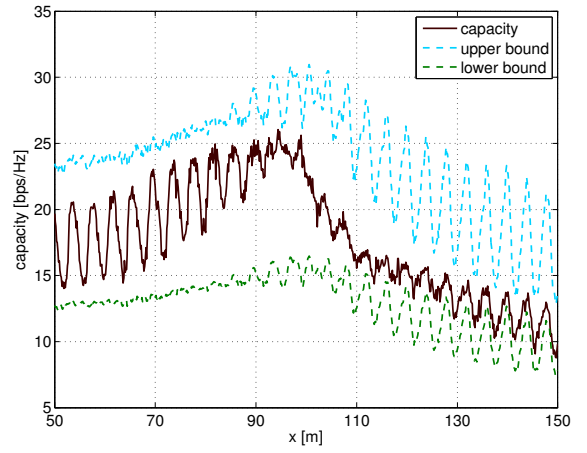
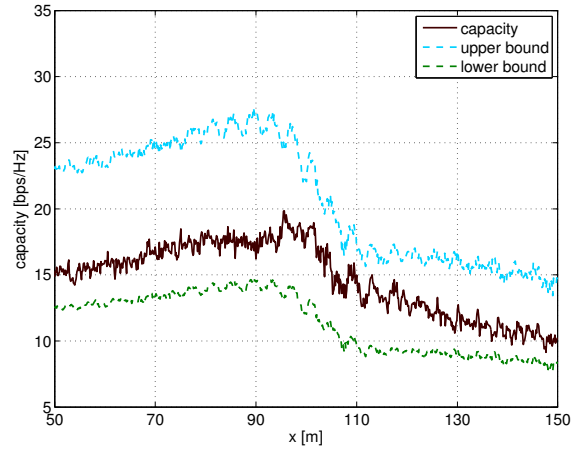(a) walking body   (b) running body

Figure F.19. The MIMO capacity for the HE_F and AB_L antenna pair.
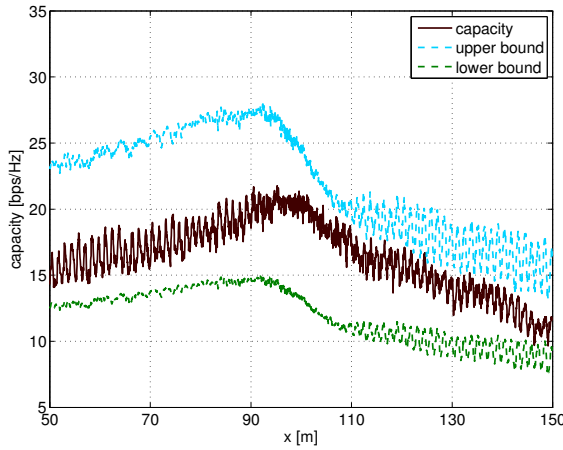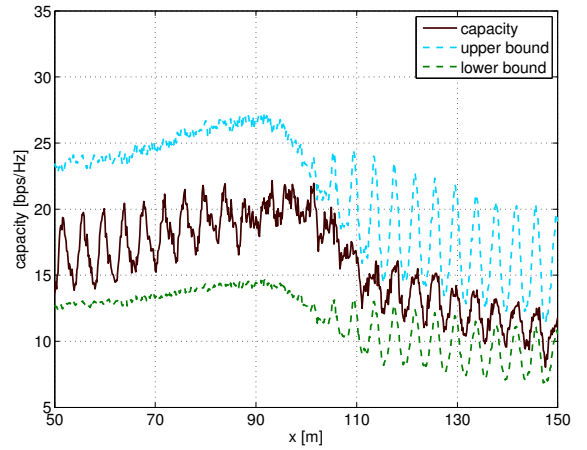
(a) walking body   (b) running body

Figure F.20. The MIMO capacity for the HE_F and AB_R antenna pair.
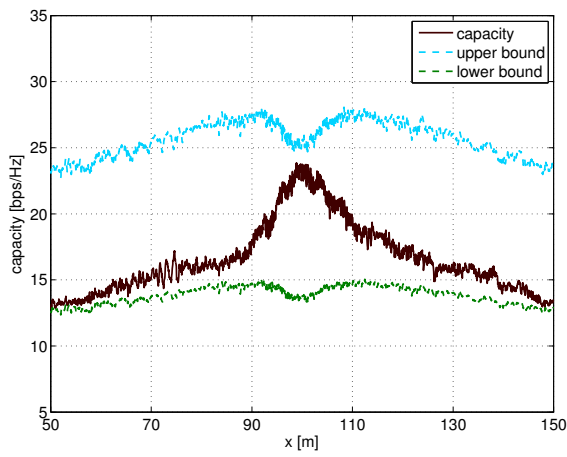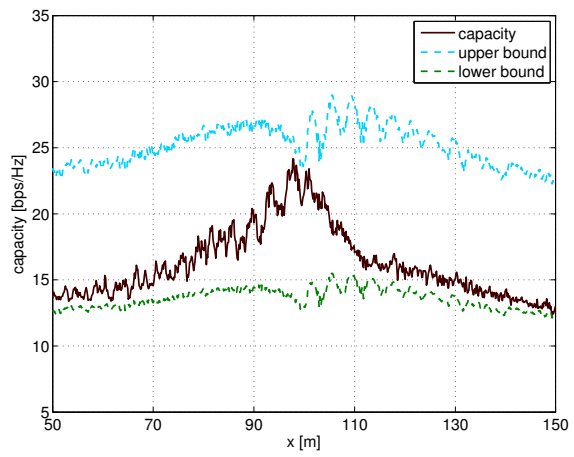
(a) walking body   (b) running body

Figure F.21. The MIMO capacity for the HE_F and TO_B antenna pair.
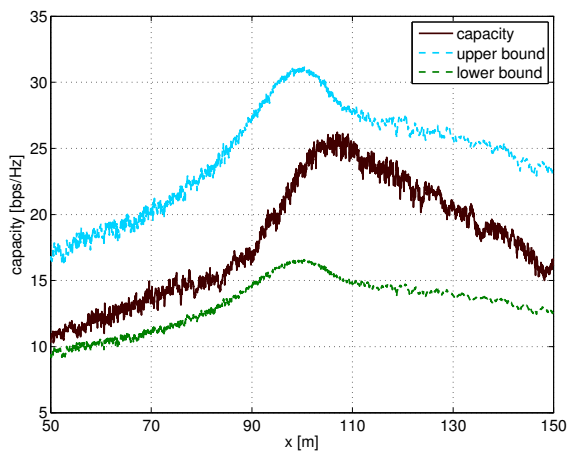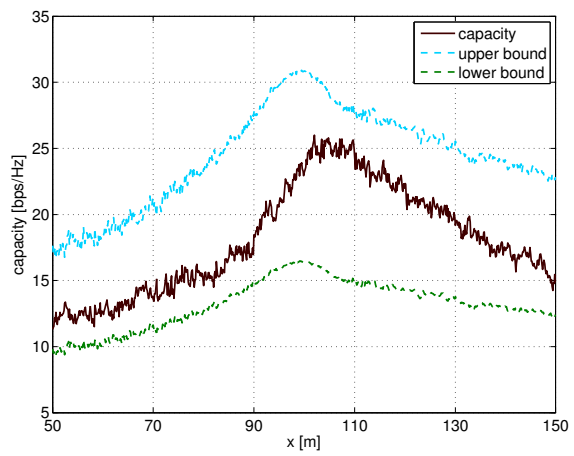
(a) walking body   (b) running body

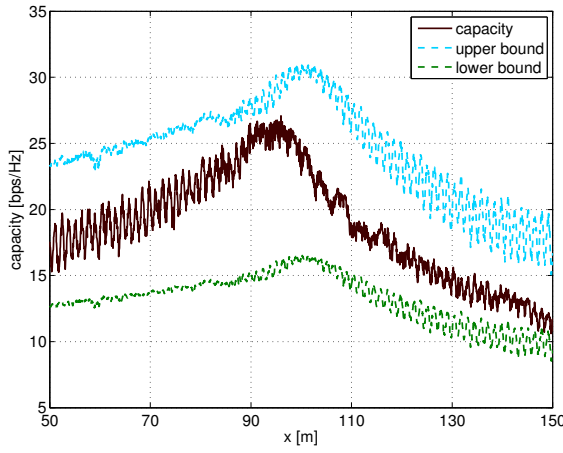Figure F.22. The MIMO capacity for the HE_B and HE_L antenna pair.
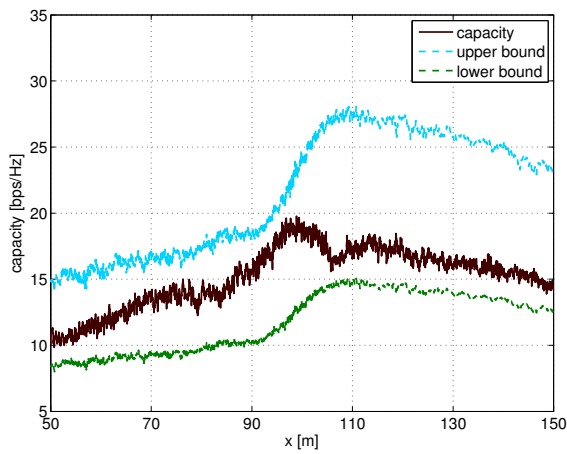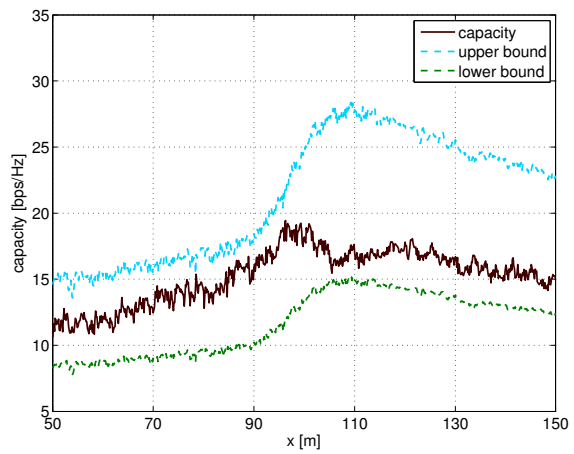
(a) walking body   (b) running body

Figure F.23. The MIMO capacity for the HE_B and HE_R antenna pair.
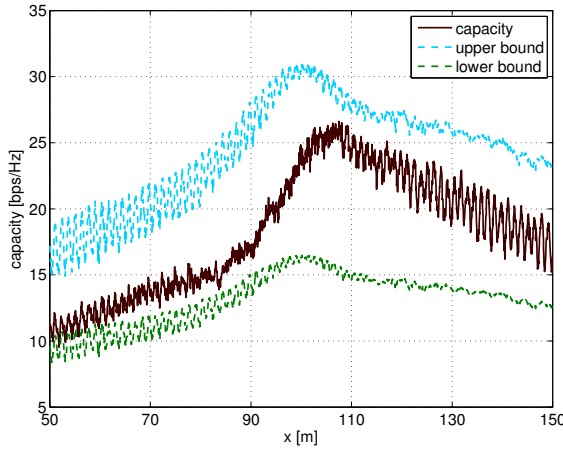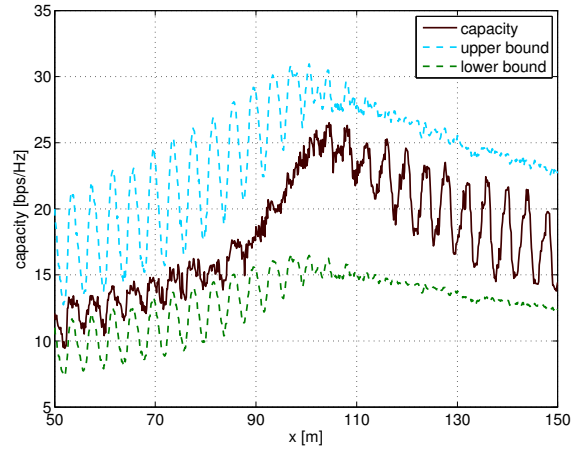
(a) walking body

(b) running body

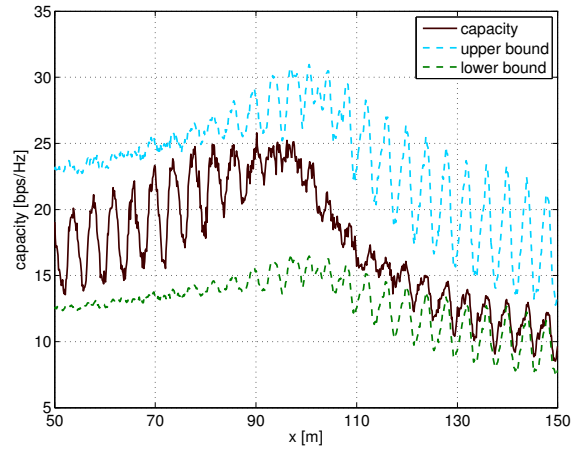Figure F.24. The MIMO capacity for the HE_B and AB_L antenna pair.
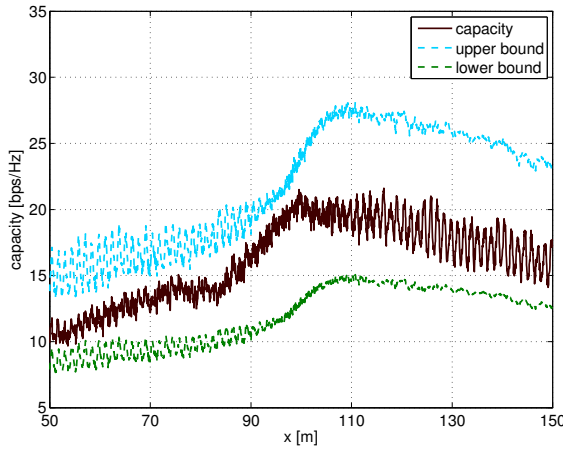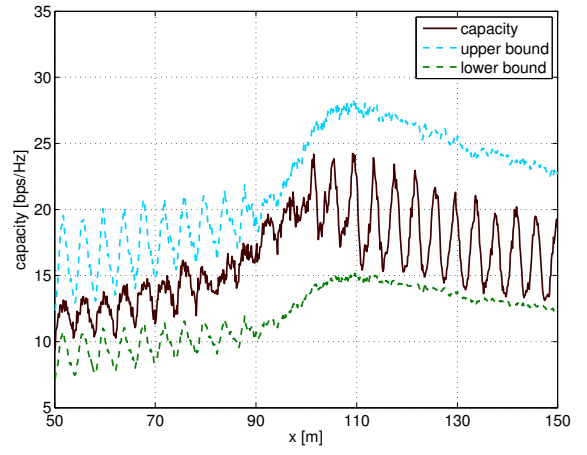
(a) walking body

(b) running body

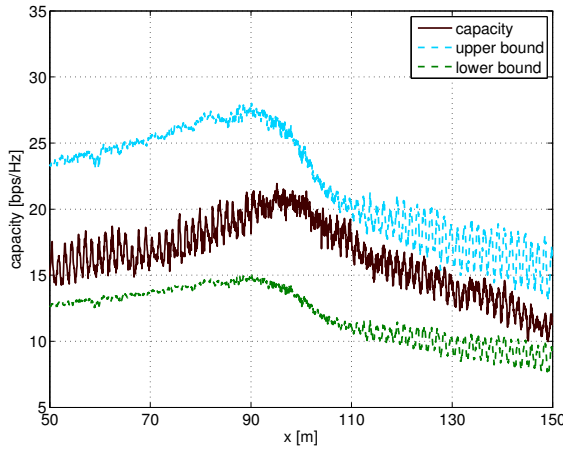Figure F.25. The MIMO capacity for the HE_B and AB_R antenna pair.
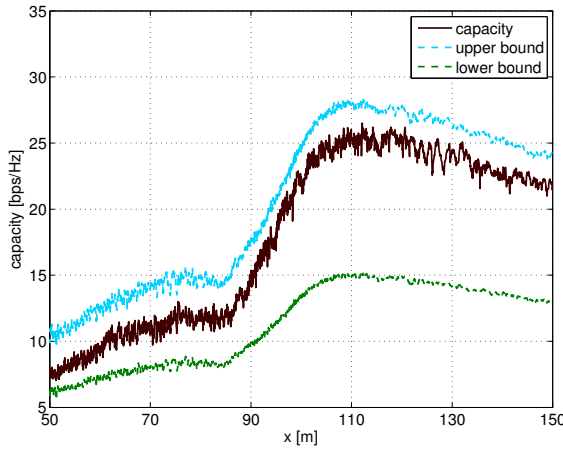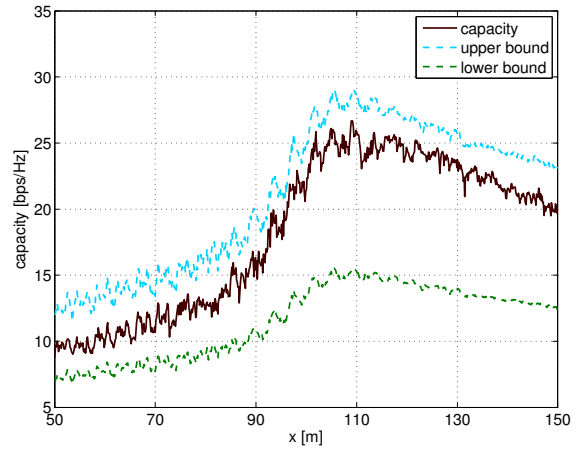
(a) walking body

(b) running body

Figure F.26. The MIMO capacity for the HE_B and TO_B antenna pair.
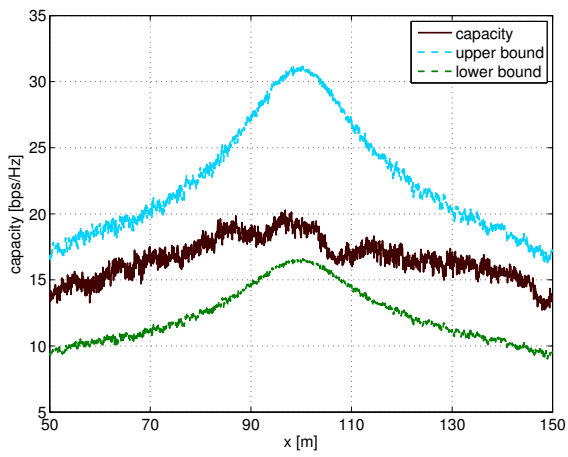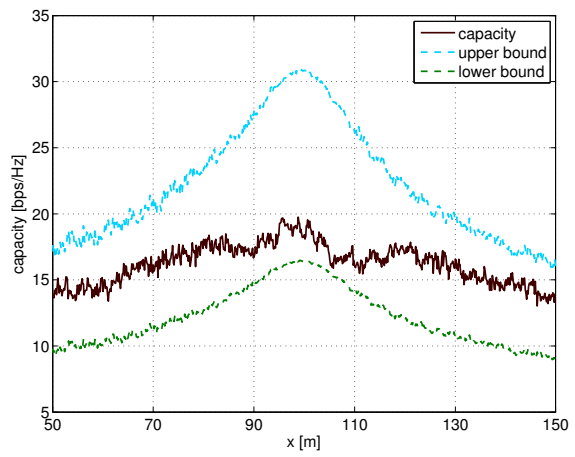
(a) walking body
(b) running body

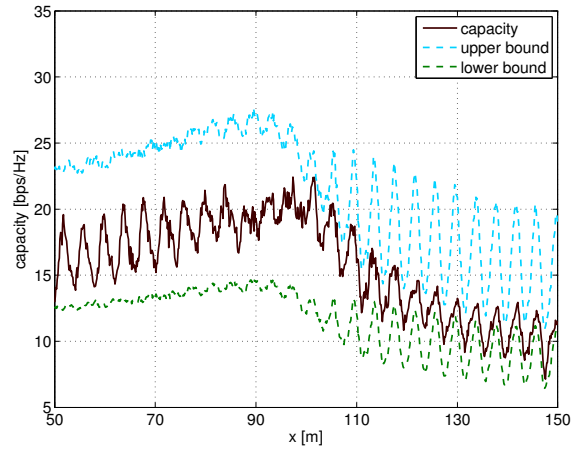Figure F.27. The MIMO capacity for the HE_L and HE_R antenna pair.
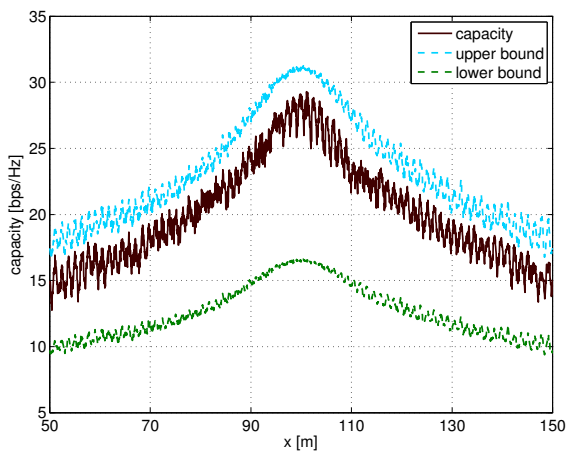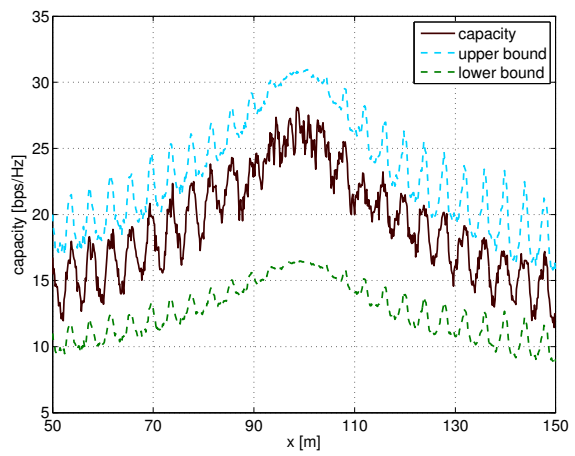
(a) walking body
(b) running body

Figure F.28. The MIMO capacity for the HE_L and AB_L antenna pair.
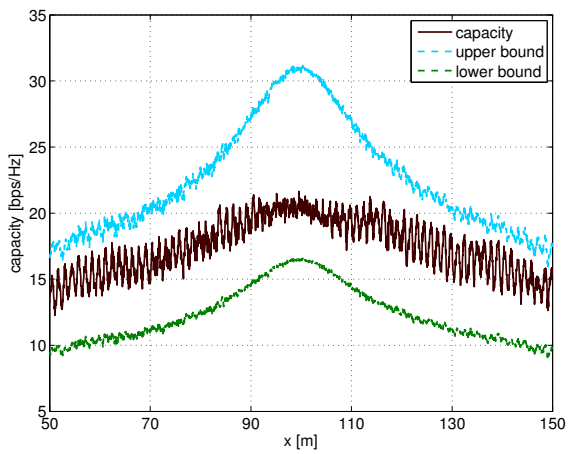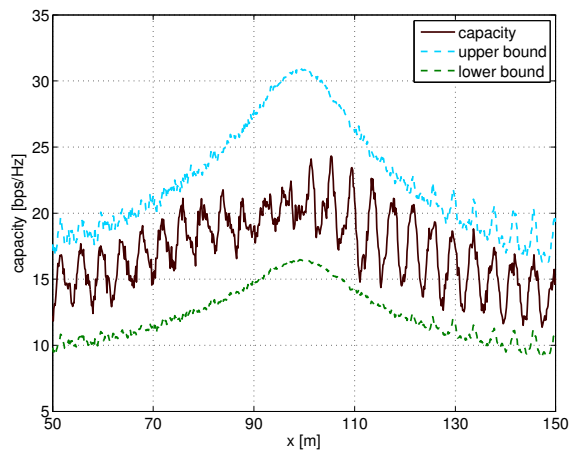
(a) walking body
(b) running body

Figure F.29. The MIMO capacity for the HE_L and AB_R antenna pair.
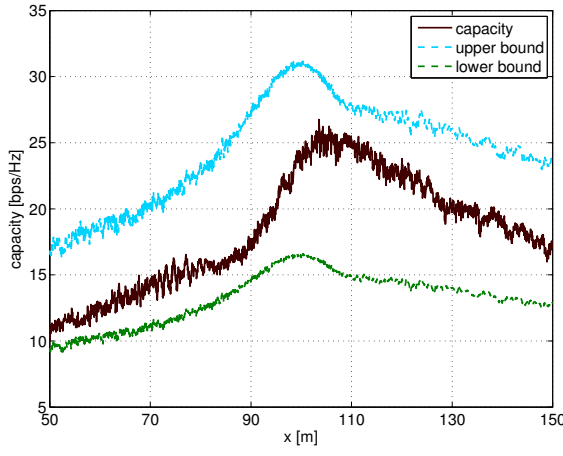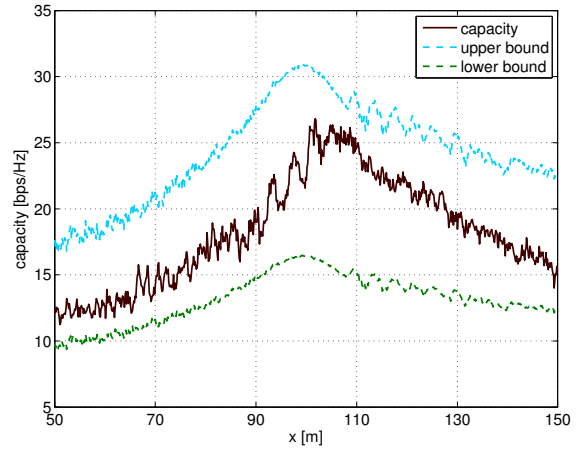
(a) walking body   (b) running body

Figure F.30. The MIMO capacity for the HE_L and TO_B antenna pair.
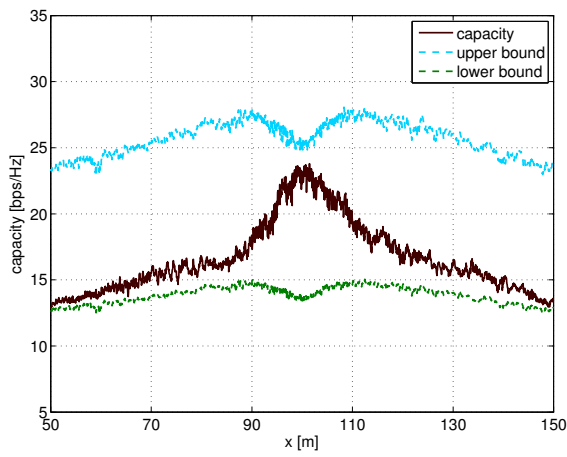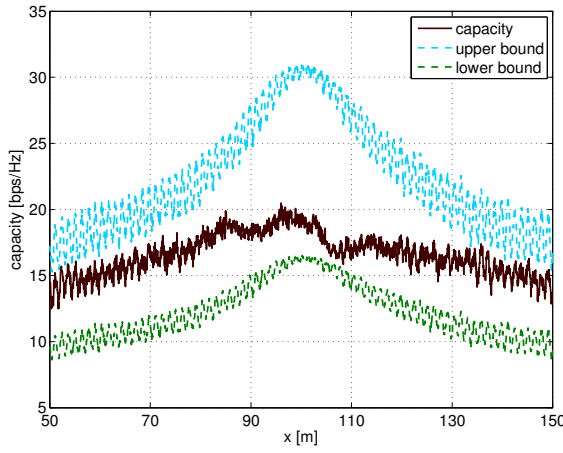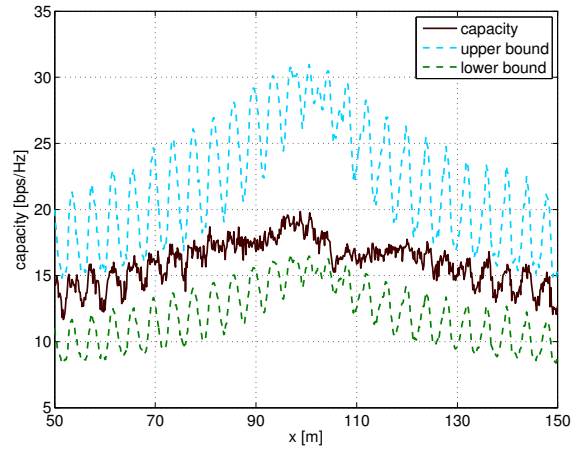

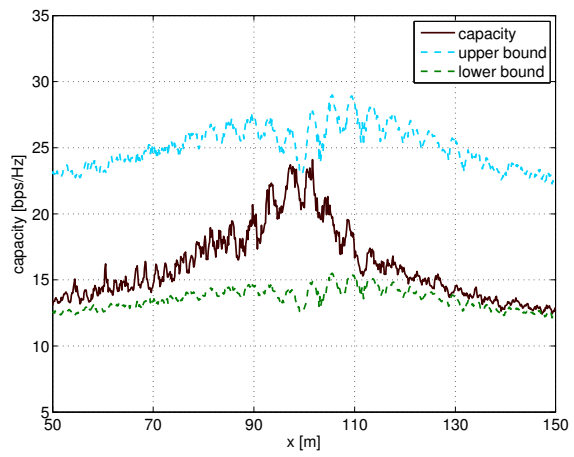(a) walking body   (b) running body

Figure F.31. The MIMO capacity for the HE_R and AB_L antenna pair.
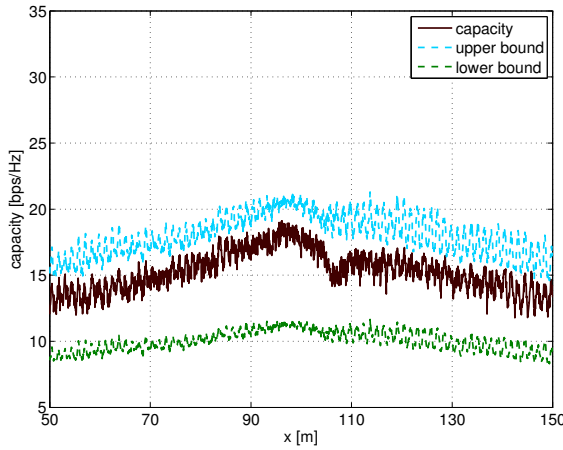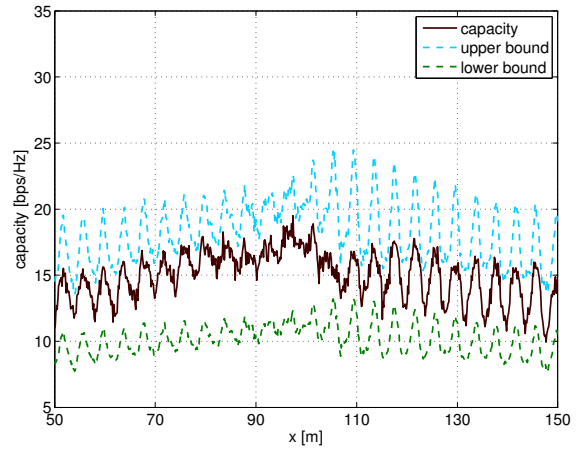
(a) walking body   (b) running body

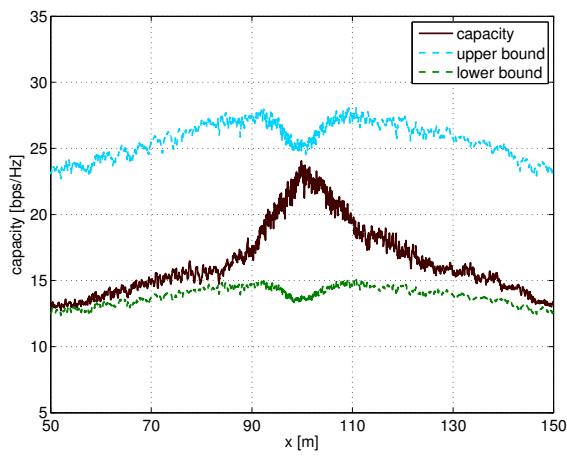Figure F.32. The MIMO capacity for the HE_R and AB_R antenna pair.
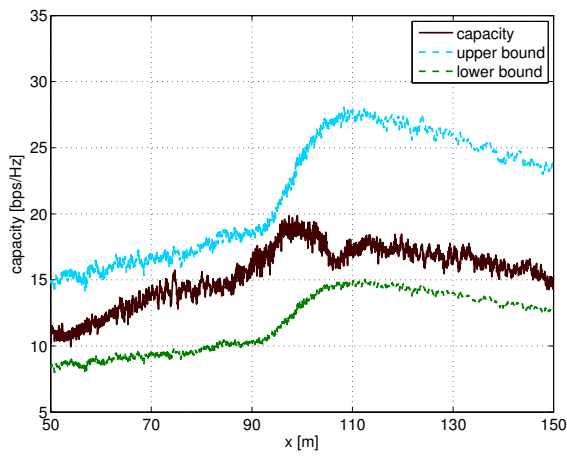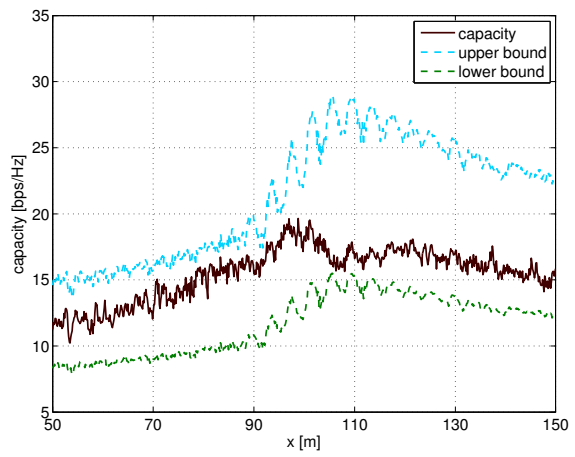
(a) walking body   (b) running body

Figure F.33. The MIMO capacity for the HE_R and TO_B antenna pair.
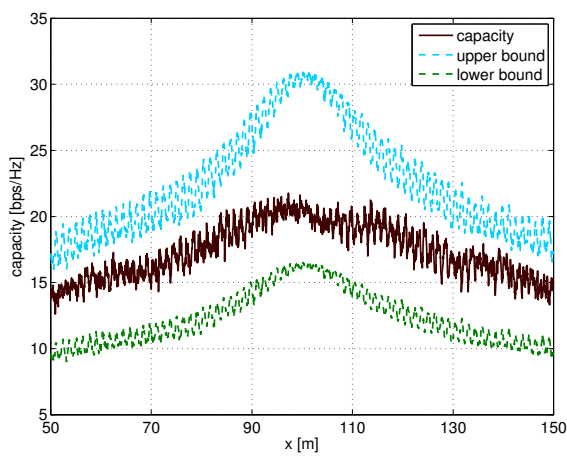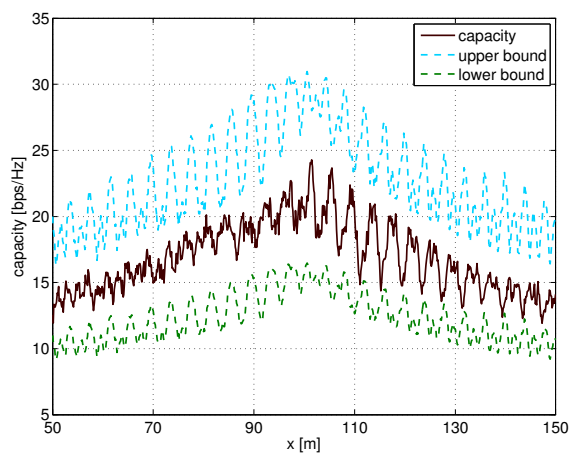
(a) walking body   (b) running body

Figure F.34. The MIMO capacity for the AB_L and AB_R antenna pair.
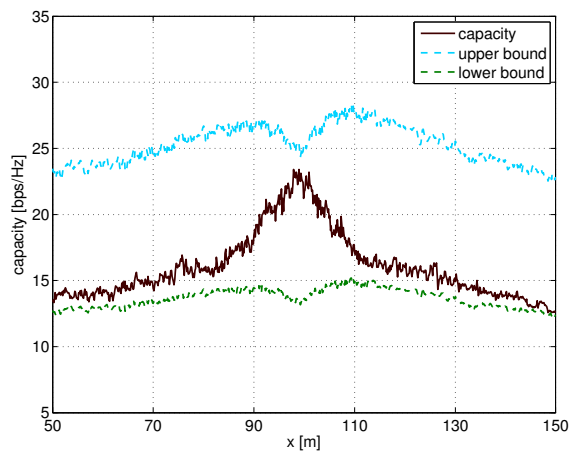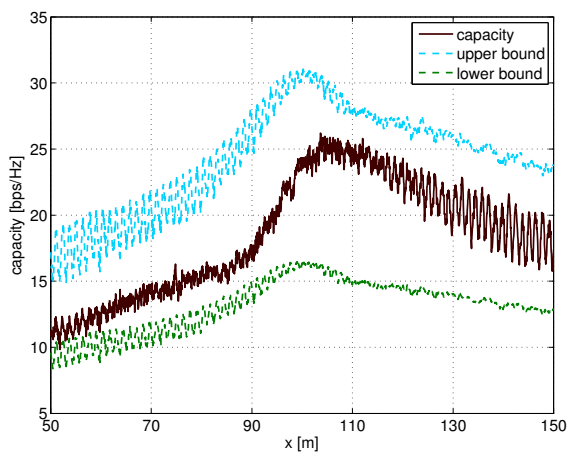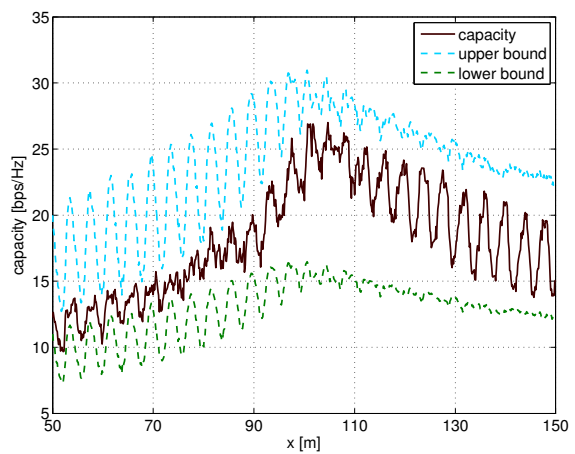

(a) walking body   (b) running body

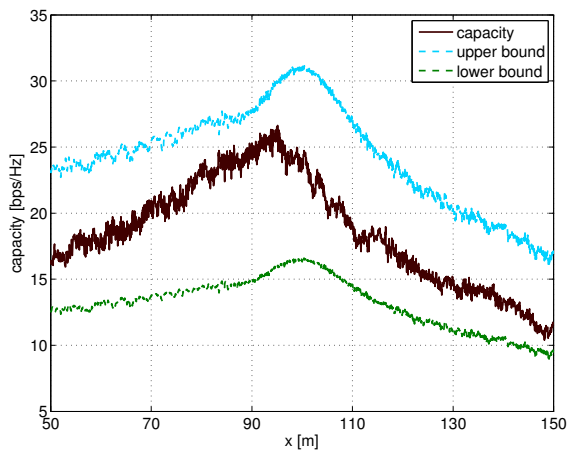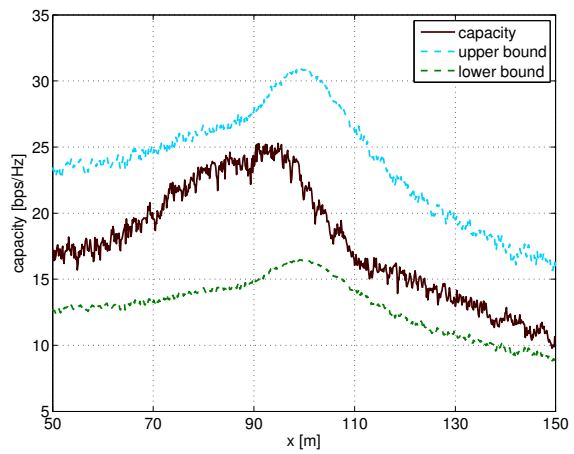Figure F.35. The MIMO capacity for the AB_L and TO_B antenna pair.
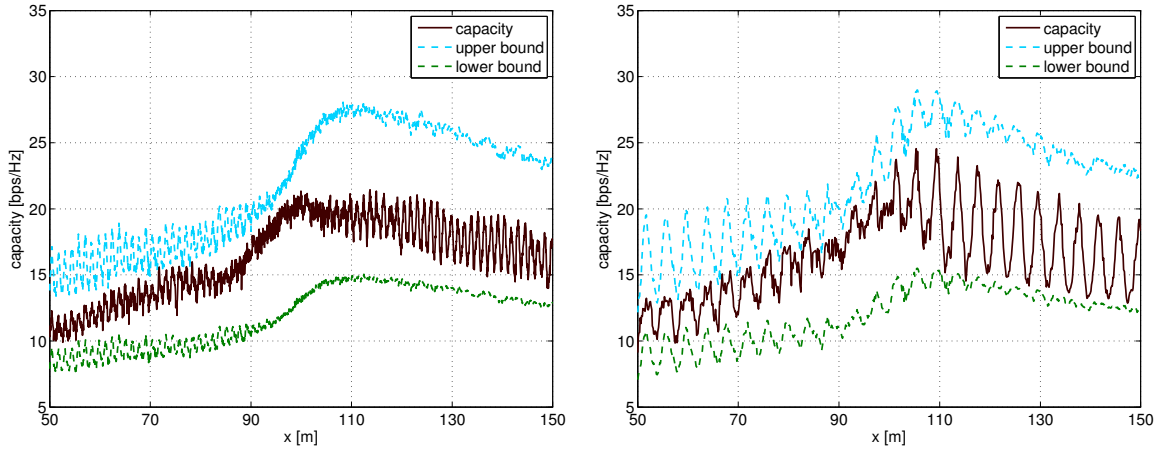
(a) walking body   (b) running body

Figure F.36. The MIMO capacity for the AB_R and TO_B antenna pair.

The statistics of the capacity of 2×2 MIMO system, for the general antenna classes are presented in Figure F.37.
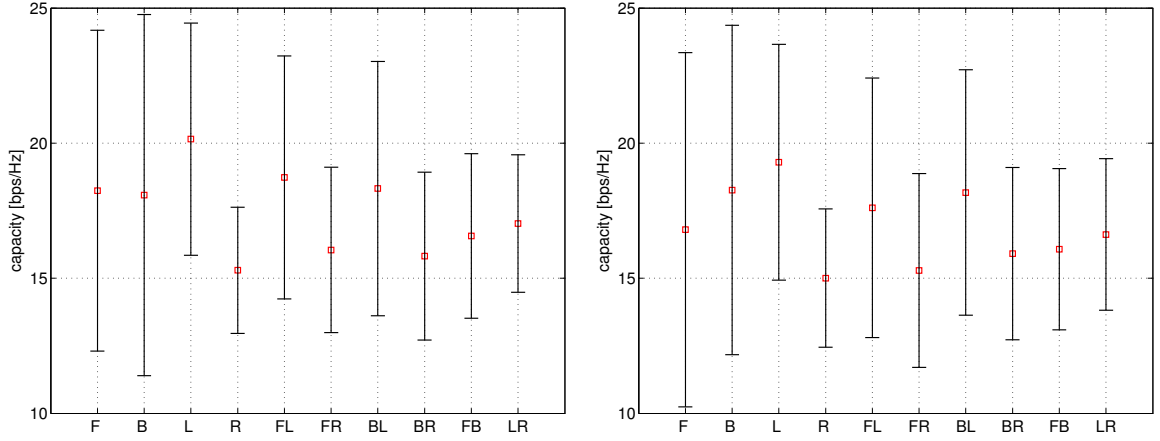
(a) walking body   (b) running body

Figure F.37. The capacity of 2×2 MIMO system, for the general antenna classes.

The following tables includes the statistics of the MIMO capacity, and MIMO capacity channel gain, for various pairs of antennas in 2×2 MIMO system, for the running body.

Table F.1. The capacity of 2×2 MIMO system, for TO_F & WA_F, for the running body.

x [m]	$\overline{C_{MIMO}}$	$\sigma_{\overline{C_{MIMO}}}$	$\overline{\sigma_{C_{MIMO}}}$	$\overline{G_{MIMO_c}}$	$\sigma_{\overline{G_{MIMO_c}}}$	$\overline{\sigma_{G_{MIMO_c}}}$
	[bps/Hz]					
[50, 150]	16.41	6.23	2.21	1.45	0.17	0.17
[50, 85]	21.60	1.37	2.25	1.59	0.05	0.16
[85, 115]	19.40	4.02	2.34	1.53	0.09	0.17
[115, 150]	8.78	1.77	2.06	1.26	0.08	0.18

Table F.2. The capacity of 2×2 MIMO system, for TO_F & HE_F, for the running body.

x [m]	$\overline{C_{MIMO}}$	$\sigma_{\overline{C_{MIMO}}}$	$\overline{\sigma_{C_{MIMO}}}$	$\overline{G_{MIMO_c}}$	$\sigma_{\overline{G_{MIMO_c}}}$	$\overline{\sigma_{G_{MIMO_c}}}$
	[bps/Hz]					
[50, 150]	17.29	6.23	2.17	1.51	0.17	0.16
[50, 85]	22.71	1.10	2.23	1.66	0.04	0.14
[85, 115]	19.98	4.05	2.28	1.59	0.08	0.16
[115, 150]	9.69	1.74	2.03	1.30	0.09	0.17

Table F.3. The capacity of 2×2 MIMO system, for TO_F & HE_B, for the running body.

x [m]	$\overline{C_{MIMO}}$	$\sigma_{\overline{C_{MIMO}}}$	$\overline{\sigma_{C_{MIMO}}}$	$\overline{G_{MIMO_c}}$	$\sigma_{\overline{G_{MIMO_c}}}$	$\overline{\sigma_{G_{MIMO_c}}}$
	[bps/Hz]					
[50, 150]	16.15	2.71	1.44	1.18	0.17	0.10
[50, 85]	15.13	1.04	1.49	1.14	0.04	0.10
[85, 115]	19.60	2.14	1.86	1.38	0.18	0.14
[115, 150]	14.34	1.22	0.88	1.06	0.04	0.07

Table F.4. The capacity of 2×2 MIMO system, for TO_F & HE_L, for the running body.

x [m]	$\overline{C_{MIMO}}$	$\sigma_{\overline{C_{MIMO}}}$	$\overline{\sigma_{C_{MIMO}}}$	$\overline{G_{MIMO_c}}$	$\sigma_{\overline{G_{MIMO_c}}}$	$\overline{\sigma_{G_{MIMO_c}}}$
	[bps/Hz]					
[50, 150]	17.87	4.55	1.92	1.37	0.19	0.15
[50, 85]	20.35	2.00	2.16	1.53	0.10	0.16
[85, 115]	21.29	3.09	2.10	1.41	0.17	0.13
[115, 150]	12.61	1.86	1.45	1.18	0.06	0.14

Table F.5. The capacity of 2×2 MIMO system, for TO_F & HE_R, for the running body.

x [m]	$\overline{C_{MIMO}}$	$\sigma_{\overline{C_{MIMO}}}$	$\overline{\sigma_{C_{MIMO}}}$	$\overline{G_{MIMO_c}}$	$\sigma_{\overline{G_{MIMO_c}}}$	$\overline{\sigma_{G_{MIMO_c}}}$
	[bps/Hz]					
[50, 150]	14.85	2.71	1.85	1.31	0.10	0.17
[50, 85]	16.62	0.94	1.82	1.25	0.04	0.14
[85, 115]	16.62	1.78	2.04	1.38	0.11	0.17
[115, 150]	11.67	1.25	1.72	1.31	0.10	0.19

Table F.6. The capacity of 2×2 MIMO system, for TO_F & AB_L, for the running body.

x [m]	$\overline{C_{MIMO}}$	$\sigma_{\overline{C_{MIMO}}}$	$\overline{\sigma_{C_{MIMO}}}$	$\overline{G_{MIMO_c}}$	$\sigma_{\overline{G_{MIMO_c}}}$	$\overline{\sigma_{G_{MIMO_c}}}$
	[bps/Hz]					
[50, 150]	17.56	4.53	1.84	1.35	0.20	0.14
[50, 85]	19.56	2.74	2.02	1.47	0.19	0.14
[85, 115]	21.14	3.08	2.05	1.43	0.16	0.14
[115, 150]	12.64	2.04	1.42	1.17	0.08	0.14

Table F.7. The capacity of 2×2 MIMO system, for TO_F & AB_R, for the running body.

x [m]	$\overline{C_{MIMO}}$	$\sigma_{\overline{C_{MIMO}}}$	$\overline{\sigma_{C_{MIMO}}}$	$\overline{G_{MIMO_c}}$	$\sigma_{\overline{G_{MIMO_c}}}$	$\overline{\sigma_{G_{MIMO_c}}}$
	[bps/Hz]					
[50, 150]	15.86	3.57	1.89	1.35	0.14	0.16
[50, 85]	17.84	1.95	1.94	1.35	0.11	0.15
[85, 115]	18.47	2.03	2.08	1.46	0.12	0.17
[115, 150]	11.77	1.66	1.68	1.26	0.12	0.17

Table F.8. The capacity of 2×2 MIMO system, for TO_F & TO_B, for the running body.

x [m]	$\overline{C_{MIMO}}$	$\sigma_{\overline{C_{MIMO}}}$	$\overline{\sigma_{C_{MIMO}}}$	$\overline{G_{MIMO_c}}$	$\sigma_{\overline{G_{MIMO_c}}}$	$\overline{\sigma_{G_{MIMO_c}}}$
	[bps/Hz]					
[50, 150]	16.27	2.79	1.45	1.20	0.17	0.11
[50, 85]	15.48	1.51	1.45	1.17	0.07	0.11
[85, 115]	19.74	2.00	1.89	1.39	0.19	0.14
[115, 150]	14.22	1.24	0.94	1.07	0.05	0.07

Table F.9. The capacity of 2×2 MIMO system, for WA_F & HE_F, for the running body.

x [m]	$\overline{C_{MIMO}}$	$\sigma_{\overline{C_{MIMO}}}$	$\overline{\sigma_{C_{MIMO}}}$	$\overline{G_{MIMO_c}}$	$\sigma_{\overline{G_{MIMO_c}}}$	$\overline{\sigma_{G_{MIMO_c}}}$
		[bps/Hz]				
[50, 150]	17.38	6.25	2.13	1.52	0.17	0.16
[50, 85]	22.82	1.11	2.16	1.67	0.03	0.14
[85, 115]	20.12	4.02	2.25	1.60	0.08	0.16
[115, 150]	9.73	1.66	2.01	1.31	0.08	0.17

Table F.10. The capacity of 2×2 MIMO system, for WA_F & HE_B, for the running body.

x [m]	$\overline{C_{MIMO}}$	$\sigma_{\overline{C_{MIMO}}}$	$\overline{\sigma_{C_{MIMO}}}$	$\overline{G_{MIMO_c}}$	$\sigma_{\overline{G_{MIMO_c}}}$	$\overline{\sigma_{G_{MIMO_c}}}$
		[bps/Hz]				
[50, 150]	16.20	2.68	1.47	1.18	0.17	0.11
[50, 85]	15.18	1.02	1.43	1.14	0.04	0.10
[85, 115]	19.67	2.09	1.94	1.38	0.18	0.14
[115, 150]	14.36	1.10	0.95	1.07	0.03	0.07

Table F.11. The capacity of 2×2 MIMO system, for WA_F & HE_L, for the running body.

x [m]	$\overline{C_{MIMO}}$	$\sigma_{\overline{C_{MIMO}}}$	$\overline{\sigma_{C_{MIMO}}}$	$\overline{G_{MIMO_c}}$	$\sigma_{\overline{G_{MIMO_c}}}$	$\overline{\sigma_{G_{MIMO_c}}}$
		[bps/Hz]				
[50, 150]	17.98	4.55	1.93	1.37	0.19	0.15
[50, 85]	20.44	2.01	2.11	1.53	0.09	0.16
[85, 115]	21.46	3.05	2.11	1.42	0.17	0.13
[115, 150]	12.68	1.71	1.54	1.18	0.05	0.15

Table F.12. The capacity of 2×2 MIMO system, for WA_F & HE_R, for the running body.

x [m]	$\overline{C_{MIMO}}$	$\sigma_{\overline{C_{MIMO}}}$	$\overline{\sigma_{C_{MIMO}}}$	$\overline{G_{MIMO_c}}$	$\sigma_{\overline{G_{MIMO_c}}}$	$\overline{\sigma_{G_{MIMO_c}}}$
		[bps/Hz]				
[50, 150]	14.92	2.67	1.85	1.31	0.10	0.17
[50, 85]	16.68	0.92	1.77	1.25	0.04	0.13
[85, 115]	16.68	1.74	2.07	1.38	0.11	0.17
[115, 150]	11.78	1.21	1.73	1.33	0.10	0.19

Table F.13. The capacity of 2×2 MIMO system, for WA_F & AB_L, for the running body.

x [m]	$\overline{C_{MIMO}}$	$\sigma_{\overline{C_{MIMO}}}$	$\overline{\sigma_{C_{MIMO}}}$	$\overline{G_{MIMO_c}}$	$\sigma_{\overline{G_{MIMO_c}}}$	$\overline{\sigma_{G_{MIMO_c}}}$
	[bps/Hz]					
[50, 150]	17.66	4.55	1.87	1.36	0.20	0.14
[50, 85]	19.60	2.81	2.06	1.47	0.17	0.15
[85, 115]	21.36	3.01	2.06	1.46	0.17	0.14
[115, 150]	12.69	1.91	1.46	1.18	0.09	0.14

Table F.14. The capacity of 2×2 MIMO system, for WA_F & AB_R, for the running body.

x [m]	$\overline{C_{MIMO}}$	$\sigma_{\overline{C_{MIMO}}}$	$\overline{\sigma_{C_{MIMO}}}$	$\overline{G_{MIMO_c}}$	$\sigma_{\overline{G_{MIMO_c}}}$	$\overline{\sigma_{G_{MIMO_c}}}$
	[bps/Hz]					
[50, 150]	15.98	3.63	1.90	1.36	0.15	0.16
[50, 85]	17.93	1.91	1.91	1.35	0.13	0.14
[85, 115]	18.67	2.21	2.10	1.48	0.11	0.16
[115, 150]	11.84	1.73	1.71	1.27	0.12	0.17

Table F.15. The capacity of 2×2 MIMO system, for WA_F & TO_B, for the running body.

x [m]	$\overline{C_{MIMO}}$	$\sigma_{\overline{C_{MIMO}}}$	$\overline{\sigma_{C_{MIMO}}}$	$\overline{G_{MIMO_c}}$	$\sigma_{\overline{G_{MIMO_c}}}$	$\overline{\sigma_{G_{MIMO_c}}}$
	[bps/Hz]					
[50, 150]	16.32	2.80	1.50	1.20	0.17	0.11
[50, 85]	15.55	1.49	1.43	1.17	0.07	0.11
[85, 115]	19.80	2.11	1.98	1.39	0.18	0.14
[115, 150]	14.24	1.12	1.02	1.07	0.04	0.08

Table F.16. The capacity of 2×2 MIMO system, for HE_F & HE_B, for the running body.

x [m]	$\overline{C_{MIMO}}$	$\sigma_{\overline{C_{MIMO}}}$	$\overline{\sigma_{C_{MIMO}}}$	$\overline{G_{MIMO_c}}$	$\sigma_{\overline{G_{MIMO_c}}}$	$\overline{\sigma_{G_{MIMO_c}}}$
	[bps/Hz]					
[50, 150]	16.32	2.59	1.51	1.19	0.16	0.11
[50, 85]	15.20	0.99	1.44	1.13	0.04	0.10
[85, 115]	19.64	2.07	1.90	1.37	0.18	0.14
[115, 150]	14.71	1.17	1.15	1.09	0.04	0.09

Table F.17. The capacity of 2×2 MIMO system, for HE_F & HE_L, for the running body.

x [m]	$\overline{C_{MIMO}}$	$\sigma_{\overline{C_{MIMO}}}$	$\overline{\sigma_{C_{MIMO}}}$	$\overline{G_{MIMO_c}}$	$\sigma_{\overline{G_{MIMO_c}}}$	$\overline{\sigma_{G_{MIMO_c}}}$
	[bps/Hz]					
[50, 150]	18.04	4.29	1.99	1.38	0.16	0.16
[50, 85]	20.09	2.13	2.07	1.50	0.10	0.16
[85, 115]	21.42	3.13	2.17	1.41	0.18	0.14
[115, 150]	13.25	1.76	1.74	1.24	0.06	0.17

Table F.18. The capacity of 2×2 MIMO system, for HE_F & HE_R, for the running body.

x [m]	$\overline{C_{MIMO}}$	$\sigma_{\overline{C_{MIMO}}}$	$\overline{\sigma_{C_{MIMO}}}$	$\overline{G_{MIMO_c}}$	$\sigma_{\overline{G_{MIMO_c}}}$	$\overline{\sigma_{G_{MIMO_c}}}$
	[bps/Hz]					
[50, 150]	15.00	2.37	1.85	1.32	0.11	0.17
[50, 85]	16.37	1.08	1.72	1.22	0.04	0.13
[85, 115]	16.61	1.70	2.04	1.37	0.11	0.17
[115, 150]	12.36	1.19	1.82	1.39	0.09	0.19

Table F.19. The capacity of 2×2 MIMO system, for HE_F & AB_L, for the running body.

x [m]	$\overline{C_{MIMO}}$	$\sigma_{\overline{C_{MIMO}}}$	$\overline{\sigma_{C_{MIMO}}}$	$\overline{G_{MIMO_c}}$	$\sigma_{\overline{G_{MIMO_c}}}$	$\overline{\sigma_{G_{MIMO_c}}}$
	[bps/Hz]					
[50, 150]	17.91	4.36	1.90	1.38	0.18	0.15
[50, 85]	19.70	2.75	2.06	1.46	0.17	0.15
[85, 115]	21.40	3.19	2.02	1.45	0.17	0.13
[115, 150]	13.29	1.85	1.61	1.24	0.10	0.16

Table F.20. The capacity of 2×2 MIMO system, for HE_F & AB_R, for the running body.

x [m]	$\overline{C_{MIMO}}$	$\sigma_{\overline{C_{MIMO}}}$	$\overline{\sigma_{C_{MIMO}}}$	$\overline{G_{MIMO_c}}$	$\sigma_{\overline{G_{MIMO_c}}}$	$\overline{\sigma_{G_{MIMO_c}}}$
	[bps/Hz]					
[50, 150]	16.17	3.36	1.92	1.37	0.13	0.16
[50, 85]	17.94	1.91	1.90	1.34	0.12	0.14
[85, 115]	18.59	2.13	2.04	1.47	0.12	0.16
[115, 150]	12.45	1.70	1.83	1.33	0.11	0.18

Table F.21. The capacity of 2×2 MIMO system, for HE_F & TO_B, for the running body.

x [m]	$\overline{C_{MIMO}}$	$\sigma_{\overline{C_{MIMO}}}$	$\overline{\sigma_{C_{MIMO}}}$	$\overline{G_{MIMO_c}}$	$\sigma_{\overline{G_{MIMO_c}}}$	$\overline{\sigma_{G_{MIMO_c}}}$
	[bps/Hz]					
[50, 150]	16.48	2.70	1.52	1.21	0.16	0.11
[50, 85]	15.58	1.48	1.45	1.16	0.07	0.11
[85, 115]	19.81	2.06	1.90	1.39	0.18	0.14
[115, 150]	14.64	1.16	1.19	1.10	0.04	0.10

Table F.22. The capacity of 2×2 MIMO system, for HE_B & HE_L, for the running body.

x [m]	$\overline{C_{MIMO}}$	$\sigma_{\overline{C_{MIMO}}}$	$\overline{\sigma_{C_{MIMO}}}$	$\overline{G_{MIMO_c}}$	$\sigma_{\overline{G_{MIMO_c}}}$	$\overline{\sigma_{G_{MIMO_c}}}$
	[bps/Hz]					
[50, 150]	18.33	4.01	1.98	1.37	0.14	0.15
[50, 85]	14.20	1.43	1.74	1.26	0.05	0.16
[85, 115]	22.41	2.82	2.24	1.46	0.16	0.14
[115, 150]	19.11	2.34	1.96	1.42	0.11	0.15

Table F.23. The capacity of 2×2 MIMO system, for HE_B & HE_R, for the running body.

x [m]	$\overline{C_{MIMO}}$	$\sigma_{\overline{C_{MIMO}}}$	$\overline{\sigma_{C_{MIMO}}}$	$\overline{G_{MIMO_c}}$	$\sigma_{\overline{G_{MIMO_c}}}$	$\overline{\sigma_{G_{MIMO_c}}}$
	[bps/Hz]					
[50, 150]	15.38	1.91	1.75	1.34	0.16	0.15
[50, 85]	13.27	1.27	1.85	1.46	0.08	0.18
[85, 115]	17.00	0.97	1.88	1.35	0.20	0.14
[115, 150]	16.21	0.88	1.52	1.21	0.03	0.12

Table F.24. The capacity of 2×2 MIMO system, for HE_B & AB_L, for the running body.

x [m]	$\overline{C_{MIMO}}$	$\sigma_{\overline{C_{MIMO}}}$	$\overline{\sigma_{C_{MIMO}}}$	$\overline{G_{MIMO_c}}$	$\sigma_{\overline{G_{MIMO_c}}}$	$\overline{\sigma_{G_{MIMO_c}}}$
	[bps/Hz]					
[50, 150]	18.26	4.24	1.96	1.40	0.17	0.15
[50, 85]	13.88	1.62	1.72	1.29	0.11	0.16
[85, 115]	22.19	2.87	2.19	1.49	0.16	0.14
[115, 150]	19.42	2.89	1.98	1.44	0.18	0.15

Table F.25. The capacity of 2×2 MIMO system, for HE_B & AB_R, for the running body.

x [m]	$\overline{C_{MIMO}}$	$\sigma_{\overline{C_{MIMO}}}$	$\overline{\sigma_{C_{MIMO}}}$	$\overline{G_{MIMO_c}}$	$\sigma_{\overline{G_{MIMO_c}}}$	$\overline{\sigma_{G_{MIMO_c}}}$
	[bps/Hz]					
[50, 150]	16.57	3.15	1.87	1.38	0.16	0.15
[50, 85]	13.61	1.52	1.87	1.40	0.08	0.18
[85, 115]	19.20	2.24	2.08	1.48	0.16	0.15
[115, 150]	17.41	2.55	1.67	1.29	0.18	0.13

Table F.26. The capacity of 2×2 MIMO system, for HE_B & TO_B, for the running body.

x [m]	$\overline{C_{MIMO}}$	$\sigma_{\overline{C_{MIMO}}}$	$\overline{\sigma_{C_{MIMO}}}$	$\overline{G_{MIMO_c}}$	$\sigma_{\overline{G_{MIMO_c}}}$	$\overline{\sigma_{G_{MIMO_c}}}$
	[bps/Hz]					
[50, 150]	18.44	5.65	2.13	1.55	0.14	0.16
[50, 85]	11.59	1.49	2.01	1.39	0.07	0.19
[85, 115]	21.49	3.91	2.28	1.63	0.07	0.15
[115, 150]	22.82	1.54	2.12	1.67	0.04	0.14

Table F.27. The capacity of 2×2 MIMO system, for HE_L & HE_R, for the running body.

x [m]	$\overline{C_{MIMO}}$	$\sigma_{\overline{C_{MIMO}}}$	$\overline{\sigma_{C_{MIMO}}}$	$\overline{G_{MIMO_c}}$	$\sigma_{\overline{G_{MIMO_c}}}$	$\overline{\sigma_{G_{MIMO_c}}}$
	[bps/Hz]					
[50, 150]	16.35	1.39	1.79	1.36	0.14	0.16
[50, 85]	16.10	1.28	1.94	1.43	0.06	0.18
[85, 115]	17.59	0.95	1.72	1.17	0.06	0.12
[115, 150]	15.67	1.13	1.71	1.47	0.07	0.17

Table F.28. The capacity of 2×2 MIMO system, for HE_L & AB_L, for the running body.

x [m]	$\overline{C_{MIMO}}$	$\sigma_{\overline{C_{MIMO}}}$	$\overline{\sigma_{C_{MIMO}}}$	$\overline{G_{MIMO_c}}$	$\sigma_{\overline{G_{MIMO_c}}}$	$\overline{\sigma_{G_{MIMO_c}}}$
	[bps/Hz]					
[50, 150]	19.56	3.84	2.09	1.53	0.08	0.16
[50, 85]	18.04	2.64	2.15	1.52	0.09	0.17
[85, 115]	24.13	2.03	2.15	1.58	0.06	0.13
[115, 150]	17.33	2.58	1.98	1.51	0.08	0.16

Table F.29. The capacity of 2×2 MIMO system, for HE_L & AB_R, for the running body.

x [m]	$\overline{C_{MIMO}}$	$\sigma_{\overline{C_{MIMO}}}$	$\overline{\sigma_{C_{MIMO}}}$	$\overline{G_{MIMO_c}}$	$\sigma_{\overline{G_{MIMO_c}}}$	$\overline{\sigma_{G_{MIMO_c}}}$
	[bps/Hz]					
[50, 150]	17.49	2.66	1.89	1.42	0.15	0.16
[50, 85]	17.08	2.04	1.89	1.50	0.11	0.16
[85, 115]	19.97	1.78	2.09	1.33	0.13	0.14
[115, 150]	15.92	2.36	1.72	1.44	0.15	0.16

Table F.30. The capacity of 2×2 MIMO system, for HE_L & TO_B, for the running body.

x [m]	$\overline{C_{MIMO}}$	$\sigma_{\overline{C_{MIMO}}}$	$\overline{\sigma_{C_{MIMO}}}$	$\overline{G_{MIMO_c}}$	$\sigma_{\overline{G_{MIMO_c}}}$	$\overline{\sigma_{G_{MIMO_c}}}$
	[bps/Hz]					
[50, 150]	18.55	3.97	1.95	1.39	0.14	0.15
[50, 85]	14.60	1.94	1.71	1.29	0.07	0.16
[85, 115]	22.65	2.77	2.19	1.48	0.16	0.14
[115, 150]	19.13	2.16	1.97	1.44	0.10	0.15

Table F.31. The capacity of 2×2 MIMO system, for HE_R & AB_L, for the running body.

x [m]	$\overline{C_{MIMO}}$	$\sigma_{\overline{C_{MIMO}}}$	$\overline{\sigma_{C_{MIMO}}}$	$\overline{G_{MIMO_c}}$	$\sigma_{\overline{G_{MIMO_c}}}$	$\overline{\sigma_{G_{MIMO_c}}}$
	[bps/Hz]					
[50, 150]	16.10	1.54	1.80	1.36	0.15	0.15
[50, 85]	15.70	1.45	1.92	1.43	0.12	0.17
[85, 115]	17.53	0.98	1.81	1.22	0.11	0.13
[115, 150]	15.41	1.23	1.67	1.41	0.12	0.16

Table F.32. The capacity of 2×2 MIMO system, for HE_R & AB_R, for the running body.

x [m]	$\overline{C_{MIMO}}$	$\sigma_{\overline{C_{MIMO}}}$	$\overline{\sigma_{C_{MIMO}}}$	$\overline{G_{MIMO_c}}$	$\sigma_{\overline{G_{MIMO_c}}}$	$\overline{\sigma_{G_{MIMO_c}}}$
	[bps/Hz]					
[50, 150]	15.13	1.71	1.88	1.49	0.08	0.17
[50, 85]	15.03	1.47	1.86	1.52	0.06	0.17
[85, 115]	16.31	1.21	2.09	1.49	0.10	0.17
[115, 150]	14.32	1.77	1.72	1.46	0.07	0.17

Table F.33. The capacity of 2×2 MIMO system, for HE_R & TO_B, for the running body.

x [m]	$\overline{C_{MIMO}}$	$\sigma_{\overline{C_{MIMO}}}$	$\overline{\sigma_{C_{MIMO}}}$	$\overline{G_{MIMO_c}}$	$\sigma_{\overline{G_{MIMO_c}}}$	$\overline{\sigma_{G_{MIMO_c}}}$
		[bps/Hz]				
[50, 150]	15.61	1.90	1.77	1.36	0.16	0.15
[50, 85]	13.62	1.53	1.85	1.49	0.09	0.18
[85, 115]	17.13	0.94	1.88	1.36	0.19	0.14
[115, 150]	16.42	0.82	1.59	1.24	0.04	0.13

Table F.34. The capacity of 2×2 MIMO system, for AB_L & AB_R, for the running body.

x [m]	$\overline{C_{MIMO}}$	$\sigma_{\overline{C_{MIMO}}}$	$\overline{\sigma_{C_{MIMO}}}$	$\overline{G_{MIMO_c}}$	$\sigma_{\overline{G_{MIMO_c}}}$	$\overline{\sigma_{G_{MIMO_c}}}$
		[bps/Hz]				
[50, 150]	17.10	2.52	1.83	1.38	0.16	0.15
[50, 85]	16.33	1.74	1.85	1.42	0.14	0.16
[85, 115]	19.91	1.66	2.02	1.38	0.16	0.14
[115, 150]	15.58	1.77	1.62	1.35	0.18	0.15

Table F.35. The capacity of 2×2 MIMO system, for AB_L & TO_B, for the running body.

x [m]	$\overline{C_{MIMO}}$	$\sigma_{\overline{C_{MIMO}}}$	$\overline{\sigma_{C_{MIMO}}}$	$\overline{G_{MIMO_c}}$	$\sigma_{\overline{G_{MIMO_c}}}$	$\overline{\sigma_{G_{MIMO_c}}}$
		[bps/Hz]				
[50, 150]	18.44	4.20	1.92	1.42	0.17	0.15
[50, 85]	14.28	2.00	1.70	1.32	0.13	0.16
[85, 115]	22.43	2.89	2.17	1.50	0.14	0.14
[115, 150]	19.34	2.83	1.91	1.45	0.18	0.15

Table F.36. The capacity of 2×2 MIMO system, for AB_R & TO_B, for the running body.

x [m]	$\overline{C_{MIMO}}$	$\sigma_{\overline{C_{MIMO}}}$	$\overline{\sigma_{C_{MIMO}}}$	$\overline{G_{MIMO_c}}$	$\sigma_{\overline{G_{MIMO_c}}}$	$\overline{\sigma_{G_{MIMO_c}}}$
		[bps/Hz]				
[50, 150]	16.68	3.10	1.85	1.40	0.16	0.15
[50, 85]	13.99	1.94	1.76	1.43	0.11	0.17
[85, 115]	19.23	2.12	2.14	1.48	0.14	0.15
[115, 150]	17.31	2.60	1.65	1.30	0.17	0.13

Annex G. MIMO Performance

The capacity performance of 2×2 MIMO system, for the running body is presented in Figure G.1 and Figure G.2.

Figure G.1. The capacity performance of 2×2 MIMO system, for the running body (part 1).

Figure G.2. The capacity performance of 2×2 MIMO system, for the running body (part 2).

The capacity performance of 2×2 MIMO system, for the walking body is presented in Figure G.3 and Figure G.4.
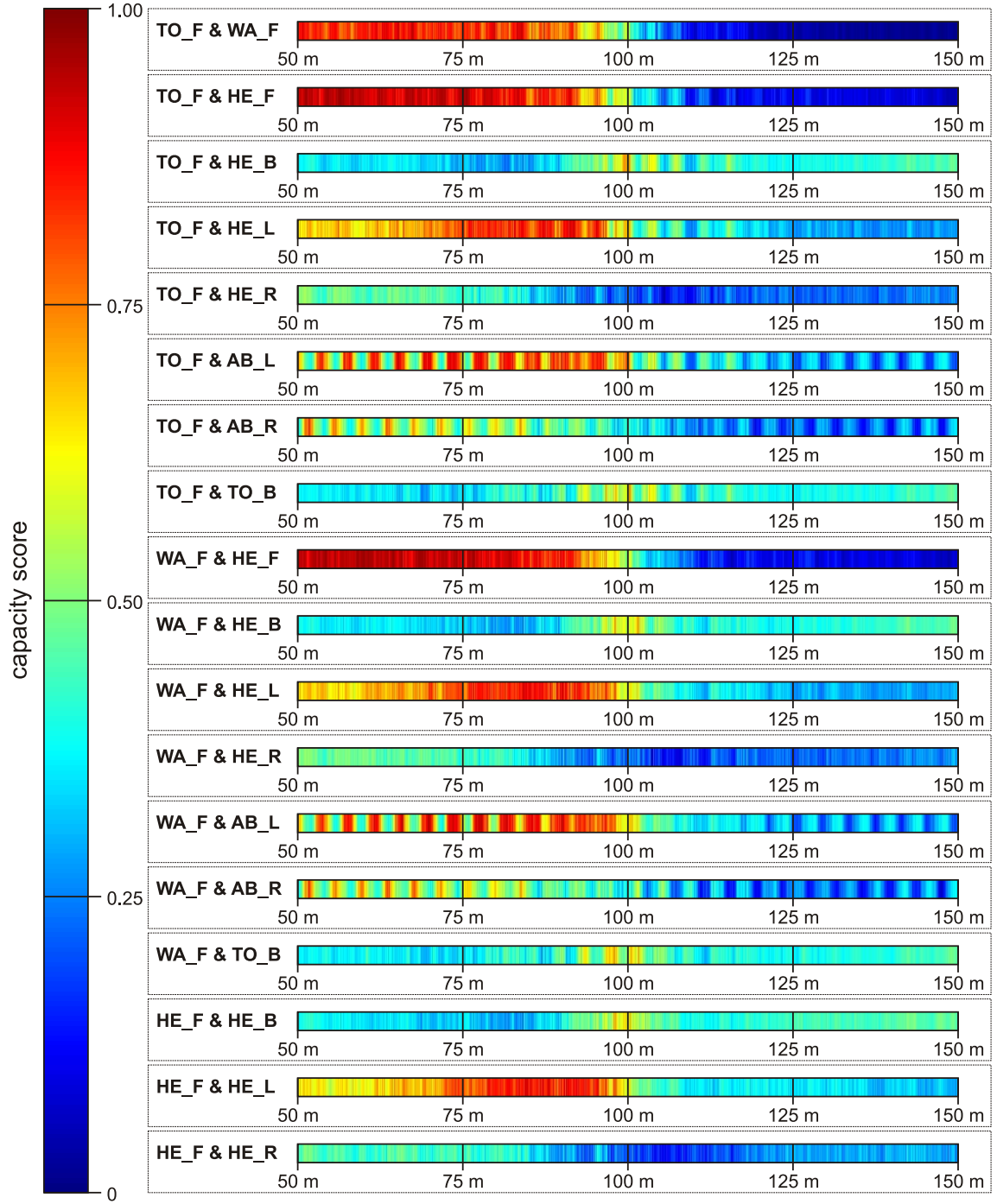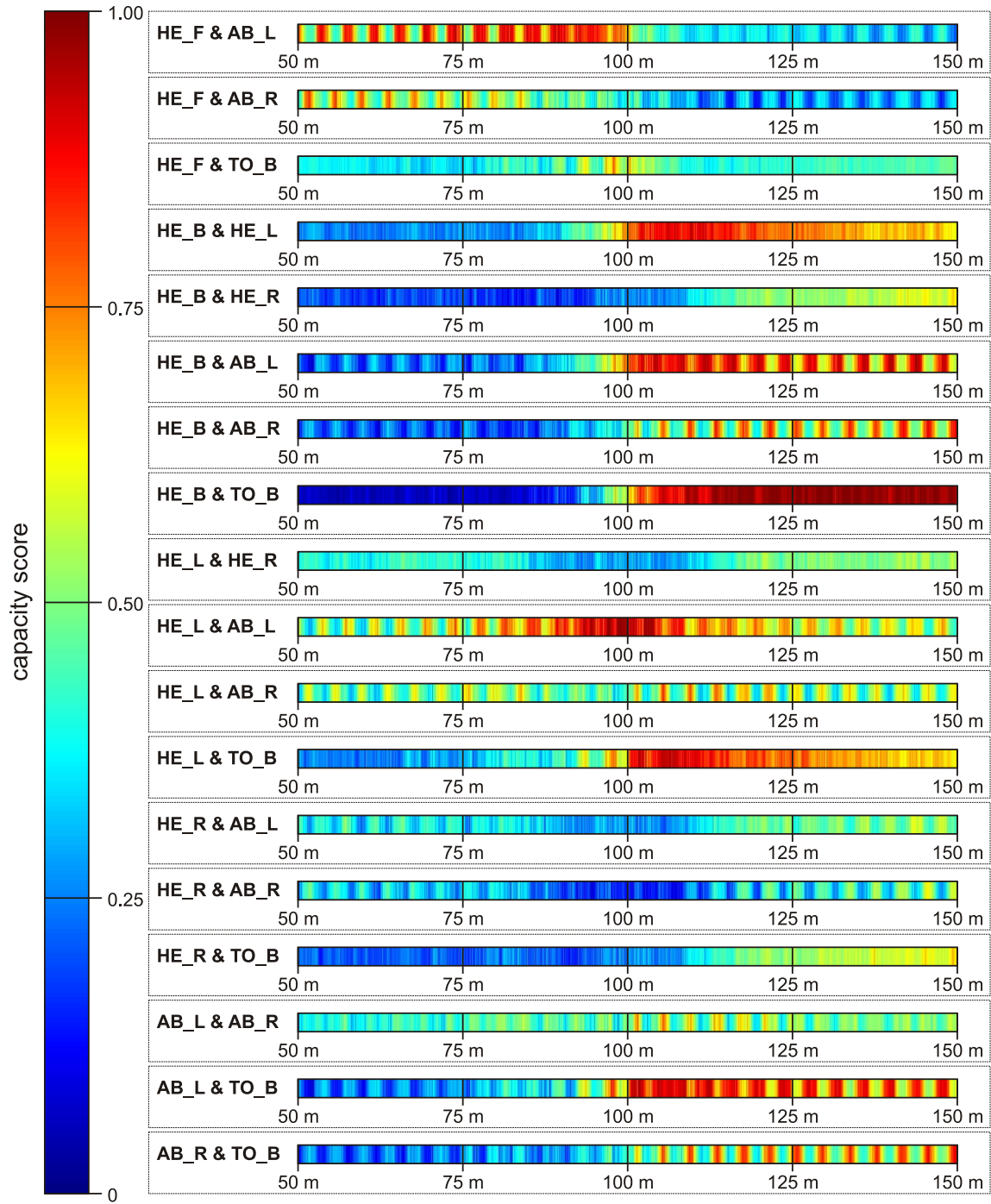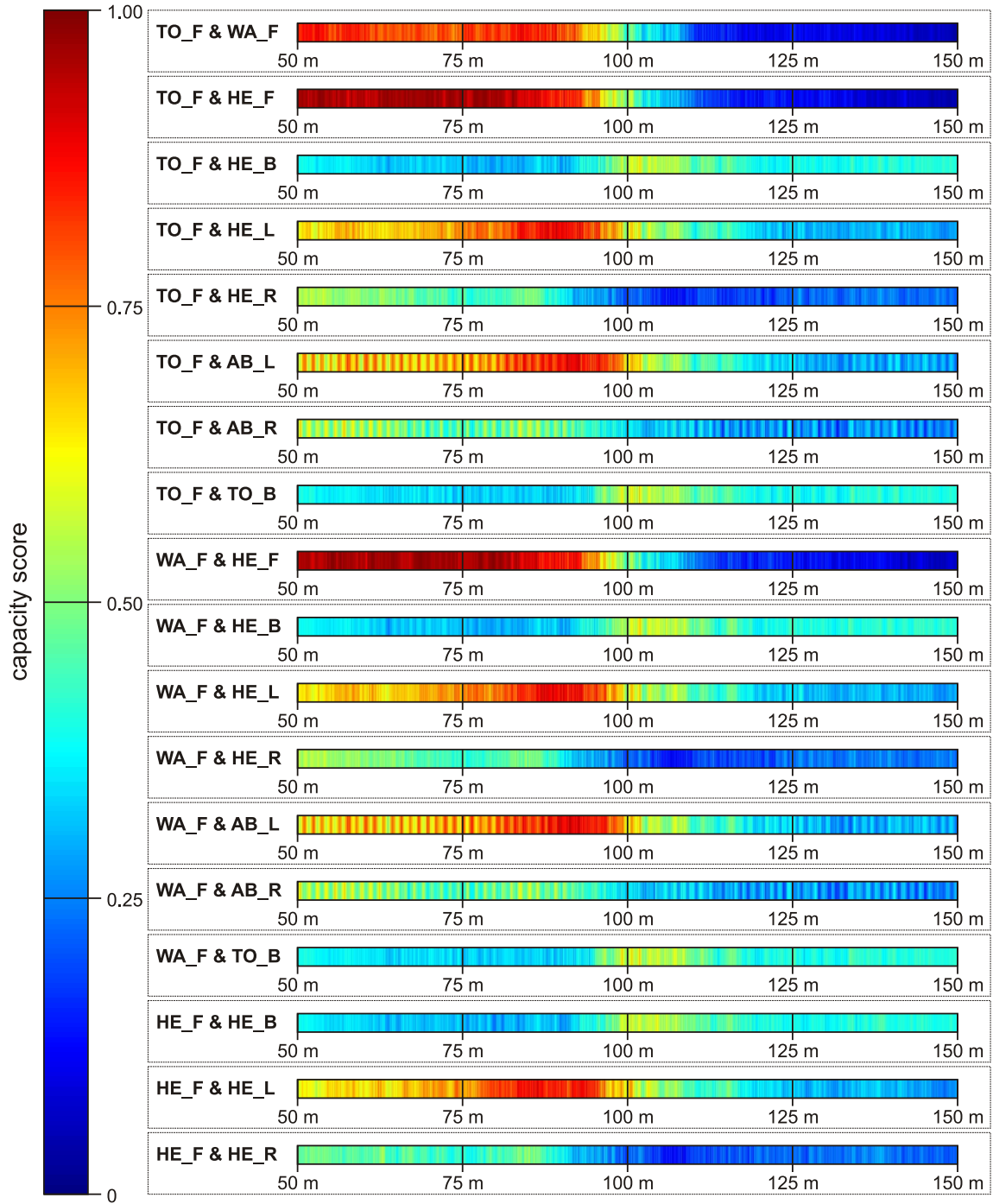

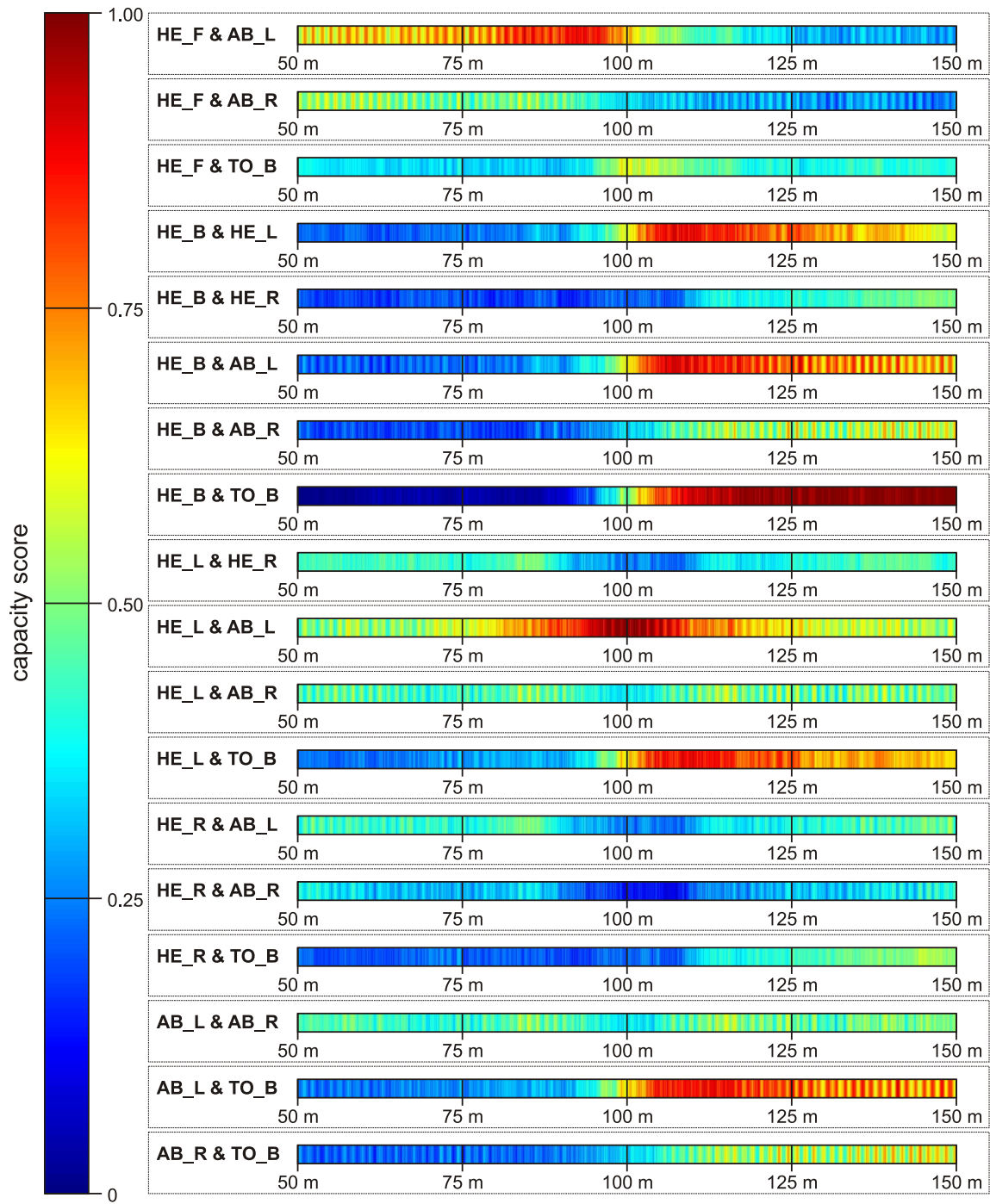Figure G.3. The capacity performance of 2×2 MIMO system, for the walking body (part 1).

Figure G.4. The capacity performance of 2×2 MIMO system, for the walking body (part 2).

References

[3GPP13]   3GPP - The 3rd Generation Partnership Project, http://www.3gpp.org, Feb. 2013.

[AAKC12]   Ahn,C., Ahn,B., Kim,S. and Choi,J., "Experimental Outage Capacity Analysis for Off-body Wireless Body Area Network Channel with Transmit Diversity", *IEEE Transactions on Consumer Electronics*, Vol. 58, No. 2, May 2012, pp. 274-277.

[AIKT11]   Aoyagi,T., Iswandi,I., Kim,M., Takada,J., Hamaguchi,K. and Kohno,R., "Body Motion and Channel Response of Dynamic Body Area Channel", in *Proc. of EuCAP'2011 - 5th European Conference on Antennas and Propagation*, Rome, Italy, Apr. 2011.

[AKTH11]   Aoyagi,T., Kim,M., Takada,J., Hamaguchi,K. and Kohno,R., "Numerical Simulations for Dynamic WBAN Propagation Channel during Various Human Movements", in *Proc. of ISMICT'2011 - 5th International Symposium on Medical Information and Communication Technology*, Montreux, Switzerland, Mar. 2011.

[ASAH09]   Abbasi,Q., Sani,A., Alomainy,A. and Hao,Y., "Arm Movements Effect on Ultra Wideband On-Body Propagation Channels and Radio Systems", in *Proc. of LAPC'2009 - Loughborough Antennas and Propagation Conference*, Loughborough, UK, Nov. 2009.

[AlCS09]   Ali,A.J., Cotton,S.L. and Scanlon,W.G., "Spatial Diversity for Off-Body Communications in an Indoor Populated Environment at 5.8 GHz", in *Proc. of LAPC'2009 - Loughborough Antennas and Propagation Conference*, Loughborough, UK, Nov. 2009.

[Asze96]   Aszetly,D., *On Antenna Arrays in Mobile Communication Systems: Fast Fading and GSM Base Station Receiver Algorithms*, Ph.D. Thesis, Royal Institute of Technology, Stockholm, Sweden, Mar. 1996.

[Bala05]   Balanis,C.A., *Antenna Theory, Analisys and Design*, 3rd ed., John Wiley and Sons, New York, NY, USA, 2005.

[Bala89]   Balanis,C.A., *Advanced Engineering Electromagnetics*, John Wiley and Sons, New York, NY, USA, 1989.

References

[CMAS12]   Cotton,S.L., McKernan,A., Ali,A.J. and Scanlon,W.G., "An Experimental Study on the Impact of Human Body Shadowing in Off-body Communications Channels at 2.45 GHz", in *Proc. of EuCAP'2012 - 6th European Conference on Antenna and Propagation*, Prague, Czech Republic, Apr. 2012.

[COST01]   COST 259, http://info.grow.inov.pt/cost259, Dec. 2001.

[COST07]   COST 273, http://info.grow.inov.pt/cost273, Dec. 2007.

[COST10]   COST 2100, http://www.cost2100.org, Dec. 2010.

[COST13]   COST IC1004, http://www.ic1004.org, Feb. 2013.

[COST89]   COST 207, *Digital Land Mobile Radio Communications*, Final Report, COST Telecom Secretariat, European Commision, Brussels, Belgium, 1989.

[COST99]   COST 231, *Digital Mobile Radio Towards Future Generation Systems*, Final Report, COST Telecom Secretariat, European Commision, Brussels, Belgium, 1999.

[CST12]   CST - Computer Simulation Technology, http://www.cst.com, July 2012.

[ChCS09]   Chandran,A.R., Conway,G.A. and Scanlon,W.G., "Pattern Switching Compact Patch Antenna for On-body and Off-body Communications at 2.45 GHz", in *Proc. of EuCAP'2009 - 3rd European Conference on Antennas and Propagation*, Berlin, Germany, Mar. 2009.

[Chri10]   Christ,A. *et al*, "The Virtual Family - Development of anatomical CAD models of two adults and two children for dosimetric simulations", *Physics in Medicine and Biology*, Vol. 55, No. 2, Jan. 2010, pp. 23-38.

[CoSc09]   Cotton,S.L. and Scanlon,W.G., "Channel Characterization for Single- and Multiple-Antenna Wearable Systems Used for Indoor Body-to-Body Communications", *IEEE Transactions on Antennas and Propagation*, Vol. 57, No. 4, Apr. 2009, pp. 980-990.

[Corr01]   Correia,L.M. (ed.), *Wireless Flexible Personalised Communications*, John Wiley and Sons, Chichester, UK, 2001.

[Cube06]   Cubero,S. (ed.), *Industrial Robotics: Theory, Modelling and Control*, Pro Literatur Verlag, Vienna, Austria, 2006.

[Czin07]   Czink,N., *The Random-Cluster Model*, Ph.D. Thesis, Technical University of Vienna, Vienna, Austria, 2007.

[DCSZ10]   Dai,H., Cai,B., Song,J. and Zhang,D., "Skeletal Animation Based on BVH Motion Data", in *Proc. of 2nd International Conference on Information Engineering and Computer Science*, Wuhan, China, Dec. 2010.

[Dziu04]   Dziunikowski,W., *Multiple-Input Multiple-Output Antenna Systems*, in Chandran,S. (ed.), *Adaptive Antenna Arrays*, Springer, Berlin, Germany, 2004.

[ETSI13]   ETSI - European Telecommunications Standards Institute, http://www.etsi.org, Feb. 2013.

[ErOu10]   Errico,R. and Ouvry,L., "A Statistical Model for On-Body Dynamic Channels", *International Journal of Wireless Information Networks*, Vol. 17, No. 3, Sep. 2010, pp. 92-104.

[FoGa98]   Foschini,G.J. and Gans,M.J., "On Limits of Wireless Communications in a Fading Environment when Using Multiple Antennas", *Wireless Personal Communication*, Vol. 6, No. 3, Mar. 1998, pp. 311-335.

[GHBN11]   Gallo,M., Hall,P.S., Bai,Q., Nechayev,Y.I., Constantinou,C.C. and Bozzetti,M., "Simulation and Measurement of Dynamic On-Body Communication Channels", *IEEE Transactions on Antennas and Propagation*, Vol. 59, No. 2, Feb. 2011, pp. 623-630.

[GaHB07]   Gallo,M., Hall,P.S. and Bozzettil,M., "Use of Animation Software in the Simulations of On-Body Communication Channels", in *Proc. of LAPC'2007 - Loughborough Antennas and Propagation Conference*, Loughborough, UK, Apr. 2007.

[Gabr96]   Gabriel,C., *Compilation of Dielectric Properties of Body Tissues at RF and Microwave Frequencies*, Brooks Air Force Technical Report, AL/OE-TR-1996-0037, San Antonio, TX, USA, 1996.

[Glas89]   Glassner,A.S., *An Introduction to Ray Tracing*, Academic Press, New York, NY, USA, 1989.

[GrNi96]   Greenwood,P.E. and Nikulin,M.S., *A Guide to Chi-squared Testing*, John Wiley and Sons, New York, NY, USA, 1996.

[HaHa06]   Hall,P. and Hao,Y., *Antennas and Propagation for Body-Centric Wireless Communications*, Artech House, Norwood, MA, USA, 2006.

[Hall07]   Hall,P.S., "Antennas Challenges for Body Centric Communications", in *Proc. of IWAT'2007 - International Workshop on Antenna Technology: Small and Smart Antennas Metamaterials and Applications*, Cambridge, UK, Mar. 2007.

References

[HeUl09]	Henneberg,M. and Ulijaszek,S., "Body Frame Dimensions are Related to Obesity and Fatness: Lean Trunk Size, Skinfolds, and Body Mass Index", *American Journal of Human Biology*, Vol. 22, No. 1, Apr. 2009, pp. 83-91.
[Hine96]	Hines,J.W., "Medical and Surgical Applications of Space Biosensor Technology", *Acta Astronautica*, Vol. 38, No. 4-8, Feb./Apr. 1996, pp. 261-267.
[IEEE13a]	IEEE 802, http://www.ieee802.org, Feb. 2013.
[IEEE13b]	IEEE 802.15 Working Group for Wireless Personal Area Networks - Task Group 6 (BAN), http://www.ieee802.org/15/pub/TG6.html, Feb. 2013.
[KHGN08]	Khan,I., Hall,P., Guraliuc,A. and Nepa,P., "Reciprocity and Repeatability of Diversity Measurements for On-Body Communication Channels at 2.45 GHz", in *Proc. of IEEE International Antennas and Propagation Symposium*, San Diego, CA, USA, July 2008.
[KTIV06]	Krogerus,J., Toivanen,J., Icheln,C. and Vinikainen,P., "User Effect on Total Radiated Power and 3D Radiation Pattern of Mobile Handsets", in *Proc. of EuCAP'2006 - 1st European Conference on Antennas and Propagation*, Nice, France, Nov. 2006.
[KhHa10]	Khan,I. and Hall,P.S., "Experimental Evaluation of MIMO Capacity and Correlation for Narrowband Body-Centric Wireless Channels", *IEEE Transactions on Antennas and Propagation*, Vol. 58, No. 1, Jan. 2010, pp. 195-202.
[KmPN96]	Knoblauch,R., Pietrucha,M. and Nitzburg,M., "Field Studies of Pedestrian Walking Speed and Start-up Time", *Transportation Research Record 1538*, Transportation Research Board, National Research Council, Washington, DC, USA, 1996, pp. 27-38.
[Kosi04]	Kosilo,T., *Mobile Terrestial Radiocommunications* (in Polish), Internal Document, Warsaw University of Technology, Warsaw, Poland, 2004.
[Kuma80]	Kumaraswamy,P., "A Generalized Probability Density Function for Double-bounded Random Processes", *Journal of Hydrology*, Vol. 46, No. 1-2, Mar. 1980, pp. 79-88.
[LEXN13]	LEXNET - Low EMF Exposure Future Networks, http://grow.inov.pt/projects/lexnet, Feb. 2013.
[LKCD11]	Liu,L., Keshmiri,F., Craeye,C., Doncker,P. and Oestges,C., "An Analytical Modeling of Polarized Time-Variant On-Body Propagation Channels with Dynamic Body Scattering", *EURASIP Journal on Wireless Communications and Networking*, Vol. 2011, Apr. 2011.

[LRDO09]   Liu,L., Roy,S., Doncker,P. and Oestges,C., "Azimuth Radiation Pattern Characterization of Omnidirectional Antennas Near a Human Body", in *Proc. of ICEAA'2009 - 11th International Conference on Electromagnetics in Advanced Applications*, Torino, Italy, Sep. 2009.

[LaFL12]   Langley,R.J., Ford,K.L. and Lee,H.J., "Switchable On/Off-body Communication at 2.45 GHz Using Textile Microstrip Patch Antenna on Stripline", in *Proc. of EuCAP'2012 - 6th European Conference on Antennas and Propagation*, Prague, Czech Republic, Mar. 2012.

[LiRa99]   Liberti,J. and Rappaport,T., *Smart Antennas for Wireless Communication: IS-95 and Third Generation CDMA Applications*, Prentice Hall, Upper Saddle River, NJ, USA, 1999.

[MCCF07]   Medeiros,C.R., Castela,A.M., Costa,J.R. and Fernandes,C.A., "Evaluation of Modelling Accuracy of Reconfigurable Patch Antennas", in *Proc. of ConfTele - Conference on Telecommunications*, Peniche, Portugal, May 2007.

[MOLC11]   Mackowiak,M., Oliveira,C., Lopes,C.G. and Correia,L.M., "A Statistical Analysis of the Influence of the Human Body on the Radiation Pattern of Wearable Antennas", in *Proc. of PIMRC'2011 - 22nd IEEE International Symposium on Personal, Indoor and Mobile Radio Communications*, Toronto, Canada, Sep. 2011.

[MREC13]   Mackowiak,M., Rosini,R., Errico,R. and Correia,L.M., "Comparing Off-Body Dynamic Channel Model with Real-Time Measurements", in *Proc. of ISMICT'2013 - 7th International Symposium on Medical Information and Communication Technology*, Tokyo, Japan, Mar. 2013.

[MaCo04]   Marques,M.G. and Correia,L.M., *A Wideband Directional Channel Model for Mobile Communication Systems*, in Chandran,S. (ed.), *Adaptive Antenna Arrays*, Springer, Berlin, Germany, 2004.

[MaCo10]   Mackowiak,M. and Correia,L.M., "A Statistical Approach to Model Antenna Radiation Patterns in Off-Body Radio Channels", in *Proc. of PIMRC'2010 - 21st IEEE International Symposium on Personal, Indoor and Mobile Radio Communications*, Istanbul, Turkey, Sep. 2010.

[MaCo11]   Mackowiak,M. and Correia,L.M., "Modelling the Influence of Body Dynamics on the Radiation Pattern of Wearable Antennas in Off-Body Radio Channels", in *Proc. of 12th URSI Commission F Triennial Open Symposium on Radio Wave Propagation and Remote Sensing*, Garmisch-Partenkirchen, Germany, Mar. 2011.

[MaCo12b]   Mackowiak,M. and Correia,L.M., "Correlation Analysis in Off-Body Radio Channels in a Street Environment", in *Proc. of PIMRC'2012 - 23rd IEEE Symposium on Personal, Indoor, Mobile and Radio Communications*, Sydney, Australia, Sep. 2012.

[MaCo12c]   Mackowiak,M. and Correia,L.M., "Towards a Radio Channel Model for Off-Body Communications in a Multipath Environment", in *Proc. of EW'2012 - 18th European Wireless Conference*, Poznan, Poland, Apr. 2012.

[MaCo13a]   Mackowiak,M. and Correia,L.M., "A Statistical Model for the Influence of Body Dynamics on the Radiation Pattern of Wearable Antennas in Off-Body Radio Channels", *Wireless Personal Communications*, 10.1007/s11277-013-1193-x, May 2013

[MaCo13b]   Mackowiak,M. and Correia,L.M., "MIMO Capacity Analysis of Off-Body Radio Channels in a Street Environment", in *Proc. of VTC'2013 Spring - IEEE 77th Vehicular Technology Conference*, Dresden, Germany, June 2013.

[MaCo13c]   Mackowiak,M. and Correia,L.M., "MIMO Capacity Performance of Off-Body Radio Channels in a Street Environment", accepted to *PIMRC'2013 - 24th IEEE Symposium on Personal, Indoor, Mobile and Radio Communications*, London, UK, Sep. 2013.

[MaMy78]   Macomber,J.H. and Myers,B.L., "The Bivariate Beta Distribution: Comparison of Monte Carlo Generators and Evaluation of Parameter Estimates", in *Proc. of 10th Conference on Winter Simulation*, Miami Beach, FL, USA, Jan. 1978.

[MaOC12a]   Mackowiak,M., Oliveira,C. and Correia,L.M., "Radiation Pattern of Wearable Antennas: A Statistical Analysis of the Influence of the Human Body", *International Journal of Wireless Information Networks*, Vol. 19, No. 3, Sep. 2012, pp. 209-218.

[MaOC12b]   Mackowiak,M., Oliveira,C. and Correia,L.M., "Signal Correlation Between Wearable Antennas in Body Area Networks in Multipath Environment", in *Proc. of EuCAP'2012 - 6th European Conference on Antennas and Propagation*, Prague, Czech Republic, Mar. 2012.

[Mack07]   Mackowiak,M., *Geometrically Based Multibounce MIMO Channel Model*, M.Sc. Thesis, IST-TUL, Lisbon, Portugal, 2007.

[Moli05]   Molisch,A.F., *Wireless Communications*, Wiley-IEEE Press, West Sussex, UK, 2006.

[NEWC11]   NEWCOM++ - Network of Excellence in Wireless Communications, http://130.192.85.4:8080/Plone, Dec. 2011.

[NEWC13]   NEWCOM# - Network of Excellence in Wireless Communications, http://www.newcom-project.eu, Feb. 2013.

[NaHH10]   Nechayev,Y., Hu,Z.H. and Hall,P., "Fading of the Transmission Channel between two Wireless Body Area Networks in an Office at 2.45 GHz and 5.8 GHz", in *Proc. of LAPC'2010 - Loughborough Antennas and Propagation Conference*, Loughborough, UK, Nov. 2010.

[OMLC11]   Oliveira,C., Mackowiak,M., Lopes,C.G. and Correia,L.M., "Characterisation of On-Body Communications at 2.45 GHz", in *Proc. of BodyNets - International Conference on Body Area Networks*, Beijing, China, Nov. 2011.

[OgHo12]   Ogawa,K. and Honda,K., "BAN Shadowing Properties of an Arm-Waving Dynamic Phantom", in *Proc. of EuCAP'2012 - 6th European Conference on Antennas and Propagation*, Prague, Czech Republic, Mar. 2012.

[OlMC11]   Oliveira,C., Mackowiak,M. and Correia,L.M., "Challenges for Body Area Networks Concerning Radio Aspects", in *Proc. EW'2011 - 17th European Wireless Conference*, Vienna, Austria, Apr. 2011.

[OlMC12a]   Oliveira,C., Mackowiak,M. and Correia,L.M., *Statistical Characterisation of Antennas in BANs*, in Guillaume de la Roche, Andres Alayon-Glazunov and Ben Allen (eds.), *LTE Advanced and Beyond Wireless Networks: Channel Modelling and Propagation*, John Wiley, Chichester, UK, 2012.

[OlMC12b]   Oliveira,C., Mackowiak,M. and Correia,L.M., "A Comparison of Phantom Models for On-Body Communications", in *Proc. of PIMRC'2012 - 23rd IEEE Symposium on Personal, Indoor, Mobile and Radio Communications*, Sydney, Australia, Sep. 2012.

[OlMC12c]   Oliveira,C., Mackowiak,M. and Correia,L.M., "Correlation Analysis in On-Body Communications", in *Proc. of EuCAP'2012 - 6th European Conference on Antennas and Propagation*, Prague, Czech Republic, Mar. 2012.

[OlMC13]   Oliveira,C., Mackowiak,M. and Correia,L.M., "Modelling On- and Off-Body Channels in Body Area Networks", invited to *IMOC'2013 - International Microwave and Optoelectronics Conference*, Rio de Janeiro, Brazil, Aug. 2013.

[Orfa96]   Orfanidis,S.J., *An Introduction to Optimum Signal Processing*, Prentice-Hall, Englewood Cliffs, NJ, USA, 1996.

[POSE12]   POSER, http://poser.smithmicro.com, Dec. 2012.

[PaJa03]   Park,S. and Jayaraman,S., "Enhancing the Quality of Life Through Wearable Technology", *IEEE Engineering in Medicine and Biology Magazine*, Vol. 22, No. 3, May/June 2003, pp. 41-48.

[Path82]   Pathak,P.H., "Uniform Geometrical Theory of Diffraction", in *Proc. of Applications of Mathematics in Modern Optics*, San Diego, CA, USA, Aug. 1982.

[Proa01]   Proakis,J.G., *Digital Communications*, Mac Graw Hill, New York, NY, USA, 2001.

[RoEr12]   Rosini,R. and Errico,R., "Off-Body Channel Modelling at 2.45 GHz for Two Different Antennas", in *Proc. of EuCAP'2012 - 6th European Conference on Antennas and Propagation*, Prague, Czech Republic, Mar. 2012.

[SBMS04]   Schumacher,L., Berger,L.T., Ramiro-Moreno,J. and Sorensen,T.B., *Propagation Characterization and MIMO Channel Modelling for 3G*, in Chandran,S. (ed.), *Adaptive Antenna Arrays*, Springer, Berlin, Germany, 2004.

[SCAD12]   SEMCAD, http://www.speag.com/products/semcad/overview, Dec. 2012.

[SHZM09]   Smith,D., Hanlen,L.W., Zhang,J.A., Miniutti,D., Rodda,D. and Gilbert,B., "Characterization of the Dynamic Narrowband On-Body to Off-Body Area Channel", in *Proc. of ICC'2009 - IEEE International Conference on Communications*, Dresden, Germany, June 2009.

[SJKM03]   Sarkar,T.K, Ji,Z., Kim,K., Medouri,A. and Salazar-Palma,M., "A Survey of Various Propagation Models for Mobile Communication", *IEEE Antennas and Propagation Magazine*, Vol. 45, No. 3, June 2003, pp. 51-82.

[SaVa87]   Saleh,A.M. and Valenzuela,R.A., "A Statistical Model for Indoor Multipath Propagation", *IEEE Journal on Selected Areas in Communications*, Vol. 5, No. 2, Feb. 1987, pp. 128-137.

[Sadi00]   Sadiku,M., *Numerical Techniques in Electromagnetics*, CRC Press, Prairie View, TX, USA, 2000.

[Sibi08]   Sibille,A., "Statistical Antenna Modeling", in *Proc. of URSI - 29th General Assembly*, Chicago, IL, USA, Aug. 2008.

[Skla97]   Sklar,B., "Rayleigh Fading Channels in Mobile Digital Communication Systems. Part I", *IEEE Communications Magazine*, Vol. 35, No. 9, July 1997, pp. 136-146.

[SmHL11]   Smith,D., Hanlen,L.W. and Lamahewa,T.A., "A New Look at the Body Area Network Channel Model", in *Proc. of EuCAP'2011 - 5th European Conference on Antennas and Propagation*, Rome, Italy, Apr. 2011.

[TaKi06]   Tavakol,V. and Kildal,P.S., "Relations between Radiation Characteristics of Small Antennas Located in Free Space and Close to Lossy Phantom", in *Proc. of IEEE Antennas and Propagation Society International Symposium*, Albuquerque, NM, USA, July 2006.

[Tela95]   Telatar,I.E., *Capacity of Multi-Antenna Gaussian Channels*, ATT Bell Labs, Technical memorandum BL011217-950615-07TM, NJ, USA, June 1995, (http://www.bell-labs.com/org/physicalsciences/pubs/lozano.pdf).

[VPop12]   Virtual Population, http://www.itis.ethz.ch/services/anatomical-models, Dec. 2012.

[VTHR10]   Vallozzi,L., Torre,P., Hertleer,C., Rogier,H., Moeneclaey,M. and Verhaevert,J., "Wireless Communication for Firefighters Using Dual-Polarized Textile Antennas Integrated in Their Garment", *IEEE Transactions on Antennas and Propagation*, Vol. 58, No. 4, Apr. 2010, pp. 1357-1368.

[VaAn87]   Vaughan,R. and Andersen,J., "Antenna Diversity in Mobile Communications", *IEEE Transactions Vehicular Technology*, Vol. 36, No. 4, Nov. 1987, pp. 149-172.

[YSKO11]   Yamamoto,N., Shirakata,N., Kobayashi,D. and Ogawa,K., "BAN Communication Quality Assessments Using an Arm-Waving Dynamic Phantom Replicating the Walking Motion of a Human", in *Proc. of ICC'2011 - IEEE International Conference on Communications*, Kyoto, Japan, June 2011.